Direct Investigation of Liquid Bridges in Relation to the Mechanisms of Particle Agglomeration in Gaseous and Liquid Media

Damiano Rossetti

A thesis submitted for the degree of Doctor of Philosophy of the University of London

Department of Chemical Engineering
University College London
London WC1E 7JE

November 2002

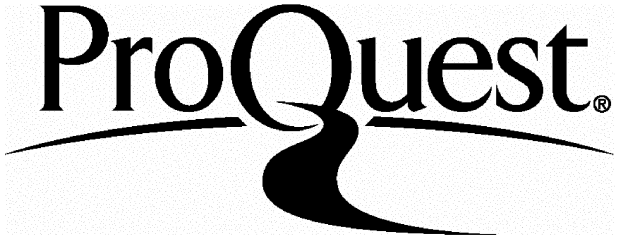

La vita e' sentimento

(Life is emotion)

To Ortensia, Luigi, Franceso, Luca and Mariadele

Acknowledgements

Funding for this project was provided by the Engineering and Physical Sciences Research Council (EPSRC Grant number GR/L77720).

I am very grateful to my supervisor, Professor Stef Simons for the opportunity he gave me to work on this project. His support was priceless, always. Mostly, I appreciated his talent to inspire the research without generating unnecessary stress. His patience and suggestions in proofreading this thesis have also been invaluable. I feel also obliged to Professor Antonino Germana' who nominated me to Stef.

I am very thankful to my friends Xavier Pepin and Marcello Murru. Xavier for his broad knowledge of surface chemistry and for the help he gave me when I was little aware of the subject. Marcello for his suggestions, criticisms, and computing skills, which have been very profitable to my research.

I also want to thank Professor Douglas Ruthven for inviting me at the Department of Chemical Engineering of the University of Maine in order to use an Atomic Force Microscope. His and his wife (Patricia) hospitality have been priceless.

The administrative and technical staffs in both Universities were very helpful and my thanks go to all of them especially to Amos Cline (Maine) who helped me with setting up the AFM.

On a personal level I want to thank Riccardo Scatolini, Michael Spyridopoulos, Federica Pratola, Paolo Pagliai, Giovanna Bruni, Paola Lettieri, Luca Cammarata, Marta Fernandez and Federico Brandani (Maine) for their friendship and support. Many other deserve special consideration and my apologies for not having mentioned them here.

Finally I would like to thank my parents, my family and Mariadele for their constant support and love.

Abstract

Particle agglomeration processes occur in a wide variety of important industrial applications, either intentionally, for product formulation purposes (e.g. pharmaceutical granulation) or unintentionally, as in the caking of powder in storage silos. Examples of agglomerated products are: fertilisers, ceramics, catalysts, pesticides, minerals, pharmaceuticals, foods (particularly 'instant' products) and detergents, where the common objective is to improve the handling and ease of use of the product.

Agglomeration can also be used as a separation technique. This is often carried out in solid/liquid suspensions, where either the desired or undesired particle species are encouraged to agglomerate by the addition of surfactants and electrolytes, so that they can then be separated from the remaining gangue. The process is referred to as spherical agglomeration, because of the final spherical geometry of the formed agglomerates; in this case the liquid binder is chosen to be immiscible with the suspending medium. Spherical agglomeration is used in the separation of minerals and valuable ores as small as 10 μm in diameter with a high grade of recovery, as well as in the manufacture of speciality chemical products.

In both agglomeration and spherical agglomeration processes the presence of particles of different wetting behaviour can create selective agglomeration of some particles at the expense of others and this phenomenon may be either beneficial, as in a selective recovery process, or undesired in the agglomeration of a formulated product. Moreover, in liquid media both the particles and the liquid binder assume a charge that can be altered by the addition of surfactants. Such conditions can largely modify the particle-to-binder interaction before any liquid bridge is formed.

This thesis reports on the extensive experimental programme undertaken to study the physiochemical properties of liquid bridges formed between pairs of particles of similar/dissimilar surface energy that are either surrounded by air or are submerged in a liquid medium. The objective was to elucidate the fundamental mechanisms governing

the initial stages of agglomeration in relation to the wetting behaviour exhibited by the particles and, for the case of a suspending liquid medium, the conditions (addition of surfactant/electrolyte) that may improve the affinity of the particle toward the liquid binder.

The experimental work on liquid bridges was carried out with a unique Micro-Force Balance (MFB), which was developed in previous work to measure liquid bridge forces in gaseous media. The present work describes the continued development of the measurement technique and its adaptation to the measurement and observation of interparticle forces in liquid media. The principal parameters investigated were the geometry (in both gaseous and liquid bulk media), the strength and the energy (in the liquid bulk medium) of a liquid bridge during separation of particles exhibiting similar or dissimilar surface energies. In the case of the experiments carried out in a liquid medium, the influence that surfactants have on the particle wetting behaviour and on the adhesiveness of the liquid bridge was also investigated.

The force exerted by a liquid bridge was largely influenced by the wetting behaviour of the liquid on the particle. Liquids that wetted both particles well produced the highest forces. This phenomenon may explain the reason why during agglomeration of different species particles with higher wettability can stay together whilst those with lower affinity toward the binder may separate again and be segregated under the influence of agitation.

The affinity of particles toward the liquid binder and its relation with the presence of surfactant/electrolytes in the bulk medium was investigated in a set of separate experiments using an Atomic Force Microscope (AFM). The latter work was undertaken at the University of Maine, USA and was aimed at determining the mutual effects that liquid bridge adhesion forces and the DLVO forces have on the mechanism of particle agglomeration in a liquid medium.

In addition a feasibility study was conducted on behalf of a pharmaceutical company, Merck, Sharp and Dohme Ltd., to determine whether the MFB technique (in the

gaseous bulk medium) could identify differences in behaviour between a paracetamol crystal and two different polymeric binders. Fresh paracetamol crystals were contacted and retracted from the two binders and differences in the amount of the liquid binder retained by the crystal were observed, which can be correlated to the mechanism of liquid binder distribution among particles during the process mixing. The success of the study demonstrated the flexibility and usefulness of the MFB approach to the investigation of real systems.

Contents

List of Figures

List of Tables

Nomenclature

a^*, a_i^*	Dimensionless separation distance with respect particle radius, generic or calculated between two configurations (i=1,2) [–]
a, a_i	Liquid bridge separation distance, generic or between particle and liquid bridge neck (i=1,2) [m]
a^*_{visc}	Dimensionless separation distance with respect particle radius in viscous regime [–]
c_i	Droplet cord length on the i^{th} (i = A,B) particle [m]
e	Deflection of flexible micropipette [m]
e	Electron charge [1.61 10^{-19} C]
e_r	Energy coefficient of restitution after particle impact [–]
f(p)	Coefficient of retardation effect [–], see (3.31)
f_r	Friction factor [–]
g	Gravity acceleration [9.81 m/s^2]
h_f	Thickness of particle coating film [m]
h_i	Height of cap of sphere for the i^{th} (i = A,B) particle [m]
h_x	Asperity height [m]
k	Boltzmann constant [1.38 10^{-23} J/K]
k_d	Dissociation constant [concentration units]
k_s	Flexible micropipette spring constant [N/m]
m	Particle mass [kg]
n,i	Frequency number for setting Burleigh motor speed (i= 1,2) [–]
n_i	number of moles of component i (i= 1,2) [mol]
n_j	number of moles of a component in the j^{th} phase (j= A,B) [mol]
n_{tot}	Total number of moles of [mol]
n^{σ}_i	Excess quantity of number of moles of component i (i= 1,2) [mol]
n^{σ}_j	Excess quantity of number of moles of a component in the j^{th} phase (j= A,B) [mol]

p	Normalised separation distance with respect wave length λ [–], $p = \frac{2\pi a}{\lambda}$
p	Wetting perimeter [m]
r	Radius of triple contact line [m]
r_i	Liquid bridge radii of curvature (i = 1,2) [m]
rx, rx_i	Refractive index, generic or of phase i (i = 1,2) [–]
t	Time [s]
u	Analytical description of the profile assumed by a particle contacting a liquid bridge, u = u(x) [m]
u_i	Liquid droplet radius on the i^{th} (i = A,B) particle [m]
v	Relative particle separation velocity [m/s]
v_{motor}	Vertical velocity of Burleigh motor [m/s]
v_o	Particle approach velocity [m/s]
w	Thermodynamic work [J]
x	Horizontal axis [m]
y, y_i	Liquid bridge ordinate, generic or calculated at point A, B (i=A,B) [m]
y', y'_i	First derivative of y, generic or calculated at point A, B (i=A,B) [–]
y"	Second derivative of y [m^{-1}]
z_i	Ions valence of species i [–]
A	Helmholtz free energy [J]
A_{br}, $A_{br,i}$	Area of the liquid bridge profile, generic or of configuration i (i = 1,2) [m^2]
A_{dew}	Solid-liquid interfacial area, usually a cap of a sphere [m^2]
A_{drop}	Liquid droplet area [m^2]
A_H	Hamaker constant [J]
A_{int}	Area of the interfaces [m^2]
$A_{SL-i,j}$	Solid-liquid interfacial area for configuration i and particle j (i = 1,2; j=A,B) [m^2]
B	Integration coefficient, $B = y_A \sin(\theta_A + \beta_A)\frac{\Delta P}{2\gamma_L} y_A{}^2$ [m]
C	Dimensionless parameter [–], $C = \sqrt{\frac{(1+2\tilde{V}_{br})^{1/3}}{\pi(1+\theta/2)^2}}$
Ca	Capillary number [–]

F	Force between particles [N]
F_b	Liquid bridge force calculated at the particle-meniscus boundary [N]
F_{br}	Liquid bridge force measured experimentally with the MFB [N]
F_c	Force between conductive particles [N]
F_i	Force between insulating particles [N]
F_{max}	Maximum liquid bridge force [N]
F_n	Liquid bridge force calculated at the neck of the meniscus [N]
F_N	Normal force between agglomerates [N]
F_T	Tangential force between agglomerates [N]
F_{vis}	Total viscous force in a liquid bridge [N]
G	Gibbs free energy [J]
$\overline{R}$	Geometric average radius, $\overline{R} = \frac{2 R_A R_B}{R_A + R_B}$, [m]
H^*	Dimensionless mean curvature [–], $H^* = \frac{\Delta P R}{2\gamma}$
${}^{j}\Gamma_i$	Surface excess concentration of component i calculated where n^{σ}_j is = 0 (i, j= 1,2) [mol/m^2]
L	Characteristic length of liquid bridge [m]
M	Integration constant [–]
N	Avogadro number [6.02 10^{-23} mol^{-1}]
P, P_i	Pressure, generic or for configuration i (i = 1,2) [Pa]
P_{ext}	External medium pressure [Pa]
Q	Mean diameter of Du Nouy ring [m]
R, R_i	Particle radius, generic or for particle ith (i = A,B) [m]
R_{ag}	Agglomerate radius [m]
Re	Reynolds number $\frac{v R \rho}{\eta}$ [–]
R_{dr},	Liquid binder droplet radius [m]
R_T	Effective radius for Derjaguin approximation [m], $\frac{1}{R_T} = \frac{1}{R_A} + \frac{1}{R_B}$
S	Entropy [J/K]
S_p	Spreading Coefficient [J],

St Stokes number [–], $St = \frac{2mv_0}{3\pi\eta R^2}$

St_{def} Stokes deformation number [–], $St_{def} = \frac{16\rho_p v_o^2}{2\tau_s}$

St_{def}^* Critical Stokes deformation number [–]

S^σ Surface excess entropy [J/K]

T Absolute temperature [K]

T_i Liquid droplet cap height on the i^{th} (i = A,B) particle [m]

U Internal energy [J]

U_C Contact potential [J]

U^σ Surface excess internal energy [J]

V Volume [m^3]

V_{br} Volume of liquid bridge [m^3]

V_{br}^* Dimensionless liquid bridge volume with respect cubed particle radius [–]

$V_{cap,i}$ Volume of cap of sphere for the i^{th} (i = A,B) particle [m^3]

V_m Volumes of revolution of the liquid bridge meniscus [m^3]

$V_{m,A}$, $V_{m,B}$ Volumes of revolution of the liquid bridge meniscus, from particle A to liquid bridge neck and from neck to particle B, respectively [m^3]

V^σ Surface excess volume [m^3]

W Rupture energy of liquid bridge [J]

W^* Dimensionless rupture energy of liquid bridge [–], $W^* = \frac{W}{\gamma_L R^2}$

$\hat{W}$ Interaction free energy per unit area [J/m^2]

W_{adh} Work of adhesion [J]

$\hat{W}_{CC}$ Electrical double layer free energy per unit area for constant potential model [J/m^2]

W_{coh} Work of cohesion [J]

$\hat{W}_{dl}$ Electrical double layer free energy per unit area [J/m^2]

W_E Electron work [J]

$\hat{W}_{PP}$ Electrical double layer free energy per unit area for constant charge model [J/m^2]

$\hat{W}_{vdW}$ Van der Waals free energy per unit area [J/m^2]

X Dimensionless factor [–], $X = (1+\frac{a}{2R})$

X_c Dimensionless liquid bridge abscissa with respect particle radius, evaluated at the contact with the particle [–]

X_d Driven movement [m]

X_f Follower movement [m]

X_i Dimensionless liquid bridge abscissa with respect particle radius, evaluated at point i [–]

$X_{min,max}$ Dimensionless X calculated at minimum and maximum liquid bridge separation distance [–]

Y_i, Y_o, Y_c Dimensionless liquid bridge ordinate with respect particle radius [–]

Y_i' First derivative of dimensionless liquid bridge ordinate evaluated at point i [–]

Y_i" Second derivative of dimensionless liquid bridge ordinate evaluated at point i [–]

Greek Letters

α_i Polynomial coefficients (i=0 to 4) [m^{-i+1}]

β, β_i Half filling angle, generic or calculated at point A, B (i=A,B) [rad]

β_c correction factor for Du Nouy surface tension measurements [–]

δ_{SH} Stern Helmholtz layer thickness [m]

ε Relative dielectric constant [–]

ε_o Vacuum dielectric constant [8.85 10^{-12} C^2 J^{-1} m^{-1}]

γ Surface tension [N/m]

γ^-, γ_i^- Electron donor component of γ^{AB}, generic or of i^{th} species (i=1,2) [N/m]

γ^+, γ_i^+ Electron acceptor component of γ^{AB}, generic or of i^{th} species (i=1,2) [N/m]

γ_{12} Interfacial tension between species 1 and 2 [N/m]

γ^{AB} Polar component of surface tension according to acid/base (Lewis) definition [N/m]

γ^d, γ_i^d	Dispersive component of surface tension generic or of i^{th} species (i=1,2) [N/m]
γ^d_L	Dispersive part of surface tension of liquid binder [N/m]
γ_{int}	Interfacial tension [N/m]
γ_L	Surface tension of liquid binder toward external medium (either gas or liquid) [N/m]
γ_{LL}	Interfacial tension in a liquid [N/m], by definition = 0
γ^P, γ_i^P	Polar component of surface tension, generic or of i^{th} species (i=1,2) [N/m]
γ_S	Surface tension of solid toward external medium (either gas or liquid) [N/m]
γ_{SL}	Interfacial tension between solid and liquid, usually binder (either in gas or liquid bulk medium) [N/m]
η	Dynamic viscosity [Pa s]
η_a	Apparent viscosity of the mixture of powders [Pa s]
κ	Inverse of Debye length [m^{-1}]
λ	Wave length of the characteristic molecular motion [m]
μ_i	chemical potential of species i (i=1,2) [V]
θ, θ_i	Contact angle generic or calculated at point i (i=A,B) [rad]
θ_i	Intrinsic contact angle [rad]
$\theta_{i,j}$	Apparent contact angle for configuration i and particle j (i = 1,2; j=A,B) [rad]
θ_Y	Young contact angle [rad]
ρ	Mass density [kg/m^3]
ρ_∞, $\rho_{\infty i}$	Bulk ion density, generic or of species i [m^{-3}]
ρ_{oi}	Surface ion density of species i [m^{-3}]
ρ_p	Bulk powder mass density [kg/m^3]
σ, $\sigma_{1,2}$	Surface charge density, generic or for particle i (i =1,2) [C/m^2]
ς_o	Dimensionless potential [–] $\frac{e\psi_0}{kT}$
τ	Line tension [N]
τ_s	Characteristic stress in the granule [N/m^2]

τ_y	Granule yield stress [N/m^2]
ω	Rotational speed of granulator [rad/s]
Ψ_d	Stern-Helmholtz potential [V]
Ψ_o $\psi_{i\infty}$	Surface electrical potential of isolated surface or of i^{th} particle (i=1,2) when particles are at infinite distance apart [V]
ψ,ψ_o	Surface electrical potential, generic or calculated at distance x_o from the surface [V]
ψ_i	Surface electrical potential on the surface i^{th} (i=0,1,2) when particles are at finite distance apart [V].
ζ	Zeta potential [V]
Γ, Γ_i	Surface excess concentration, generic or of component i (i=1,2) [mol/m^2]
Λ	Average shear rate of the mixer [rad/s]
Ω	Angle between normal to liquid bridge profile and x axis [rad]

Chapter 1

1 Introduction

Agglomeration is a particle design process and is defined as formation of larger granules "by agitation or random motion of a bed of particles" [1]. Primary particles are agglomerated in larger grains to generate specific size or shape or to enhance particle properties, such as the rate of dissolution or bulk density, with the common objective of improving both the manufacturing and the final use of a product.

Agglomeration finds application in many industries including mineral processing, agricultural and chemical products, pharmaceuticals, detergents, and foodstuffs (particularly 'instant' products). It occurs either by the collision and successful adherence of primary feed particles into discrete granules [2] or by growth centred around a nucleus onto which particles collide and attach themselves to form a layer [3]. In both cases it is favoured by addition of a liquid (binder), which forms liquid bonds between particles that hold them together ("wet" or "binder-induced" agglomeration). According to Iveson et al. [4], the turnout of products manufactured by wet agglomeration is estimated at 1 trillion US$ in the US alone.

Wet agglomeration can be performed in either a gaseous or a liquid suspending medium. This latter technique is prevalently employed by the mineral industry (spherical agglomeration) and more recently for pharmaceutical drug production (spherical crystallization). When the suspending phase is a liquid, the binder has to be immiscible with it.

Despite its large commercial use, wet agglomeration is not fully understood and many authors have contributed to gain a better picture of agglomeration phenomena over the last fifty years [4]. Difficulties in predicting agglomeration consist of determining the complex interaction of a large number of particles, usually of different species, both

with themselves and with the liquid binder under different conditions of particle agitation, binder selection and binder distribution.

The desired attributes of the product granules are controlled by the combination of basic particles-binder interaction and operating parameters, such as agitation speed and binder distribution. Whilst the latter factors influence process optimisation, the study of the basic interaction provided by formation of liquid bridges between particles determines whether or not a liquid binder is suitable for a certain mixture of powders that may exhibit difference surface energies.

The focus of the work presented in this thesis is the measurement and the comparison with existing theory of the adhesiveness of liquid bridges formed between pairs of spherical particles as small as 50 μm, of either similar or dissimilar surface energies, formed in either a gaseous or a liquid bulk medium. Particle surface energy influence the geometry, the adhesiveness and the energy stored during the liquid bridge separation. Liquid bridge forces were measured using a Micro-Force Balance developed at UCL.

In the liquid phase work, the effects induced by surface active agents and electrolytes have also been considered in terms of adhesiveness of the liquid bridge and DLVO (Derjaguin, Landau, Verwey, Overbeek) interaction between the binder and the particles to understand the conditions that might favour agglomeration. The DLVO interaction between particles and liquid binder droplets was measured using an Atomic Force Microscope available at the University of Maine (US).

The major results of the present research can be summarized in the fact that the surface energies of the particles compared to that of the liquid bridge largely influence the distribution of binder between particles, as soon as a liquid bridge is broken. This binder distribution is very important at the agglomeration drying phase because the more the liquid binder is spread between particles the more homogeneous the net of solid bridges will be, which will have beneficial consequences on the mechanical properties of the product granules.

Chapter 2 focuses on wet agglomeration in both gaseous and liquid media. In the case of a gaseous suspending phase, the mechanisms of nuclei formation, granule growth and breakage are reviewed together with some theoretical models available in the literature for the description of these phenomena. The schematic of operation of a few process agglomerators (tumbling drums, high shear mixers, fluidised beds) is presented before analysing the experimental work available in the literature on the influence that process parameters have on agglomeration. For the liquid bulk medium the spherical agglomeration process is presented together with the application field where it is employed. The final part of the chapter describes the spherical crystallization process, which seems a promising technique to prepare drugs of very close specifications in a liquid medium.

Chapter 3 describes adhesive forces between particles that are relevant to the agglomeration phenomena in both liquid and gaseous media. Liquid bridge forces are analysed in term of a combination of capillary, surface tension and viscous effects after the fundamental equation (Young Laplace) for the description of the geometry assumed by a liquid bridge is reviewed. The energy stored by a liquid bridge is also considered as being an important parameter during granule deformation. The interactions arising from sintering and crystallization of liquid bridges are briefly reviewed. Van der Waals, electrical double layer and electrostatic forces are summarized as electrical effects and described in section 3.3, where the combined action of van der Waals and electrical double layer forces (DLVO interaction) is also presented. In the case of van der Waals and double layer interactions, the force between different surfaces has been derived using the Derjaguin approximation, which permits the derivation of the force between simple geometries (cylinders, spheres, plane) from the energy per unit area arising between flat surfaces. Special attention has been dedicated in deriving different models for the electrical double layer interaction between planar surfaces considering the possibilities that during the approach of the surfaces either the potential or the charge can remain constant. The chapter concludes with a comparison between forces responsible for agglomeration in a gaseous medium, in which liquid bridges are shown to have the greatest magnitude.

In order to understand how a liquid binder behaves when in contact with a particle, surface chemistry is considered in chapter 4. The nature of surface tension force is briefly reviewed in terms of basic interactions in the bulk of a liquid. Decomposition of surface tension according to different basic forces is made and used to derive a model for calculating the interfacial tension between two different liquids. The wettability of a liquid on a solid is then introduced in terms of the contact angle at a triple line interface: solid-binder-bulk phase. Definitions of Young's (thermodynamic), intrinsic and apparent contact angles are given and discussed. The line tension effect is also considered in terms of modification induced to the contact angle and to the thermodynamic energy of the interface. The section on wettability is closed by explaining the phenomenon of contact angle hysteresis and the influence it has on the geometry assumed and on the energy stored by liquid bridges. The chapter moves on with the effect surfactants have on the interfacial tension at a liquid bi-phase explained by adsorption mechanisms at the liquid interface. Surfactant adsorption is also considered on the surface of either a particle or a binder droplet (suspended in liquid bulk medium) in terms of surface charge modifications explainable either by formation of hemi-micelles or potential determining ion effect. This surface charge modification largely influences the interaction between particles and oil. The chapter ends by presenting the experimental work of a few authors who have successfully used surfactants to increase the interaction between particles and an oil phase (both suspended in a liquid) and to promote particle agglomeration.

Chapter 5 details the experimental equipment and procedures employed for the observation of the geometry of liquid bridges formed in either a gaseous or liquid medium and for force measurements (liquid bridge and DLVO interaction) taken in the liquid bulk medium. Two main devices were used: a Micro-force balance (UCL) and a more traditional Atomic Force Microscope (University of Maine – US). The MFB was the result of a previous doctoral project [5] and was designed to take liquid bridge force measurements (in the order of 10^{-8} N) between micron-sized particles in a gaseous phase (air). The technique employs glass micropipettes to hold micron-sized particles under a microscopic objective and to form a liquid bridge between pairs of them. The

chapter explains how this technique was adapted to perform similar experiments in a liquid medium. Essentially a different geometry of micropipettes and an optical clear dish were used. These micropipettes are made by 'pulling' capillary tubing to desired thickness enabling also the tip size to be varied. The straight elongated micropipettes are then deformed to the desired geometry using a gas torch and a pipette bender, both actions requiring some skill and dexterity. Liquid bridge force measurements can be either taken using electronic acquisition data or by image analysis. The second method was preferred because it allowed more flexibility in administering larger volumes of liquid bridges. The DLVO interaction between a particle and a liquid binder, immiscible with the suspending liquid phase, was investigated using an AFM at the Department of Chemical Engineering of the University of Maine (US), thanks to an invitation by the Head of Department, Prof. Douglas Ruthven. The equipment allowed for differences in the particle-binder interaction to be distinguished according to both type (anionic, cationic) and concentration of surfactant dissolved in the bulk medium. The method used to prepare and run an experiment using the AFM is described in section 5.2.5. The measurement of the surface tensions and contact angles of the bridging liquids were carried out using the Du Nouy-ring and Wilhelmy-plate methods in conjunction with a processor tensiometer. Material used for the experiments reported in this work together with method of particle surface functionalisation (silanisation) are reported in section 5.3.

Chapter 6 presents three major developments in understanding the role of liquid bridges and electrical forces (only considered for the liquid bulk medium) in agglomeration related processes. The geometry of liquid bridges was observed in either of the two media and related to the surface properties exhibited by particles. Differences in the liquid bridge geometry resulted as a consequence of the wettability exhibited by the particle towards the liquid binder. Secondly, for the experiments carried out in the liquid bulk medium, the different liquid bridge geometries were analysed in relation to the adhesiveness, the capillary pressure and the energy stored during liquid bridge separation. A thermodynamic approach to evaluate the energy of liquid bridges between two configurations is also presented. The third section illustrates the effects the addition

of different surfactant/electrolyte has on both the liquid bridge adhesiveness (MFB experiments) and the particle binder-interaction (AFM experiments).

Chapter 7 reports on additional investigations carried out during the course of this work that had direct industrial support. Using the MFB the adhesiveness of different liquid binders commonly used in the pharmaceutical industry (PVP, HPMC) has been tested between paracetamol crystals. Investigation of wettability and distribution of liquid after liquid bridge rupture were also investigated.

Conclusions and recommendations for the direction of future work are presented in chapter 8. Chapter 9 lists all of the references cited in this work.

The Appendix section is divided into five parts (A-E). Appendix A contains surface chemistry data (surface tension, interfacial tension and contact angle) obtained using a Kruss K12 Tensiometer. Some of these data were used when analysing the results detailed in Chapter 6.

Appendix B describes the mechanical measurements carried out to determine the force constant of the flexible (force measuring) glass micropipette. The design and capabilities of the MFB control electronics is described in Appendix C. The acquisition of data from and output of control functions to the electronics is computer controlled via an A/D board and specially written computer code (Appendix C.2). The processing of the acquired data and calibration checks that were carried out on the equipment is detailed in Appendix C.3.

Appendix D contains additional data for the experiments carried out using the AFM equipment. The experiments were run using software detailed in part D.1, whilst the data processing and the calibration control are reported in Appendix D.2.

The final Appendix (E) contains a list of the publications, conferences, seminars and company reports related to the work presented in this thesis.

Chapter 2

2 Particle agglomeration in gas and liquid media

A particle size enlargement process, either in a gas or liquid medium, is any process whereby small particles are gathered into larger, relatively permanent masses in which the original particle can still be distinguished. Particle size enlargement processes encompass a variety of unit operations or techniques dedicated to granulation and agglomeration.

The terms agglomeration and granulation may vary in meaning between different industries and different fields of research. Definitions are given by Sherrington and Oliver [1], who described granulation as "the building up of clusters of powder from powder or powder/binder mixtures excluding the production of granules by comminution of larger bodies" and agglomeration as "granulation by agitation of random motion of a bed of particles". The term granulation is therefore the more general and includes, for example, the formation of granules from roll pressing and extrusion.

The objective of granulation technology is the systematic production of agglomerates of closely specified properties. Compared with finely dispersed powders, granulation can lead to the following benefits [6]:

- provision of a defined quantity for dispensing and metering, as in agricultural chemical granules or in pharmaceutical tablets
- elimination of dust handling hazards or losses, as in briquetting of waste fines
- reduced caking and lump formation, as in the granulation of fertilizer
- improved flow properties, as in the granulation of pharmaceuticals for tabletting or ceramics for pressing
- increased bulk density for storage
- control of solubility, as in instant food products
- control of porosity and surface-to-volume ratio, as with catalyst supports

- improvement of heat transfer characteristics, as in ores or glass for furnace feed
- removal of particles from liquid, as with polymer additives which induce clay flocculation

Method	Product size (mm)	Granule density	Scale of operations	Additional comments	Typical application
Tumbling granulators	0.5 to 20	Moderate	0.5/800 ton/hr	Very spherical granules	Fertilizer, iron ore, non iron ore, agricultural chemical
Drums					
Discs					
Mixer granulators	0.1 to 2			Handles very cohesive material well, both batch and continuous	Chemicals, detergents, clays, carbon block, pharmaceuticals, ceramics
Continuous, high shear		Low to high	up to 50 ton/hr		
Batch, high shear		High	up to 500 kg batch		
Fluidized granulators	0.1 to 2			Flexible, relatively easy to scale, difficult for cohesive powders, good for coating applications	Continuos – fertilizers, inorganic salts, detergents. Batch – pharmaceuticals, agricultural chemicals nuclear wastes
Fluidized beds		Low	100 to 900 kg batch		
Spouted beds		Moderate	50 ton/hr		
Wurster coated					
Centrifugal granulators	0.3 to 3	Moderate to high	up to 200 kg batch	Powder layering and coating applications	Pharmaceutical, agricultural chemicals
Spray methods	0.05 to 0.5	Low		Morphology of spray dried powders can vary widely	Instant food, dyes, detergents, ceramics
Spray drying					
Prilling	0.7 to 2	Moderate			Urea, ammonium nitrate
Pressure compaction		High to		Very narrow size distribution, very sensitive to powder flow and mechanical properties	Pharmaceutical, catalyst, inorganic and organic chemicals, plastic preforms, metal parts, ceramics, clays, minerals, animal feeds
Extrusion	>0.5	very high	up to 5 ton/hr		
Roll press	>1		up to 50 ton/hr		
Tablet press	>10		up to 1 ton/hr		
Molding press					
Thermal process					
Sintering	2 to 50		up to 1 ton/hr	Strongest bonding	Ferrous and non ferrous ores, cement clinkers, mineral, ceramics
Liquid system	< 0.3	low	up to 10 ton/hr	Wet processing based on flocculation properties of particulate feed	Coal fines, soot and oil removal from water, metal dycarbite, silica hydrogels waste sludge and slurry
Immiscible wetting in mixers					
sol-gel processes					
Pellet flocculation					

Table 1 Granulation processes and applications (after [6]).

Table 1 presents some technologically relevant methods and applications of granulation processes.

Granulation finds applications in a wide range of industries, including mineral processing, agricultural products, detergents, pharmaceuticals, foodstuffs and specialty chemicals. In the chemical industry alone it has been estimated that 60% of products are manufactured as particulates and a further 20% use powders as ingredients [4]. A significant proportion of these will be in granule form

When a liquid binder, usually in the form of an aqueous solution of a polymeric compound (for example PVP, polyvinylpyrrolidone) is added to an agitated bed of the bulk mixture, the process is referred to as *wet* or *binder-induced* agglomeration.

Binder-induced agglomeration performed in either a gaseous or a liquid bulk medium is the process that can benefit most from the study presented in this thesis. Principles regulating mechanisms of agglomerate formation in both media will be therefore discussed in the following sections together with the aspects intended to be examined by work reported in this thesis. To avoid tedious repetitions, in the rest of this thesis binder-induced agglomeration will be referred to simply as agglomeration. Other forms of granulation, such as agglomeration brought about by pressure compaction, extrusion methods or by heat processes (heat reaction, fusion) are not the central focus of the work reported here and hence, will be not discussed further.

2.1 Particle agglomeration in gas media

Agglomeration in gas media (usually air) is the most important of the granulation techniques and is commonly used in the mineral, chemical, pharmaceutical and food industry to add value to products by improving handling characteristics, ease of use and physical properties, as elucidated in the previous section.

Despite its widespread use, economic importance and almost fifty years of research, the early studies dating back to the work of Capes and Danckwerts [7], agglomeration has

remained more of an art than a science. Due to the large number of parameters that might influence the agglomeration growth, there is no formal methodology for the design or operation of granulation circuits. Engineers do not predict the granulation behaviour of new formulations from their fundamental properties, neither has it been known how to vary a formulation in order to obtain a desired change in product properties [4].

Agglomerates form if primary particles in the bulk mixture collide and successfully adhere to each other. When a liquid binder is sprayed, poured or melted onto a bed of dry particles, which is agitated or mixed to favour the contact with the liquid, lens-shaped liquid menisci (liquid bridges) form and are able to keep particles together. The liquid meniscus is defined as being the curved surface of a liquid with another fluid, which is supported at least by one solid surface [8]. Tumbling drums, fluidised bed or high shear mixers are devices commonly used to provide the appropriate conditions of agitation to the bed of powder, yet introducing a mechanical shear stress that may rupture bonds already formed within an agglomerate. The growth rate of agglomerates, which depends on the equilibrium between bond formation and bond disruption is therefore influenced by the type of apparatus used for agglomeration.

2.1.1 Adhesive forces inside agglomerates

Inside granules different mechanisms of adhesion keeps particles together preventing the agglomerate breakage. These force arises from the adhesiveness of liquid bridges, from electrostatic and van der Waals (electrical/quantum mechanical) effects and from internal friction due to particle-particle contact. The contribution of liquid bridges can be split in three parts which account for the capillary pressure effect due to the curvature of the liquid bridge, to the surface tension of the liquid binder acting around the perimeter of the bridge cross-section and to the viscous effect arising from the deformation of the liquid bridge. Contrary to capillary and surface tensions effects, the viscous contribution is a strain-rate dependent term. It is worth noting that surface tension and viscous effects always act to prevent particle separation whilst the capillary effect can either be favourable or unfavourable to particle adhesion according to the

pressure inside the meniscus which depends on the configuration of the liquid bridge and ultimately on the volume of the liquid and on the interparticle separation distance. Pressure deficiencies of the liquid bridge (in comparison with the external medium) create a suction effect between particles whilst a positive gauge pressure diminishes the overall adhesiveness. Liquid bridge, electrostatic and van der Waals forces are extensively reviewed and compared in chapter 3 for the case of gaseous bulk suspending medium

The most difficult term to model among the internal granule interactions is undoubtedly the friction component despite a simple physical formulation that holds for the contact between rigid bodies of regular geometry. Friction forces, F_T, originate tangentially to particle contact and oppose any shearing action intended to separate the two bodies. Their magnitude is proportional to the normal load exerted between the bodies, F_N, according to a friction coefficient f_r, as indicated in (2.1). The friction coefficient theoretically can be unity but for common materials varies in the range between 0.1 and 0.5

$$F_T = f_r F_N \tag{2.1}$$

The picture presented above is much more complicated when real particles are taken into account which can be deformable [9], rough and of irregular shape. In this latter case phenomena of particle interlocking can also occur due to contact of irregular area presenting large asperities [10]. Evaluating the friction force inside a deformed agglomerate is not trivial because both the adhesive interparticle forces described above (liquid bridge, electrostatic and van der Waals effects) and the repartition (among single particles) of the mechanical action induced on the granule by agitation have to be taken into account to evaluate F_N from which F_T is calculated. Therefore computer simulations are usually required for determining the deformation of agglomerates [11]. The problem of the determination of friction forces is further complicated by the content of liquid binder inside the granule, which can lubricate the contact between particles reducing the friction coefficient (see section 2.1.4).

In the final stage of the agglomeration, during the phase of drying, the liquid bridges will solidify between particles, due to evaporation of the binder solvent. The formation of solid bridges, briefly reviewed in section 3.2, confers the final strength to the agglomerate, i.e. its ability to resist external mechanical action.

2.1.2 Mechanisms of agglomerate growth

A recent approach for the investigation of agglomeration processes [6, 12] recognizes three different stages of the agglomerate formation, as shown in Figure 2-1:

- *Wetting and nucleation*, where the liquid binder is brought into contact with a dry powder bed, and is distributed throughout the bed to give a distribution of nuclei granules
- *Consolidation and coalescence*, where collisions between two granules, granules and feed powder, or a granule and the equipment lead to granule compaction and growth
- *Attrition and breakage*, where wet or dried granules break due to impact, wear or compaction in the granulator or during subsequent product handling

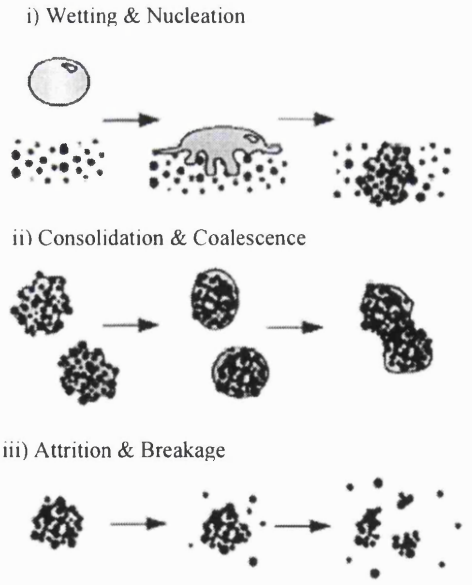

Figure 2-1 Agglomeration growth: (i) wetting and nucleation, (ii) consolidation and coalescence, (iii) attrition and breakage (after [4]).

i) Wetting and nucleation mechanisms

The initial state of agglomeration, where the liquid binder is added to a bed of dry powders and redistributes among particles, is a very delicate phase of the granulation process because it can influence the properties and characteristics of the final product. The initial area where the liquid and the particle first come into contact is called the *nucleation zone* [4]. Two processes are important in the nucleation zone: the *nuclei formation* and the *liquid binder distribution.* The demarcation line between these two phenomena is difficult to draw and any attempt of modelling should take into account their mutual influence.

The formation of small agglomerates of primary particles (nuclei) and the distribution of liquid binder depend essentially on the surface properties of the liquid/particle pair, on the physical properties of the binder and on the initial size of the droplet. Surface properties are usually characterized by the wettability of the powder towards the binder and the ability of the binder to spread across the surface of the dry powder. Both these parameters, discussed in section 4.2, influence the capability for a particle to form larger contact with the binder, which ultimately is beneficial to the distribution of the binder between particles and to the adhesion of liquid bridges formed between pairs of particles. Rowe [13] reported that a larger spreading coefficient favours the mechanical properties of granules obtained after drying. These aspects will be discussed in more detail in chapter 7, whilst the experimental evidence of the role wettability has on both the liquid binder distribution and the adhesiveness of liquid bridges will be presented in section 6.1 and 6.2, respectively.

A model to describe the influence the droplet size has on the nuclei formation has been proposed by Schaefer and Mathiesen [14], who suggested two possible mechanisms of nucleation. If the drop is large compared to the particles, nucleation will occur by immersion of the smaller particles into the larger drop and produces nuclei whose inner pores are entirely saturated by the liquid (see Figure 2-1b). Nucleation with relatively small drops (same size as the primary particles) will occur by distribution of the drops on the surface of the particles, which will then start to coalesce by formation of

individual liquid bridges (see Figure 2-1b). The influence of the droplet size on the mechanisms of the further steps of granule growth and the correlation with the final granule dimension will be discussed in the next section.

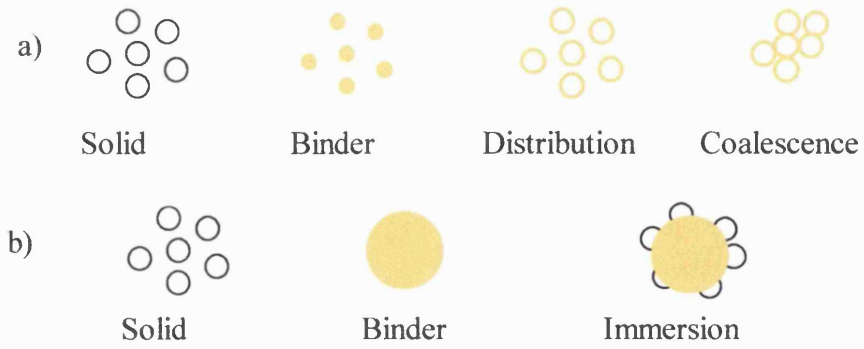

Figure 2-2 The nucleation formation mechanism may depend of the relative sizes of the binder droplet to primary particle size. (a) Coalescence and (b) immersion nucleation mechanisms in presence of (a) small and (b) large binder droplets in comparison to particle size (adapted from [4]).

ii) Granule consolidation and coalescence: growth mechanisms

Granule growth occurs whenever material in the mixing equipment collides and sticks together. For two large granules this process is traditionally referred to as *coalescence*, whereas the sticking of fine material onto the surface of large pre-existing granules is often termed *layering*. These growth processes may begin as soon as liquid is added to an agitated powder mass i.e. simultaneous with the wetting and nucleation stage and may continue well after liquid addition has been completed. In some systems, however, insufficient liquid is added to promote further growth and the granule size is determined purely by the nucleation conditions.

ii-1) Layering model of agglomerate growth: The "Schaafsma" approach

Layering growth is the stage following the nucleation mechanism presented in Figure 2-2b (large binder droplets). Once the surface of the droplet is completely covered with particles, further increase is possible following liquid drainage from the kernel of the agglomerate towards the external surface where new layers of particles can adhere. In fact, if a pore at the surface of the granule is sufficiently filled with binder liquid, a free particle can be attached by liquid bridge formation (see top of Figure 2-3). This model

of growth has been proposed by Schaafsma et al. [3] who considered the liquid drainage to be the growth limiting process due to the resistance of liquid flow. The liquid flow is induced by capillary pressure difference between the pores inside the agglomerate and the pores with lower saturation near the surface of the agglomerate. The capillary pressure differences between pores can be described as a function of the saturation difference. The liquid saturation inside the granule, defined as the ratio of the binder volume to the total free volume and considered unity for the initial configuration of the agglomerate, decreases during the granule growth following the depletion of liquid, which results from drainage towards the surface. The minimum value of the saturation is reached when no further liquid can arrive at the granule surface and hence the agglomeration growth terminates, as illustrated in the bottom part of Figure 2-3. According to the authors, the model is valid for low shear granulators where breakage of the primary granule is not likely to occur during mixing.

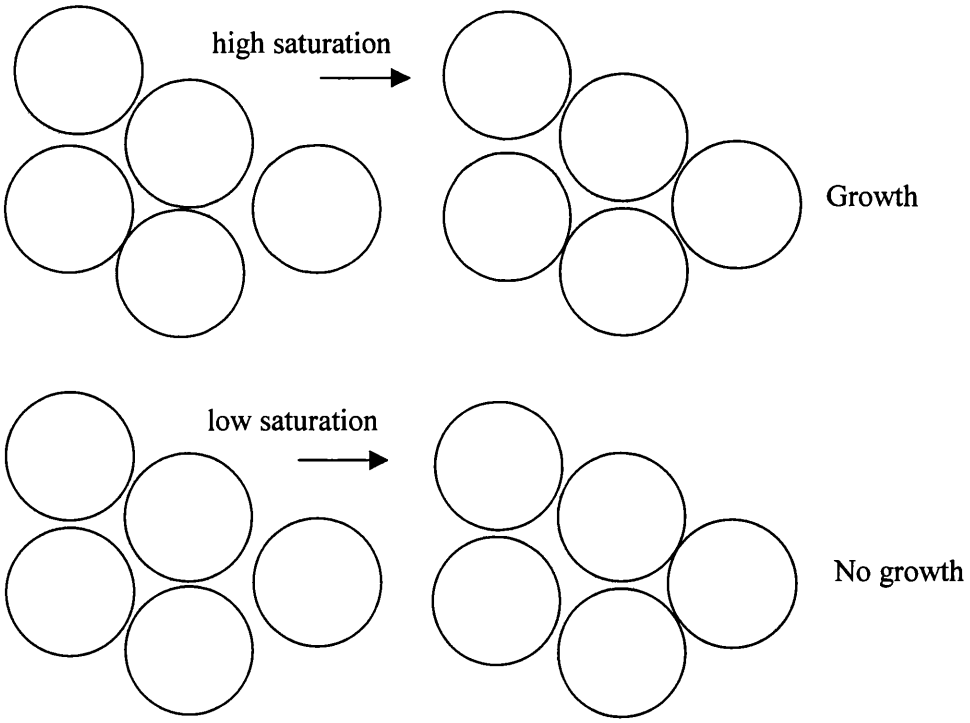

Figure 2-3 Agglomerate growth model according to Schaafsma et al. [3].

The model gave good agreement with data obtained by experiments granulating lactose with different PVP solutions. The final size of the granule was also predicted and

correlated to the initial drop size of the binder. A power law correlation resulted, as indicated in (2.2):

$$R_{dr} \propto R_{ag}^{0.89} \tag{2.2}$$

where R_{dr} and R_{ag} are the radii of the droplet and agglomerate, respectively. This result corresponds very well with data from other authors whose work has been reported in a detailed review on agglomeration mechanisms presented by Iveson et al. [4]. In fact, the relation is shown to hold with little variation of the exponent coefficient (from 0.8 to 0.85) for fluidised bed granulators with varying initial binder droplet size in the range from 35 to 3000 μm.

ii-2) Coalescence model of agglomerate growth: the "Ennis" approach

A different approach for modelling the agglomeration growth was followed by Ennis et al. [2], who assumed the increase of the granule size to be the consequence of particle/small granule collisions followed by possible coalescence. This model, contrary to that proposed by Schaafsma et al. [3], holds for the case of particles vigorously agitated, which is more relevant to the conditions experienced in many types of equipment where impact velocities as high as 1 m/s would typical result [4]. Ennis et al. [2] developed an expression for the minimum velocity of wet particles to investigate whether collisions give rise to rebound or 'capture'. Although both surface tension and viscous mechanisms were analysed, it was shown that the latter could be very significant and effectively dominate the surface tension, which was therefore neglected.

Ennis et al. [2] based their analysis of the rebound or capture mechanism on a dimensionless Stokes number defined as the ratio of the kinetic and viscous forces. When two spherical particles of equal radius R and mass m, coated with liquid of viscosity η, approach from opposite directions speed v_o along the center-to-center axis, the operating Stokes number, St, is:

$$St = \frac{2mv_0}{3\pi\eta R^2} \tag{2.3}$$

For capture to occur the Stokes number must be below a critical value St*:

$$St^* = 2(1 + \frac{1}{e_r})\ln(\frac{h_f}{h_x}) \tag{2.4}$$

where e_r is the coefficient of restitution of the impact, h_f is the thickness of the coating film and h_x the asperity height. The schematic of Ennis et al.'s model is shown in Figure 2-4:

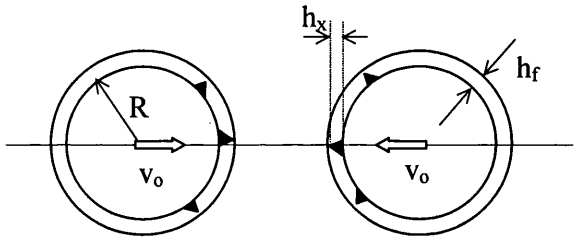

Figure 2-4 Schematic of two colliding particles, each of which is covered by a viscous binder layer of thickness h_f.

In any agglomerator, there will be a range of particle velocities and possibly a maldistribution of binding liquid, giving rise to a distribution of operating Stokes number, St. Whether this distribution falls above or below St* will govern the rate and mechanisms of agglomerate growth, in so far as success of particle collisions in terms of rebound or "capture" are concerned. Three granulation regimes were defined according to the magnitude of St in comparison to St*, which are summarised in (2.5).

$St << St^*$	non-inertial regime (all collisions successful)	(2.5)
$St \cong St^*$	inertial regime (some collisions successful)	
$St >> St^*$	coating regime (no collisions successful)	

For fine powders, growth often occurs by all three of the above mechanisms, proceeding through them as agglomerate size and St increase. Quantifying where the boundaries of the regimes occur depends on gaining a knowledge of all the variables. According to Ennis et al. [2], in the case of a drum granulator with a rotational speed of ω, the relative agglomerate velocities are of the order of $v_o = 2R_{ag}\omega$, where R_{ag} is the agglomerate radius. Substituting the expression of the velocity, v_o, into (2.3) the operating Stokes number result as per (2.6):

$$St = \frac{16\rho_p R_{ag}^2 \omega}{9\eta} \tag{2.6}$$

where ρ_p is the mass density of the bulk powder.

In order to relate their model to granulation processes, Ennis et al. [2] assumed granules to be non-porous, surface-wet, solid spheres with elastic, or near elastic, behaviour on collision. In reality, granules will either plastically deform on impact, fracture or break-up, leading to growth by either coalescence or crushing and layering. In certain conditions, granules will also be surface-dry.

The Stokes' approach developed by Ennis overpredicts the size of the agglomerates for highly viscous binders (200 to 500 cS). This can be explained by the fact that at high viscosities the squeezing of the binder from the inside of an agglomerate toward the surface to form the layering coat is retarded, which limits further growth.

Ennis et al's model [2], despite some simplifications, represents a significant step in focusing on the governing parameters in agglomerate formation in the presence of liquid binders and is a useful and simple criterion to predict the size of agglomerates as a function of both the binder viscosity and agglomerator speed.

ii-3) Population balance model

The complex mechanisms of agglomerate formation where granules, after reaching a critical size, may either continue to grow or break up into smaller units, has led to the

development of mathematical models based on a stochastic approach, where the growth is determined following a random probability distribution and the overall behaviour of the granulating mixture is analysed statistically. Such models count the collisions between pairs of granules, modifying the size distribution as long as smaller granules coalesce to form larger ones.

Adetayo et al. [16], basing their studies on the Stokes regime approach proposed by Ennis et al. [2], modelled the granule growth with a sequential two-stage kernel. In the first stage or non inertial regime (see (2.5)), growth occurs by random coalescence, independent of granule size or particle kinetic energy, with the initial distribution of binder being all important. In this stage all the Stokes numbers defined by (2.6) lie below the critical Stokes number (2.4) and therefore all collisions are successful. The granule size distribution is predicted to narrow quickly to an equilibrium size distribution. As the granule growth occurs, the operating Stokes number defined by (2.6) will exceed the critical St* resulting in collision rebound. In this second stage, which is much slower than the first, growth becomes more controllable, with granule deformation being more important. By selecting the time for completion of stage one, Adetayo et al. [16] were able to determine the initial stage of granulation before switching to stage two. The extent of granulation in the first stage was found to be proportional to the liquid saturation, with a critical saturation being required for second stage growth to occur.

Good agreement with experimental data was demonstrated for a range of moisture contents, granulation times and initial size distributions.

iii) Breakage of wet and dry granules

Breakage, either of wet or dry granules is another important aspect of granulation processes. As has been shown in the previous section, the equilibrium between granule formation and breakage is the condition that limits the granule size during the wet phase of agglomeration. On the other hand, breakage of dried granules generates dusty fines resulting, in general, in an impoverishment of the final characteristics.

Few investigations have studied the problem of wet agglomerate breakage. Tardos et al. [12] have proposed a model based on the approach introduced by Ennis et al [2] for the agglomerate coalescence. They defined a Stokes number for the particle deformation as the ratio of the kinetic energy to that required for deformation according to (2.7):

$$St_{def} = \frac{16\rho_p v_o^2}{2\tau_s} \tag{2.7}$$

in which τ_s is some characteristic stress in the granule, which generally depends on the granule yield strength, τ_y, the apparent viscosity of the mixture, η_a, the average shear rate on the mixer, Λ and to a flow index, n, according to (2.8):

$$\tau_s = \tau_y + \eta_a \Lambda^n \tag{2.8}$$

In the work reported in [12], however, the value of τ was assumed to be equal to the yield strength, τ_y, by verifying the apparent viscosity to be negligible in comparison to the yield strength of the material.

Tardos et al. [12] considered the breakage to occur when the Stokes deformation number, St_{def}, exceeded a critical value St^*_{def}. The authors [12], however, did not give a general formulation of this critical value, St^*_{def}, which would apply to different configurations of mixing equipment. The critical Stokes deformation number was determined experimentally only for a constant shear fluidised bed granulator (Couette device). In this equipment, breakage occurs principally under shearing action and not on impact with the impeller as in other mixing equipment (see next section). The critical deformation number for the Couette device resulted in the value of ~0.2.

Despite the fact that the model is not fully general it proves that dimensionless energetic analysis can give very useful information at any stage of the granulation process. No attempt has been made since to determine a general expression for the critical deformation number that applies to different mixing conditions.

Most granulation processes involve drying granules either directly in the mixing equipment, at the end of the agglomeration process or immediately after granulation in a separate drier. Attrition or fracture of the granules during drying or subsequent handling is generally undesirable. Dry granules fail in brittle or semi-brittle fashion i.e. they fail in tension by the propagation of pre-existing cracks which concentrate stress. Thus, the fracture stress may be much less than the inherent tensile strength of bonds between particles in the granule. When such situations occurs, the tensile stress concentrating near the crack tip is much higher than the applied stress, leading to local material failure near the crack tip. The energy released for crack formation provides the energy to extend the fracture [17], which eventually triggers the granule breakage. When the crack tip is much smaller then the granule size, the agglomerate tends to break into smaller fragments (fragmentation), whilst for crack tips of the same dimension as the granule, wear, erosion and attrition are the breakage mechanisms, which lead to generation of fine dust rather than small fragments [4].

2.1.3 Agglomeration equipment

In this section only equipment commonly used for wet agglomeration processes are considered. These devices granulate the initial powders by agitation methods and can be divided into tumbling drum, mixer and fluidised bed agglomerators. Other devices used in different agglomeration processes, such as pressure compaction and heat reaction, are extensively reviewed in [18].

i) Tumbling drum agglomerator

Tumbling drum agglomerators are used extensively in the process industries, as for example for the production of fertilizers and in the mineral industry. Continuous agglomeration can be brought about by adding binding liquid to a solid feed material whilst subjecting the mixture to the rolling action of a rotating drum. The agglomerate growth mechanism, rate and final size are dependent on many factors including the feed particle size distribution, the liquid content, the residence time and rotational speed. Many designs of tumbling agglomerator exist (for a comprehensive review see Pietsch [18]), a typical example being the balling drum agglomerator (Figure 2-5). Here the

tumbling motion causes particles to collide and, if the attractive or adhesive forces are high enough, coalesce.

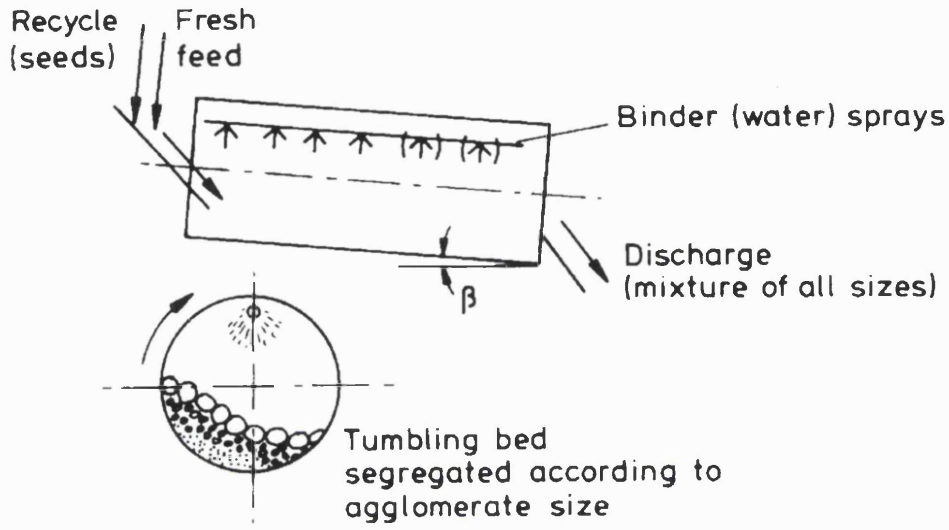

Figure 2-5 Schematic of tumbling drum agglomerator [18].

Fresh material and recycle seeds (nuclei) are fed into the top end of the drum. Initially separation takes place, with fines concentrating at the bottom of the drum. Thus the binding liquid sprayed onto the bed primarily wets the larger coarse particles. These binder-coated particles then go on to pick up fines as they travel through the bed. If binder is added over the entire length of the drum, growth will occur throughout and oversized, wet, and relatively loose agglomerates may discharge.

If binder is only added for part way along the drum, growth towards the discharge end is limited due to lack of binder. In this case, an equilibrium between size enlargement and size reduction with secondary growth (bonding of fragments) occurs. The material discharged does not contain oversized agglomerates and tends to be more uniform, drier and stronger. Often a curing step takes place to allow solid bridges to form and thus considerable strengthening of the agglomerate to occur.

ii) Mixer agglomerators

Mixer agglomerators are used in many industries, including in the production of pharmaceutical, food products and carbon black. The mixers within these vessels are designed to provide both a rubbing and shearing action to accomplish both mixing and size enlargement. As a result it is possible to process plastic and sticky powder feeds, with the kneading action of the mixer producing denser agglomerates than is possible with the tumbling methods. These mixer agglomerators can be either operated batchwise or continuously, the mechanisms of agglomerate formation varying for each case.

Batch mixer agglomerators are generally used in low capacity, high value situations, such as the production of pharmaceuticals and a typical example is the high shear mixer shown in Figure 2-6.

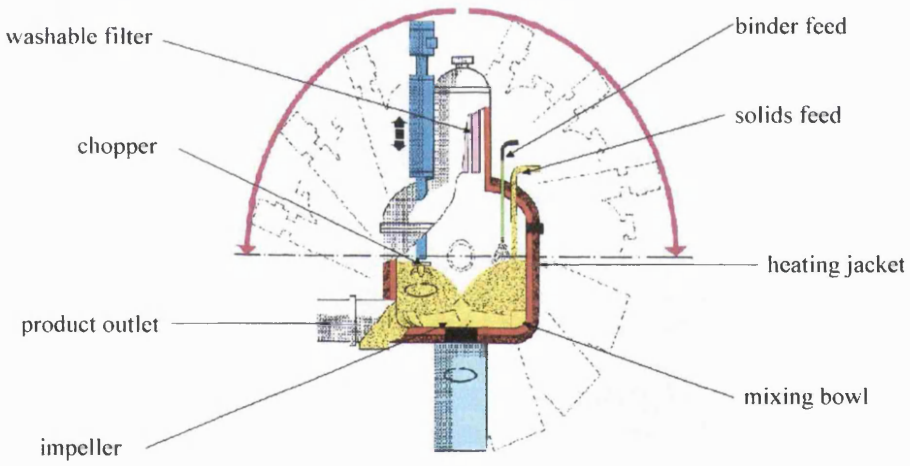

Figure 2-6 Schematic of high shear mixer for pharmaceuticals production. By permission of Romaco (UK) Ltd.

In this type of equipment binder and primary powders are mixed at high speeds (typically 300 rpm and higher) in order to improve the liquid binder distribution as well as to reduce the processing time. On reaching equilibrium, batch mixer agglomerators produce agglomerates of more uniform size, which is dependent largely on the amount of binder present. To prevent formation of very large granules most mixer agglomerators are fitted with choppers (also known as intensifiers and turbulisers),

which break up oversized granules and allow the fragments to reagglomerate with fines still present. The drying phase is carried out in the same vessel by means of heating jackets. During the phase of drying vacuum is usually maintained in the chamber to favour binder solvent evaporation. The device shown in Figure 2-6 also has a tilting action to maximise the heat transfer during drying with the jacketed walls.

Continuous mixer agglomerators are used in the production of fertilisers, china clay products and carbon black. They typically process between 20 and 30 tonnes of material per hour, but can go up to several hundred tonnes per hour. Examples include pin mixers (Figure 2-7) [19]. These consist of a cylindrical shell within which rods (pins) attached to a shaft rotate at high speeds. Feed is added, immediately moistened and then the material moves through mixing, agglomerating and densifying zones before being discharged as granules. The control mechanisms possible are limited as compared to those with the batchwise process and as a result granular products from continuously operating equipment feature wider particle size distributions and normally lower apparent density.

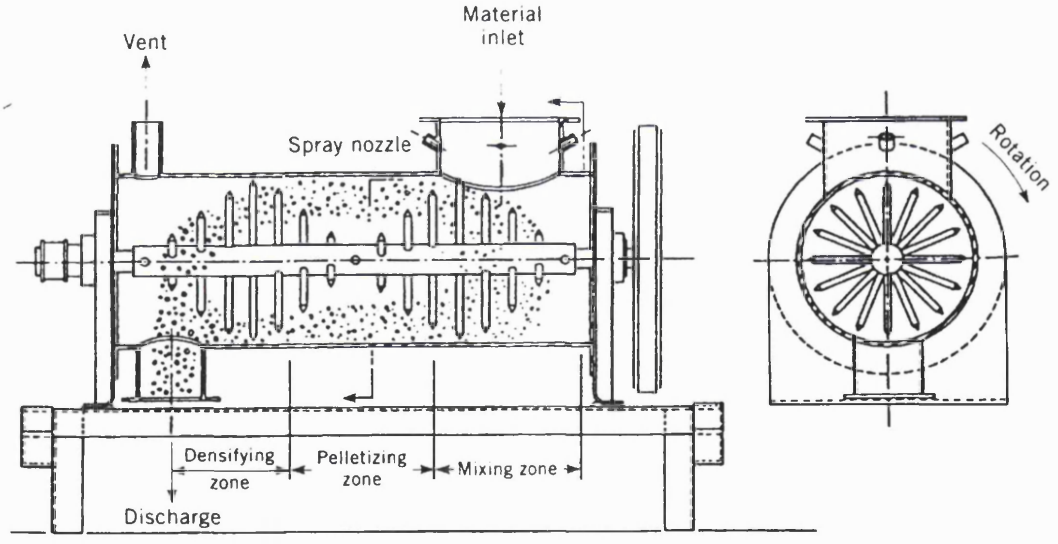

Figure 2-7 Schematic of a pin mixer used in the wet-agglomeration of carbon black. The pelleting zone is where agglomeration growth and consolidation take place (after [19]).

iii) Fluidised bed agglomerators

Fluidised bed agglomerators belong to the group of aerodynamically driven processes where the contact between particles is not promoted by mechanicalagitation equipment. Fluidised agglomerators may operate either in batch or continuous mode, the schematic of the equipment being essentially the same, with the latter mode increasing the production capacity. Figure 2-8 shows the principal features of a continuous fluidised bed granulator [18].

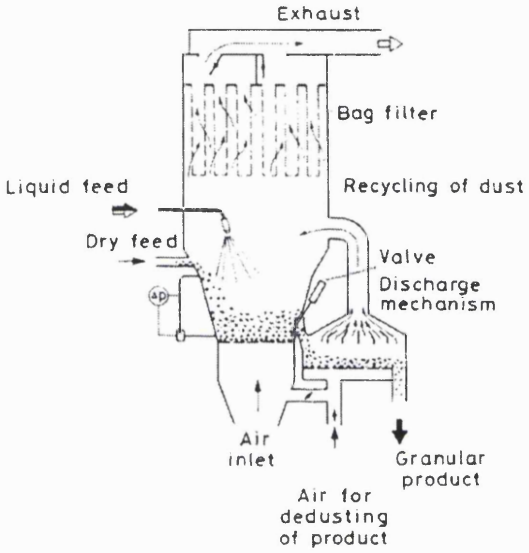

Figure 2-8 Schematic of continuous fluidised bed agglomerator (after [18]).

At the bottom of the equipment a perforated plate with openings between approximately 50 and 100 μm diameter serve to uniformly distribute the fluidising gas entering from below the plenum. Gas velocities at the bottom of the fluidisation chamber are typically between 0.4 and 1.5 m/s and inlet temperature may vary between 40 and 200oC. Binder solution is introduced through spray nozzles, whilst feeding powders can be brought in from suctions ports. The position of the nozzle relative to the fluidised bed affects product size distribution. A larger area of particle/liquid contact results in a more uniform agglomerate distribution and avoids local overwetting. To achieve better liquid distribution the nozzles are placed high above the fluidised bed. Nozzles can also be placed in a downcomer near the base of the unit. Granulated product can be removed from the bottom of the bed through a valve arrangement. Air is blown into the chamber

where the product is collected to remove dust, which is conveyed back to the fluidised bed. At the top of the equipment bag filters usually prevent loss of feeding material. In a fluidised agglomerator granules grow more by layering than by coalescence mechanisms, whilst granulation and drying take place simultaneously. These conditions confer a smoother surface to the final product. Because of the growth mechanism-taking place in a low-density bed of turbulently moving particles, the resulting agglomerates are less compact and more fragile than those obtained with other mixing equipment. These products, though, dissolve more readily in water, which can be useful for certain industrial applications (drugs, food, etc.).

2.1.4 Predicting and controlling agglomerate formation

The desired attributes of the product granules are controlled by a combination of formulation (choosing the liquid binder for the required feeding powder) and process characteristics (choosing the type of granulator and the operating parameters). Since so many variables influence agglomeration processes it is in generally difficult to fully predict the properties of the final products from initial conditions.

Iveson and Lister [20] state that two classes of granule growth can be observed depending on whether the granules are deformable or not. For weak deformablesystems with a narrow size distribution of coarse particles, granules grow steadily with time. The granules formed in this type of system are deformable and coalesce easily. The deformability of the granules allows energy to be absorbed so that they may resist separating forces within the granulator. As a result, often no maximum size is reached. The growth rate increases with increased liquid content. The second type of granule growth defined by the authors [20] occurs in strong, non-deformable systems (fine particles, wide size distribution) with slow rates of consolidation. Here, after initial nucleation, there is a period of little or no growth (defined as the induction period), followed by a period of rapid growth when liquid is squeezed to the granule surfaces. With increasing liquid content the length of the induction period decreases. A maximum size of granule is reached when the torque exerted on the granules by the agglomerator prevents further coalescence.

The liquid content inside the agglomerate can be considered in terms of the saturation of the pore space between the constituent particles. Under some conditions of initial liquid distribution, the agglomerate growth starts from nuclei, small aggregates of primary particles held together by pendular liquid bridges (Figure 2-9a). As soon as more liquid is added the funicular state is reached (Figure 2-9b), where the bridges coalesce and liquid and a few air bubbles that are increasingly compressed by the mixing forces occupy the pore space. When all the pore space is saturated (Figure 2-9c) liquid can be squeezed from within the agglomerates to the external surface and the granule can increase its size by adhering dry particles from the bulk. Over the saturation value, particles are completely engulfed in liquid (Figure 2-9d). Granulation then becomes an impractical operation because the particles tend to stick excessively to the walls of the equipment [7].

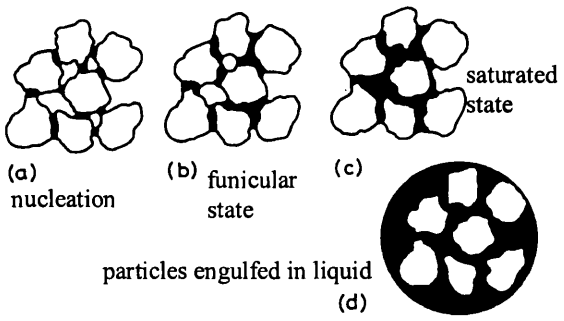

Figure 2-9 Distribution of liquid inside agglomerates (after [18]).

Figure 2-9 also shows that during the phase of liquid addition the friction coefficient between particles, referred to in the previous section, can vary extensively due to lubrication of the particle contact area.

Having identified the two mechanisms of granule growth, Iveson and Lister [19, 20] proposed that granule growth behaviour (in terms of the deformation Stokes number) is a function of the system's liquid binder saturation and rate of consolidation and they summarized their observations in the granule growth regime map presented in Figure 2-10. The authors stated that at very low concentrations of binder, particles will either

remain as separate entities or form nuclei due to Van der Waals interactions, but will not grow any further. At slightly higher liquid saturations, either nuclei will form which will not grow, or for weak, highly deformable systems a non-granular 'crumb' material will be produced. For medium amounts of binder, deformable granules will grow steadily, whilst low deformation granules will consolidate more slowly (induction). At high levels of liquid binder, all systems grow rapidly. At very high liquid contents, slurry is formed.

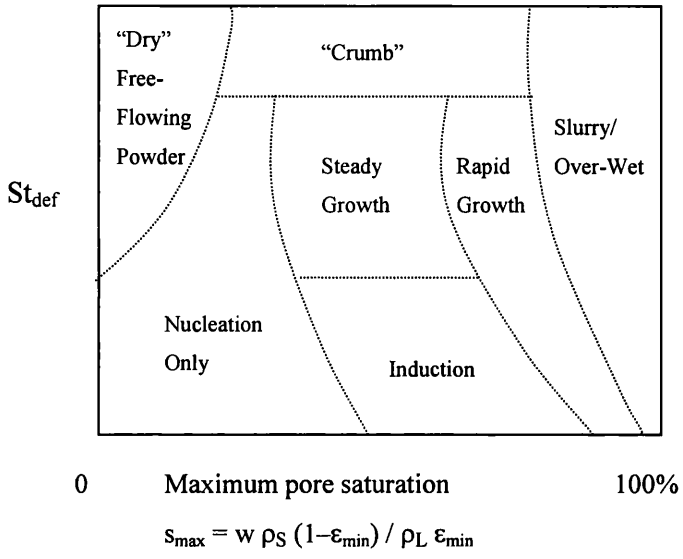

Figure 2-10 Granule growth regime map. The deformation Stokes number, St_{def}, is defined according to (2.7), s_{max} is the maximum pore granule saturation, w is the mass ratio of liquid to solid, ρ_S and ρ_L are solid and liquid densities, respectively and ε_{min} is the minimum porosity the formulation reaches for that particular set of operating conditions (adapted from [20]).

Many authors e.g. [20, 21] seem to agree that the degree of binder dispersion indicates the quality of the mixing between the powder and the binder fluid, and is reflected directly in the nuclei and product size distribution. In cases where all particles are coated with equal amounts of binder, there will be a narrow size distribution. When the binder is unevenly distributed throughout the solid, some granules will become more saturated than others, resulting in their preferred growth. This has been confirmed by other workers [22, 23] in experimental studies where the proportion of "lumps", defined

as granules larger than 2 mm, was used as a measure of binder dispersion. All studies were performed in mixer granulators, and several different methods of adding the binder solutions were used. Atomisation together with a high impeller speed produced the best binder distribution. The concentration of lumps was highest during the initial liquid addition phase i.e. the lumps were formed during nucleation, not during the growth phase. In order to achieve uniform binder distribution, Iveson and Lister [20] stated that it is desirable to have a large spray area, small binder droplets, low viscosity binders and good agitation of the binder through the solid. In this respect the design of the binder spraying nozzles to control the size and the distribution of the liquid binder also assumes an important role to improve the characteristic of the final product.

The method of adding the binder has been a matter of experimental investigation by Knight et al. [24]. A low viscosity (81mPas) polyethylene glycol binder (melting point 43-46°C) was used with 4 to 23 μm diameter calcium carbonate particles in a high shear mixer. The contact angle of the binder on the solid was found to be 60 degrees. Three techniques were used to add the binder:

- Pour on. Molten binder was poured directly onto the solid. Mixing then commenced
- Spray-on. Molten binder was sprayed onto the powder with the impeller already rotating.
- Melt-in. The binder was added as solid flakes to the surface of the powder. Mixing was then started. They estimated (from torque and temperature measurements) that melting occurred in just less than 3 minutes.

Knight et al. found that when liquid was poured on, the distribution of the liquid was produced solely by the action of mechanical mixing. Spraying the liquid on gave small droplets of liquid distributed throughout the powder. The mechanical mixing then produced a more uniform liquid distribution. The melt-in method was found to give a non-uniform liquid distribution and was dependent on the mechanical mixing. They stated that although initially the liquid distributions differ for the different addition methods, ultimately they all depend on prolonged mechanical mixing to give uniform binder distribution.

The increase of the binder viscosity in relation to the size of particles was investigated by Keningley et al.[25]. Calcium carbonate having particle sizes in the range 8–230 μm diameter (separated in four batches of 8, 50, 80, 230 μm diameter sizes) was granulated in a high shear mixer using silicone oils having viscosities in the range 10^{-4}– 56 Pa s. They observed that it was possible to agglomerate particles over a narrow range of liquid-to-solid ratios (between 0.4 and 1.1 vol/vol) by varying the mixing time (between 15 s and 20 min) and that the reduction of the particle size went along with an increase of the liquid-to-solid ratios. These results were independent of the binder viscosity up to 1 Pa s. Using binders having viscosities above this value, the maximum liquid-to-solid ratio (used for smaller particles) was increased, whilst the minimum liquid-to-solid ratio (used for larger particles) remained unchanged. This behaviour agrees with the conclusions of Ennis et al. [2] (see section 2.1.2) that a viscous binder might retard the rate of compaction.

Less attention has been paid to the study of the effect binder surface tension has on the consolidation mechanisms. Ritala et al. [26] found that varying binder surface tension from 48 to 68 mN/m did not appear to significantly affect consolidation. Iveson and Lister [27] found that decreasing binder surface tension from 72 to 31 mN/m in a tumbling drum, increased the rate of consolidation but decreased the extent of consolidation (consolidation time).

The effect of equipment speed on consolidation is variable. Increasing pan rotation speed or mixer impeller speed can increase the rate of compaction due to better agitation conditions [26]. However, the resistance of the granule to the external mechanical action can be a limiting factor to the granule formation, as has been shown by Eliasen et al. [28], who found that for low viscosity binders in a high shear mixer, increasing impeller speed increased the amount of breakage and shear which delayed densification, resulting in less-spherical granules with a higher porosity.

2.2 Particle agglomeration in liquid media: the spherical agglomeration process

The treatment of finely dispersed particles in various kinds of aqueous, organic, emulsion or foam phases forms an important part of the processing route of many diverse chemicals, mineral and biological products. To understand the influence between the macroscopic bulk properties and microscopic particle behaviour is fundamental in understanding the governing parameters of a desired process, either being a separation technique, the formulation of a stable dispersed product (e. g. paint) or the kinetic control in a reaction vessel. As a result of different bulk medium conditions, in fact, particles can either experience strong attraction, forming larger agglomerates (unstable dispersion), or remain in a dispersed state (stable configuration).

Since the behaviour of fine particles is dominated by surface effects rather than by bulk properties [29], traditional separation techniques, such as filtration or particle settling, lead to poor rates of recovery without tackling the problem of selectivity, unless particles of the same species are agglomerated together (selectively agglomerated).

Particle-particle interaction in a liquid medium is more complicated than that in a gaseous phase. This is readily explained by the larger influence that electrical double layer and van der Waals forces have on the stability of suspended dispersions. The double layer effect, which will be extensively reviewed in section 3.3.3, is a specific interaction for particles submerged in a liquid. This latter interaction can be either attractive or repulsive depending on the surface charge of the particles and on the type and nature of any chemical species dissolved in the solution. Van der Waals attraction, on the contrary, is less sensitive to addition (in the solution) of chemical reagents and between particles of the same species is always attractive. In order to modify the relative influence of van der Waals and electrical double layer interactions, electrolytes or polymers are commonly used to promote selective agglomeration in the particle recovery processes.

A different way to favour particle agglomeration consists of adding small amounts of a second liquid, immiscible with the suspending medium and able to form liquid bridges between the particles. Under appropriate conditions of agitation, this method can lead to agglomerate formation in a similar way as has been described in section 2.1 for the gaseous suspending medium. Differences with the gaseous phase methods yet exist and lie in the possibility of adding surface active agents (surfactants, see section 4.4) to the liquid bulk medium in order to promote the affinity of a desired species towards the binder and control selectively the agglomeration (selective recovery). Non-agglomerated particles can still be recovered from a suspending medium if they remain attached to air bubbles, which are formed in the liquid, and are transported to the surface of the slurry.

Based on the previous methodologies, different processes have been developed as recovery techniques.

Coagulation and *flocculation* [30] are two processes largely and successfully employed for recovery and separation. Coagulation is the process in which dispersed particles are agglomerated by the addition of an electrolyte, which reduces the potential of the electrical double layer on the particles, thereby favouring the attractive van der Waals interaction to drive agglomerate formation. Flocculation, on the other hand, occurs when a low concentration of polymer is added to a dispersion of particles. Polymers are long hydrocarbon chains that adsorb on the particle surface, whilst segments of their molecule can protrude in the solution. Thereby, as particles approach one another the hydrocarbon chains might overlap and the bonds produced by these polymeric bridges result in adhesive forces that keep the particles agglomerated. *Flotation* is another separation technique widely used in the mineral industry. The water-ore slurry is conditioned with a frothing agent and sprayed with air to create a copious supply of bubbles. A collecting agent is also added to the slurry to increase the affinity of the desired mineral toward the air bubbles. The air bubbles, together with their attached mineral particles, rise to the surface of the pulp where they are removed from the system. According to the US Bureau of Mines, 293 flotation plants processed 485

million tons of ore in 1980 [31]. Flocculation, coagulation and flotation do not represent the focus of the work reported here and they will not be investigated further

Agglomeration of suspended particles promoted by addition of an immiscible liquid binder is commonly referred to as s*pherical agglomeration*, because of the final spherical geometry of the agglomerates. The separation method is based on differences in surface chemistry, which involves the selective adsorption of suitable surfactants and electrolytes onto the valuable particles to increase the affinity towards the liquid binder, but leaving the unwanted gangue dispersed in the aqueous pulp. In an aqueous suspending medium usually oil is used as binder collector and therefore the conditioning of the desired particles, through addition of surfactants able to increase the affinity toward the organic phase, is also called *hydrophobization*. When an oil phase is added to the aqueous medium, liquid bridges are preferentially formed between the hydrophobic species that can thus be agglomerated with a high degree of selectivity [29]

In the spherical agglomeration process, the agglomerates start to grow when sufficient binder liquid is added. The mechanism of growth starts with a flocculation regime during which particles form flocs, loose open chains of particles held together by pendular liquid bridges. In the following growth step, the flocs start to form pellets, closed chains of particles entrapping flocs and liquid medium. The porosity of the flocs decreases, as entrapped dispersion medium is squeezed out and eventually the pore space within the pellets is completely filled with binder liquid.

In the last step, agglomerates reach a constant mean size that is presumably the size where a balance between adhesive and separating shearing forces has been reached (Figure 2-11). This growth mechanism resembles the coalescence mechanism seen in Figure 2-2a.

This growth mechanism shown in Figure 2-11 is reported by Bos and Heerens [32] who measured, using a light scattering technique, changes in agglomerate size with time for different types of solid dispersion, such as glass limestone and aluminium silicate, recovered from carbon tetrachloride using water/glycerol mixture as the binding agent.

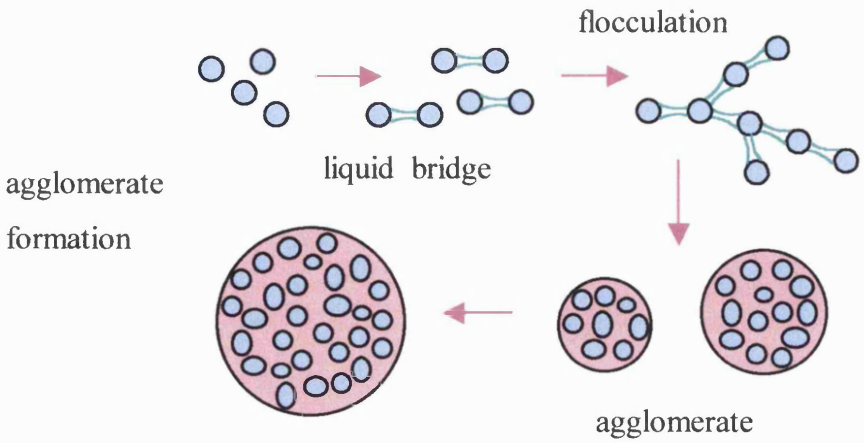

Figure 2-11 Schematic diagram of the spherical agglomeration process for the case of small liquid binder droplets.

A different growth mechanism can be predicted in the presence of larger binder droplets, similar to the immersion mechanism shown in Figure 2-2b. In this situation particles migrate towards the organic phase driven by electrical interactions (van der Waals and electrical double layer), which is enhanced by addition of appropriate surfactants and electrolytes. The growth can be predicted using the layering model proposed by Schaafsma et al [3] (see section 2.1.2), provided the agitation is not too strong.

The growth mechanism is also a function of the liquid binder added. Capes and Darchovich [33] reviewed the method of coal fines recovery in the process of coal bonification (from ashes and sulphurs) using spherical agglomeration. Using a fine coal stream from a preparation plant containing coal particles all finer than 0.5 mm diameter, a variety of types of agglomerates were obtained as the amount of oil binder was increased from less than 5% wt. up to 30% wt. In the lower range of oil loading only a few pendular bridges were formed between the particles and an unconsolidated floc structure resulted. With larger amounts of oil (in the 5-15% range) the chain-like floc structure was replaced by more compact three dimensional agglomerates. In this region the agglomerates grew in size and reached a peak strength and compaction near the saturated region (see Figure 2-9c), when the void space in the interior of the agglomerates was just filled with oil. Beyond the 15% level agglomerates became soft

paste-like cohesive lumps in which the solids were essentially dispersed in the bridging liquid.

The first commercial applications based on the spherical agglomeration technique date back to the 1920s and were tailored to mineral industry processes [34]. However, despite the good performance achieved in industrial plants and the excellent results obtained in laboratory tests for different type of ore recovery (see section 4.4.3), the process has not yet received widespread commercialisation, a major drawback with respect to other recovery techniques (flotation, coagulation, flocculation) being the increased cost due to the oil binder.

Commercial and pilot plants are reported in the literature in the following areas.

- purification of fine coal from sulphur and ashes [34] [35]
- recovery of fine valuable minerals, either as a main process or integrated in a gross extraction process to recover mineral fines from waste gangue, increasing the total grade of recovery [29, 36, 37]
- oil sand ore separation to recover bitumen [38]

Recent studies have been undertaken in order to apply spherical agglomeration to other industrial sectors, such as the deinking of recycled paper [39].

In the work reported here, liquid bridge adhesion between pairs of particles suspended in a liquid bulk medium and the electrical interaction (double layer and van der Waals) between particles and liquid binder have been investigated, both theoretically and experimentally, for the case of particles of different surface energies and for different bulk medium solutions of electrolytes/surfactants, in order to gain a better understanding of the basic phenomena regulating spherical agglomeration processes.

2.2.1 Spherical crystallization process

More recently, the spherical agglomeration technique has been used for the manufacture of high value products, such as crystalline pharmaceutical drugs [40-42]. In this latter

application crystals of drugs are agglomerated in a liquid medium in presence of a solvent that promotes crystallization of smaller crystals dispersed in the liquid giving rise to increase of the drug size. This method is also known as *spherical crystallization* [43]. This technique, which presents many analogies with the spherical agglomeration process, is illustrated in Figure 2-12.

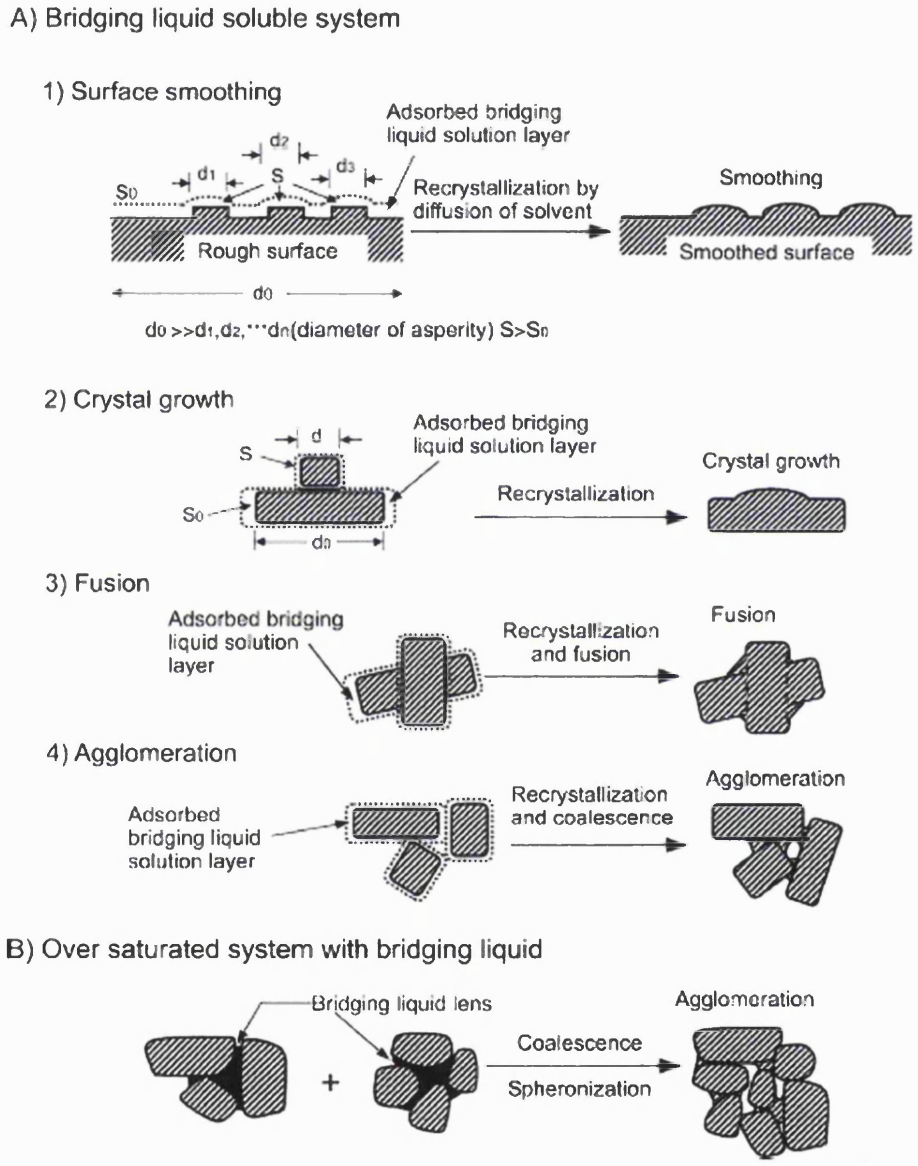

Figure 2-12 A) Diffusion-controlled recrystallization mechanism and fusion model in a bridging liquid soluble system. S and So are solubilities of dissolved crystals in the bridging film, which depends on the roughness of the surface; d and d_i (i=0 to 3) are characteristic lengths of the crystal surface. B) Agglomeration model in an oversaturated (supersaturated) system with bridging liquid (after [42]).

In the spherical crystallization process the bridging liquid is soluble in the bulk medium until the saturation concentration at which point it becomes immiscible with the suspending phase. Before saturation the bridging liquid is immediately dispersed and preferentially wets the surface of primary crystals forming an adsorbed bridging liquid layer, which partially dissolves the crystals (see Figure 2-12A1).

In the bridging layer the concentration of dissolved crystal increases near small and rough crystalline surfaces, which promotes diffusion until an equilibrium concentration is obtained in the bridging layer. At this point, some bridging liquid can counter diffuse from single crystals or from the contact area between primary crystals back to the suspending medium. A solubility change results from this counter diffusion of bridging liquid, which induces recrystallization (reprecipitation) of the dissolved crystalline material whose effect is to smooth coarse surfaces or to fuse primary crystals (see Figure 2-12A1-2-3). According to this process coarse crystals grow more quickly than smooth ones and solid bridges are easily formed at the cross-contact points of primary crystals.

If the concentration of the suspending medium is saturated with the bridging liquid the recrystallization and fusion phenomena stop because the bridging liquid remains immiscible in the suspending phase. At this point agglomerates grow due to formation of liquid bridges between crystals according to the more traditional spherical agglomeration technique (Figure 2-12B).

Spherical crystallization appears very promising to the pharmaceutical industry as a crystal engineering process able to control simultaneously the particle size of the primary crystal and of the agglomerate. Using this technique, packability, flowability and compressibility characteristics of an antirheumatic drug were improved [41] and the production of dry powder for inhalation (antiasthma steroids) was more easily controlled [42].

The latter achievement marks a significant departure from the use of spherical agglomeration as merely a separation technique to one that can be used to produce high-valued chemicals.

2.3 Challenges to our understanding

The analysis of the main factors influencing the agglomeration of particles in either a gaseous or a liquid medium has pointed out that the engineering of agglomerated products of required characteristics can be quite difficult to achieve. During the formation of agglomerates different parameters can be altered that affect the properties of the final product. These modifications, though, cannot change the intrinsic interaction between the powder mixture and the liquid binder, which ultimately may promote or prevent the agglomerate formation.

The focus of the work that will be reported in this thesis is to investigate the basic interactions existing between solid and liquid binders in order to ascertain the relative importance of liquid bridge adhesiveness, particle wettability and particle surface energy, binder redistribution after liquid bridges rupture and, for the case of a liquid bulk medium, the influence surfactants and electrolytes have on the basic particle-binder interaction.

Chapter 3

3 Adhesion forces between particles

The term *"adhesive force"* generally relates to the minimum force needed to separate particles adhering to one another in either a gaseous or liquid media. Some adhesive mechanisms (van der Waals, electrostatic, liquid bridge forces) assume an identical formulation regardless of the bulk medium and are derived by simply adjusting the physical constants of the surroundings. Other mechanisms, such as the electrical double layer effect, are very specific for particles interacting in a polar liquid medium (e.g. aqueous). In this chapter, liquid bridge interactions, being the main cause of adhesion in this study, will be discussed in detail. Van der Waals and double layer forces are also examined to explain the interaction between particles and liquids. These interactions govern, for example, the agglomeration of particles in liquids and therefore are strictly related to the scope of the work presented here. Electrostatic forces will be described briefly and the magnitude of different adhesive mechanisms will be compared for the case when the bulk medium is a gas. Other adhesion mechanisms such as solvation or structured effects and hydrogen bonds are beyond the scope of this thesis and hence will not be covered here.

3.1 Adhesive forces arising from liquid bridges

The intentional addition of a small amount of liquid (liquid binder) to an agitated set of particles can cause those particles to agglomerate. This type of process, known as wet agglomeration, is of considerable technological importance and a lot of interest has been dedicated to the study of pendular liquid bridges, which is the configuration assumed by the liquid between the particles. The study of the geometry, the adhesive force and the rupture energy of liquid bridges assumes a key role in the understanding of the initial agglomerate behaviour. The formation of agglomerates appears to be governed by a balance between the rupture energy of liquid bridges and the particle kinetic energy and hence the study of the liquid bridge adhesive force (also referred to as the strength of the

liquid bridge) in relation to the type of liquid binder and the surface properties of the particulate is required for fundamental understanding.

Liquid bridge forces arise from both capillary and surface tension effects, which are static forces and are detailed in sections 3.1.4, and from the viscous component, reviewed in section 3.1.5, which becomes more important during dynamic separation.

The force that holds particles together is ultimately related to the ability of a liquid binder to wet the particles, in order to form effective bonds. Therefore the study of the geometry assumed by a liquid bridge is essential in determining the adhesive force. Liquid bridges formed between two particles assume a lens shaped profile, which can be described theoretically by the Young Laplace equation. Being able to solve this equation for various conditions is important to the development of agglomeration models.

3.1.1 The Young Laplace equation

Whether a liquid bridge is formed in a gaseous medium or in a second immiscible liquid, the configuration assumed by the bridge meniscus, at rest, is implicitly defined by the Young-Laplace equation (3.1):

$$\Delta P = \gamma_L \left(\frac{1}{r_1} + \frac{1}{r_2}\right) \qquad (3.1)$$

Equation (3.1) relates the difference in hydrostatic pressure $\Delta P = P - P_{ext}$ across the vapour-liquid or liquid-liquid interface (P, P_{ext} are the pressures inside the bridge and in the external medium, respectively), to the local radii of curvature r_1, r_2 (see Figure 3-1) and to the interfacial tension γ_L between the liquid bridge and the external medium [44].

The configuration of the liquid bridge can be readily obtained from (3.1) once the local radii of curvature are rewritten in analytical terms, which, by using a cylindrical coordinates system, results in (3.2) [45]:

$$\frac{\Delta P}{\gamma_L} = \frac{1}{y(1+y'^2)^{1/2}} - \frac{y''}{(1+y'^2)^{3/2}} \tag{3.2}$$

where y' an y" are the first and second derivative of the liquid bridge profile, which is described by the function y(x).

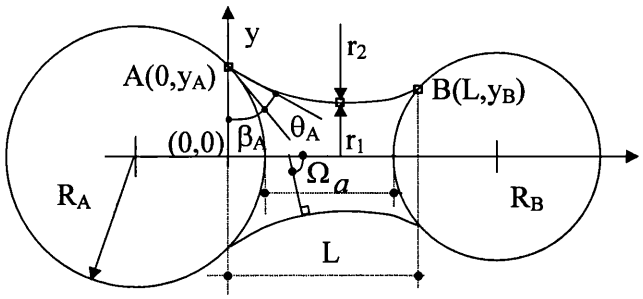

Figure 3-1 Geometric parameters describing a liquid bridge between unequal particles.

For relatively "large" liquid bridges the geometry of the liquid bridge is influenced by the gravitational distortion. In this latter situation the profile mean curvature is not uniform throughout the liquid bridge and (3.1) must change accordingly, as detailed by Mazzone et al. [46]. According to these authors, gravity has negligible effects on the bridge geometry when (3.3) is verified [46]:

$$\frac{gL^2\Delta\rho}{\Delta P\, R} \square 1 \tag{3.3}$$

where g is the gravity acceleration, L, some characteristic length of the bridge and $\Delta\rho$, the difference of densities between the liquid binder and the external medium. "Small" liquid bridge volumes are defined as those meeting (3.3) as opposed to "large" volumes where gravity does have an effect on the geometry of the bridge.

The solution of the Young Laplace equation has been studied by Orr [44], for liquid bridges formed between a sphere and a flat surface, in terms of elliptical integrals. He also classified possible liquid bridge geometries according to the meridional curvature,

defined as $-\frac{d}{dx}(\sin\frac{\Omega}{R})$, where Ω is the angle made by the normal to the meniscus with the axis of symmetry, as indicated in Figure 3-1.

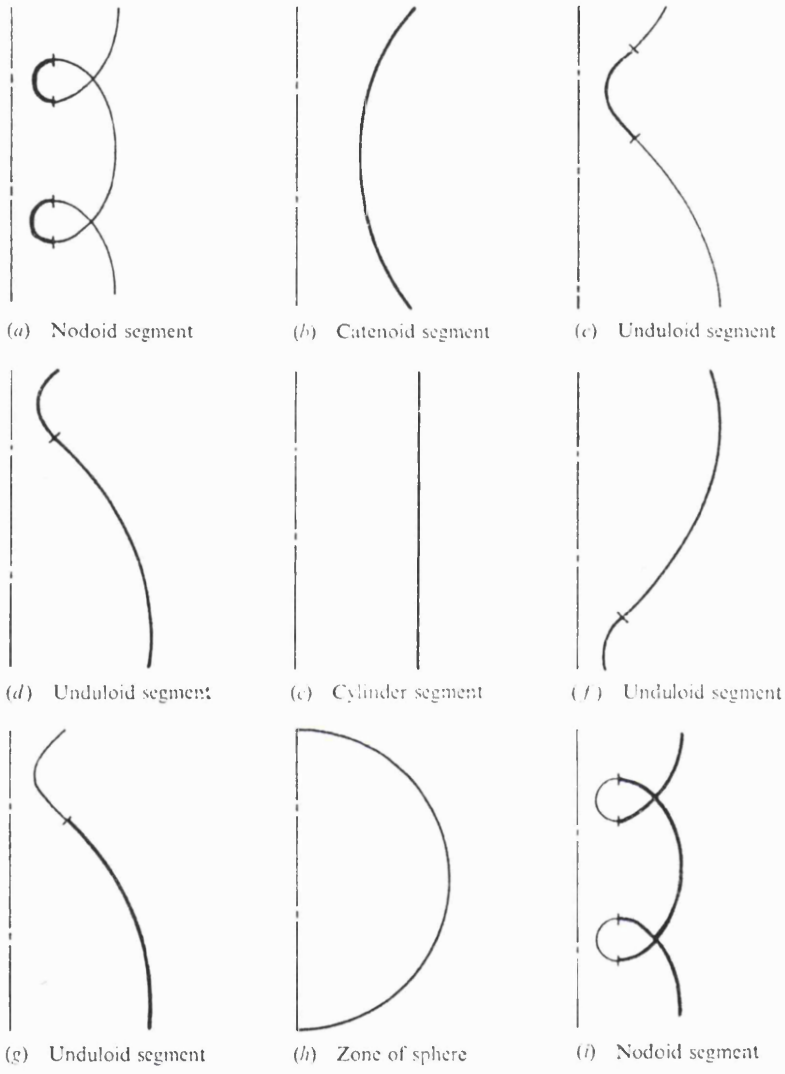

Figure 3-2 Profiles of axisymmetric menisci of uniform mean curvature (after [44]).

In Figure 3-2 the meridional curvature is negative in inserts (a) to (c); it is negative in the top part and positive in the bottom branch of insert (d) and vice versa in insert (f); it is zero in insert (e) and positive from insert (g) to (i); tick marks represents the inflection points. Considering the mean curvature, it is negative in insert (a) (which leads to a pressure inside the meniscus lower than that of the surrounding medium), it is zero in insert (b) and positive in all the other situations.

Equation (3.2) can be rearranged into a Bernoulli type differential equation and, following classical integration, (3.4) is obtained, where B is an integral constant [45]:

$$\frac{y}{(1+y'^2)^{1/2}} = \frac{\Delta P}{2\gamma_L} y^2 + B \tag{3.4}$$

By replacing either of the two y'_i with $\mathrm{cotg}(\theta_i+\beta_i)$ into (3.4) (i refers to the point A and B), the constant B can be evaluated, which, for the point A, becomes:

$$B = y_A \sin(\theta_A + \beta_A) \frac{\Delta P}{2\gamma_L} y_A^2 \tag{3.5}$$

If the coordinates of both points A and B are substituted into (3.4), the constant B can be eliminated, as per (3.6):

$$\frac{\Delta P}{2\gamma_L} = \frac{y_A \sin(\theta_A + \beta_A) - y_B \sin(\theta_B + \beta_B)}{y_A^2 - y_B^2} \tag{3.6}$$

Equation (3.6) allows the ΔP across the interface to be calculated once the interfacial tension γ_L and the boundary values of the bridge profile, y_A, y_B, $(\theta_A+\beta_A)$, $(\theta_B+\beta_B)$, are known. Equation (3.2) can only be solved analytically in a few cases [45] though, such as when the angle $\theta + \beta = 90^\circ$ on both the equi-sized particles. Hence a numerical solution is in general required.

3.1.2 Numerical solution of the Young Laplace equation

A numerical method to solve the Young Laplace equation is given in [47], where a symmetrical liquid bridge, between equi-sized particles of radius R, is considered, as indicated in Figure 3-3.

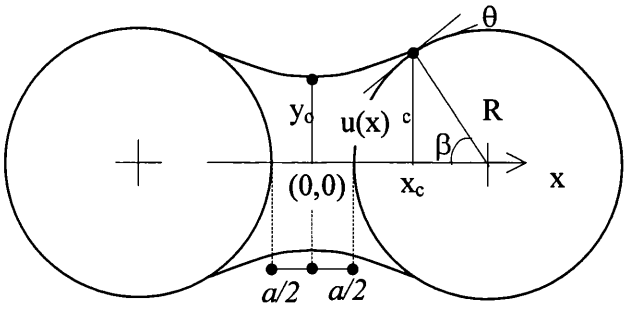

Figure 3-3 The Lian et al. physical model, (after [47]).

The solution of the bridge profile can be approximated through a truncated Taylor series in order to obtain the recurrence equation:

$$Y_{i+1} \cong Y_i + Y_i'(X_{i+1} - X_i) + \frac{1}{2} Y_i''(X_{i+1} - X_i)^2 + \ldots\ldots \quad i = 0, 1, 2, \ldots\ldots \tag{3.7}$$

where Y, X are dimensionless coordinates with respect to the particle radius R. Rearranging (3.4) and (3.2), the expressions for Y_i', Y_i'' are determined as shown in (3.8) and (3.9), respectively:

$$Y_i' = \sqrt{\left(\frac{Y_i}{\sin\beta \sin(\beta + \theta) + H^*(Y_i^2 - \sin^2\beta)} \right)^2 - 1} \tag{3.8}$$

$$Y_i'' = \frac{1 + Y_i'^2}{Y_i} + 2H^* (1 + Y_i'^2)^{3/2} \tag{3.9}$$

by considering that at X_c, $Y_c = \sin\beta$ and $Y_c' = \text{cotg}(\beta+\theta)$, whilst $2H^*$ is the dimensionless mean curvature, $2H^* = \frac{\Delta P R}{\gamma_L}$.

Due to the configuration symmetry, Lian et al. [47] studied only the half profile, from the neck position Y_o, to the contact point with the particle, Y_c. Liquid bridge

configurations were evaluated from contact through to rupture by considering a fixed contact angle θ and a constant liquid bridge volume. The configurations assumed by the liquid bridge for different separation distances *a*, can be determined by specifying values for both H^* and the half-filling angle β. When the solutions of the Young Laplace equation were analysed, two possible configurations resulted in agreement with (3.2) for the selected set of volume and contact angle (Figure 3-4).

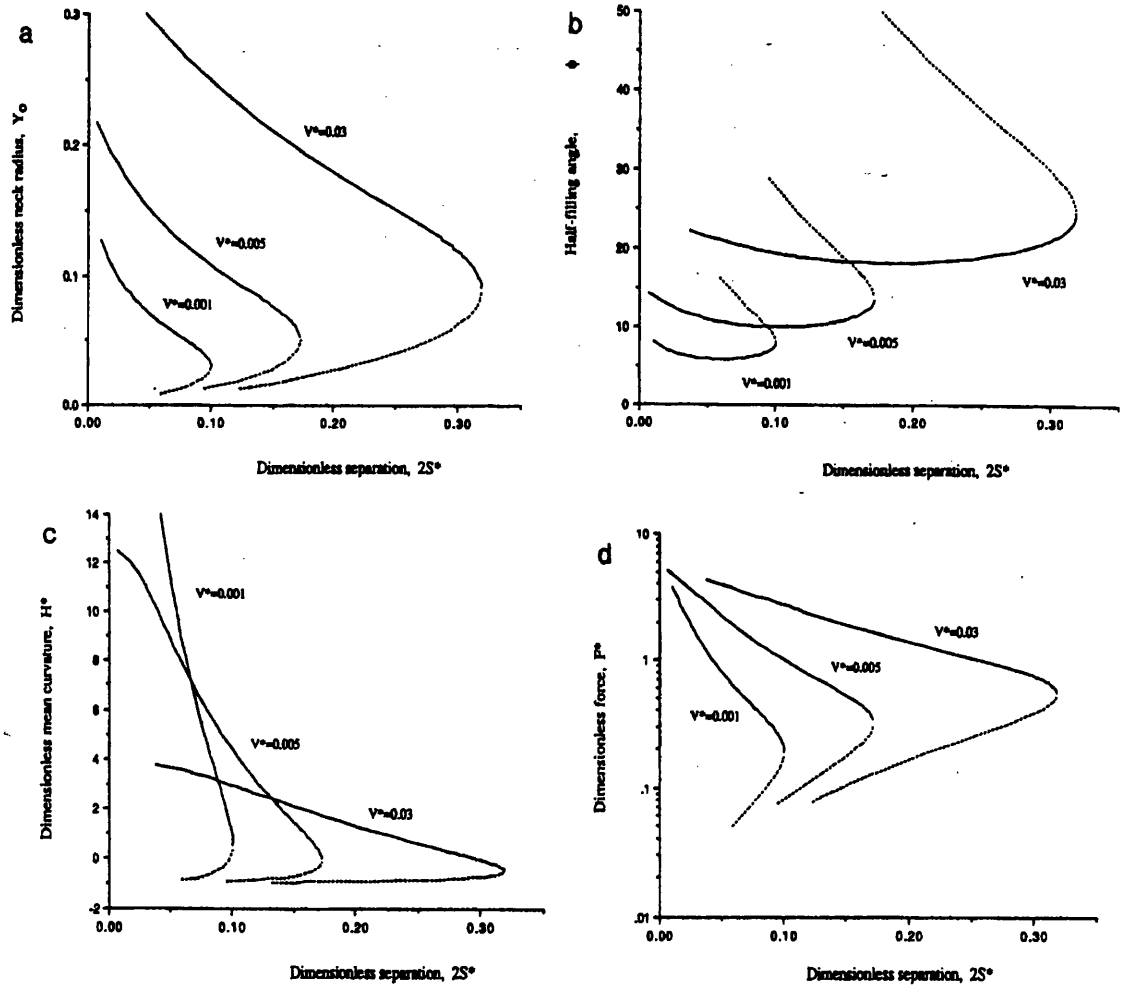

Figure 3-4 Stable (——) and unstable (-----) numerical solutions of the Young Laplace equation at different dimensionless separation distances S^* (=*a*/R) for a range of dimensionless liquid bridge volumes V^* and zero contact angle in terms of (a) the dimensionless neck radius, (b) the half-filling angle ϕ, (c) the dimensionless mean curvature H^* and (d) the dimensionless total liquid bridge force F^*, (after [47]).

This result had already been noted by Erle et al. [48] and De Bisschop et al. [45], who identified the stable configuration as the one that minimizes the free Helmholtz energy A of the liquid bridge. In the analysis presented by De Bisschop et al. [45], the rupture configuration was recognised as occurring when the two solutions became coincident.

If we regard u(x) as the profile of the particle wetted by the liquid binder and x_c the abscissa of the binder to particle contact point (Figure 3-3), the free Helmholtz energy A can be written as (3.10) [45] (see also sections 3.1.7 and 4.2.3):

$$A = 2\pi \int_{x=0}^{x=x_c} \left[2\gamma_L\, y(1+y'^2)^{1/2} - 2\gamma_L \cos\theta\, u(1+u'^2)^{1/2}\right]dx + (P_{ext} - P)V_{br} \qquad (3.10)$$

where the first term under the integral represents the energy stored within the liquid bridge surface, the second term is the energy contribution due to the surface of the particle wetted by the binder, $-PV_{br}$ is the energetic contribution due to the "PV-work" and $P_{ext}\ V_{br}$ is a constant (V_{br} is the volume of the liquid bridge) whose physical meaning is the energy involved in displacing the suspending medium and replacing it with the liquid bridge.

The solution method proposed by Lian et al. [47] introduces a significant simplification by assuming a constant contact angle θ throughout separation. In real cases, this situation does not apply because the contact angle varies according to the interaction exhibited with the particle. Effects of contact angle hysteresis on the liquid bridge separation can be observed in both gaseous and liquid suspending media and will be detailed later in this thesis in chapter 6.

Another question arises on whether the volume of the liquid bridge can be assumed invariable during separation. Simons and Fairbrother [49] and more recently Pepin et al. [50] have shown that this volume, during separation, is either constant or varying according to the wettability of the powder. Between two perfectly wettable particles, the liquid binder tends to saturate the particles first, by forming a liquid reservoir, before

being available to form liquid bridges. In such conditions, during separation, the volume of the binder can vary at the expense of the volume held in the reservoirs.

Due to the limitations of the numerical model proposed by Lian et al. [47] when applied to real cases, a computer program has been used for the solution of differential equations, which is based on a finite difference method using a central differencing scheme [51]. The profile of the liquid bridge is discretised in 250 points and the ordinates of the liquid bridge form a vector that is calculated recursively until convergence is reached. The convergence criterion is met when the quadratic sum of the non-dimensional residuals (difference of correspondent elements of the profile vector calculated at two consecutive iterations) is $< 10^{-5}$. In section 6.1.2 the theoretical solutions of the Young Laplace equation will be compared with the experimental configurations recorded at different steps of liquid bridge separations. The program, which has been written at UCL by M. Murru for the solution of differential equations for catalytic reactors, has been adapted to produce the solution of the Young-Laplace equation. The code cannot be divulged in this thesis because it has not yet been published by the author.

In order to avoid the complexity of the solution of (3.2) simplified models exist for the description of the geometry assumed by a liquid bridge. Among these the *toroidal* method (see section 6.1.1), which approximates the liquid profile with an arc of circumference, has gained some interest from researchers. During the course of this work a new approximation based on a *parabolic* method has been developed which will be discussed in chapter 6.

3.1.3 Rupture distance of a liquid bridge

When the separation distance of a liquid bridge held between two particles is increased, the meniscus displaces until a certain critical bridge separation is attained, at which point the bridge becomes unstable and ruptures. The rupture of a liquid bridge is a very rapid process, which involves some complex phenomena, and only a relatively fast camera (i.e. 500 frames/s) can investigate the evolution of the liquid breakage [52].

Recorded sequences of pendant drops deformed under the effect of gravity show that near rupture the meniscus is similar to an umbilical cord, of finite length and thin radius, joining the two liquid masses which are about to separate. The phenomena involved in the disruption of a cylindrical meniscus were studied by Plateau [15] in terms of the increasing instability of the shape due to the formation of capillary waves generated by external disturbances. The capillary waves narrow the thin umbilical cord and eventually the bridge breaks. During rupture some satellite drops may form as a consequence of this process so that the volume of the bridge is not exactly conserved [52], whilst viscous dissipation also occurs due to the rapid process of liquid redistribution of the separated droplets.

De Bisschop and Rigole [45] stated that as separation distance is increased the half-filling angle (β in Figure 3-1) decreases continuously and rupture occurs when it reaches a minimum. It was subsequently observed by Mazzone et al. [46] that a minimum half-filling angle is indeed reached, but that stable bridges can exist on increasing the separation distance beyond this point with β actually increasing before rupture. As shown by Lian et al. [47] (see Figure 3-4b), theory predicts the observed rise in the half-filling angle before the critical separation distance is reached.

Following on from the solutions shown in Figure 3-4, Lian et al. [47] derived a simple relationship between the rupture distance and the bridge volume. By plotting the dimensionless volume $V_{br}^{*} = V_{br}/R^3$ against the dimensionless rupture distance $a^{*} = a/R$, they proposed the following relationship,

$$a^{*} \cong (1+0.5\theta)\sqrt[3]{V_{br}^{*}} \qquad (3.11)$$

where θ is the solid-liquid contact angle expressed in radians. This equation is very important in all the cases where the evaluation of the rupture distance is needed, as for example in the calculation of the rupture energy of a liquid bridge, which will be addressed in section 3.1.6.

3.1.4 The static liquid bridge force: the capillary and surface tension effects

Starting from the early works of Fisher [53], many papers have reported calculations of the static liquid bridge force and it has been shown that it depends on the separation distance between the particles, the particle-to-particle and the binder-to-particles volume ratios, the surface tension of the liquid bridges and the contact angles that the liquid makes with the particles [10]. A literature review has revealed (see Table 2) that most studies have been focused on the strength of a liquid bridge between relatively large particles (a few mm in diameter) suspended in a gaseous medium (usually air) exhibiting the same surface properties and high wettability towards the binder. This approach, which is very valuable for the amount of data made available and the good agreement with values predicted by theory, neglects the common size scale of agglomerated particles (sub 250 μm) and the important role that contact angle hysteresis plays during the stretching and rupture of a liquid bridge. An extensive survey of pendular liquid bridges in gaseous medium can be found in [54].

Reference	*Particles-Binder*	*Contact angle*	*Particle radius*
[46]	Stainless steel-DBT	~10°	1.98 mm
[49]	Silanised glass – Silicone oil	<20°	<100 μm
[55]	Ruby – Silicone oil	~10°	4 mm
[56]	Sapphire – Silicone oil	0°	2.3 mm

Table 2 Referenced works on liquid bridge force measurements between two particles in a gaseous medium (air). DBT stands for dibutylphtalate.

The static force exerted by a liquid bridge is made up by two parts; that due to the interfacial tension and that due to the hydrostatic pressure within the bridge, determined from the Young Laplace equation (3.1).

In order to calculate the liquid bridge force formed between two particles, two different approaches are commonly used. In the first case, the force is determined by considerations at the neck of the bridge [53], as per (3.12), whilst the second method considers the interfaces between the particles and the liquid bridge [44], as per (3.13):

$$F_n = 2\,\pi\, r_1\, \gamma_L - \pi r_1^2 \Delta P \qquad (3.12)$$

$$F_b = 2\,\pi\, R \sin\beta\, \gamma_L \sin(\beta+\theta) - \pi\, R^2 \sin^2\beta\, \Delta P \qquad (3.13)$$

with the symbols defined as above. In (3.12) the surface tension and the capillary pressure terms multiply the circumference and the area of the bridge neck, respectively, whilst in (3.13) the circumference and the area of the contact between the particle and the liquid are used instead (see Figure 3-1). In both expression (3.12) and (3.13), which are developed for spheres of identical size (for dissimilar particles R is replaced by the geometric average radius $\overline{R}$; $\overline{R} = \frac{2 R_A R_B}{R_A + R_B}$), the effect of gravity is neglected.

In the set of experiments reported in section 6.2, the application of the two methods lead to slightly different values due to errors in the numerical approximation of the bridge meniscus (see section 3.1.2) and in the determination of the geometric quantities (bridge neck, particle-to-binder contact angle) obtained form image analysis (see also section 5.1.8).

Wolfram and Pinter [57] alternated water and *n-hexane* as liquid binder and suspending medium, respectively and showed how density differences between the two liquids generate instability in the strength and post rupture binder distribution due to the increase of gravity effects as the liquid bridge volume increases (from 0.01 to 0.5 ml). They also recognised the importance played by surfaces of different energy (PTFE and glass) in relation to the geometry of, and the energy stored by, a liquid bridge during separation.

As pointed out by Mazzone et al. [46], gravity is also to be taken into account with "large" binder volumes (see section 3.1.1 for definition of large and small volumes), although its effect can be significantly reduced by performing experiments in a second liquid of nearly the same density as the binder [58].

When "small" volumes of binder are administered between highly wettable particles in contact (contact angle ~ 0^{o}), liquid bridges assume a nodoid configuration [44] with a negative mean curvature ($r_1 > 0$, $r_2 < 0$ and $|r_1| > |r_2|$), as indicated in Figure 3-5. The pressure deficiency (i.e. $\Delta P < 0$) across the liquid bridge leads to a higher adhesion force than the case where the gauge pressure, ΔP, is positive , according to (3.12) or (3.13).

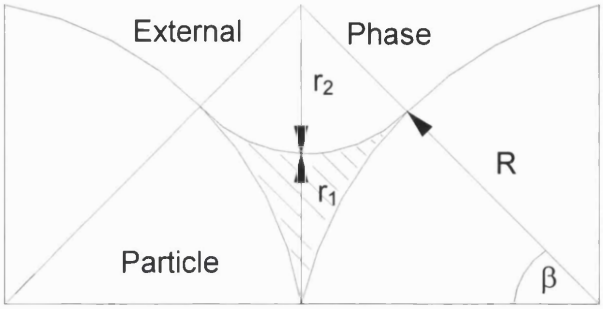

Figure 3-5 Nodoid configuration of a liquid bridge.

The magnitude of the liquid bridge force is difficult to compute exactly, even for simple geometries (sphere-to-plane or sphere-to-sphere), because the bridge forms an interface of constant curvature in order to satisfy (3.1). Fisher [53] developed the *toroidal* approximation, assuming that an arc of a circumference can approximate the exact nodoid configuration (Figure 3-5) of a liquid bridge formed between perfectly wettable particles in contact (i.e. $\theta = 0$). From geometric considerations he obtained (3.14), which compares favourably with the values obtained via the solution of the Young Laplace equation [46, 47].

$$F = \frac{2\pi R\ \gamma_L}{1 + \tan\beta/2} \qquad (3.14)$$

In this thesis a parabolic approximation will be presented that results in a much simpler and more robust mathematical expression that can be used to evaluate the principal physical and geometric liquid bridge parameters (i.e. contact angle, curvature and strength of the liquid meniscus) [50, 59, 60]. The development of this approximation, its experimental validation and the comparison with the traditional *toroidal* method, will be detailed in chapter 6.

The configuration assumed by the liquid bridge in Figure 3-5, however, is not fully general. In many agglomeration processes, particles exhibiting different surface properties might be processed together and therefore discrepancies in surface energy can create problems during agglomeration, as some particles can be selectively wetted at the expense of others [61]. In this scenario, during particle separation, the liquid binder can recede from particles exhibiting lower surface energies which, as separation distance is increased, turns the profile of the liquid bridge from a nodoid geometry to one that is unduloid [60]. The geometry assumed by a liquid bridge in such conditions will be discussed in section 6.1.

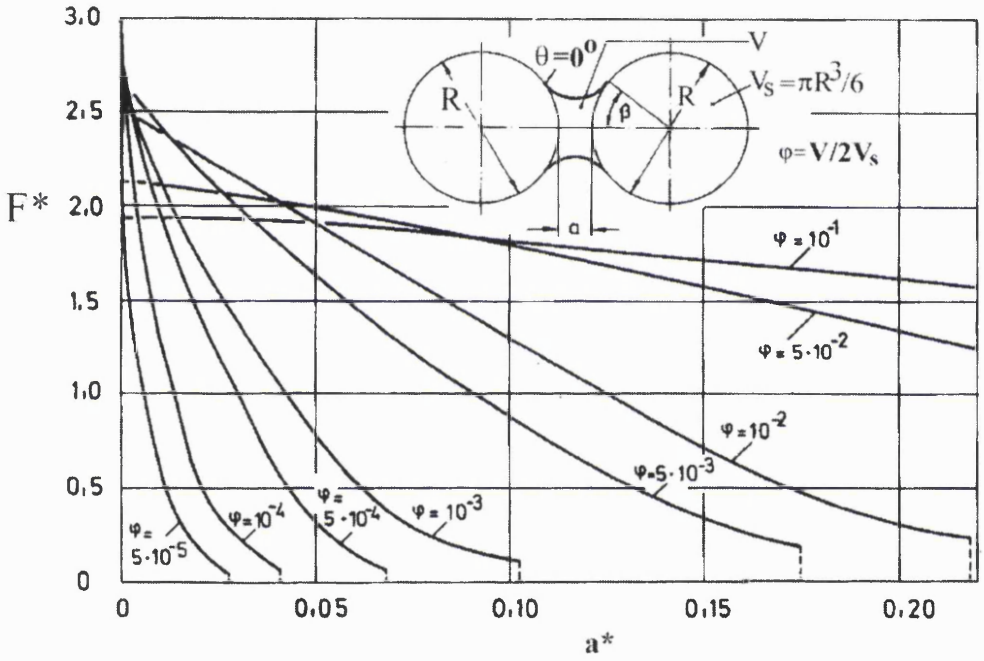

Figure 3-6 Theoretical dimensionless adhesion force F* (=F/γR) of a liquid bridge between two equal spheres against the dimensionless separation a* (=*a*/R). The parameter, φ, is the volume of the liquid bridge divided by the volume of the spheres (after [62]; the author indicated the diameter of the spheres as R).

Different authors [10, 47, 62] have investigated the effects that separation has on the strength of liquid bridges formed between perfectly wettable particles. The trend reported in Figure 3-6 shows a force decrease through separation as a consequence of

the thinning of the bridge neck and the increase of the capillary pressure. It should be noted that, as the relative bridge volume φ becomes smaller, the force reacts sensitively to the variation of the interparticle distance.

The trend shown in Figure 3-6, however, is valid only for the case for quasi-static separation and constant volume as well as $\theta = 0$. It will be shown later how this trend differs under non perfect wetting conditions, non constant volumes and dynamic situations where viscous forces become dominant. Experimental data reported in [46, 49, 58] agree with the trend of Figure 3-6, although the force appeared to reach a maximum at small but non zero separation distances, which is not predicted by theory.

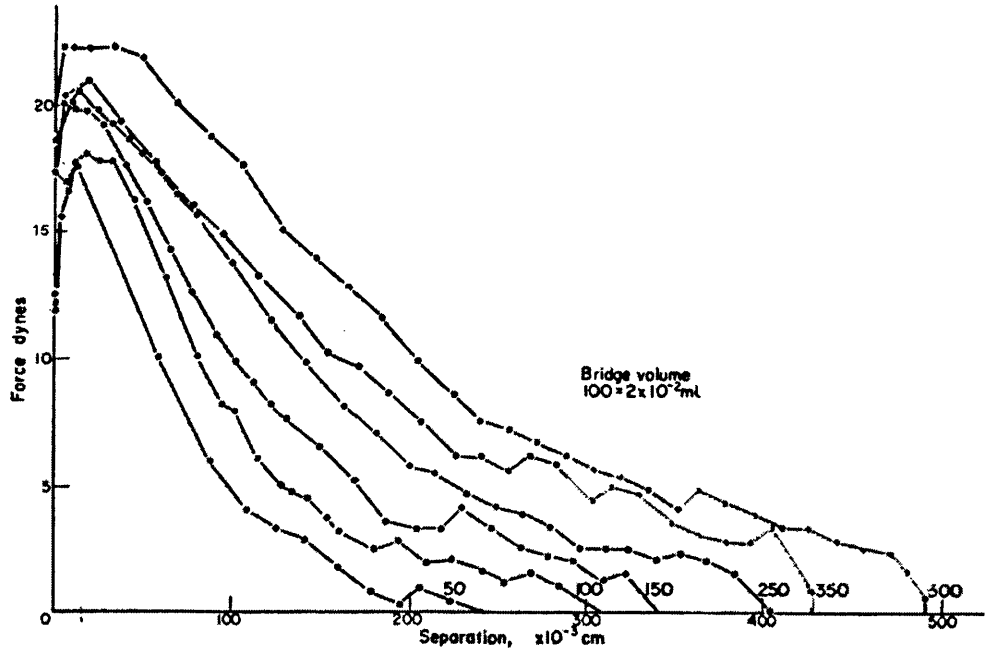

Figure 3-7 Force/separation curves for oil bridges between two polythene spheres (radii 15 mm) suspended in water (after [58]).

Mason and Clark [58] attributed the initial raise of the attractive force (see Figure 3-7) to an initial finite contact angle greater than zero that then reduces to zero as separation increases. The possibility of a decrease in contact angle is related to the amount of volume administered and leads to a change in the profile curvature. In this situation, the capillary pressure reaches a minimum, which leads to the initial increase of the liquid

bridge force. The diminution of the capillary pressure during the first steps of separation has been observed in a set of experiments between glass ballotini suspended in water held by a silicone oil liquid bridge, which will be presented in section 6.2.

Simons and Fairbrother [49] managed to measure liquid bridge forces between particles much smaller in size (23 μm radii), whixh is presented in Figure 3-8. Although the judgment of where the particle contact occurred was an arbitrary decision made by microscopic observation, the trend already shown in Figure 3-7 clearly appears.

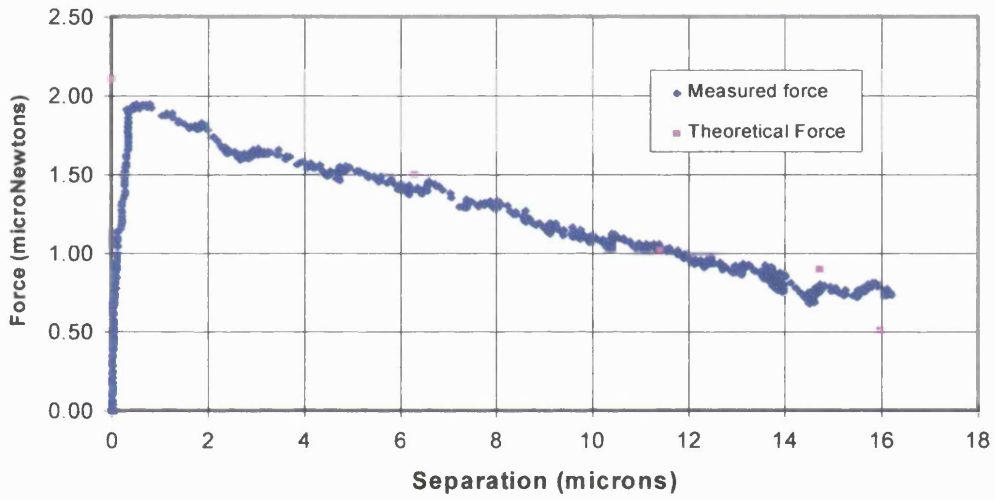

Figure 3-8 Force versus separation for a silicone oil liquid bridge holding two glass silanised ballotini of 23 μm radii suspended in air (after [49]).

3.1.5 Viscous force

During dynamic liquid bridge separations the shear stress inside the liquid gives rise to an additional force, which depends on the viscosity η of the liquid binder.

The expression of the viscous force between two equi-sized spheres held by an infinite liquid bridge (the particles are submerged in the liquid) is given by (3.15) which is valid when the particle radius is large in comparison to the distance of closest approach ($R \gg a$) [55, 63]. In this situation, at low Reynolds numbers ($Re = \frac{v \rho R}{\eta}$, with v being the

particles separation speed), the flow of liquid in the region between the surfaces may be described by the lubrication approximation [64], which assumes the flow to be similar to that between parallel palates where the velocity field is large in the direction orthogonal to that of separation whilst derivatives in the direction of separation are dominant. In (3.15) the radius R is replaced by the geometric average radius, $\overline{R}$, for particles of dissimilar size

$$F_{vis} = \frac{3}{2} \pi \eta R^2 \frac{1}{a} \frac{da}{dt} \tag{3.15}$$

In section 6.2, (3.15) will be used to compare the magnitude of the viscous force with the total liquid bridge static force of either (3.12) or (3.13) during the separation of a finite liquid bridges whilst the regimes where either capillary or viscous forces become dominant will be given in terms of the capillary number $Ca = \frac{v\eta}{\gamma_L}$ which expresses the ratio between viscous and surface tension effects.

Although for liquid bridges of finite volume such an analysis of the viscous contribution ignores the existence and the influence of the bridge meniscus on the region of the particles closest approach, the use of (3.15) is justified in the limit of small capillary numbers ($Ca < 10^{-3}$), small gap distances ($a^* \sim 0.01$) and sufficient bridge volumes ($V_{br}^* \sim 0.05$) [65]. Small capillary numbers, in fact, imply that the viscosity do not effect the liquid bridge interface, whilst the restraints on the distance of closest approach and on the amount of liquid bridge volumes justify a lubrication analysis for the viscous contribution. Under these circumstances (3.15) can be added to the force equation of either (3.12) or (3.13) for dynamic separations. By choosing (3.12), the more general expression of the liquid bridge force becomes:

$$F = 2 \pi r_1 \gamma_L - \pi r_1^2 \Delta P + \frac{3}{2} \pi \eta R^2 \frac{1}{a} \frac{da}{dt} \tag{3.16}$$

The force curves generated by (3.16) will be compared in section 6.2 with the experimental data obtained in the studies reported here.

Pitois et al. [55], noted that in the regime where viscous forces are dominant the Lian et al. formula (3.11) underestimates the bridge rupture distance. They also quantified the variation between the viscous regime rupture distance, a^*_{visc}, and (3.11) as being proportional to the square root of the separation velocity:

$$a^*_{visc} - a^* \propto \sqrt{v} \tag{3.17}$$

3.1.6 Rupture energy of a liquid bridge

The energy required to deform or break agglomerates is an important parameter in agglomeration processes and can be related to the power consumed by the process [11, 65]. Models intended to evaluate the energy required to deform agglomerates have attempted to scale up the single particle interaction to macroscopic behaviour [11]. The basic terms considered in the models are the energy stored by capillary forces and the energy dissipated by friction and viscous effects. The contribution due to capillary forces has been studied in detail [66, 67] and the formulae proposed below can be used in either gaseous or liquid media by simply selecting the appropriate physical constants.

The rupture energy of a liquid bridge is usually calculated by integration of the force exerted by a meniscus throughout separation, from contact to rupture. Simplifications of the force expression are usually introduced, due to the difficulty in dealing with the general problem of the liquid bridge deformation. Two models, proposed by Simons et al. [66] and by Pitois et al. [67], are discussed below and will be compared in section 6.2 with the experimental energy required to deform and break a liquid bridge formed in a liquid medium. In both models only the energy arising from capillary and surface tension forces is evaluated.

The model proposed by Simons et al. [66] is derived by integration of the total liquid bridge force calculated using the *toroidal* approximation [68] and is written as:

$$F = \pi \gamma_L R (1+X \tan\beta - X \sec\beta) \frac{X \tan\beta}{X \sec\beta - 1} \qquad (3.18)$$

where $X = (1+\frac{a}{2R})$ and β is the half filling angle, equal, for geometric similarity, to that shown in Figure 3-1. In the integration of (3.18) through separation distance a, the half filling angle β was considered a constant. The approximation, due to the difficulty in relating the angle β to the separation distance a, seems reasonable for particles that exhibit a strong interaction towards the binder, where the solid liquid interface stays almost constant (see sections 6.1.2 and 6.2) [59]. In any case it has been shown theoretically by Lian et al. [47] (see Figure 3-4b) that the overall change in β is small for perfectly wetted spheres. The expression of the dimensionless rupture energy, $W^* = \frac{W}{\gamma_L R^2}$, calculated between any two configurations X_{min} and X_{max} is as follow:

$$W^* = 2\pi \left[\frac{X^2}{2}(\tan^2\beta \cos\beta - \tan\beta) + X \sin^2\beta + \tan^2\beta \cos^3\beta \ln (X \sec\beta - 1)\right]_{X\,max}^{X\,min} \qquad (3.19)$$

in which X_{max} refers to the rupture distance and is calculated using equation (3.11). Equation (3.19) yields (3.20) when plotted against the dimensionless liquid bridge volume.

$$W^* = 3.6 \sqrt{V_{br}^*} \qquad (3.20)$$

Pitois et al. [67] used a different simplified expression for the total liquid bridge force:

$$F = 2 \pi \gamma_L R \cos\theta \left[1 - \left(1 + \frac{2V_{br}}{\pi a^2 R}\right)^{-1/2}\right] \qquad (3.21)$$

By using the approximation that θ stays constant throughout separation, (3.21) is integrated with respect to the separation distance a, to obtain the rupture energy, which in non-dimensional form reads as (3.22):

$$W^* = \left[2\pi a^* \cos\theta \left(1 - \left(1 + \frac{2V_{br}^*}{\pi (a^*)^2}\right)^{1/2}\right)\right]_{a_1^*}^{a_2^*} \tag{3.22}$$

If $a_1^* = 0$ and $a_2^* = (1+\theta/2)\sqrt[3]{V_{br}^*}$ (see (3.11)), equation (3.23) is obtained:

$$W^* = 2\pi \cos\theta \left[(1+\theta/2)(1-C)\sqrt[3]{V_{br}^*} + \sqrt{\frac{2V_{br}^*}{\pi}}\right] \tag{3.23}$$

where $C = \sqrt{\frac{(1+2V_{br}^*)^{1/3}}{\pi(1+\theta/2)^2}}$, θ is the contact angle expressed in radians, whilst W^* and V_{br}^* are defined as above. The formulae (3.20) and (3.23) proposed above depend only on global parameters, such as volume and contact angles. The usefulness of these expressions lies in their application to analytical and numerical modelling of deformation and fracture of particulate materials, where it is impractical to calculate the rupture energy from single liquid bridges directly. Studies on the fracture mechanisms of compacts and agglomerates show that the release of stored energy during crack formation provides the energy to extend the crack [17, 69]. In a wet bulk solid, crack extensions occur by rupture of liquid bridges and it is therefore necessary to have a simple expression to calculate the energy involved in this process.

Lian et al. [11] have studied, by computer simulations, the deformation behaviour of moist agglomerates formed in a gaseous system. The model is focused on the dissipation mechanisms of the kinetic energy upon collision of two agglomerates, which is illustrated in Figure 3-9. Dissipation of kinetic energy for the moist deformed agglomerates was not solely due to the viscous resistance and breakage of the interstitial liquid bridges, but also to rearrangement (plastic deformation) of the particle structure, which involves friction dissipation according to the theories of Johnson [9]. By setting

the viscosity of the binder at 10mPa s and the collision velocities in a range between 0.5 and 5 m/s, the viscous force was found to account for the dissipation of about 60% of the initial kinetic energy. Energy dissipated by friction was also very significant (~30%), whilst the energy dissipated as a result of rupturing the internal liquid bridges was only a small proportion, at around 5%. Despite the small contribution to the overall deformation energies, the authors pointed out the important implications that liquid bridge breakage has on the internal damage suffered by the agglomerates.

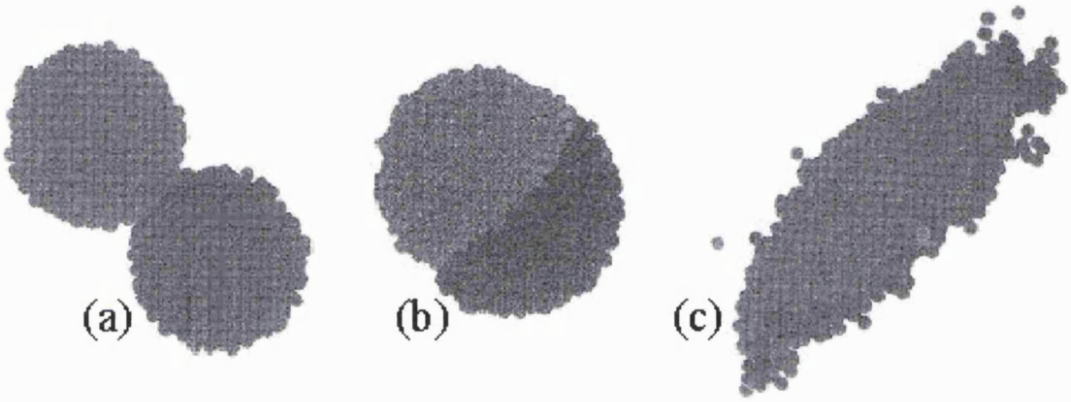

Figure 3-9 Visualizations of computer simulated wet agglomerates for an interstitial fluid viscosity of 10 mPa s after impact at relative velocities of (a) 0.5 m/s, (b) 2.0 m/s and (c) 5.0 m/s (after [11]).

It is quite complex to measure how much single interactions contribute to the energy dissipation of deformed agglomerates. Qualitatively results are reported by Pepin et al. [70] and by Holm et al. [71] who both found the friction to be the mechanism of highest dissipation. Pepin et al. [70] recorded the energy consumption (measured via the torque of the impeller motor) to agglomerate large lactose particles by using different binders of similar surface tension and viscosity ranging from 2 to 251 mPa s. They noted no major differences between the power consumption plots and concluded the viscous dissipation to be negligible for the set of physical quantities investigated.

3.1.7 Thermodynamic approach to the energy stored by a liquid bridge

On a thermodynamic basis, a liquid bridge can be considered a closed system that changes its energy by means of the work done from the external surroundings, whilst its

mass remains constant. The latter assumption seems reasonable for immiscible fluids, such as those dealt with during the experimental work of this project. On the energetic aspect, it is usually assumed that the liquid bridge elongation is adiabatic but not irreversible, which means that some of the external work performed to separate the particles is transformed into heat as a consequence of viscous dissipation. Viscous forces can be neglected after comparison with the magnitude of capillary and surface tension forces, which will be addressed in section 6.2. For the viscosity and separation rate used for this experimental work the comparison showed the assumption to be legitimate. This is not a general case though, as Pitois et al. detailed in [55, 67, 67]. Because a liquid bridge is supposed to exchange work but not heat with the environment, a suitable way to describe its deformation between any two configurations is through the variation of the Helmholtz free energy A, which is defined by (3.24):

$$\Delta A = \Delta U - \Delta(TS) = -w \tag{3.24}$$

where T is the temperature, S the entropy and w the work exchanged with the environment (by convention w is positive when it is done on the external surroundings). U is the internal energy, which for a system containing some interfaces of area A_{int} and surface energy γ_{int}, is defined by (3.25).

$$U = -PV + \Sigma\gamma_{int}A_{int} + TS \tag{3.25}$$

By substitution, (3.24) becomes:

$$\Delta A = (P_1 - P_2)V_{br} + \gamma_L(A_{br,2} - A_{br,1}) + \sum_{A,B}(\gamma_{SL} - \gamma_S)_2 A_{SL,2} - \sum_{A,B}(\gamma_{SL} - \gamma_S)_1 A_{SL,1} = -w \tag{3.26}$$

in which the first term of the central part of the equation is the work associated with liquid bridge pressure variation and the second is related to the stretching of the liquid bridge surface A_{br}. The third and fourth terms represent the variation of the energy associated with the solid liquid interfaces between configurations 1 and 2 and must be calculated on both the particles A and B. These terms will be discussed in more detail in section 4.2.2, together with the significance of the term $(\gamma_{SL} - \gamma_S)_{1,2}$, in which the

subscript S refers to the interfacial energy between the solid and the suspending medium and SL to that of the solid liquid interface. At this stage it is adequate to know that the terms $(\gamma_{SL} - \gamma_S)_{1,2}$ are related to the variation of the contact angle at the particle-binder interface between any two configurations (1 and 2) assumed by the liquid bridge during separation.

Equation (3.26) will be expressed in terms of the apparent contact angle (see (4.11) in section 4.2.2) and used in section 6.2 in order to determine the thermodynamic rupture energy of a liquid bridge and to compare it with values obtained from (3.19) and (3.22).

3.2 Other mechanisms of particle adhesion: sintering and crystallization of dissolved materials

When solid particles are brought into contact at sufficiently high temperatures, sinter bridges may arise in the contact zone. Partial melting to form a sintered neck can also occur due to the heat of friction generated by mutual rubbing of particles. The initial sintering temperature strongly depends on the particle size. An exponential decrease with decreasing particle size is reported by Berbner et al. [72] for titanium nitride (TiN). In general, the mechanisms behind the formation of a sintering neck are quite complex and involve diffusive migration of atom vacant sites from the contact area to the particle surface, which leads to a counter-migration of atoms from the particle to the sintering neck. Other phenomena also occur, such as differences in the equilibrium vapour pressure in the particle-neck zone, which gives rise to mass transfer through the gas phase; viscous flow and externally applied pressures are also recognised as mechanisms of sintering neck formation [72] [73]. It is difficult to express sintering phenomena as a rule and only empirical formulae can be given in terms of the sintered neck growth [72], which ultimately depends on certain physical properties, such as the surface tension and the viscosity of the melting material.

The crystallization of dissolved material is important in all processes involving the drying of agglomerates. Many agglomerates in fact are produced by addition of solute to the liquid binder. When the agglomerates are dried, the solvent binder evaporates and

crystals form between particles which give rise to a higher strength in comparison with that exerted by liquid bridges; in general high drying rates increase the magnitude of this force [10].

Sintering and crystallization of dissolved materials both give rise to higher forces than liquid bridges. These two mechanisms, however, are very specific either to high temperature processes or in the final stages of the agglomerate formation. Niether situation do not represents the central focus of the work reported here and hence, will not be discussed further.

3.3 Interaction arising from electrical effects

The electrical interaction between particles arises from elementary charges in the matter and is scaled up to macroscopic bodies by summing all the combinations of pairwise intermolecular interactions. The term electrical interaction encompasses different types of forces (van der Waals, electrostatic, double layer), which depend on the nature of the surrounding medium and can be responsible for the formation of particle agglomerates in either liquid or gaseous media. Apart from the double layer effect, which is a specific liquid medium interaction, the others can manifest themselves in both media. In particular, the van der Waals interaction, schematically presented in Figure 3-10a (see also section 3.3.2), is always present even between uncharged particles, yet is an electrical effect. The electrostatic force is maybe the simplest to formulate and arises from the coulombic interaction of charged particles (see Figure 3-10b and section 3.3.5). The electrical double layer force (see Figure 3-10c and section 3.3.3) is a specific interaction for charged particles submerged in a liquid medium that contain dissociated ions. The counterions present in solution are attracted from the charged particles and gather to form an electronic cloud around them. The interaction of this atmosphere of ions gives rise to the double layer interaction.

When particles are suspended in a liquid and agglomerated through the addition of an immiscible liquid binder, the interaction between the particle and the binder is regulated by the effects of both van der Waals and double layer forces (see DLVO theory, section

3.3.4). For dissimilar surfaces interacting through water, the van der Waals contribution will generally be attractive. However, if the interacting surfaces have dissimilar charges, the electrical double layer can be either attractive or repulsive or even change from one to the other with changes in the separation distance. As a result of these two complex forces, the affinity of the particle towards the binder can be increased or totally depressed. The interaction of glass particles and oil droplets both submerged in water, which is relevant to the work presented here, has been investigated via an atomic force microscope (AFM) and will be presented in section 6.3.2. The set-up of the AFM used for this set of experiments will be described in section 5.2.

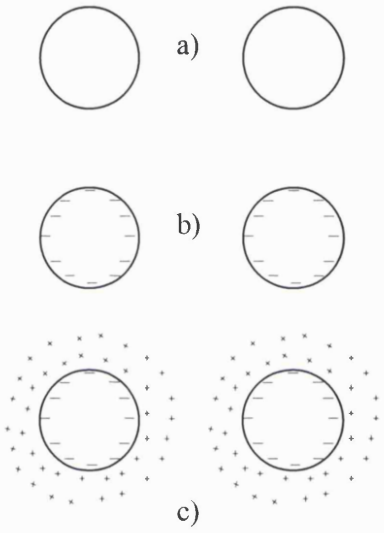

Figure 3-10 Electrical interactions between spherical particles: a) van der Waals force between uncharged particles, b) electrostatic force, c) electrical double layer interaction in a liquid medium.

3.3.1 The Derjaguin approximation

The interaction resulting from van der Waals and double layer effects between the most common curved surfaces (cylinder, sphere) can be calculated through the Derjaguin approximation (3.27) [74]:

$$\frac{F}{R_T} \approx 2\pi\left(\hat{W}_{dl} + \hat{W}_{vdW}\right) \tag{3.27}$$

which is a relation between the van der Waals, $\hat{W}_{vdW}$ and double layer $\hat{W}_{dl}$ interacting free energy per unit area between parallel plates to the force F between the curved surfaces scaled by the effective radius R_T. The effective radius R_T is defined as $\frac{1}{R_T} = \frac{1}{R_A} + \frac{1}{R_B}$ and R_A and R_B are the radii of curvature of the two surfaces. Between a flat plate and a sphere of radius R (3.27) becomes.

$$\frac{F}{R_T} \approx 2\pi\left(\hat{W}_{dl} + \hat{W}_{vdW}\right) \tag{3.28}$$

Due to the Derjaguin approximation the plate-plate configuration becomes a fundamental expression in the theoretical investigation of van der Waals and double layer interactions.

3.3.2 Van der Waals forces

Most molecules, despite carrying no net charge, possess an electrical dipole according to the distribution of the electrons inside the molecule. Such molecules are called polar molecules. Van der Waals forces are the outcome of three main interactions: dipole–dipole (Keesom force), induced dipole–dipole (Debye force) and induced–induced dipoles effects (dispersion force). These three components are profoundly different in nature even though their magnitudes are, in all cases, inversely proportional to the sixth power of the distance separating pairs of atoms/molecules. Dispersion forces, however, are always present in contrast to the other two types that might or might not occur according to the presence of polar molecules. Hence, dispersion forces assume a fundamental role in physical phenomena such as colloidal adhesion, surface tension, molecular adsorption and surface wetting and will be discussed briefly.

Van der Waals dispersion forces are quantum mechanical in nature and may be intuitively understood by regarding the induced pole effect of a non-polar atom immersed in an electric field. In general they can be effective from large distances (greater than 10 nm) through to interatomic spacing (about 0.2 nm).

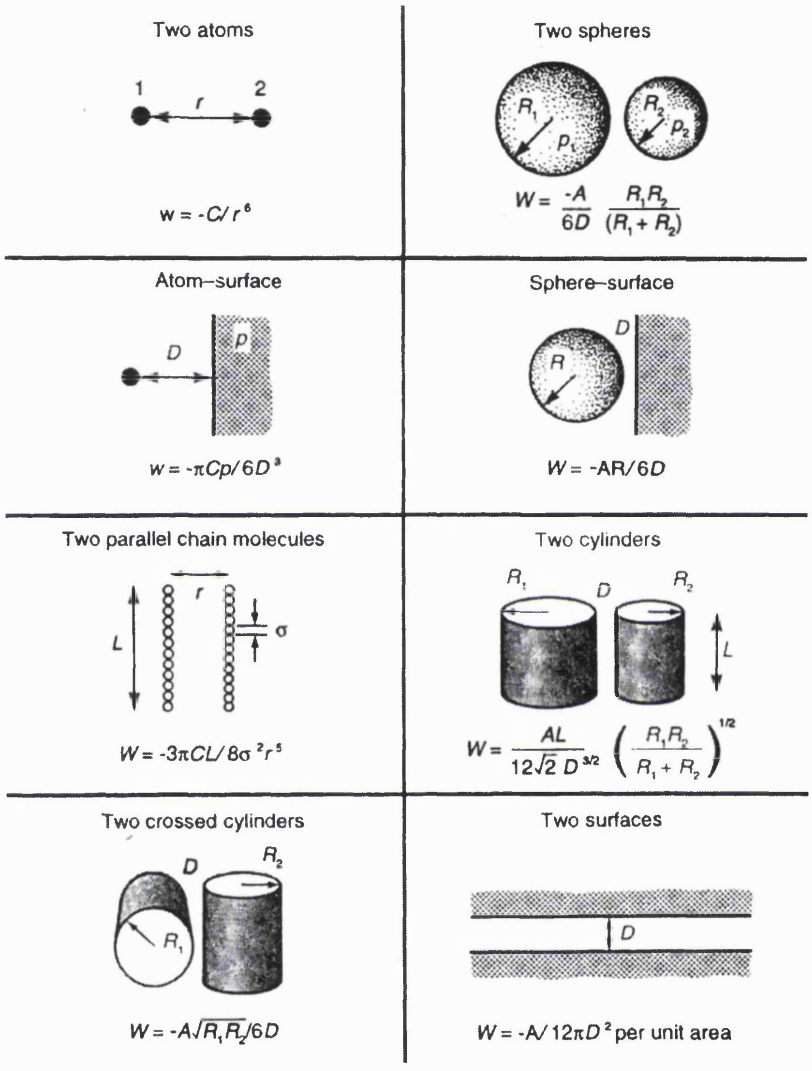

Figure 3-11 van der Waals interaction energy between bodies/atoms of different geometry, calculated on the basis of pairwise additivity (after [74]). In the figure r and D represent the interparticle distance between atoms and bodies, respectively, σ is the molecular diameter and L is either a body or a polymer chain length, W and w (idicated as $\hat{W}$ in the text) are the van der Waals *pairwise* potential of the force acting between bodies and/or atoms, respectively, A is the Hamaker constant [75].

For a non-polar atom, such as helium, the time average of its dipole moment is zero, yet at any instant there exists a finite dipole given by the instantaneous position of the electrons around the nuclear protons. This instantaneous dipole generates an electric field that polarises any nearby neutral atom, inducing a dipole moment in it. The resulting interaction between the two dipoles gives rise to an instantaneous attractive force between the two atoms and the time average of this force is finite.

The complexity of van der Waals forces is also due to the fact that they are not generally *pairwise additive* and so the microscopic interaction between two induced dipoles cannot be scaled up to macroscopic bodies without some simplification. This limitation is due to the fact that the field emanating from any molecule reaches a second molecule both directly and by 'reflection' from other molecules that were also polarised by the field. In a rarefied medium these 'reflection' effects are small and the assumption of additivity holds [74]. Hamaker [75] calculated the *pairwise additive* interactions for the most common geometries, as shown in Figure 3-11.

Between two planar surfaces at a distance a apart the interaction free energy per unit area results from:

$$\hat{W} = -\frac{A_H}{12\pi a^2} \tag{3.29}$$

where A_H is the Hamaker constant, which when positive gives rise to attractive interaction. The symbol of the Hamaker constant (A_H) is defined differently from Figure 3-11 to avoid confusion with the thermodynamic Helmholtz free energy classically identified as A and introduced earlier in this chapter.

Between condensed states (either solid or liquid) across a vacuum, the Hamaker constant is in a range between 10^{-19} and 10^{-20} J. In the case of two bodies surrounded by a fluid medium different from a vacuum, the fluid must be taken into account when the interaction between the two bodies is calculated. As a result of this the overall interaction can drastically diminish and even reverse sign when the bodies are made of

different composition [75]. Values of the Hamaker constant for two identical bulk bodies interacting in vacuum can be found in [74, 76]

The approximation due to the additivity of the single dipole effect is not the only one used by the Hamaker method. When two atoms are an appreciable distance apart, the time taken for the electric field of the first atom to reach the second atom and return (the electric field propagates at the speed of light) can become comparable with the period of the fluctuating dipole itself. When this happens the field returns to find that the direction of the instantaneous dipole of the first atom is now different from the original and thus less favourably oriented for an attractive interaction. This second effect is called the *retardation effect* [74]. The corrected expression for (3.29) including the retardation effect can be found in Hunter [77] and is given in (3.30):

$$\hat{W} = -\frac{A_H}{12\pi a^2} f(p) \tag{3.30}$$

where $f(p)$ is a function defined as:

$$\begin{aligned} f(p) &= 1.01 - 0.14p \quad 1 < p < 3 \\ f(p) &= \frac{2.45}{p} - \frac{2.04}{p^2} \quad 3 < p < \infty \end{aligned} \tag{3.31}$$

where the term $p = \frac{2\pi a}{\lambda}$, expresses the separation in terms of the wave length of the characteristic molecular motion λ. The major consequences of the retardation effect is to limit the range of the van der Waals forces. The term $f(p)$, in fact, reduces the value of $\hat{W}$ in (3.30). Despite the fact that $f(p)$ increases with p (which is a function of the interparticle distance a) and can be as high as 0.59 when p=3, the total attraction energy, $\hat{W}$, would be down of a factor 4 for p=3, which makes less penalising neglecting the retardation effect. The term λ, which is at the basis of the calculation of the factor p, is difficult to calculate and therefore (3.29) will be used here instead.

3.3.3 The electrical double layer

Between similar small particles interacting in a liquid medium the van der Waals forces are generally attractive and we may expect the particles to easily come close enough together to adhere and form a larger mass. In fact, this does not happen because particles suspended in a liquid medium with high dielectric constant assume the same charge sign and the resulting electrical repulsion can prevent coalescence. On the other hand, specific adsorption can lead to oppositely charged surfaces between different particles and hence an attractive interaction might result. The present section briefly covers these phenomena, which have been extensively detailed by Israelachvili [74] who summarised the original work from Grahame [78].

In general, a neutral surface immersed in a polar (e.g. aqueous) medium can be charged in different ways:

- by dissociation of surface neutral groups that migrate in the liquid medium, leaving behind a net counter-ion charge (e.g. the dissociation of protons from surface carboxylic group –COOH $\quad COO^- + H^+$)
- by adsorption on the surface of ions attracted by the counter part of a neutral molecule already adsorbed on the surface.
- by adsorption of ions from solution onto oppositely charged surface sites

Whatever the charging mechanism, the final surface charge is balanced by an equal but oppositely charged region of counterions, some of which are bound, usually transiently, to the surface within the so called Stern-Helmotz layer of thickness δ_{SH}, whilst others form an atmosphere of ions in rapid thermal motion close to the surface, known as the diffuse layer. Counterions, which come off from the surfaces or dissociate from any electrolytes present in the solution, migrate towards the charged surface and screen the electrostatic interaction for other counterions lying further away from the surface. A schematic of the Stern-Helmholtz and diffuse layers for an isolated, negatively charged, surface is shown in Figure 3-12 for a solution containing electrolytes. The combination of these two layers is known as the electrical double layer.

It is common to relate the thickness of the diffuse layer to a characteristic length $\frac{1}{\kappa}$ known as the Debye length, which is calculated using equation (3.32):

$$\kappa = \left(\frac{\sum \rho_{\infty i} e^2 z_i^2}{\varepsilon \varepsilon_0 k\, T} \right)^{1/2} \qquad (3.32)$$

where $\rho_{\infty i}$ are the number densities (m^{-3}) of ions in the bulk, e is the proton charge (e = 1.609 x 10^{-19} C), z_i is the valence of the ions (the index i refers to all the ions dissolved in the solution), ε is the relative dielectric constant of the suspending medium (dimensionless), ε_0 is the permittivity of a vacuum (ε_0 = 8.852 x 10^{-12} C^2 J^{-1} m^{-1}), k is the Boltzmann constant (k = 1.381 x 10^{-23} JK^{-1}) and T the temperature expressed in Kelvin.

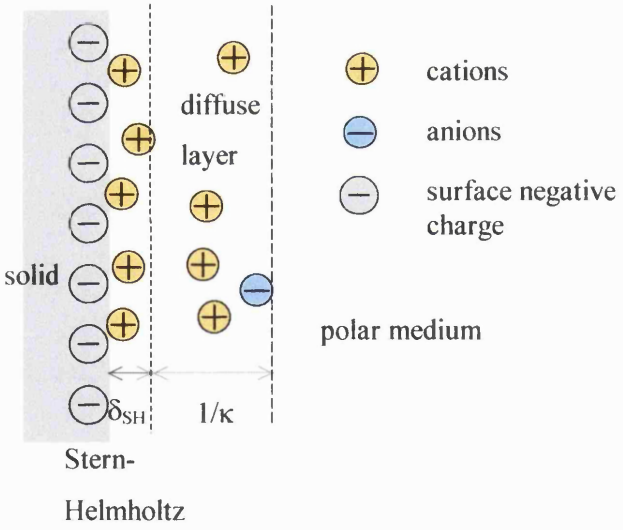

Figure 3-12 Schematic of Stern-Helmholtz and diffuse layer in an electrolyte solution.

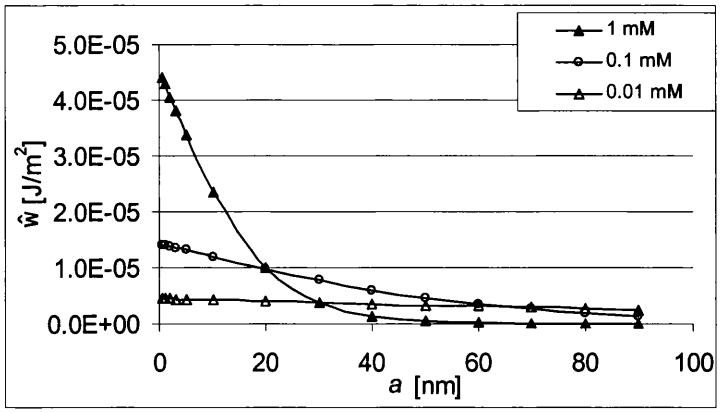

Figure 3-13 Electrical double layer interaction energy per unit area versus separation distance between planar surfaces immersed in a 1:1 electrolyte solution of different concentration. The curves are calculated using (3.41), considering a potential of 25mV between surfaces.

It can be seen that as the electrolyte concentration increases (i.e. $\rho_{\infty i}$ increases) the Debye length decreases. Since the interaction between charged surfaces starts as soon as their double layers overlap, the more diffuse the double layer (i.e. low electrolyte concentration) the greater the distances between the surfaces where the interaction begins. A more concentrated electrolyte solution will interact strongly as shown in Figure 3-13.

The magnitude of the Debye length, therefore, depends on the properties of the solution and not on those of the surface such as surface charge or potential. For a 1:1 electrolyte solution (e.g. NaCl) at 298 K ($\varepsilon \sim 78.5$), the Debye length can be calculated using (3.33), where the concentration is expressed in M (mol/dm^3). For a 10^{-4} M solution $\frac{1}{\kappa}$ results in a value of 30.4 nm, which becomes 0.96 nm for a 0.1M solution.

$$\frac{1}{\kappa} = \frac{0.304}{\sqrt{[NaCl]}} \qquad (3.33)$$

The simplest approach to evaluate the electrical double layer effect (in terms of the interaction energy per unit area) is to consider a planar surface in a pure liquid, such as

water where, apart from the H_3O^+ and OH^- ions, the only ions in the solution are those that come off the surface (counterions). However, more commonly, charged surfaces interact in a solution that already contains electrolyte ions. The distribution of ions away from the a surface where the electrical potential is ψ_0, can be determined from (3.34):

$$\rho_{0i} = \rho_{\infty i}\, e^{\frac{-z_i e\psi_0}{kT}} \tag{3.34}$$

where ρ_{0i} and $\rho_{\infty i}$ are the number densities of the ions on the surface and in the bulk, respectively. From the ion distribution on the surface it is possible to determine the surface charge density σ:

$$\sigma^2 = 2\varepsilon\varepsilon_0 kT\left(\sum \rho_{0i} - \sum \rho_{\infty i}\right) \tag{3.35}$$

Equation (3.35), known as the Grahame equation, is valid only for isolated surfaces and for the specific case of a NaCl aqueous solution becomes:

$$\sigma^2 = 1000N\,2\varepsilon\varepsilon_0 kT\left([Na^+]_\infty\, e^{\frac{-e\psi_0}{kT}} - [Na^+]_\infty + [Cl^-]_\infty\, e^{\frac{e\psi_0}{kT}} - [Cl^-]_\infty\right) \tag{3.36}$$

where N is the Avogadro number ($N = 6.022 \times 10^{23}$ mol^{-1}) and the factor 1000N transforms the concentration expressed in mol/dm^3 (indicated in square brackets) into ion density (m^{-3}). In the bulk, $[Na^+]_\infty = [Cl^-]_\infty$ and therefore equation (3.36) rearranges into (3.37):

$$\sigma = \sqrt{2000\,N\,\varepsilon\varepsilon_0 kT\,[Na^+]_\infty}\left(2\cosh(-\frac{e\psi_0}{kT}) - 2\right)^{1/2} \tag{3.37}$$

The starting point for determining the double layer energy per unit area between two charged surfaces is to study the electrical potential confined between two parallel surfaces. The potential at point x away from a surface depends on the total volume

charge density of the ions at point x and is described by Poisson's equation, which for a 1:1 electrolyte is written as (3.38) [79]:

$$\frac{d^2\psi}{dx^2} = -\frac{e\rho_\infty}{\varepsilon\varepsilon_0}\left(e^{\frac{-e\psi}{kT}} - e^{\frac{e\psi}{kT}}\right) = \frac{2e\rho_\infty}{\varepsilon\varepsilon_0}\sinh\left(\frac{e\psi}{kT}\right) \tag{3.38}$$

The solution of (3.38) is quite complex and depends on the boundary conditions defined for the two surfaces during the approach. In general, when two charged plates are brought closer together, neither the charge nor the potential remain constant. These two quantities are related by (3.39):

$$\frac{d\psi}{dx} = \frac{\sigma}{\varepsilon\varepsilon_0} = \sqrt{\frac{2kT\rho_\infty}{\varepsilon\varepsilon_0}}\left(2\cosh\left(\frac{e\psi}{kT}\right) + M\right)^{\frac{1}{2}} \tag{3.39}$$

This latter equation, formally equivalent to (3.37) (cosh is an even function and therefore does not depend on the sign of its argument), states that both ψ and σ might vary as the plate separation changes whilst their values are linked by M, which depends on the separation distances itself and is a function of the surface charge/potential rearrangements, as surfaces approach [80]. When the two surfaces are at infinite distance apart M=2. Two models are commonly used to describe the double layer interaction. Within these models the two surfaces either maintain a constant potential (PP) or a constant charge (CC) while the separation distance reduces.

Mc Cormack et al. [80] studied the exact solution of (3.38) for the interaction between planar surfaces of dissimilar potential according to a PP model. They found that the Ψ profiles that satisfy (3.38) are expressed in term of Jacobi elliptical integrals. Based on these solutions they also have given the exact expressions for the double layer energy per unit area calculated with the PP method, $\hat{W}_{PP}$, which again results in a function of Jacobi elliptical integrals and is not easy to use in spreadsheet calculations. The interaction energy of the CC model, $\hat{W}_{CC}$, can be calculated from that of the PP model according to (3.40) [80], in which $\psi_{i\infty}$ (i = 1,2) is the surface potential when the particles

are at infinite distance apart. The difficulty of using (3.40) is due to the fact that $\hat{W}_{PP}$ must be re-calculated during the surface approach according to the different boundary conditions exhibited by the surfaces, whose modification can be very difficult to determine (see (3.39) for the relation between ψ and σ):

$$\hat{W}_{CC}(\psi_1,\psi_2,a) = \hat{W}_{PP}(\psi_1,\psi_2,a) + \frac{2\rho_\infty kT}{\kappa}\left[4\cosh\frac{\psi_{1\infty}}{2} + 4\cosh\frac{\psi_{2\infty}}{2}\right.$$

$$\left. + \left(\frac{e^2}{\varepsilon\varepsilon_0\kappa k^2T^2}\left(\sigma_1(\psi_1-\psi_{1\infty}) + \sigma_2(\psi_2-\psi_{2\infty})\right)\right) - 4\cosh\frac{\psi_1}{2} - 4\cosh\frac{\psi_2}{2}\right] \qquad (3.40)$$

An approximated expression for the double layer energy per unit area between flat surfaces of unequal but constant potential at distance *a* apart has been given by Hogg et al. [81] and results in (3.41). This equation will be used in section 6.3.2 in order to verify the attraction measured via an atomic force microscope between a silicone oil droplet and a glass surface submerged in water.

$$\hat{W}_{PP}(a) = \frac{\varepsilon\varepsilon_0\kappa}{2}\left(\left(\psi_1^2+\psi_2^2\right)\left(1-\frac{1}{\tanh(\kappa a)}\right)+\frac{2\psi_1\psi_2}{\sinh(\kappa a)}\right) \qquad (3.41)$$

The approximated solution (3.41) strictly holds for potentials equal or lower than 25mV. The authors, however, showed that even at 75 – 100mV the difference with the exact solution is within 7%.

Gregory [82] has proposed the approximate expression (3.42) for interaction energy between surfaces of same charge magnitude under the constant charge model, which shows a good agreement with the exact solution. In (3.42) ς_0 is the non dimensional potential defined as $\frac{e\psi_0}{kT}$. Unfortunately a simple approximation for surfaces of different charge magnitude is not available in the literature.

$$\hat{W}_{CC}(a) = \frac{2\rho_\infty kT}{\kappa}\left(2\varsigma_0 \ln\frac{\sqrt{1+\varsigma_0^2\,\mathrm{cosech}^2(\kappa a/2)}+\psi_0\coth(\kappa a/2)}{1+\varsigma_0}+\kappa a\right.$$

$$-\ln(\varsigma_0^2 + \cosh \kappa a + \sqrt{1 + \varsigma_0^2 \operatorname{cosech}^2(\kappa a/2)} \sinh \kappa a)) \qquad (3.42)$$

Figure 3-14 shows the energy per unit area between planar surfaces in a 1:1 electrolyte solution calculated with the approximated PP and CC models according to equations (3.41) and (3.42), respectively. When the surfaces are at a certain distance apart ($\kappa a > 3$) the two models give almost the same values due to the fact that the charge and the potential on each surface are related from (3.37).

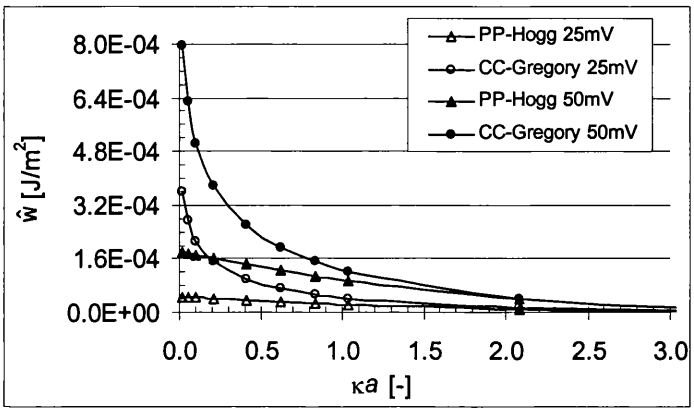

Figure 3-14 Interaction energy per unit area between two planar surfaces immersed in a 10^{-3} M solution of a 1:1 electrolyte (NaCl for example). The potential of the two surfaces at large distance apart ($\kappa a > 3$) is either 25mV or 50mV. The curves represent the approximated solution calculated from the constant potential (PP) [81] and the constant charge (CC) [82] models. The reciprocal of the Debye length (κ) is 1.04×10^8 m^{-1}.

As shown by Israelachvili [74] for surfaces at closer distance ($0.1 < \kappa a < 1$), the CC model gives higher interaction energy than that evaluated by the PP assumption. In Figure 3-14 the interaction is increasingly repulsive as distance decreases due to the same sign and magnitude of the potentials.

The interaction of plane surfaces of dissimilar magnitude can lead to quite different situations; the qualitative analysis proposed by Mc Cormack et al. [80] is summarised in the following points:

- CC interaction (constant charge)
    1. like charges are always repulsive
    2. surfaces of unlike charges change from attraction to repulsion as the separation reduces, except when the charges on the two surfaces have same magnitude and opposite sign, where the interaction is again always attractive.

- PP interaction (constant potential)
    1. surfaces of unlike potential will always attract
    2. like (not identical) surfaces switch from attraction to repulsion during approach. Surfaces with identical potential will always repel.

The transition from repulsion to attraction under the PP model of like charges can be verified by equation (3.41) and will be shown in more detail in section 6.3.2 for the case of the interaction between a glass sphere and a droplet of oil submerged in an electrolyte solution.

In the formulae presented so far the electrical double layer has been approximated with the diffuse layer by assuming that the ions dispersed in the electrolyte solution are point charges. The finite size of the charges, however, limits the inner part of the diffuse layer to the boundary with the Stern-Helmholtz layer (see Figure 3-12) in which ions (predominantly counterions) are transiently bound to the surface within a very close distance from the surface δ_{SH} (typically one ion depth). The surface electrical potential ψ_o rapidly varies through the thickness δ_{SH} and reaches the value ψ_d at the interface with the diffuse layer, as indicated in Figure 3-15a. It is also possible, especially for surface-active counter ions, for reversal of charge to take place (see Figure 3-15b). In this situation the counterions that are adsorbed within the Stern-Helmholtz layer, can associate tightly through the interaction of their hydrocarbon tails and overturn the point of zero potential on the surface. This phenomenon will be described in more detail in section 4.4.1.

The determination of Ψ_0 is limited by the availability of the physical data in the Stern-Helmholtz layer, as for example the dielectric constant ε, whose value cannot be assumed as being equal to that in the bulk. The potential Ψ_d, however, can be estimated from electro kinetic measurements. The zeta potential ζ, which follows from measurements of the charge mobility at the interface between the two layers, can be reasonably assumed as being close in value to the electrical potential ψ_d.

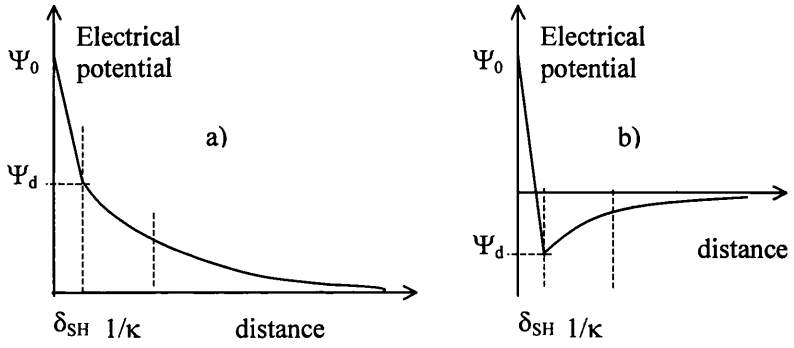

Figure 3-15 a) Schematic of electrical potential variation through distance, b) reversal of charge due to the adsorption of surface-active counter ions.

Gu and Li [83, 84] measured the zeta potential of glass and silicone oil droplets immersed in solutions of different electrolytes and surfactants. Their data have been valuable to part of the experimental work reported in this thesis, which concerns measurements of the interactions between glass ballotini and silicone oil droplets in solutions of different electrolytes and surfactants (see section 6.3.2). Their data [84] will be presented in chapter 4, where the nature of surfactants is also discussed.

Potential-determining ions

In some cases the ions in solution can promote dissociation of surface sites and, therefore, the variation of their concentration in the bulk is able to modify the potential/charge configuration of the surface. These species are called potential-determining ions. A general case of surface site dissociation is described by amphoteric surfaces, which contain both anionic and cationic groups to which other ions can bind through the mechanism of specific adsorption. The dissociation equilibrium of such

species can be written according to (3.43) and (3.44), in which M represents the bulk element.

$$\text{—M–OH} + OH^- \quad \text{—M–}O^- + H_2O \tag{3.43}$$

$$\text{—M–OH} + H^+ \quad \text{—M–}OH_2^+ \tag{3.44}$$

In the equilibrium balance presented in (3.43) and (3.44) both the concentrations of the OH^- and H^+ groups in the bulk determine the charge on the surface and therefore are potential determining ions. The dissociation constants related to (3.43) and (3.44) determine how sensitive the surface is to the concentration of a specific ion. The concept of potential-determining ions is however quite general and is not restricted only to OH^- and H^+ ions. For example, it can be induced by polar surfactants not specifically adsorbed by the surfaces, as has been observed by Gu and Li [84, 84] for glass in an aqueous solution of sodium dodecyl sulphate, which will be detailed in section 4.2.2.

This method of surface charging can be used to describe the variation of the potential of glass submerged in water at increasing pH, as illustrated in Figure 3-16. The electrical nature of the glass/water interface is strongly determined by the pH of the aqueous phase due to dissociation of surface hydroxyl groups.

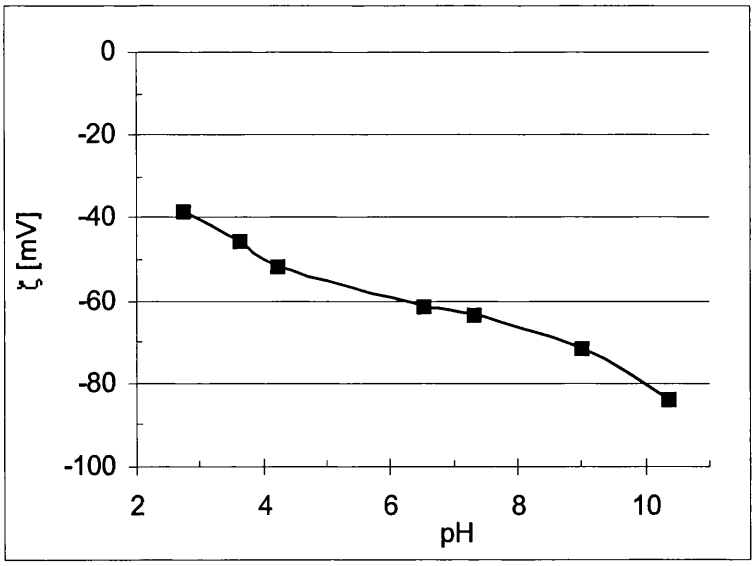

Figure 3-16 Variation of the zeta potential (ζ) of a glass surface with pH of aqueous phase (after [84]).

Glass on the surface exists in its silanol form (—SiOH) whose equilibrium follows (3.45) [85], which is formally equivalent to (3.43). From (3.46), where k_d is the reaction dissociation constant, it can be seen that the concentration of H^+ influences that of the $—SiO^-$ ions.

$$—SiOH \quad —SiO^- + H^+ \tag{3.45}$$

$$k_d = \frac{[-SiO^-][H^+]}{[-SiOH]} \tag{3.46}$$

The analysis of the electrical double layer in the presence of charge regulating ions is more complex than the basic theory given here and has been reviewed by Chan et al. [86].

3.3.4 DLVO theory: van der Waals and double-layer forces acting together

In the case of the interaction of charged material in a liquid medium, the DLVO theory separates the total interaction in two contributions: the van der Waals and the double layer effects. Importantly, the total interaction free energy can be taken as the sum of these two contributions whose single behaviour have been detailed in the previous sections.

Of the two effects, the van der Waals interaction is not as sensitive to the electrolyte concentration as the double layer is and therefore can be considered constant with respect to the pH and ion concentration of the solution. Furthermore, the van der Waals attraction must exceed the double layer repulsion (for equally charged particles) at very small interparticle distances a, if the two surfaces are to adhere. Van der Waals attraction between planar surfaces is in fact a power law interaction proportional to $1/a^2$ (see section 3.3.2), whilst the double layer repulsion rises much more slowly as $a \rightarrow 0$. Figure 3-17 shows schematically the total interaction energy of a colloidal system under different conditions of surface charge and electrolyte concentration for two equi charged surfaces.

The curves of the total interaction energy versus interparticle distance show the evolution of the state of a colloidal suspension under the van der Waals and double layer effect. When the interaction energy presents a relative minimum, the colloidal system remains in a stable (dispersed) state, whilst for the absolute minimum the system is easily agglomerated due to the attraction force.

The curve "a" in the lower inset of Figure 3-17 shows the situation of highly charged particles dispersed in a dilute electrolyte. The strong long-range repulsion between the particles is summarised by the presence of the energy peak that forms an energetic barrier (usually at a separation distance between 1 and 4 nanometers) to agglomeration. Particles whose interaction distance lies on the right size of the barrier have not enough energy to overcome the peak and move in the region of rapid agglomeration ($W<0$ with diminishing distances).

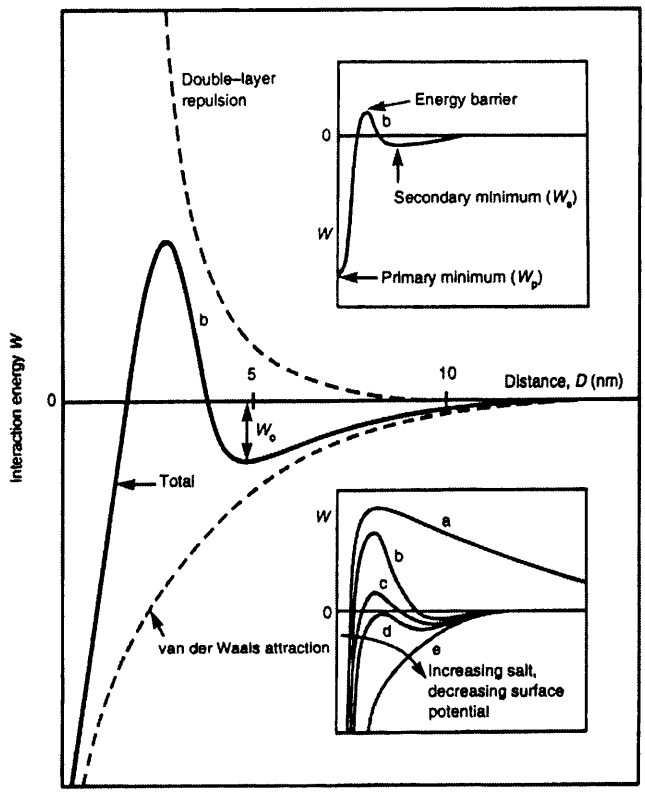

Figure 3-17 Schematic energy, W, versus distance profile of DLVO interaction (after [74]), the separation distance is indicated as D. W_p is the primary minimum, W_o or W_s indicates the secondary minimum.

When the electrolyte solution is more concentrated and therefore the surface charge is reduced (Figure 3-17 upper inset), the curve presents a contact value called the primary minimum, W_p, an energy barrier and a secondary energy minimum, W_s, on the right hand side of the energy barrier. Though the primary minimum determines the stable thermodynamic aggregate configuration, the height of the barrier is still too high to be overcome by the particles at any time during their reciprocal interaction and so they remain either in the secondary minimum or are totally dispersed in the medium. Particles "sitting" in the secondary minimum maintain this mean constant separation distance between them and exist as loose flocs.

As the charge density decreases further, the energy barrier reduces more and more which leads to slow aggregation known as flocculation (Figure 3-17 lower inset curve "c"). Above a certain concentration (called the *coagulation concentration*) the energy barrier falls below the W=0 axis and the regime is of rapid coagulation (Figure 3-17

lower inset curve "d"). When the surface charge approaches zero, the interaction is dominated by the van der Waals forces.

In section 6.3.2 the interaction of a glass particle and a droplet of oil submerged in different solutions of electrolyte/surfactants will be analysed in terms of the resulting effects of the double layer and the van der Waals interaction. In brief, the interaction energy in an aqueous solutions of 10^{-3} and 10^{-4} M of NaCl has resulted in always being attractive, with the van der Waals forces overturning the double layer effect as the separation distance has been decreased. On the other hand, the addition of different surfactants has proved to either enhance or prevent completely this attraction.

3.3.5 Electrostatic forces

Particles with opposite charge attract each other. Different mechanisms can lead to a particle being charged, e.g. as a result of particle contacts accompanied by transfer of electrons or due to mechanisms of friction, grinding or electron adsorption. The type of interaction differs according to whether the particles are conductive or insulating. Between two conductors, the interaction depends on the contact potential U_C, which is the difference in the electron work functions W_E between the two bodies. The electron work function W_E is the energy needed to remove an electron from its metal. If two metals with different work functions are brought into contact, electrons pass from the metal with the lower work function to that with the higher one, which then becomes negatively charged until an equilibrium state is reached. The contact potential U_C depends ultimately on the combination of material and on the surface state of the particles [10]. Between two spheres of radius R, the resulting interaction between conductors is given by:

$$F_c = \frac{\pi \varepsilon \varepsilon_o U_C^2 R}{2a} \tag{3.47}$$

The interaction between insulators is calculated with the assumption that on each particle, the excess charges distribute homogeneously on the solid surface and therefore

the Coulomb law can be applied. Between spheres of radius R the force of interaction is given by (3.48):

$$F_i = \frac{\pi \sigma_1 \sigma_2 R^2}{\varepsilon \varepsilon_0 (1 + a/2R)^2} \qquad (3.48)$$

where σ_1 and σ_2 are the surface charge densities of the two particles. It is interesting to note that, since ε=1 in vacuum and ε=78.5 in water, from (3.47) and (3.48) it results that the force between conductors is enhanced in a water medium whilst between insulators it is depleted.

3.4 Relative magnitude of adhesive forces in the gas and liquid bulk media

The largest attraction forces occur for adhering particles that are nearly in contact (contact distance 4 Å). Suitable values for the variables on which the different interactions depend give rise to the graph plotted in Figure 3-18 and Figure 3-19 for the gaseous and liquid bulk medium, respectively. The graphs refer to two theoretical equi-size spheres and show the liquid bridge strength to be the highest across the entire particle size range.

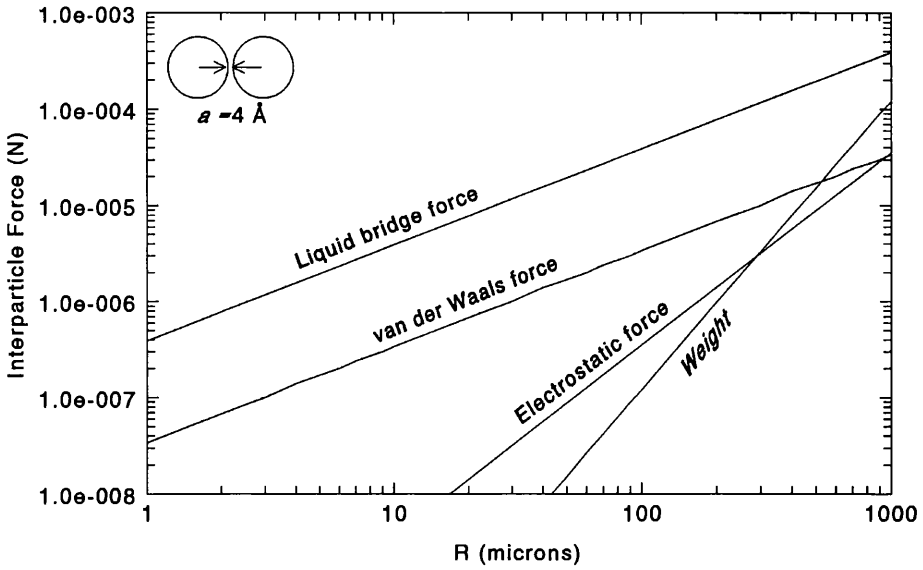

Figure 3-18 Magnitude of interparticle forces for single-point contact between two equal theoretical spheres suspended in air. Particle weight is plotted for comparison.

Liquid bridge $F = \frac{2\pi R\ \gamma_L}{1 + \tan\beta/2}$ [53]

$\gamma_L = 72.7$ mN/m, $\beta = 20°$

van der Waals $F = \frac{R\ A_H}{12\ a^2}$ [74]

$A_H = 6.5\ 10^{-20}$ J, $a = 4$ Å

Electrostatic $F = \frac{\pi \sigma_1\ \sigma_2\ R^2}{\varepsilon\ \varepsilon_0 (1 + a/2R)^2}$ [10]

$\sigma_{1,2} = 10\ \mu C/m^2$, $a = 4$ Å, $\varepsilon_o = 8.9\ 10^{-12}\ C^2/Nm^2$, $\varepsilon = 1$

Weight $F = \frac{4\pi R^3\ \rho_p\ g}{3}$

$\rho_p = 3000\ \frac{kg}{m^3}$ (particle density), $g = 9.81\ m/s^2$

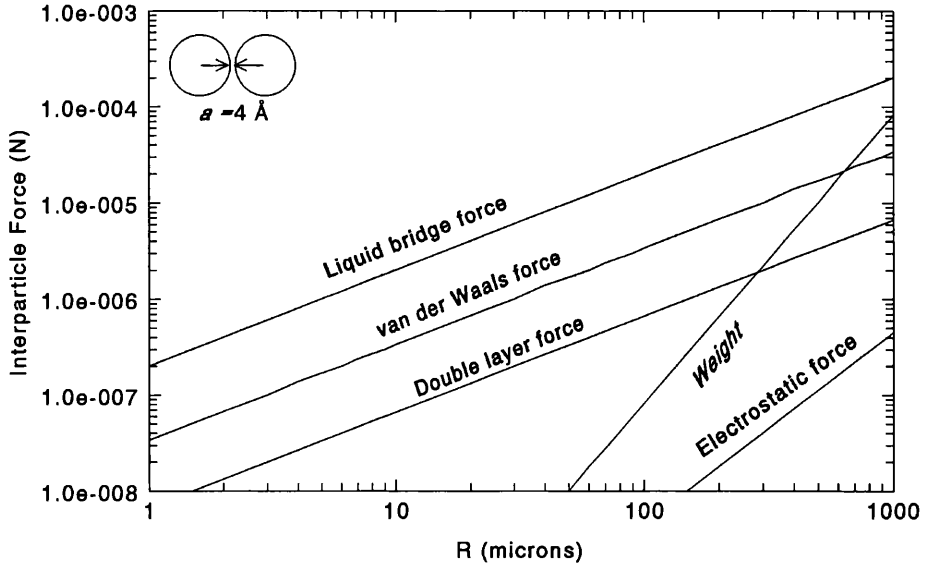

Figure 3-19 Magnitude of interparticle forces for single-point contact between two equal theoretical spheres suspended in liquid medium. Particle weight is plotted for comparison.

Liquid bridge $F = \frac{2\pi R\ \gamma_L}{1 + \tan\beta/2}$ [53]

$\gamma_L = 37.8$ mN/m, $\beta = 20°$

van der Waals $F = \frac{R\ A_H}{12\ a^2}$ [74]

$A_H = 6.5\ 10^{-20}$ J, $a = 4$ Å

Double Layer $F = \pi R \frac{\varepsilon\varepsilon_0\kappa}{2}\left(\left(\psi_1^2 + \psi_2^2\right)\left(1 - \frac{1}{\tanh(\kappa a)}\right) + \frac{2\psi_1\psi_2}{\sinh(\kappa a)}\right)$ [81]

$\psi_1 = 25$ mV, $\psi_2 = -25$ mV, $\kappa = 1.04 \times 10^8\ m^{-1}$, $a = 4$ Å, $\varepsilon_o = 8.9\ 10^{-12}\ C^2/Nm^2$, $\varepsilon = 78.5$

Electrostatic $F = \frac{\pi\sigma_1\ \sigma_2\ R^2}{\varepsilon\varepsilon_0(1 + a/2R)^2}$ [10]

$\sigma_{1,2} = 10\ \mu C/m^2$, $a = 4$ Å, $\varepsilon_o = 8.9\ 10^{-12}\ C^2/Nm^2$, $\varepsilon = 78.5$

Weight $F = \frac{4\pi R^3\ (\rho_p - \rho_L)\ g}{3}$

$\rho_p = 3000\ \frac{kg}{m^3}$ (particle density), $\rho_L = 1000\ \frac{kg}{m^3}$ (bulk medium density), $g = 9.81\ m/s^2$

The force models assume the particles to be perfectly smooth and rigid, which is not always accomplished with real particles. Looking at the interaction between a sphere

and a flat plane, Seville et al. [73] pointed out that van der Waals forces should be calculated by using a characteristic length to be derived from the roughness of the particle instead of from its gross radius. Under these assumptions van der Waals and weight forces are comparable as soon as particles reach a diameter of ~100μm and not ~1mm, as would be predicted if the particle radius is used as the geometric controlling factor. This situation is commonly experienced; particles of 100μm size, in fact, can be found adhering to surfaces and resisting the force of gravity, which does not happen for 1mm particles.

From Figure 3-18 and Figure 3-19 liquid bridge forces are greater than the other adhesive mechanisms, therefore allowing larger particles to adhere to each other. It is also to be noted that, contrary to the other attraction mechanisms, the magnitude of liquid bridge forces can be easily adjusted by varying the amount and the properties of the liquid used as the binder [73], hence the practical relevance to agglomeration processes. In the liquid bulk medium however, van der Waals and double layer forces play an important role in the preliminary phase of liquid bridge formation, as will be elucidated in section 6.3.2.

Chapter 4

4 Surface chemistry and thermodynamics of surfactants adsorption

The wetting behaviour of a solid-liquid interface, regardless of the suspending bulk medium, is an important phenomenon in various industrial processes such as agglomeration, spherical agglomeration, flotation, detergency and printing. The affinity of a liquid toward a particle is governed by the wettability, which is a measure of how easily the liquid can wet the particle. The wettability of a solid surface by a pair of immiscible fluids is governed by the balance of pairwise interfacial energies and is characterized by the contact angle, which is the angle formed by the intersection of the interfaces bounding the three phases. In "wet agglomeration" processes the affinity of a liquid binder towards the particles strongly influences the geometry of the formed liquid bridges with consequences on the resulting adhesion force. The relation between geometry of a liquid bridge and the wettability of a solid particle has been investigated in the work presented in this thesis, considering both gaseous and liquid suspending media and will be discussed in chapter 6. In particular, for the case of particles suspended in a liquid medium, the possible geometries assumed by liquid bridges, which depend on the surface energy of the particle substrate, are analysed in terms of the resulting liquid bridge strength.

In the industrial processes cited above it is very important to have an appropriate description of the interface at which the solid, the liquid and/or the vapour phase arrive into contact in order to interact under mechanisms of energetic stability. In the liquid phase, for example, modifying the interfacial energies by means of surface active agent (surfactants) can induce dramatic changes to the particles wettability and consequently to their interactions, regardless of the presence of a liquid binder. Surfactants, which are more frequently used when particles are suspended in a liquid, adsorb on to the existing interfaces (solid-liquid or liquid-liquid) and vary the surface charge and the mutual

interaction between the particle and its environment. The interaction of surfactants with dissolved particles generally promotes formation of substrate layers onto the solid particle, which ultimately depends on the solubility of the particles and on the pH of the solution [29]. The influence of surfactant on the strengths of silicone oil liquid bridges between glass particles suspended in water has also been investigated in this thesis and will be presented in section 6.3.1.

4.1 The nature of surface tension forces

The first law of thermodynamics applied to a generic system containing an interface (i.e. liquid-gas or liquid-liquid) is:

$$dU = -PdV + \gamma_{int}\, dA_{int} + \Sigma_i\, \mu_i dn_i + TdS \qquad (4.1)$$

where S refers to the entropy, n_i to the number of moles of the components present in the system whose chemical potential is μ_i and A_{int} is the area of the interface whose surface tension is γ_{int}. Equation (4.1) can be rewritten in terms of the Gibbs free energy:

$$dG = VdP + \gamma_{int}\, dA_{int} + \Sigma_i\, \mu_i dn_i - SdT \qquad (4.2)$$

The surface tension γ_{int}, which represents the energy required to form a fresh new surface of area A_{int}, is the free energy per unit area when the pressure, temperature and the numbers of moles of the components remain constant. Surface tension is, in general, a property either of the solid or liquid state. Our interest is related to liquid bridge deformation and therefore the problem is focused on the liquid state.

Long-range interactions (van der Waals, and hydrogen bond forces, if any) are responsible for the liquid aggregated state. Surface tension can be explained from the unbalanced surface equilibrium of these fundamental interactions, as is shown in Figure 4-1. The molecules located within the bulk are, on average, subjected to an equal force of attraction in all directions, whereas those located at the liquid–air interface experience unbalanced attractive forces, resulting in a net inward pull. Since as many

molecules as possible leave the liquid surface for the bulk, a spontaneous contraction of the interfacial area results [79].

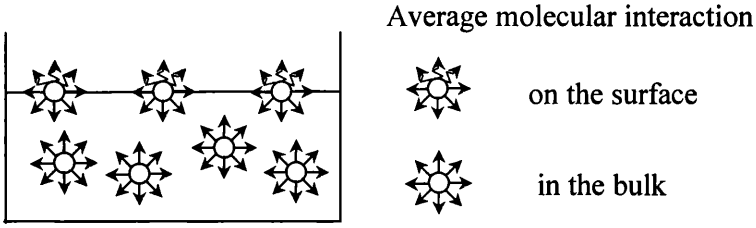

Figure 4-1 Attractive forces between molecules at the surface and in the interior of a liquid.

As a result of these combined long-range effects, Fowkes [87] selected two main parameters to describe the surface tension. In equation (4.3), γ^d (dispersion part) is the resultant of van der Waals dispersion interactions, whilst γ^p (polar part) accounts for both the effects arising from the polarity of the molecules (permanent dipoles interaction) and the hydrogen bond forces when present.

$$\gamma = \gamma^d + \gamma^p \tag{4.3}$$

Some models have been derived to describe the interfacial tension of a two-phase system, γ_{12}, as a function of the surface energy of the two pure components. These models are based on the assumption that at the interface, a molecule of component 1 will be attracted with a force equal to γ_1 by other molecules of its own phase and with an average force $f(\gamma_1, \gamma_2)$ by the molecules of component 2. Reversing the reasoning for any molecule of component 2 and estimating $f(\gamma_1, \gamma_2)$ as $\sqrt{\gamma_1^d \gamma_2^d}$ (i.e. the geometric mean of the two γ^d components), it is possible to write γ_{12} as per (4.4). Fowkes justified this assumption by arguing that between immiscible liquids the interaction should be principally dispersive.

$$\gamma_{12} = \gamma_1 + \gamma_2 - 2\sqrt{\gamma_1^d \gamma_2^d} \tag{4.4}$$

This approximation, which is particularly suitable for systems in which at least one component has a purely dispersive nature (a water–hydrocarbon interface for example) gives appropriate results also for other systems such as the mercury–water interface, where polar and metal bond components also play a strong role in the overall interaction [77]. Equation (4.4) will be modified in Appendix A.2 to account for polar effects between the two phases, in order to calculate the surface tension of the water–silicone oil interface. More recently, van Oss et al. [88] have proposed a different breakdown of the surface tension components. The polar part γ^{AB} accounts for the Lewis acid–base behaviour of the species. Lewis acids are electron pair acceptors and Lewis bases are electron pair donors. In (4.5) γ^+, γ^- are the electron acceptor and donor surface tension components, respectively.

$$\gamma^{AB} = 2\sqrt{\gamma^+\gamma^-} \tag{4.5}$$

The interfacial tension between two phases (solid–liquid for example) is defined according to (4.6) [88]. Equation (4.6) is a very important relation, which allows the calculation of the surface energy of a solid via contact angle measurements against liquids whose surface tension decomposition is known [89].

$$\gamma_{12} = \gamma_1+\gamma_2 - 2\sqrt{\gamma_1^d\gamma_2^d} - 2\sqrt{\gamma_1^+\gamma_2^-} - 2\sqrt{\gamma_1^-\gamma_2^+} \tag{4.6}$$

Table 3 summarizes the surface tension decomposition of some solvents and polymers and is based on the reference $\gamma^+ = \gamma^- = 25.5$ mN/m assumed for water. However, the values of the coefficients γ^+, γ^- are not unequivocal but strongly depend on the reference choice made for water. A different reference value for water is commonly considered and is based on the consideration that the Lewis acid activity is 6.5 times stronger than the base. In this scale γ^+ =65 mN/m and γ^- =10 mN/m [90].

Material	γ	γ^d	γ^{AB}	γ^+	γ^-
water[1]	72.8	21.8	51	25.5	25.5
glycerol[1]	63.1	33.1	30	3.92	57.4
diiodomethane[2]	50.8	50.8	–	–	–
polyethylene (PE)[2]	36.3	36.3	–	–	–

Table 3 Dispersive and Lewis acid-base surface tension decomposition. Units are in mN/m. The reference used for water is $\gamma^+ = \gamma^- = 25.5$mN/m ([1] after [89], [2] after [90]).

Despite the different scale, the component γ^{AB} of the water must be independent of the reference used and in fact, by means of (4.5), a correct 51 mN/m is calculated.

4.2 Equilibrium of a liquid over a solid substrate: contact angle, line tension and interaction energies

A droplet of liquid on a solid has a tendency to spread on to the surface. The balance of the attraction of the liquid for the surface and the attraction for itself governs whether and how far the liquid spreads. Young derived a unique relation between the interfacial energies and the contact angle θ_Y (the subscript Y refers to this definition) in the case of an infinitely extended droplet on an ideal surface, which is defined as a smooth, chemically homogeneous, rigid and non reactive solid phase (Figure 4-2).

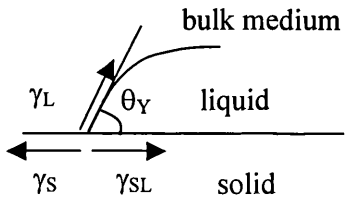

Figure 4-2 Contact angle θ of an infinitely extended droplet on a ideal solid.

The Young contact angle can be assumed as a thermodynamic quantity and is defined according to (4.7), in which the subscripts S and L, when alone, refer to the solid or

liquid property with respect to that of the suspending bulk medium, respectively, whilst γ_{SL} is the solid liquid interfacial tension:

$$\gamma_L \cos\theta_Y = \gamma_S - \gamma_{SL} \tag{4.7}$$

The Young contact angle, however, is difficult to verify experimentally due to the real nature of the solid surface and to the finite size of the droplets. The effect of the size of the droplet is accounted for by the line tension τ, an additional term which is the one-dimensional analogue of the surface tension. The effects of the roughness and the heterogeneity of real surfaces are usually recognized by the presence of the hysteresis of the contact angle, which can assume different values according to how the experiments are performed. These two effects are presented in the following section, whilst the experimental evidence of the role hysteresis has on the geometry of a liquid bridge will be detailed in chapter 6 for the case of both gaseous or a liquid suspending medium.

The adhesion between a solid and a liquid phase is usually investigated in terms of the adhesion energy, which is the energy required to separate the two phases and is discussed in 4.2.3 together with the energy involved in the deformation of the three phase contact line (hysteresis energy) and the energy involved in destroying a liquid phase (cohesion energy).

4.2.1 Line tension and hysteresis effects

Line tension τ is a force (N), or more appropriately an energy per unit length (J/m), that depends on the curvature $\frac{1}{r}$ of the triple contact line and affects the force equilibrium as showed in Figure 4-3.

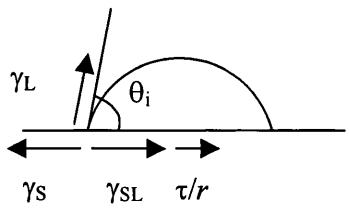

Figure 4-3 The effect of contact line curvature on the equilibrium of a droplet.

By minimisation of the droplet free energy with respect to any arbitrary parameter (for example the height of the droplet) it is possible to find the force equilibrium at the triple contact line. In this minimisation it is implicitly assumed that gravity has no effect. This is valid for droplets that form the cap of a sphere at the equilibrium configuration. The new equilibrium configuration is defined in terms of the intrinsic contact angle θ_i, as suggested by Marmur [91]:

$$\gamma_L \cos\theta_i = \gamma_S - \gamma_{SL} - \frac{\tau}{r} \tag{4.8}$$

By comparison with (4.7) it is possible to relate the line tension to the difference between the Young and the intrinsic contact angle as per (4.9).

$$\cos\theta_Y - \cos\theta_i = \frac{\tau}{r\gamma_L} \tag{4.9}$$

In literature the theoretical and experimental analysis of line tension effects is contentious and controversy exists over magnitude and sign [92]. Drelich [93] reviewed the experimental works carried out on three phase systems involving a solid surface and reports line tension magnitudes in the range from 10^{-12} to 10^{-10} N. Since these value are quite small, line tension effects can be neglected in the thermodynamic approach proposed in the following section to study the elongation of a liquid bridge and which will be experimentally verified in section 6.2. Li and Steigmann [94] proposed that the ambiguity over the line tension sign may be caused by the roughness and the heterogeneity of the surface on which the contact angle are measured. However their

conclusion was that on an ideal surface the line tension is a positive quantity as required by considerations of stable thermodynamic equilibrium. Equation (4.9) should be modified in the case of droplets formed on a spherical particle, illustrated in Figure 4-4, where β is the half filling angle and (4.10) is the modified formula for the line tension [95].

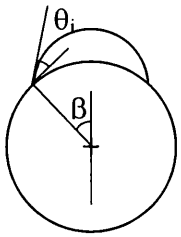

Figure 4-4 Droplet formed on a spherical particle.

$$\cos\theta_Y - \cos\theta_i = \frac{\tau}{r\,\gamma_L}\cos\beta \qquad (4.10)$$

Difficulties in the experimental verification of the Young's relation commonly occur on real surfaces. A given system produces different contact angles depending on how the experiment is performed and the angle measured on a real surface is generally referred to as the apparent contact angle [96]. In particular, careful experiments show two relatively reproducible values of the contact angle; one as the three-phase line advances across the surface and one as it recedes (Figure 4-5). Traditionally, this difference in advancing and receding contact angles, θ_{adv}–θ_{rec}, is denoted as the contact angle hysteresis.

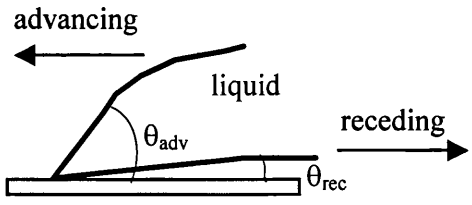

Figure 4-5 Advancing and receding contact angle.

Many authors explain the contact angle hysteresis as the resulting effect of the roughness and heterogeneity of the surface. Joanny and De Gennes [97] studied the effect of a single heterogeneity as a cause of hysteresis. They showed that hysteresis occurs when the extension of the defect, such as a small heterogeneity, is above a certain threshold. Extending this to a dilute system they obtained the formulae for the advancing and receding contact angle in terms of distribution of defect strength or defect sharpness. Schwartz and Garoff [98] theoretically studied the capillary rise of a liquid on a vertical plate whose surface was covered by patches of a low energy material (i.e. grease on a clean substrate). They applied a free energy minimization technique in order to find the stable configuration of the meniscus profile associated with several double periodic (vertically and horizontally) coverage patterns. Contact angle hysteresis resulted linked to the existence of a metastable range, i.e. to the presence of multiple minima in the total energy function. Hysteresis also depended strongly on the geometry of the patterns rather than only on fractional coverage. The models reviewed clearly show that practical formulae are difficult to obtain in order to predict the extent of hysteresis on real surfaces for which spatial heterogeneity functions or pattern distributions are impossible to retrieve. Hence, experimental data are therefore mandatory. In the course of this project the hysteresis (towards glycerol) of glass ballotini (either silanised or untreated) has been studied and related to the profile assumed by a liquid bridge holding pairs of ballotini of either similar or dissimilar surface energy (see chapter 6). It has been shown that this profile can be either a nodoid or an unduloid depending on whether the particles have a large or reduced hysteresis, respectively. A further study on glass particles suspended in water and held by silicone oil bridges revealed a larger adhesive force in favour of liquid menisci formed between particles characterized by larger wetting hysteresis. This study will be detailed in section 6.2.

4.2.2 Thermodynamics of a liquid bridge in relation to the apparent contact angle

In the previous section it has been noted how care must be taken in dealing with contact angles. Because several configurations are possible at a liquid solid substrate,

depending, for example, on the mechanical action exerted on the interfaces, it is always preferable to deal with the apparent contact angle instead of the Young contact angle. In this regard equation (3.26), introduced in section 3.1.7 to describe the energy associated to a liquid bridge from a thermodynamic point of view, can be expressed in terms of the apparent contact angle formed at a particle-binder interface. It is then possible to substitute for both particles A and B the term $(\gamma_{SL}-\gamma_S)_{1,2}$ relative to the configuration 1 and 2, with the expression $-\gamma_L\cos\theta_{1,2}$, respectively. This substitution results in (4.11):

$$\Delta A = (P_1-P_2)V_{br} + \gamma_L(A_{br,2}-A_{br,1}) - \gamma_L \cos\theta_{2,A} A_{SL\text{-}2,A} - \gamma_L \cos\theta_{2,B} A_{SL\text{-}2,B} + \gamma_L \cos\theta_{1,A} A_{SL\text{-}1,A} + \gamma_L \cos\theta_{1,B} A_{SL\text{-}1,B} = -w \quad (4.11)$$

At least one more component should be included in (4.11), the line tension energy. However, this term is omitted due to its magnitude, which makes it practically negligible as detailed in the previous section.

4.2.3 Adhesion cohesion and hysteresis energies

The adhesion energy W_{adh} is the energy required to separate two distinct phases [99] (for example, a solid and a liquid suspended in liquid/gaseous medium). By using the same convention for the subscripts, this energy is defined by (4.12)

$$W_{adh} = (\gamma_S + \gamma_L - \gamma_{SL})\, A_{SL} \quad (4.12)$$

During separation two new interfaces are gained, γ_S and γ_L, both of area A_{SL}, whilst the existing solid liquid interface is lost. By using (4.7), we can rearrange (4.12) as in (4.13):

$$W_{adh} = \gamma_L(1+\cos\theta_Y)\, A_{SL} \quad (4.13)$$

The latter definition involves the contact angle to be assumed as the thermodynamic value defined by Young. A different definition can be chosen if we regard the adhesion

energy in term of the advancing or receding contact angle, respectively, which will be addressed in the following section.

The energy required to separate a single phase of area A is termed the cohesion energy, W_{coh} [99] and is defined by (4.14). If we recall that no interface exists in a single liquid ($\gamma_{LL} = 0$) the equation becomes:

$$W_{coh} = (\gamma_L + \gamma_L - \gamma_{LL})\, A = 2\, \gamma_L\, A_L \qquad (4.14)$$

Adhesion and cohesion energy assume an important role in the phenomena related to the spreading of a liquid on to a substrate. Following the example of agglomeration, the more a liquid spreads across the surface of the particles, the larger the surface area of contact within the granules, which leads to a greater strength of adhesion.

The ability for the binder to spread across the particles is determined by the spreading coefficient, S_P, (4.15), defined as the difference of the adhesion and cohesion energies:

$$S_P = W_{adh} - W_{coh} \qquad (4.15)$$

The more the binder is able to adhere to the drug (favoured by a high work of adhesion, W_{adh}) compared to its tendency to self-associate (favoured by a low work of cohesion , W_{coh}), the better the spreading and subsequent binding.

From the work of adhesion it is possible to define the energy related to the hysteresis of the contact angle, W_{hist}. This quantity is defined by (4.16) [57, 100] as the difference of work of adhesion [100, 101] between any two liquid configurations that characterize an advancing and a receding phase.

$$W_{hist} = \gamma_L (\cos\theta_{adv} - \cos\theta_{rec}) A_{SL} \qquad (4.16)$$

4.3 Surface excess quantities

The study of an interface is very complex because it is a very thin region where some thermodynamic quantities change from one phase to the other. Gibbs studied a simplification of the problem, proposing to split any system that contains an interfacial region into 3 parts: two bulk phases and an almost "zero thickness" interface. The bulk phases are characterised by constant thermodynamic parameters up to an interface that acts like a discontinuity wall between the two of them. The thermodynamic quantities that characterise the interfacial region are usually called *surface excess quantities*. The concept of the Gibbs dividing surface can be easily explained analysing the variation of number of moles of water molecules, at the water air interface as shown in Figure 4-6. In the real situation the transition between water and air occurs in a finite length (between the dividing surfaces A and C) whilst in the Gibbs approximation it is possible to select an arbitrary barrier, either at A or at B, that separates the two pure bulk phases. In Figure 4-6 n_A and n_B represent the moles of water when the bulk is extended up to the surface A or B respectively and n^σ_A or n^σ_B are the relative surface excess moles. The relation between n and n^σ is given by equation (4.17) that expresses the constancy of the total number of moles n_{tot}.

$$n_{tot} = n_A + n^\sigma_A = n_B + n^\sigma_B \qquad (4.17)$$

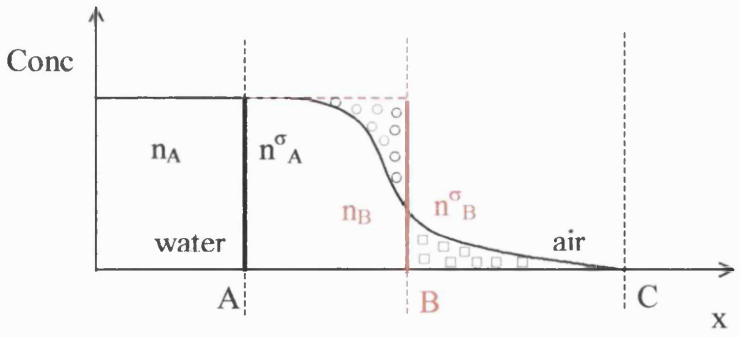

Figure 4-6 Schematic illustration of surface excess quantities.

The surface excess concentration of a component at an interface of area A_{int} is defined by (4.18):

$$\Gamma = \frac{n^{\sigma}}{A_{int}} \tag{4.18}$$

The surface excess concentration, Γ, depends upon the position of the dividing interface. It is possible to chose the position so that $\Gamma = 0$. This choice reflects a simple geometric criterion. There is a position of the interface where the number of moles (circles) virtually gained by extending the bulk phase up to the interface is equal to the number of moles (squares) lost on the left of the dividing surface. If we assume that the balance of the number of mole occurs at surface B, $n_{tot} = n_B$, whilst $n^{\sigma}_B = 0$ and $\Gamma = 0$ [99]. The thermodynamics of the interface can be derived from the first thermodynamic law applied to the excess quantities (characterized by superscript σ) as per (4.19).

$$dU^{\sigma} = -PdV^{\sigma} + \gamma_{int}\, dA_{int} + \Sigma_i \mu_i\, dn^{\sigma}_i + TdS^{\sigma} \tag{4.19}$$

Rewriting (4.19) in term of finite quantities it is possible to obtain (4.20):

$$U^{\sigma} = -PV^{\sigma} + \gamma_{int}\, A_{int} + \Sigma_i \mu_i\, n^{\sigma}_i + TS^{\sigma} \tag{4.20}$$

By differentiating (4.19) and equating it to (4.20), (4.21) results:

$$-V^{\sigma}dP + S^{\sigma}dT + \Sigma_i\, d\mu_i\, n^{\sigma}_i + A_{int}\, d\gamma_{int} = 0 \tag{4.21}$$

For a two components system at constant pressure and temperature (4.21) becomes:

$$d\gamma = \Gamma_1\, d\mu_1 + \Gamma_2\, d\mu_2 \tag{4.22}$$

in which the subscript "int" is eliminated for simplicity of notation. Figure 4-7 shows an example of a two-component system formed by a solvent and a solute, in the proximity of a vapour phase.

Since the choice of the dividing surface is completely arbitrary, it is a common rule to set the virtual surface in the position where the solvent excess is zero ($\Gamma_1 = 0$).

However, the excess concentration of the second component (solute) must be calculated with respect to this surface.

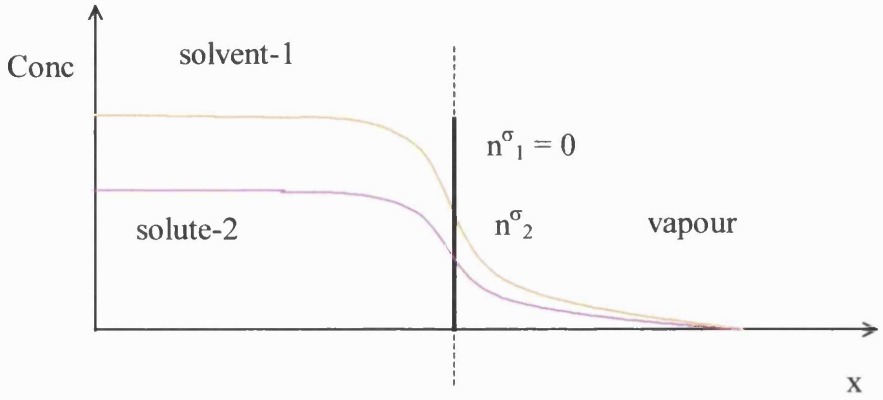

Figure 4-7 Surface excess concentration for a two component system.

The excess of the second component is written as ${}^1\Gamma_2$ to remind us that the dividing surface is set at a point where $n^{\sigma}_1 = 0$. Equation (4.22) can be rewritten as per (4.23), from which it clearly results that components positively adsorbed at an interface (${}^1\Gamma_2 > 0$) lower the surface tension of the interface and are said to be surface active.

$$d\gamma = - {}^1\Gamma_2 \, d\mu_2 \qquad (4.23)$$

Surface active agents have an important role in many technological processes and therefore will be looked at in some detail in the following section.

At the present point it is worth noting that the single excess surface concentration Γ_i is a quantity related to the choice of the dividing surface whilst the relative difference ${}^j\Gamma_i$ is a constant of the system. For a two component system this can be easily understood from equation (4.23). The variation of γ with respect to the potential μ_2 is a physical characteristic of the system and so ${}^1\Gamma_2$ must be constant throughout the interface.

4.4 Surface active agents (surfactants) and micelles

Surface active agents (surfactants) are components that are soluble in both water and oil solvents. The structure of these components is formed by a hydrocarbon group (tail part) responsible for the oil or air affinity and by a polar head group responsible for the interaction with the water. Surfactants are classified as anionic, cationic and non-ionic according to the charge left on the tail group after dissociation of the electrolyte head group in an aqueous phase. Some examples of the three species are summarised below and the functional head parts, based on which surfactants are classified, are indicated in bold.

Anionic	Sodium dodecyl sulphate (SDS):	$CH_3(CH_2)_{11}$ **SO_4^-** Na^+
Cationic	Cetyl trimethilammonium bromide (CTAB):	$CH_3(CH_2)_{15}$ **$N(CH_3)_3^+$** Br^-
Non Ionic	Polyethylene oxides:	$CH_3(CH_2)_{11}$ O $(CH_2)_2$ OH

When dissociated surfactants become adsorbed at an air-water or oil-water interface, they are able to locate their hydrophilic heads in the aqueous phase and allow their hydrocarbon tails to escape into the air or oil phase, as shown in Figure 4-8 [79].

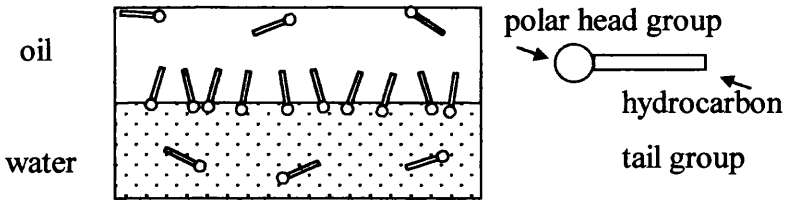

Figure 4-8 Adsorption of surfactants at the oil-water interface.

In general, the interaction between an aqueous solution and the polar head group of the surfactant is sufficiently strong to drag the hydrocarbon part into the solution where surfactants can adsorb onto dissolved charged particles and modify the mutual electrical interactions. Due to their peculiar nature, surfactants are technologically widely used as controllers of colloidal stability (liquid-liquid emulsion, for example) and of the wetting behaviour of an air (oil)-water system on a solid substrate. Surfactants are, in fact, largely employed in relation to detergency, emulsion stability, flotation and other

mineral separation processes based on selective coagulation (e.g. spherical agglomeration) [102].

As predicted by equations (4.23), the addition of a surfactant to an interface lowers the surface tension at the interface provided the surfactant is positively adsorbed ($\Gamma > 0$). When the concentration of surfactant is increased, a point known as the critical micelle concentration (CMC) can be reached. At this point, the surfactant molecules in the bulk solution agglomerate into spherical, cylindrical or laminar 'micelles' with the hydrocarbon groups clustering together in such a manner that they are surrounded and hidden by the polar groups in order to minimize the contact with the aqueous solution (see for example Figure 4-9). This behaviour can be ascribed to the "hydrophobic interaction" between the hydrocarbon tails and the aqueous solution [74]. Generally, at concentrations of surfactant above the CMC, surface and interfacial tensions do not decrease further. Figure 4-10 shows schematically the variation of surface tension with increase of solute added. The decrease of the surface tension of water upon addition of an anionic surfactants (SDS, sodium dodecyl sulphate) will be presented in Appendix A.1.

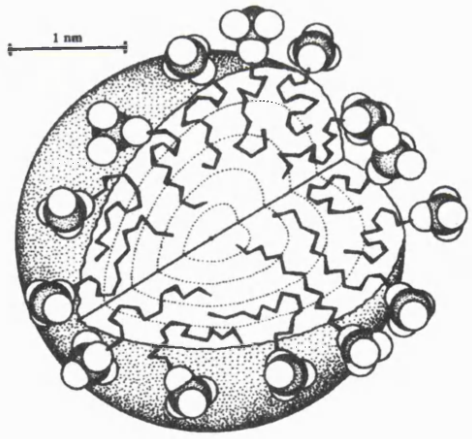

Figure 4-9 Schematic of a sodium dodecyl sulphate micelle (after [74]).

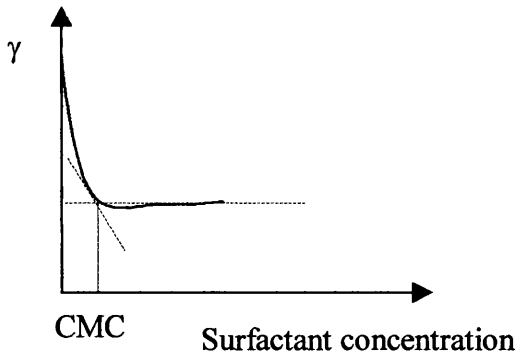

Figure 4-10 Schematic variation of surface tension γ against the concentration of dissolved solute (after [79]).

4.4.1 Surfactant adsorption at the solid liquid interface: hemi-micelles

The adsorption of surfactant ions on a charged particle can be considered as a special case of the specific adsorption of ions referred to in the treatment of the electrical double layer [78], which has been summarised in section 3.3.3. The main differences are that monovalent electrolyte counterions cannot change the sign of the zeta potential at the solid-liquid interface, whilst surfactants can easily do so. The adsorption isotherm for an ionic surfactant on an oppositely charged substrate, for example sodium dodecyl sulphonate on alumina, is typically S-shaped (see Figure 4-11). The shape of the isotherm is believed to reflect three distinct modes of adsorption. In the bottom region of Figure 4-11 the surfactant adsorbs mainly by ion exchange and behaves as an electrolyte in the proximity of the charged surface (the potential remains almost constant). In the central part of the S-shaped curve, there is a marked increase in adsorption, resulting from interaction of hydrophobic tails of oncoming surfactants ions with those previously adsorbed. In this adsorption region the original charge of the solid is neutralized and eventually reversed. The aggregation of the hydrophobic groups, which might occur at concentrations well below the CMC, has been called hemi-micelle formation [103]. The hemi-micelle concentration (HMC) is localised at the intersection between the bottom and the central part of the S-shaped curve [104].

Because of the charge assumed by the surface, surfactants adsorbed in the Stern-Helmholtz layer must necessarily be oriented with the charged heads towards the surface and with the tails sticking out into the liquid.

If surfactants are adsorbed tightly through hydrophobic tail interaction, a minimum surface area of the hydrocarbon tails will be in contact with water, in much the same way micelles form in the bulk solution. The schematic of hemi-micelle formation is presented in Figure 4-12.

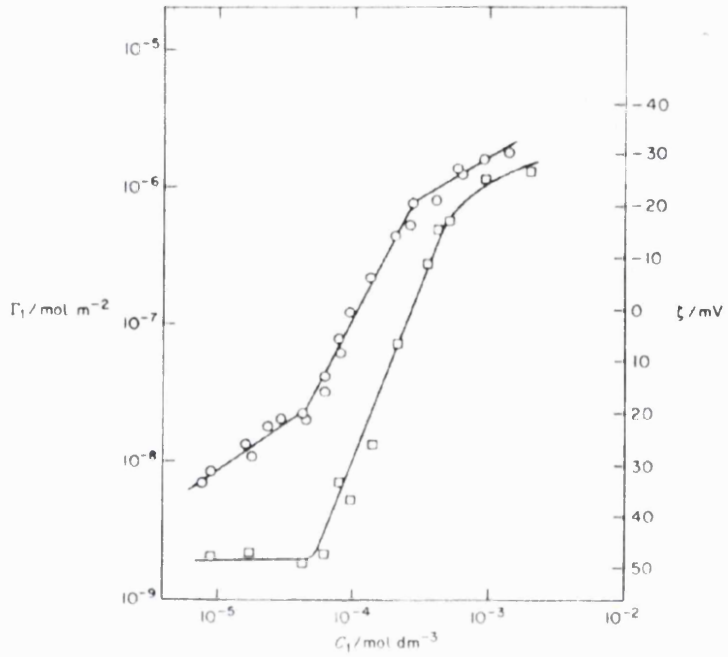

Figure 4-11 The adsorption isotherm of sodium dodecyl sulphonate on alumina (o) and the corresponding zeta potential ζ of the alumina particle as a function of the equilibrium surfactant concentration (□), at pH 7.2 and ionic strength 2 x 10^{-3} M. (after [102]).

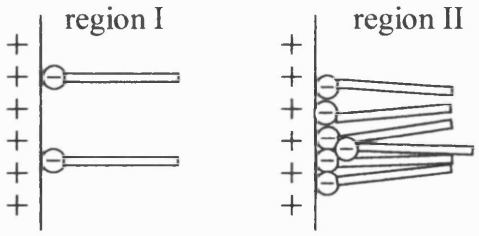

Figure 4-12 Adsorption of an anionic surfactant onto a positively charged surface by ion exchange (region I) and hemi-micelle formation (region II).

In the upper part of the adsorption profile of Figure 4-11 the slope of the isotherm is reduced because the adsorption due to the hemi-micelle mechanism must now overcome

electrostatic repulsion between the oncoming ions and the similarly charged solid [105]. Zejac et al. [85] noted that the onset of this new region corresponds to the formation of micelles and the corresponding concentration can be regarded as the CMC. Figure 4-11 makes clear that even small amounts of an appropriate surfactant can lead to enormous variation in the interaction between particles, in terms of colloidal stability or wetting behaviour.

4.4.2 The three phase system; glass-water-silicone oil

Part of the focus of the work presented in this thesis was to study the mechanisms behind spherical agglomeration and to investigate how the use of surfactants could benefit particle recovery. Glass ballotini suspended in water and held by a silicone oil liquid bridge has been used as a model for spherical agglomeration. The ability to modify the surface physiochemistry of glass and of the water-oil interface can be achieved by two oppositely charged surfactants, the cationic cetyl trimethilammonium bromide (CTAB) and the anionic sodium dodecyl sulphate (SDS). Since equipment to measure zeta potential and surfactant adsorption were not available, data of interest were retrieved from the extensive literature [83, 84, 106, 107]. Figure 4-13 and 4–14 show the zeta potential of glass and silicone oil droplets, respectively, as a function of the concentration of the two surfactants SDS and CTAB.

Glass, which is highly hydrophilic, is negatively charged in pure water from pH3 (~ –40mV) to pH 10 (~ –90mV) [84] (see section 3.3.3). The cationic surfactant CTAB reduces the surface potential (see Figure 4-13) due to hemi-micelle formation. Unfortunately the graph does not identify the hemi-micelle concentration ($<10^{-6}$ M), which appears to occur at a concentration well below the CTAB critical micellar concentration (9.1×10^{-4}M [108]).

The anionic surfactant SDS has an opposite effect on glass and it can be considered as a potential-determining ion [84] in the sense that its concentration influences the glass potential (see section 3.3.3).

The addition of an electrolyte to a surfactant solution has a marked effect on the HMC and CMC, which can both be reduced by an order of magnitude. Atkin et al.[106] have measured the adsorption of CTAB on to silica in a solution of potassium bromide (KBr) and found that the CMC and HMC (~1mM and ~0.2mM, respectively, when no electrolyte is added) dropped to 0.2mM and 0.01mM, respectively, in the presence of 0.01 M KBr.

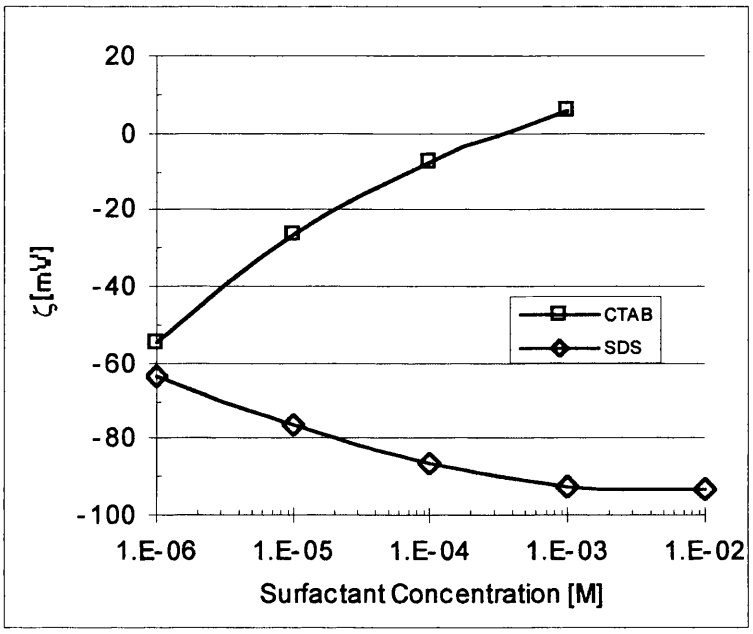

Figure 4-13 Zeta potential (ζ) of a glass surface as a function of the surfactant concentration of SDS and CTAB (after [84]).

Surfactants added into a bulk medium that contains a liquid-liquid interface, also affect the interfacial potential. Figure 4-14 reflects the potential modifications induced by SDS and CTAB at a silicone oil-water interface. A similar trend as for the glass-water interface results (Figure 4-13).

In order to establish the condition that would favour the recovery of particles in the spherical agglomeration process, the opposing behaviour of CTAB and SDS has been investigated and results are presented in sections 6.3. CTAB, contrary to SDS increases the zeta potential of the glass surface and can be used to increase the affinity towards oil droplets. Measurements of contact angles and of glass-oil (in water) interaction, the

latter taken by an atomic force microscope (AFM), confirmed what was expected (see section 6.3). Some preliminary experiments were also carried out in order to establish any liquid bridge force variation due to the CTAB surfactant action. Since surfactants are very effective even at low concentration where the reduction of the binder-medium interfacial tension is minimal, their action should be beneficial to the liquid bridge strength in terms of the increased wettability between the particle and the binder. However, the results presented in section 6.3 do not seem to show a particular beneficial effect.

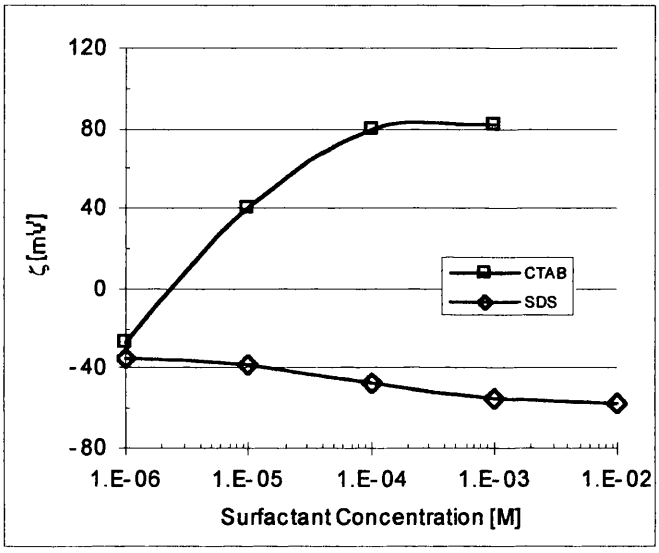

Figure 4-14 Zeta potential (ζ) of silicone oil droplets as a function of the surfactant concentration of SDS and CTAB (after [83]).

4.4.3 The use of surfactants in spherical agglomeration processes

The use of surfactants is a crucial part of the spherical agglomeration process. In the previous sections it has been shown that particles can be conditioned in order to change their affinity towards an oil phase. In the spherical agglomeration process, usually an organic phase is used to recover valuable particles from an aqueous medium. Also, the modification of the surface properties can be tailored to the specific species that are to be recovered. Kelsall and Pitt [29] used a cationic surfactant (dodecylamine) to selectively recover wolframite mixed with quartz, which are both negatively charged in water. In their experimental work they found that the degree of recovery is not only

influenced by the concentration of the appropriate surfactant but also by the pH of the solution. The pH of the solution determines the hydrolization of dodecylamine molecule into the protonated form available for adsorption. By accurately controlling the pH and the surfactant concentration they managed to reach a very high recovery of wolframite (~100%), which could drop abruptly away from the optimum parameters.

Sadowski [37] employed the spherical agglomeration process to recover selectively a species from a mixture of salt-type minerals (barite, calcite, magnesite, dolomite) by using n-heptane as the binder and sodium oleate as the surfactant. When only a singular mineral was present in the slurry it could be recovered at specific pH and surfactant concentration, which were found to be characteristic for any of the salt type minerals. Despite this fact, selectivity recovery of barite was not achieved from a 1:1 mixture of barite and a carbonate mineral (calcite, magnesite, dolomite) by using the same conditions that favoured the recovery of barite when present alone in the slurry. In the 1:1 mixture sodium oleate caused hydrophobic aggregation (coagulation) of both the mineral particles. Sodium lignin sulphonate added before the sodium oleate caused a beneficial selectivity to be obtained by preventing the surfactant (sodium oleate) being adsorbed on the carbonated minerals. Sodium lignin sulphonate is of the family of modifier agents, which can either prevent collector adsorption on a mineral surface or make the surface hydrophilic. The same author [36] investigated the agglomeration of aqueous calcite suspensions through addition of n-heptane in the presence of sodium oleate. Results were correlated to the prediction obtained from the DLVO theory, which showed an energy barrier to agglomeration not revealed from the experimental findings. The model was improved by adding a hydrophobic term, which proved the aggregation to be driven by hydrophobic interaction. Spherical agglomeration is an interesting and viable solution to the recovery and separation of particles. The process drawback is that any system has to be investigated by preliminary assays in order to determine the pH, the type of surfactant or modifying agent that will maximise the agglomeration of a specific particle leaving any unwanted material in the gangue. Hence, the objective of this work, to provide a fundamental basis for the selection of appropriate process conditions, is of great significance for future process design and applications.

Chapter 5

5 Experimental set-up in gaseous and liquid media: the Micro-force balance (MFB) and the Atomic Force Microscope (AFM)

The study of liquid bridges formed between pairs of particles either suspended in a gaseous or a liquid medium is important to agglomeration processes. The possibility of measuring how the adhesion of liquid bridges is affected by the shape and the surface energy of the particles and by the physiochemical properties of the liquid binder provides very valuable information for the early stage of agglomeration. Previous works obtained data for macroscopic (a few mm diameter) particle-particle interactions (see section 3.1.4), neglecting the common size scale of agglomerated particles, usually sub 250 μm in diameter . In order to fill the lack of data for microscopic particles a micro-force balance (MFB) capable of measuring forces between microscopic particles and recording, visually, the geometries liquid bridges attain under a range of conditions, has been designed and successfully employed by R. Fairbrother at the Department of Chemical Engineering of University College London [5]. The MFB apparatus, which in the original work of Fairbrother was used essentially for investigations of liquid bridges formed in air, had the possibility to be adapted to take measurements in a liquid medium. The present project has involved both experiments in gaseous and liquid media whose procedures will be detailed in the following sections. The MFB has attracted the attention of a large pharmaceutical company (Merck Sharp & Dohme^{TM}), which was interested in testing the adhesiveness of different binders holding paracetamol crystals in order to gain useful information on the optimal formulations required for granulation. This work will be detailed in chapter 7.

Part of the study of particle-particle interaction in a liquid medium involved collaboration with the Chemical Engineering Department at the University of Maine

(US), where an atomic force microscope (AFM) was available to take measurements of the interaction between glass ballotini and silicone oil droplets submerged in aqueous solutions of surfactants and/or electrolytes. The phenomena of agglomeration in a liquid medium are further complicated by the presence of long-range DLVO forces that may prevent or increase the interaction between a particle and a liquid binder before any liquid bridge is formed. These forces are largely influenced by the solution conditions such as pH and the type of surfactant/electrolyte added to the solution.

5.1 The MFB in gaseous and liquid media

The experimental equipment consists of an Olympus BX60 optical microscope fitted with an adapted stage, on which two micromanipulators are employed to hold micropipettes, to the ends of which particles are attached. A third micropipette is then used to add a measured amount of bridging liquid between the particles. The force is calculated by measuring how much a pre-calibrated pipette bends as the particles are separated (under piezoelectric or manual control), allowing forces down to 10^{-9} N to be resolved.

This equipment enables the liquid bridge forces between particles to be measured with both gas and liquid as the surrounding bulk medium. The rupture sequence is captured on video by a camera acquiring 25 frames/sec and image analysis software is used to measure the volume of the bridge, the separation distance at which the bridge ruptures, the contact angles and the adhesive force measured by the deflection of the pre-calibrated pipette. This latter quantity can also be measured electronically via a reflecto optic device (see next section). The schematic of the MFB layout is shown in Figure 5-1

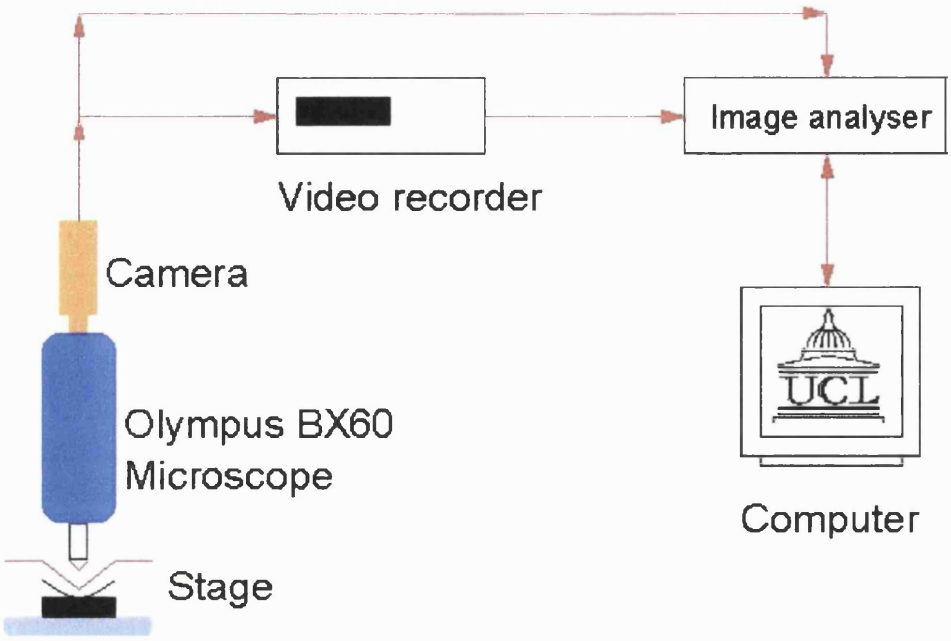

Figure 5-1 Schematic of the MFB equipment layout.

5.1.1 The Micro-Force Balance

The micro-force balance (Figure 5-2), capable of measuring the forces between microscopic particles attached by pendular liquid bridges, was designed in collaboration with Dr. L.R. Fisher of the University of Bristol, Physics Department.

The main procedure for forming and taking measurements of liquid bridge separations is essentially the same for the gaseous and the liquid surrounding medium. For the latter to take place, particles must be submerged in an optically clear dish (Figure 5-2) and an appropriate shape of the micropipettes is required. The technique for forming the geometry of the pipettes for the experiments in a liquid medium is discussed in 5.1.2. Although Figure 5-2 shows the glass dish, the pipettes attached to micromanipulators A and B are shaped for gaseous medium experiments. Apart from the differences in the micropipette geometry the following description of the experimental procedure for measuring, via electronic control, the force of the liquid bridge applies to both media.

Initially, a rigid micropipette (along the direction of the liquid bridge separation), with a particle attached to one end, is clamped onto micromanipulator B (static pipette), with

the particle being placed under the objective lens of the microscope. Fine adjustment in all three dimensions is achieved using the individual plane micrometers of the micromanipulator.

The second particle, attached to a pre-calibrated flexible micropipette, is then placed under the objective in contact with the first particle (Figure 5-2). Again, fine adjustment can be made using the micrometers of the micromanipulator. This micromanipulator A also incorporates a 30μm expansion piezo-electric crystal (PEC), which allows the pipette to be driven remotely (see Figure 5-3).

Because piezo-electric crystals exhibit non-linear expansion and hysteresis with respect to applied voltage, a Linear Variable Differential Transducer (LVDT) is fitted to monitor the PEC's expansion.

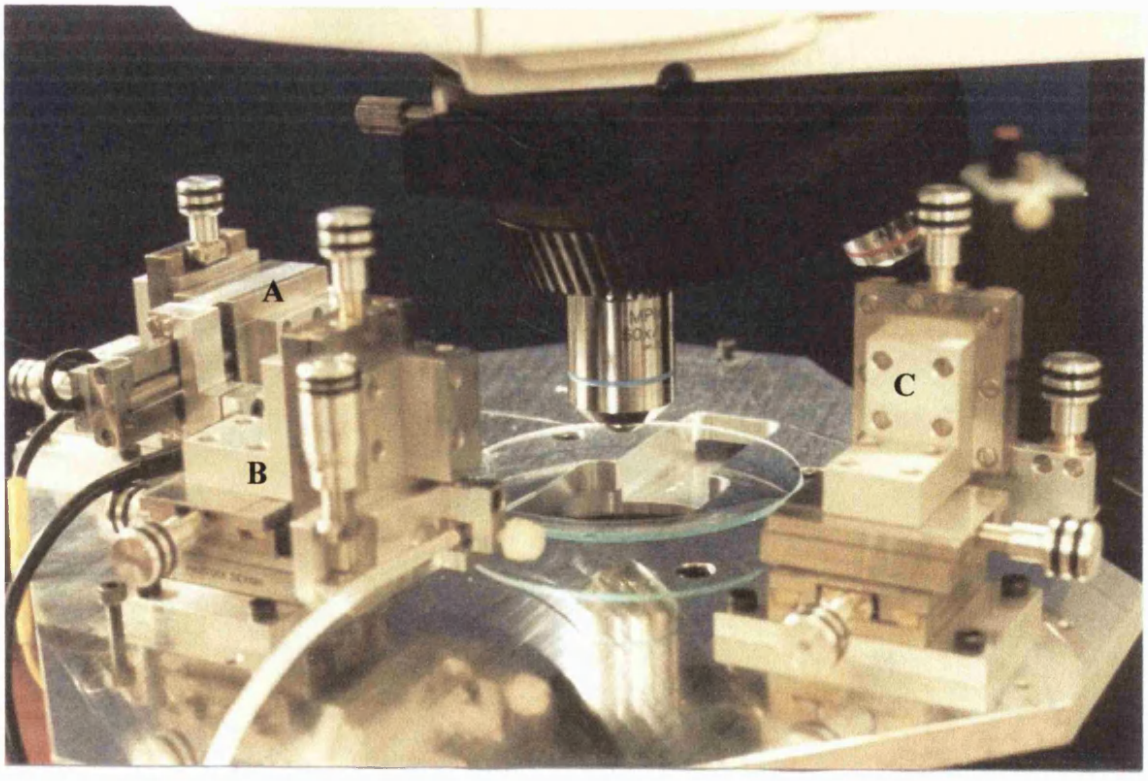

Figure 5-2 Photograph of the micromanipulation stage.

Key for Figure 5-2

A Flexible pipette micromanipulator, which is remotely driven.

B Rigid pipette micromanipulator

C Feed micropipette micromanipulator

To form the bridge, binder liquid is fed through a third micropipette onto the particles. The feeding micropipette is pre-loaded with the binder before being mounted on micromanipulator C.

Once a drop of liquid binder is formed on the particle attached to the rigid pipette, the two particles are first brought together to form the bridge and then separated until rupture of the bridge occurs. This is achieved by either applying a signal causing the PEC to expand or by acting manually on the micromanipulator. At this point the flexible pipette is driven away and the force of the liquid bridge causes the flexible pipette to bend, with the bend being proportional to the force. Under electronic control, separation can take place at different speeds in the range of 0.5 to 10 μm/sec. On the 90° bend nearest the pipette tip a small piece of aluminium foil is fixed (see Figure 5-3). Due to the separation movement imposed, the bend in the flexible pipette deflects proportionally to the strength exerted by the bridge. The deflection of the pipette is calculated as the difference of movement between the base of the pipette and the centre of the bend, whose movement is acquired by an optical follower with a resolution of order 75 nm. To control the optical follower a reflecto-optic (RO) sensor is used to linearly detect the position of the edge of the reflective foil in its field. The RO sensor works by transmitting a beam of light and measuring how much is reflected back. The output from the sensor, when focused on the edge of the reflective foil reads a constant voltage. Movement onto the reflective foil causes an increase in the output voltage and movement away, a decrease. To keep the sensor focused on the edge of the foil, control electronics are used to drive a second 15μm expansion PEC. The expansion is measured by a LVDT (Figure 5-3).

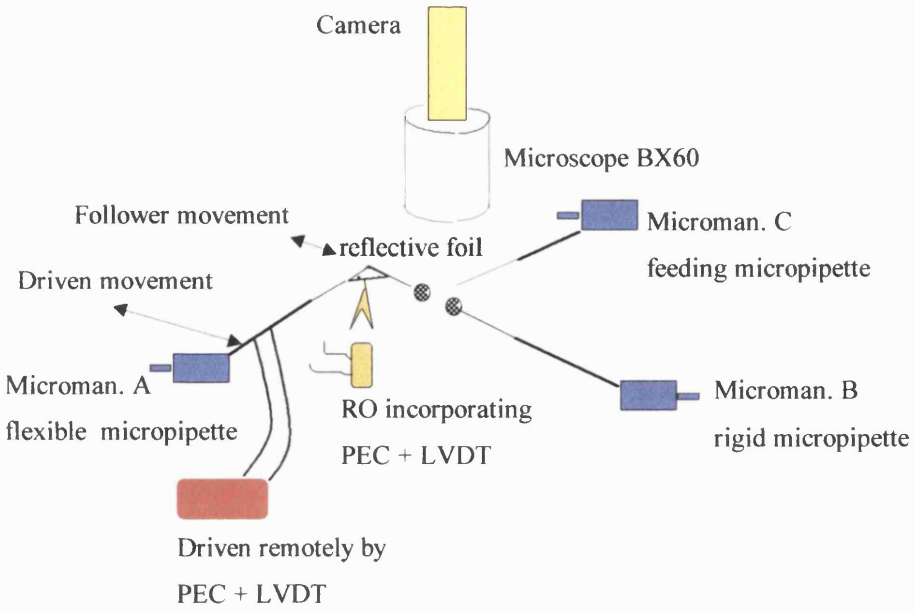

Figure 5-3 Schematic of the experimental set-up in a gaseous medium.

The flexible pipette is pre-calibrated to determine its spring constant (usually between 0.05 and 0.5 μN/μm) and the total force exerted is thus calculated as illustrated in Figure 5-4, which shows the steps to formation and separation of a liquid bridge. In Figure 5-4a, the flexible pipette (whose spring constant is k_s), is approached by the rigid pipette on to which a silicone oil droplet has been previously administered. At a certain close distance between the two particles, the flexible pipette "jumps" towards the other pipette to form the liquid bridge, with "e" being the deflection with respect to the undisturbed configuration (Figure 5-4b). Figure 5-4c shows the separation sequence. When the thick base of the flexible pipette is driven away (distance X_d), the centre of the bend follows but is "retarded" by the strength of the bridge and, in general, the distance X_f is different from X_d. The force of the bridge can eventually be calculated as:

$$F_{br} = k_s (X_d - X_f) + k_s e \qquad (5.1)$$

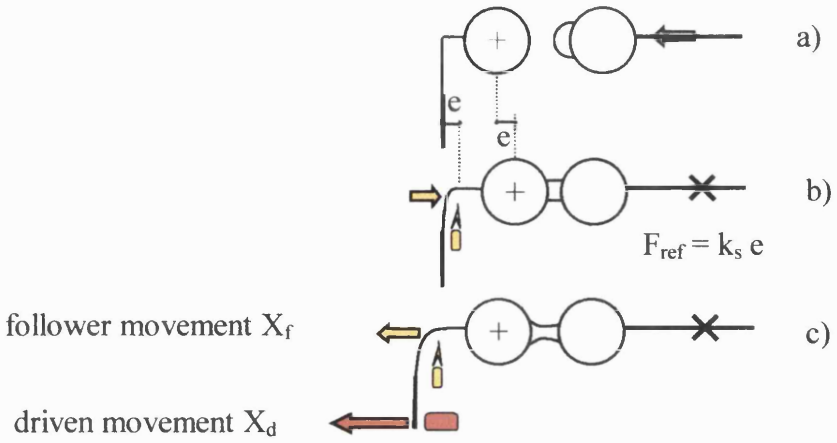

Figure 5-4 Schematic of the method to calculate the strength of a liquid bridge during separation: a) particles separated, b) liquid bridge formation, c) liquid bridge separation.

The separation of particles and monitoring of the LVDTs is computer controlled via an analogue-to-digital interface. The code for the program can be found in Appendix C.2. The set-up procedure for the LVDTs and details of their accuracy and control is presented in Appendix C.1 for both measurements in liquid and gaseous media. Because of the restriction imposed on the maximum separation by the limited movement of the two PECs (30 and 15 μm for the driven micro-manipulator, and the follower, respectively) the electronic force measurements can be applied to liquid bridge volumes not larger than 6500μm^3. Unfortunately the liquid bridge volume cannot be dosed "a priori" but it is calculated after deposition on the particle by image analysis. In this respect only the experience of the user can help in understanding whether the volume dispensed is correct for the electronic set-up. The adhesive force of larger volume liquid bridges can still be calculated by evaluating the deformation of the flexible pipette via image analysis from the recorded separation sequence whose applicability is only restricted by the field of view of the optical microscope. (see section 6.2 for force measurements obtained with both the electronic and image analysis method). In this latter situation the experiment is carried out without any electronic aid and the separation is achieved by acting manually on the micromanipulator B.

Measurements in a liquid medium are achieved by submerging the particles, which are attached to appropriately shaped pipettes, in an optical clear dish made in the glass blower workshop of the Department of Chemistry at University College London. The

dimensions (mm) of the optical dish are 75 x 8 x 2 mm (ID x Height x Thickness). The schematic of the experimental set-up is shown in Figure 5-5, whilst the formation of the appropriate micropipettes is detailed in the following section.

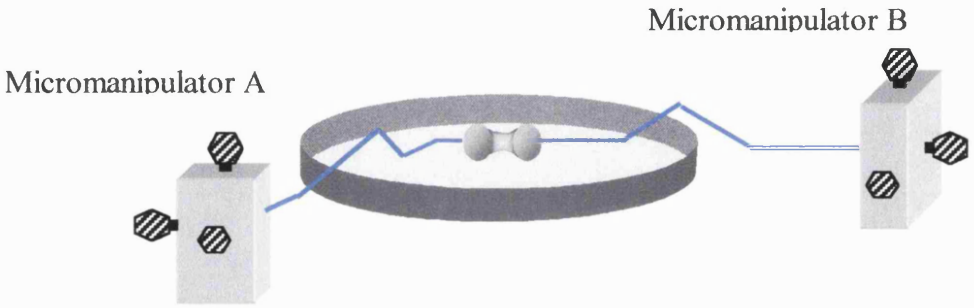

Figure 5-5 Schematic of the assembly for liquid bridge measurements in a liquid medium. In the picture the feeding micropipette is not shown.

After the three pipettes (the feeding micropipette is not shown in Figure 5-5) are clamped to the micromanipulators and are put in position under a water objective in the empty dish (~ 5 mm below the rim), the aqueous solution is poured inside the dish until it covers the particles. Particles are then focused under the water objective and the liquid binder (silicone oil for the experiments of this project) is administered on one of the particles. Again the experiment can be carried out in either an electronic or manual way according to the binder volume dispensed.

5.1.2 Pipette preparation

The micropipettes are produced from 100mm lengths of 1.1mm O.D., 0.76mm I.D. borosilicate glass tubing (Supplier: Plowden and Thompson Ltd., Dial Glass Works, Stourbridge, West Midlands DY8 4YN.)

A pipette puller (Figure 5-6) is used to produce the micropipettes by means of two nichrome wire heating elements. The relative position of these elements to the borosilicate tubing allows micropipettes of varying size (length and diameter) and stiffness to be produced.

The borosilicate capillary tubing is passed through the jeweller's four-jaw chuck at the top of the puller, down through the top melting element and the bottom cutting element. The chuck is then tightened around the tubing. The bottom of the capillary tubing is then attached to the plunger by placing a small piece of silicone capillary tubing around the glass and pushing the top of the plunger onto the tubing. The frictional force between the two keeps them attached.

A voltage is then applied across the top heating element. This element consists of a 0.5 mm diameter nichrome wire wound 11 or 12 times to produce a cylinder of around 4 mm O.D. and 11 mm in length. Ideally the turns should not be separated by more than the thickness of the wire. The amount of current flowing through, and thus the temperature of the element can be varied by a potentiometer on the power supply. The temperature of the element, should be adjusted so the glass starts moving, at a constant rate, after around 15 seconds. Through extensive production of pipettes, the time of 15 seconds seems to provide the correct rate of melting in the glass. The rate of descent of the plunger is controlled by a small capillary at its base that provides for the egress of air. By varying the voltage on the melting element it is possible to control the rate of descent.

Towards the end of the plunger's descent a microswitch on the plunger vertical stand (Figure 5-6) is used to redirect the current flow from the melting element to the cutting element and to make a plane straight edge on the pipette tip. This fact is very important for the feeding pipette in order to have a regular flow of binder liquid on to the particles when the liquid bridge is formed. The cutting element consists of a one turn coil of 0.25 mm O.D. located as close to the pipette as possible. Again the current to the element is varied via a potentiometer on the power supply. The temperature should be adjusted so that the cut takes around 10 seconds. A pipette prepared in such a way consist of a variable size tubing whose thick end is clamped to the micromanipulator whilst the thin end (between 20 and 30 μm radius) is used to attach the particle (Figure 5-7).

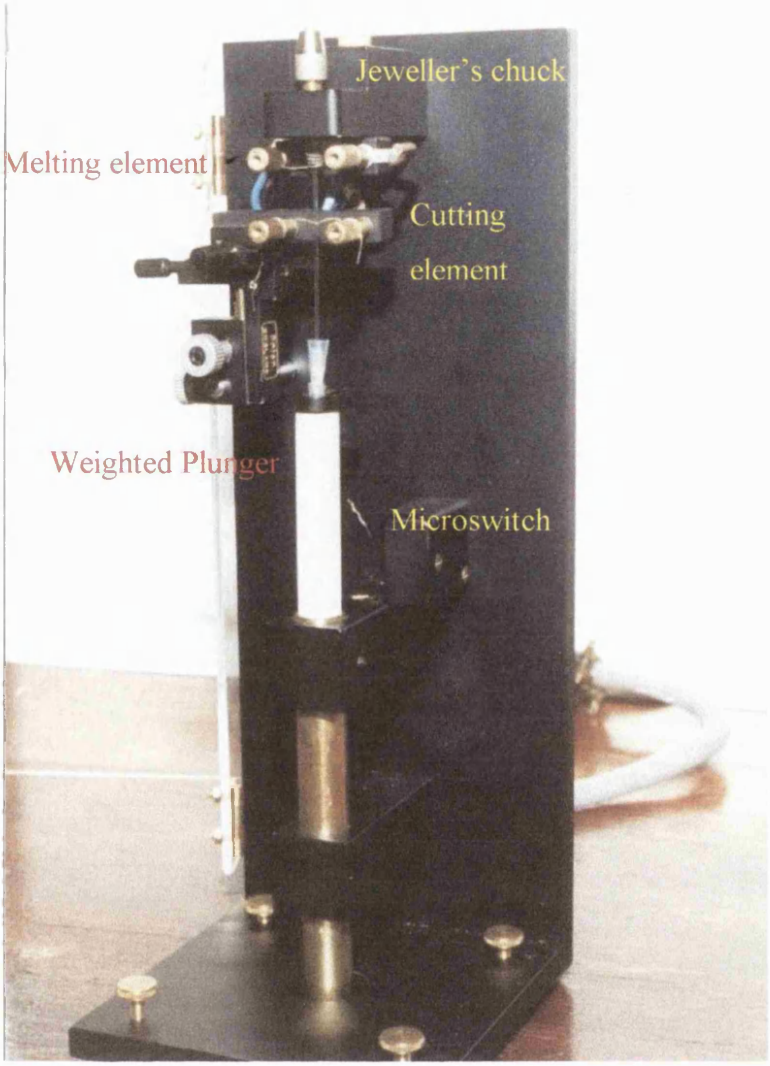

Figure 5-6 Photograph of the pipette puller.

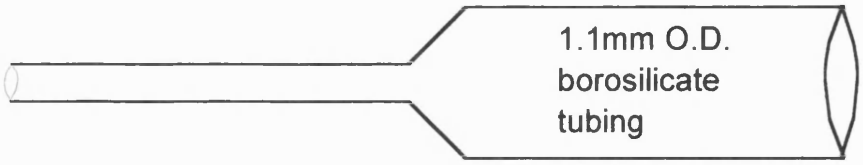

Figure 5-7 Schematic of a micropipette; particles are attached to the 'thin' end and the 'thick' end is mounted in the micromanipulator

In Figure 5-8 and 5–9 the pipette used for the experiments in gaseous and liquid media are presented, respectively, whilst in Figure 5-10 the typical dimensions of the pipette used for the experiments in liquid media are given.

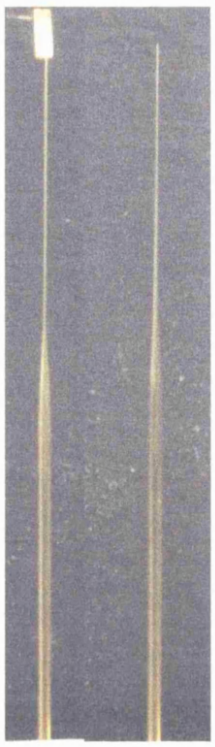

Figure 5-8 Micropipette for gaseous experiments. Flexible (left) and rigid (right) pipettes with respect to the direction of the liquid bridge deformation. On the flexible pipette is attached the aluminium foil (dim. 150 x 500 μm). The overall pipette length is ~100 mm.

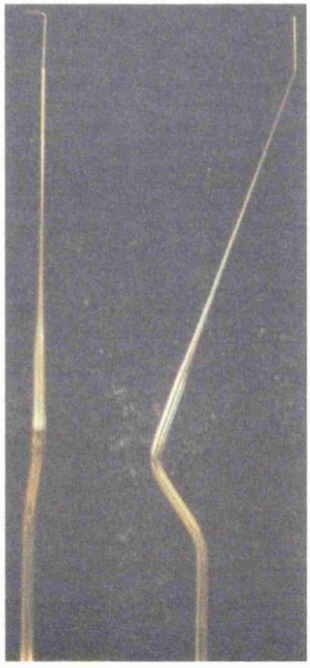

Figure 5-9 Front (left) and lateral (right) views of a flexible pipette used for the experiments in a liquid medium. The rigid pipette would be similar in shape without the top 90° bend.

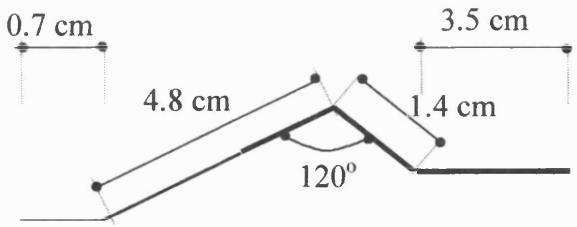

Figure 5-10 Typical pipette dimensions for liquid bridge experiments in liquid media. The bend on the thin end of the flexible pipette (not represented in the picture) must be ~3 mm in length at a right angle with the thin straight end of the pipette.

5.1.3 Pipette bender

The pipette bender (Figure 5-11) allows a predetermined length of glass to be bent at an angle to the main body of the micropipette. This is achieved by placing the pipette over a 0.5 mm O.D. section of heated nichrome wire and allowing the end of the pipette to fall under its own weight until the desired angle is reached. Adjustments can be made to the horizontal and vertical position of the wire, the angle of the stage and its proximity to the element. The first bend must be a right angle followed by ~5mm of glass, which fits with the geometry of the RO device relative to the micromanipulator. This is all what is required for the gas phase work.

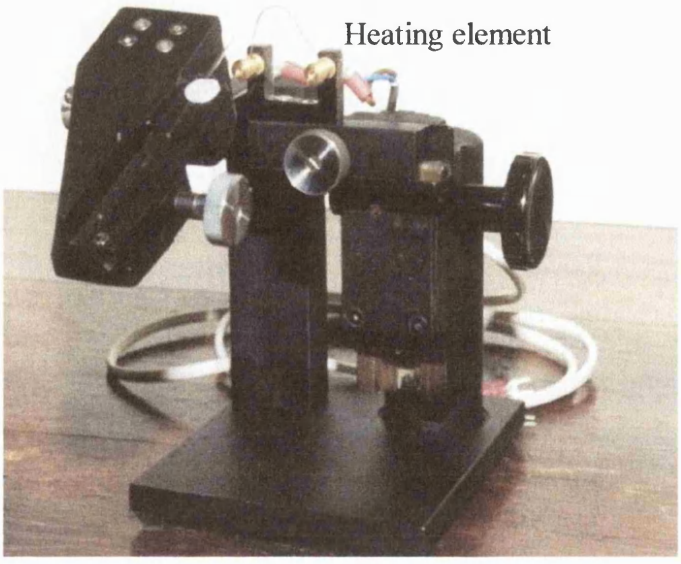

Figure 5-11 Photograph of the pipette bender.

For the liquid phase work the additional bends on the thick part of the pipette are made by a gas torch regulated at a low flame and waiting for the pipette to deform to a desired angle under its own weight. The bends of the thin part are obtained using the pipette bender.

5.1.4 Attaching particles to micropipettes

After suitable micropipettes have been produced, it is necessary to attach the particles and achieve a stable bond that will survive even when are submerged in water. This is achieved manually with the aid of the microscope. On the stage, a clean microscope slide is placed onto which the desired particle has been positioned alongside a drop of Loctite Gel ® glue. Before depositing the glue the slide should be gently tapped on the bench to get an uniform spreading of particles on the slide. The thin end of the pipette is first dipped in the glue and then put under the objective in order to attach a particle from those focused under the microscope. When a suitable particle has been located, a gentle touch with the pipette tip secure a strong bond. The small amount of Loctite Gel ® (left on the pipette after dipping it into the glue drop) allows ~ 45s for dry curing, which is enough for selecting and attaching the particle. By using Loctite Gel ®, the pipettes can be used in an experiment immediately after the particle has been attached.

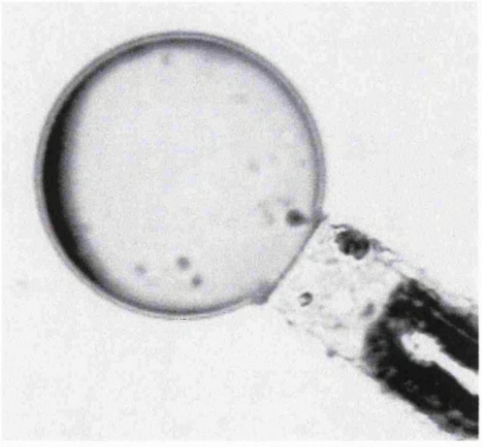

Figure 5-12 Image showing the tip of the pipette submerged in water with a particle attached.

5.1.5 Measurement of the pipette force constant

By hanging a known weight over the 90° bend of the flexible micropipette and measuring the displacement of the pipette tip the force constant can be calculated. This is achieved by mounting the pipette in the static pipette micromanipulator, focusing and noting the fine focus micrometer reading. The weight is then placed over the bend, the pipette brought back into focus and the micrometer reading again noted. A calibration value of deflection against force for the pipette is then determined (Appendix B).

5.1.6 The Olympus BX60 microscope

The Olympus BX60 microscope (see Figure 5-13) employs the UIS (universal infinite system) optical system and can be used for both transmitted and reflected light illumination.

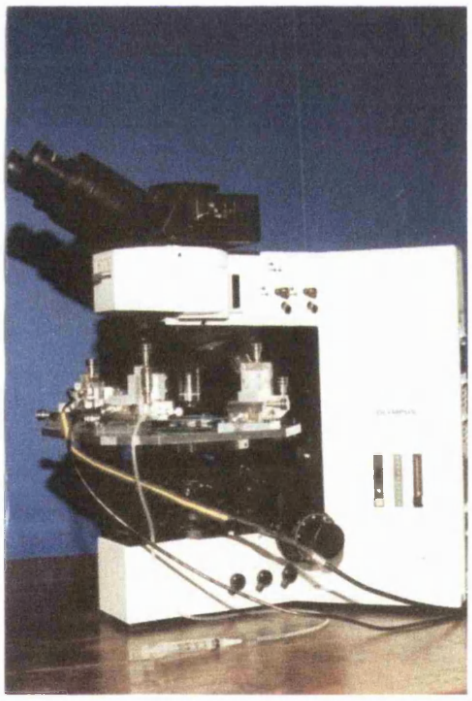

Figure 5-13 The BX60 Olympus microscope with the fitted stage.

Coarse and fine adjustment is facilitated by the adjustment knob, which is calibrated in microns. Four objective lenses for gaseous medium (5x, 10x, 20x and 50x) and one for the liquid medium (20x) allow liquid bridges between particles down to 3μm (limit of

optical microscopy) in diameter to be viewed. The maximum size of particle is limited by the field of view. The field of view with the 5x objective is 4.4mm. Information about the characteristics of each objective is printed on the casing. The water objective is recognizable among the others for having a plastic white casing.

5.1.7 Capturing the image

The observation tube of the microscope allows the image to be viewed directly or via a video camera. Usually the light path is split, 20% for the binocular eyepieces and 80% for the camera, although if brighter observation is required 100% can be directed to either. One eyepiece (left) also contains a micrometer graticule divided into one hundred units. Table 4 provides the calibration for the eyepiece

Objective lens	1 eyepiece graticule unit equals
5x	20μm
10x	10μm
20x	5μm
50x	2μm

Table 4 Eyepiece graticule calibration.

The camera (a JVC S-VHS colour video camera) is attached to the observation tube via an U-TV1X video attachment and an U-CMAD C–mount adapter. The camera has a resolution of 752 (H) x 582 (V) pixels. The Y/C output of the camera is connected to the S-VHS input of the video.

The images obtained from the camera are recorded using a Panasonic S-VHS video recorder. This allowed a rupture sequence to be recorded and then played back frame-by-frame to allow measurements to be taken via an image processor.

Individual frames from the video are viewed on the computer screen and captured using a video image viewing computer package Screen Machine (supplier Fast Electronic

GmbH). This consists of an internally fitted board and a software package, allowing conversion of analogue images into standard digital image formats.

5.1.8 Processing the image

After the image is captured using the Screen Machine package, it is analysed using the commercial software Microsoft PowerPoint. Of the wide range of digital output formats, the most suitable Screen Machine can produce for PowerPoint is a 256 shades of grey JPG. It is then possible to measure distances, angles and the geometry of the profiles directly from the images (see Figure 5-14) once the calibration factor between the image and the real dimension is known. This factor depends on the magnification of the objective lens used and is calculated by direct observation of a reference 1 mm graticule subdivided into a hundred parts (two adjacent ticks are separated by 10 μm). The calibration factors for the different objective lenses are given in Table 5.

Objective lens	PowerPoint to real dimension [μm/cm]
5x	61.2
10x	30.6
20x	15.3
50x	6.12

Table 5 Calibration factor for the determination of real dimensions from PowerPoint images.

Since the smallest distance that can be resolved using PowerPoint is 0.01 cm, the resolution limit of the software is 0.15 μm with a 20x objective. An additional source of error is introduced when the boundary of the liquid bridge meniscus or the geometry of the particles are marked using graphical tools provided with the PowerPoint software (blue points and red circles in Figure 5-14). This latter error is reduced by adjusting the focus of the objective in order to improve the contrast between the liquid bridge meniscus, the particles and the surrounding medium. The errors due to the PowerPoint capability and to the quality of the images affect both distances and angles and their values are reported in Table 6.

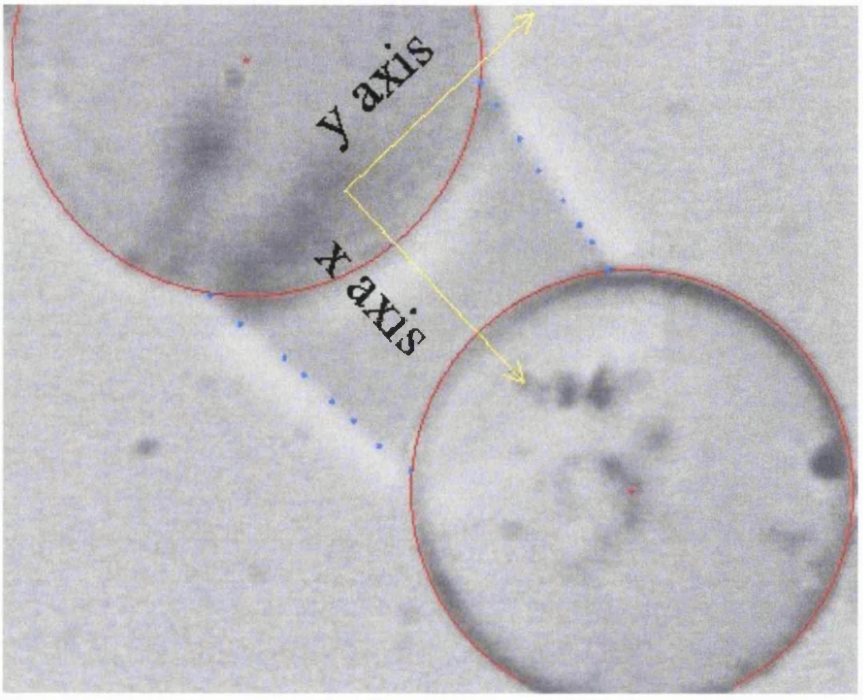

Figure 5-14 Liquid bridge image analysed with PowerPoint. The blue points and the red circles are drawn to enhance the relevant liquid bridge and particle geometry and are common tools of the software.

Objective lens	Error for position [μm] PowerPoint / Image		Error for angles [deg] PowerPoint / Image	
5x	± 0.61	± 2	±1.5	±2
10x	± 0.3	± 1	±1.5	±2
20x	± 0.15	± 0.5	±1.5	±2
50x	± 0.076	± 0.25	±1.5	±2

Table 6 Images analysis errors for measurements of distances and angles obtained using PowerPoint.

In order to determine, via image analysis, the force exerted by the liquid bridge during particle separation, the movement of the particle attached to the flexible pipette is compared with the initial reference position. By using a micropipette of spring constant in the value of 0.2 μN/μm, which is common to the force experiments performed, the error due to image analysis (using a 20x objective) is ±0.13 μN, which is very small

compared to the value that have been measured (in the order of 1.5–5 μN) in the experiments that will be presented in sections 6.2 and 6.3.1.

5.2 The AFM in liquid medium

A five months period of the present research project was spent at the Department of Chemical Engineering of the University of Maine (US), thanks to an invitation by the Head of Department, Prof. Douglas Ruthven. The collaboration with this University was set in order to use AFM equipment available in the Department of Chemical Engineering to take measurements of the long range force arising during the approach, and before any contact, between glass ballotini and a silicone oil droplet both submerged in aqueous solutions of surfactant and/or electrolyte. This AFM was designed at the University of Maine [109, 110] in order to measure the interaction between a particle and an air bubble submerged in water and to determine the deformation of the air-water interface.

In principle the AFM is a very simple device based on the optical lever technique in order to amplify the deflection of a thin cantilever, which interacts, directly or through an attached particle, with the sample to be investigated. AFM are either used to create a topographical image of a surface by scratching it with the cantilever tip or to investigate long range forces between two samples, one of which attached to the cantilever tip. In both cases a laser beam is reflected off the upper cantilever surface (usually gold or aluminium coated to enhance reflectance) and collected by a photodiode, which transforms position differences of the incedent light to a voltage signal.

Commercial cantilever tips are typically pyramidal in shape and are 3 to 4 microns in height. The tips have radius of curvatures anywhere from 200 to 300 Angstroms or less, and are made from silicon nitride, Si_3N_4. Cantilevers must be flexible yet resilient with force constants anywhere from 10^{-2} to 10^{2} N/m and have resonance frequencies greater than 10 kHz. Once the movement of the cantilever is known, the interaction force is determined and magnitudes down to 10^{-9} N can be resolved.

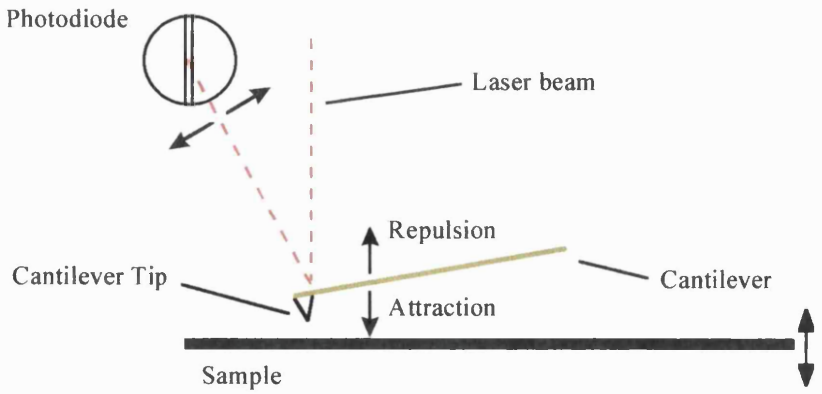

Figure 5-15 Schematic of the AFM measuring technique.

The following sections summarize briefly the design of the AFM at the University of Maine and detail the set-up and the data acquisition method for the experiments between a glass particle (~15 μm radius) and an oil droplet submerged in aqueous solutions of surfactants and electrolytes.

5.2.1 The AFM at the University of Maine

The AFM at the University of Maine was the result of two doctoral research projects intended to measure the interaction between a particle and an air bubble [109] and, by the addition of an interferometric unit, to detect the deformation of the air water interface during particle bubble interaction [110]. The interferometer unit is able to sense the water air interface by measuring the interferometric patterns formed between the direct and the reflected laser beam signals going to and reflected back from the apex of the water-air interface. Figure 5-16 shows the apparatus at the completion of Paulsen's doctorate [109].

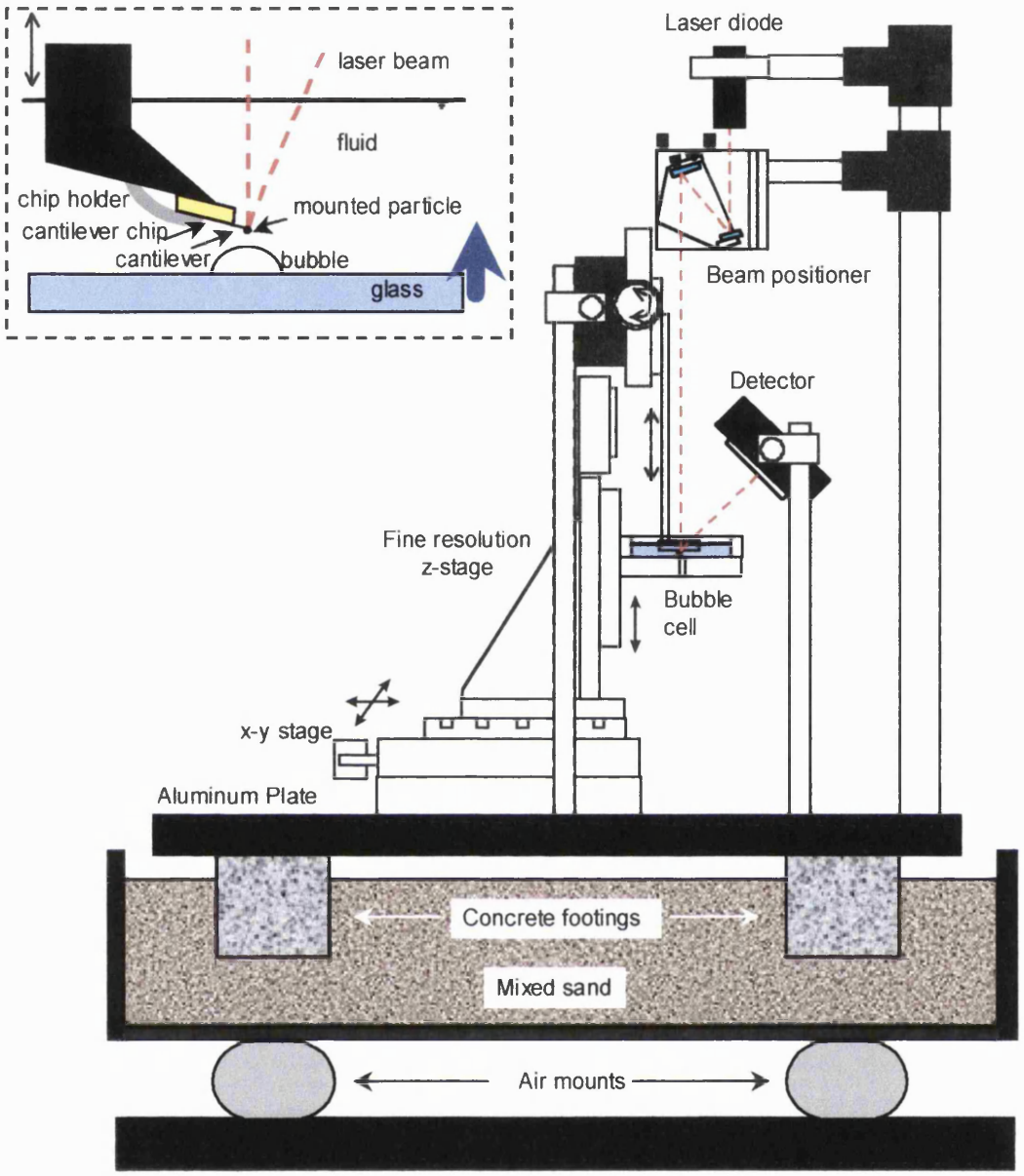

Figure 5-16 Schematic of the original AFM design by Paulsen [109]. Insert shows the view inside the bubble cell, illustrating the cantilever measurement technique.

The equipment can be divided into four functional groups:

- cantilever holding and positioning system
- equipment for the positioning and driving of the cell
- equipment used to measure the movement of the particle during the interaction,
- isolation of the apparatus from extraneous noise.

i) Holding and positioning the cantilever

Much like a commercial AFM system, a cantilever chip containing the cantilevers is mounted such that it remains stationary during an experiment and a sample is translated up from below. As the cantilever chip is held in place, the cantilevers attached to it are free to interact with either the bubble or the oil droplet as it is slowly moved towards the cantilever. The upper inset of Figure 5-16 shows a view of such a situation where a commercial cantilever (obtained from Digital Instruments) is mounted to a cantilever chip holder developed by Parks Scientific Instruments. This holder is part of a vertical racked shaft that is coupled with a pinion (moved by a knob) to provide the vertical cantilever coarse positioning. The cantilevers from Digital Instruments are standard gold coated, V-shaped silicon nitride Nanoprobe cantilevers (model NP or DNP) with integral pyramidal tips and resonance frequencies from approximately 5 to 50 kHz. Four various cantilevers of different spring constants can be attached to one cantilever chip (0.06, 0.12, 0.32 and 0.58 N/m), which can be distinguished by the thickness and length (100 or 200 μm), as illustrated in Figure 5-17.

In the original design the holder and cantilever chips are submerged in approximately 15 ml of fluid contained in a Plexiglas cell designed at the University of Maine. Before the cantilever and the holder are submersed, either a bubble or oil droplet is placed on the bottom of the cell.

The method of formation of the oil droplet, which is relevant to the set of experiments presented in section 6.3.2, will be detailed in section 5.2.5.

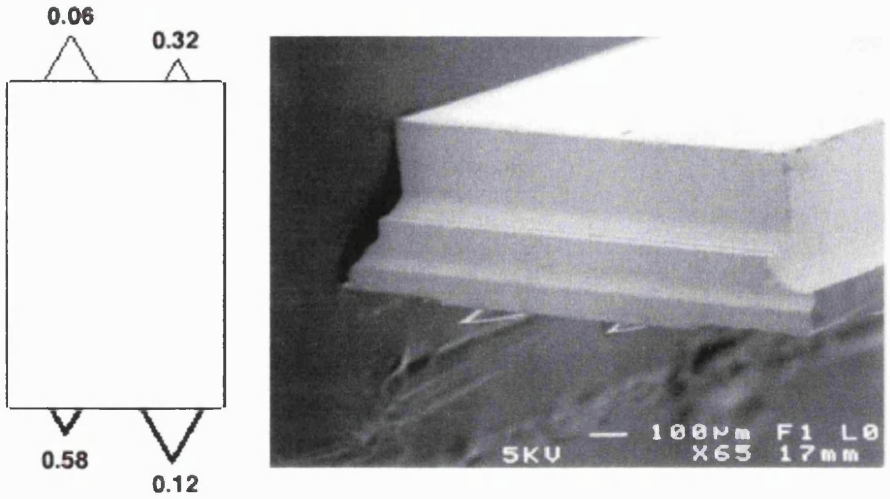

Figure 5-17 Silicon Nitride cantilevers from Digital Instruments. The spring constant indicated on the left picture is in N/m.

ii) Cell movement

The movement of the cell towards the cantilever is obtained by using a piezoelectric Inchworm motor (model IW-700) and a TS-300 z-axis counterbalanced stage. These are controlled by a 6000 ULN motor controller and power supply interfaced with a personal computer. By using Vis Sim control software through a Computer Boards, Inc. CIO-DAS08 analog/digital data acquisition and control board, the motor could be computer controlled. Figure 5-18 shows a schematic of the positioning system. The motor, stage, and controller are provided as a package from Burleigh Instruments, Inc. The IW-700 Inchworm motor is a piezoelectric motor which consists of an alumina shaft in a LZT (lead zirconate titanate) sleeve which has three sections. The motion is provided through the sequential activation of three piezoelectric sleeves. Through a sequence of expansions and contractions of the piezo sleeves, which clamp the alumina shaft, motion can be achieved. The motor has a mechanical resolution of 4 nm with a speed range from 4 nm/sec to 2 mm/sec and a total range of travel of 25 mm. The alumina shaft can push loads up to 1.5 kg in the vertical direction. These motors are high voltage devices, which require a motor controller for operation. The 6000 ULN controller is a high voltage and current device, which provides a 512 step voltage staircase for smooth motion. The controller is operated through the CIO-DAS08 control board plugged into the PC. It controls function operations such as stop/go, forward/reverse, and motor

speed. Motor speed is regulated by supplying an input clock frequency using the CIO-DAS08 control board counter to send square wave frequencies to the controller with a maximum allowable input frequency of 500 kHz.

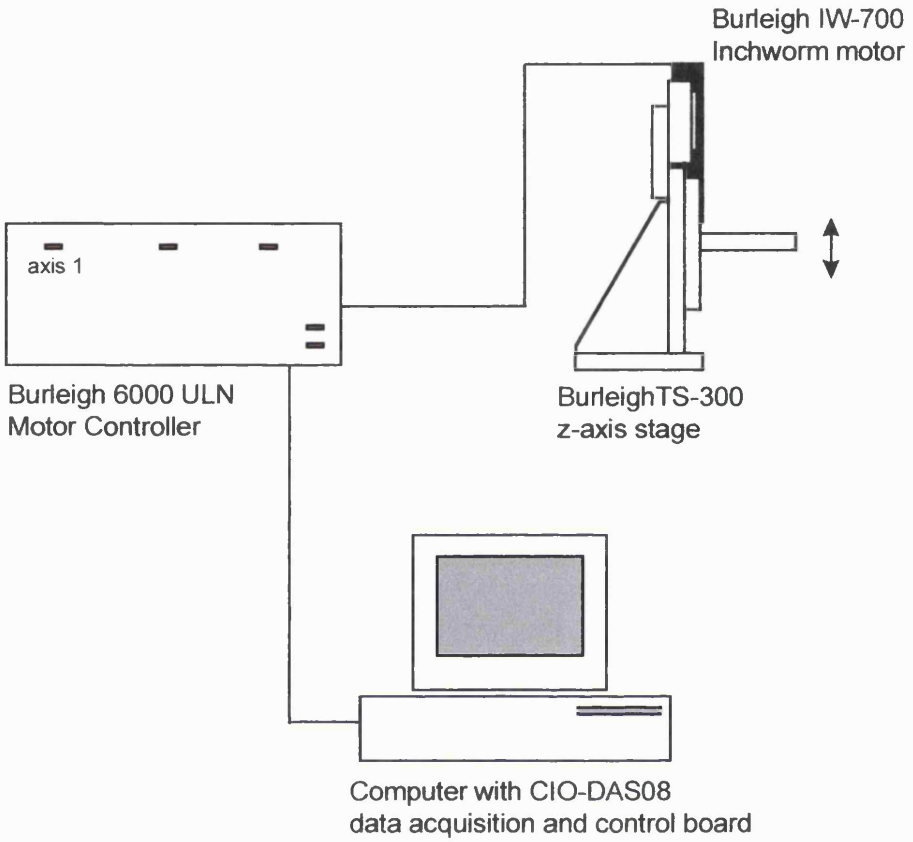

Figure 5-18 Schematic of the vertical positioning system showing the Burleigh Instruments piezoelectric Inchworm motor, high voltage motor controller, and z-axis translation stage, along with computer control.

The nominal frequency in Hertz required for a desired shaft velocity of the motor is given by the Burleigh manufacturers in (5.2). Vis Sim software can then be used (Appendix D.1) to give a desired shaft velocity supplying a given input frequency through the CIO-DAS08 control board using (5.2).

$$v_{motor}\,(\text{mm/s}) = \frac{2 * 0.0039}{\frac{1000}{frequency(Hz)} + 0.0002} \tag{5.2}$$

The Inchworm motor shaft is connected to the TS-300 z-axis stage through a motor mount and the stage provides a platform for the cell assembly. The TS-300 z-axis stage is a single-axis, crossed roller bearing stage with up to 50 mm of total vertical travel and will counterbalance up to 1.5 kg to avoid inertial effects. However, the motor is equipped with only 25 mm of travel so the usable range of travel for the stage is 25 mm, which is more than adequate for the experiments. In order to allow horizontal positioning of the bubble/droplet with respect to the cantilever and attached particle, the TS-300 z-axis stage is mounted on a x-axis and y-axis positioning stage. By using hand micrometers this allows the operator to position the particle directly over the apex of the bubble/droplet.

This combination of computer, controller, motor, and stage can provide the necessary movements for either a bubble or droplet to make contact with a particle-mounted cantilever.

In the original Paulsen design [109], the bubble cell was placed on a horizontal platform connected to a vertical translation z-stage. Due to the changes made by Berg [110] with the introduction of an interferometric unit, a Plexiglas skirt was added to the original cell in order to gain an appropriate height from the interferometer lens (see Figure 5-22).

iii) Acquisition of cantilever movement

Deflections of the cantilever are measured using the gold coated cantilevers described previously from Digital Instruments. A light beam from a 1 mW laser diode from Imatronics is aligned using a precision laser beam aligner from Oriel with four individual screw adjustments for vertical and horizontal translation and vertical and horizontal angle adjustment. The light beam is reflected off the backside of the cantilever toward the detector. The position of the reflected beam is measured using a LSC 30-D silicon position sensitive device (PSD) from UDT Sensors with an active surface area measuring 30 mm long by 4 mm wide. The PSD is then coupled with a Model 301 DIV position sensing amplifier, available from Graseby Optronics. The PSD and the amplifier generate an analog output (voltage) proportional to cantilever position

in the range of +/– 10 V, which is interfaced to a second computer through the analog input channels of the CIO-DAS0801, an improved model of the board used for the control of the piezoelectric vertical translation. The complete set-up for the cantilever detection system is shown in Figure 5-19.

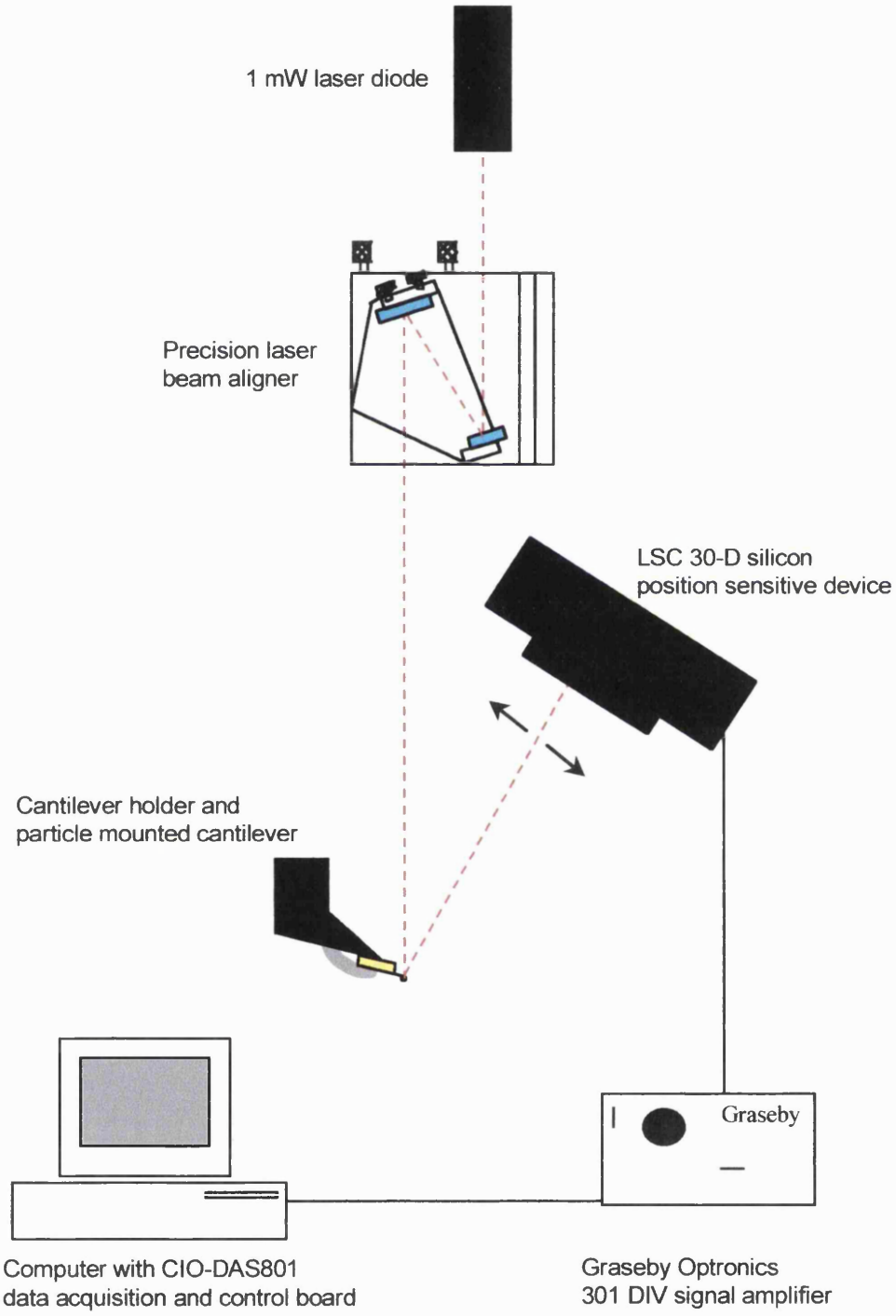

Figure 5-19 Schematic of the cantilever detection system.

Data sent to the CIO-DAS801 board are logged by dedicated software (Softwire) and stored as data file.

The conversion factor from the voltage reading to the cantilever movement is discussed in Appendix D.2 and is reached by using the vertical translation stage to move a solid glass surface against a glass sphere mounted on the cantilever in distilled water. From the known speed of the Inchworm motor and from the reading of the cantilever voltage it is possible to calibrate the data acquisition system.

Paulsen [109] asserted that with appropriate vibration control the arrangement could give an accuracy of approximately ± 5 nm on the cantilever position, which seems quite large for double layer interaction that can be significant over tenths of nanometer distance. This information was not available when the collaboration with the University of Maine was set.

iv) Antivibrational plate

The apparatus is secured to an aluminium base plate measuring 610 mm by 610 mm wide and 13 mm thick, which is placed on four concrete footings measuring 89 x 89 x 89 mm placed near the corners of the base plate. The concrete footings are set in approximately 100 mm of mixed sand (~50 kg), which is placed in a welded box frame measuring 610 x 915 mm supported by four air vibration mounts. Low-pressure air (20-25 psig) was supplied to the table to continuously keep the air mounts expanded. This combination of air and sand mounting proved sufficient for damping outside vibrations.

5.2.2 Interferometer system addition and other modifications to the original apparatus

The interpretation of AFM results between a particle and a non rigid surface is always complicated by the understanding of the interface mobility. The ability of measuring the bubble surface position was the motivation behind the modifications made by Berg [110] who added an interferometer unit to Paulsen's AFM [109]. The layout of the

AFM at the University of Maine is shown in Figure 5-22. Unfortunately, the interferometric system did not show the same measuring capability for the oil-water interface, as will be detailed in the following section.

The system supplied by Zygo Corporation (Middlefield, CT) used a non-contact probe interferometer to focus the laser light beam onto the bubble surface. Resolution of the interferometer was approximately 2.48 nm with a focused spot size on the bubble of 60-90 μm. This particular system used a single stabilized He-Ne laser source (1 mW) to emit a beam with two frequencies separated by exactly 20 MHz. One frequency was used as the measurement beam and one as the reference. A fiber optic pickup was employed to carry the fringe pattern (described below) to a detector and accumulator contained in the control unit. Software was supplied by Zygo to measure the mobility of the surface focused under the laser beam. The original measurement technique used to record bubble surface position is shown schematically in Figure 5-20. The non-contact probe split the two distinct frequencies, using one for the reference signal (shown as black in Figure 5-20), which passed straight through the beam splitter and was reflected off the retro reflector, maintaining a fixed beam length to be eventually collected on the fiber optic pick-up. The second frequency was used as the measurement beam (shown as magenta in Figure 5-20), which was turned 90 degrees upward and sent to the bubble surface. The reflected signal from the bubble (shown as yellow Figure 5-20) then re-entered the probe and after final deflection toward the fiber optic pick-up was combined with the reference beam. From the fiber optic pick-up the recombined beam is conveyed to a detector inside the Zygo unit via a fiber optic cable and processed in order to evaluate any movement of the interface.

The alignment of the interferometer in order to work with the air bubble interface was made by Berg according to the manual of the instrument, but the procedure was, unfortunately, not reported in his thesis [110]. As recommended by Zygo, the distance between the upper lens of the interferometer beam splitter (non contact probe) and the focused target must be 44 mm.

As the path length of the measurement beam changes, an interference pattern develops between the two frequencies. The fringe bands are then counted by a photo-detector and accumulator located in the control unit of the Zygo interferometer.

In order to measure the movement of the bubble surface by means of the interferometric system, Berg modified the original cell used by Paulsen. He substituted the original bottom of the cell with a stainless steel plate that had a 2 mm hole drilled in it as a reservoir for the bubble The bottom of the reservoir was composed of an optical window with MgF_2 anti-reflective coating, through which the interferometer beam passed to reach the interior surface of the bubble. The new cell assembly used by Berg is shown in Figure 5-21.

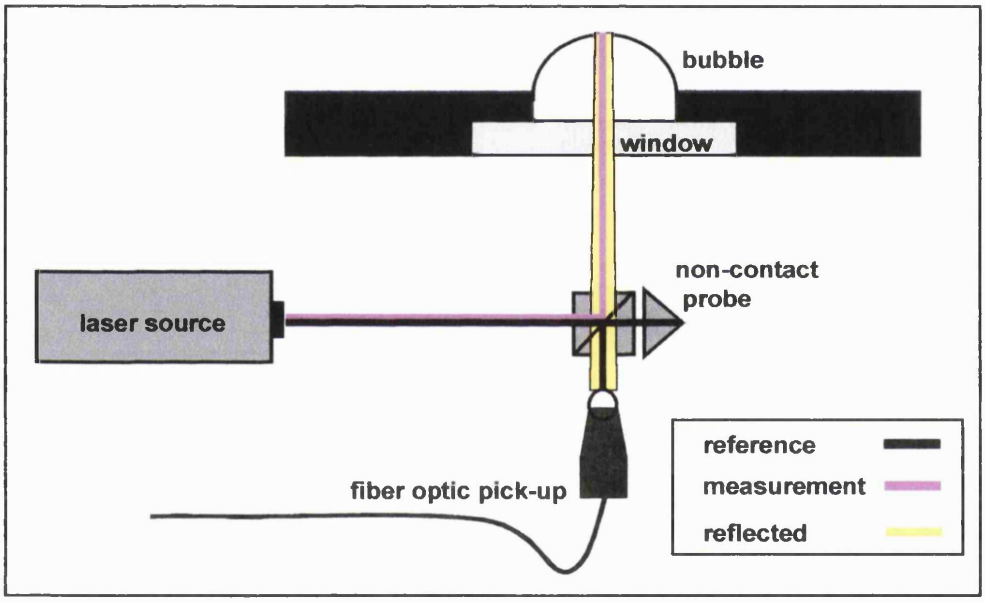

Figure 5-20 Schematic showing the interferometer measurement technique. Legend designates different portions of laser beam. The distance between the upper lens of the interferometer beam splitter and the focused spot must be 44 mm.

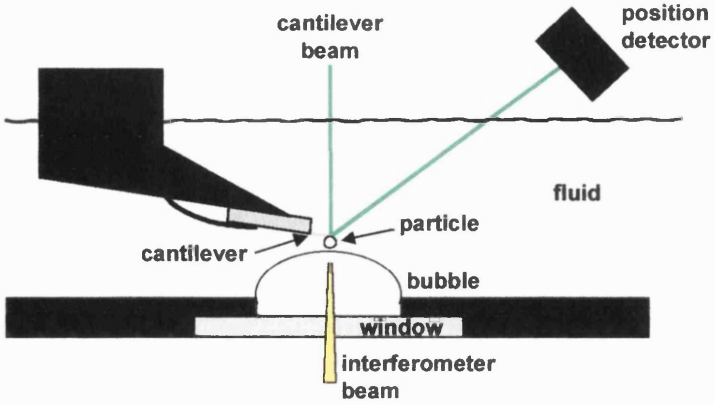

Figure 5-21 View inside the bubble cell, illustrating the bubble and particle measurement technique as modified by Berg.

A centre aperture in the TS-300 Burleigh z-axis stage allowed the upper lens of the interferometer access to the bottom of the water cell, as shown in Figure 5-22. The cell was also provided with a Plexiglas skirt screwed on the base of the Burleigh TS 300 z-axis stage, in order to gain an appropriate height to ease the focusing of the apex of the bubble before an experiment was carried out. Through fine adjustments with the Burleigh TS 300 z-axis stage the apex of the bubble was focused at ~44 mm above the upper lens of the beam splitter. To ascertain that the apex was correctly focused, Berg used the Vis Sim software to drive the Burleigh motor at very low speed (0.5 μm/s) whilst the output voltage on the Zygo equipment resulting from the interferometric laser patterns was controlled. This voltage rises from 3.7 to 4.15V as a target is approached and at last focused. The reading on the Zygo interferometer is not direct but passes through a multimeter connected to a voltage pick-up point on the Zygo front panel.

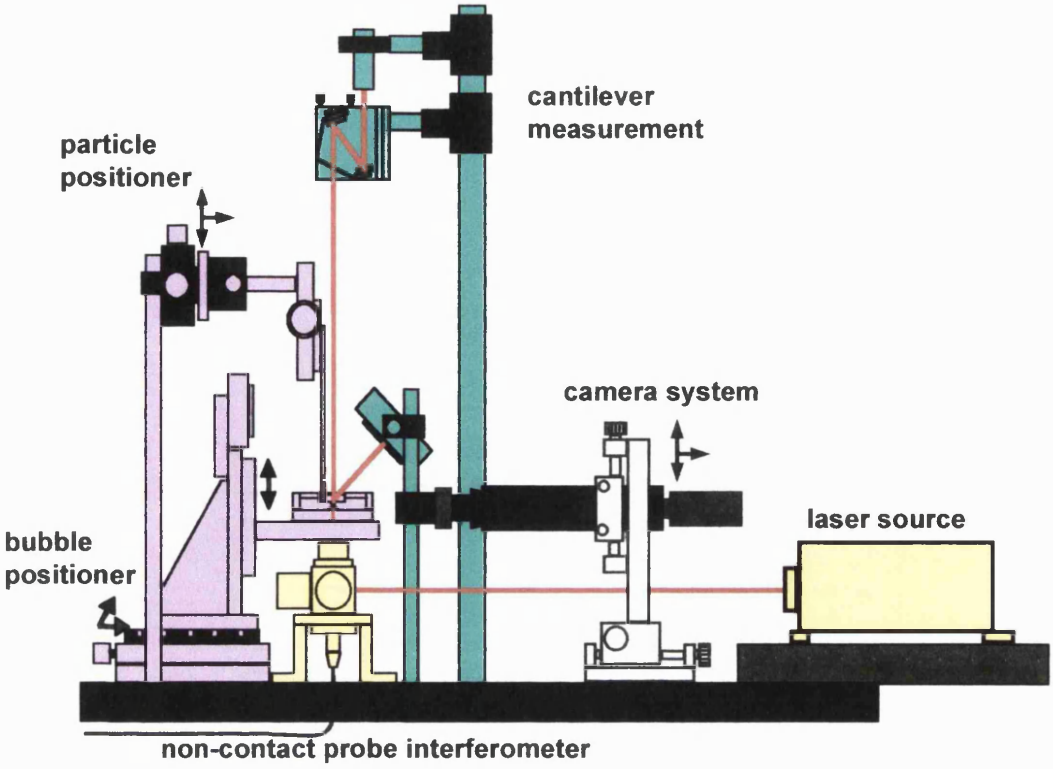

Figure 5-22 Schematic of the force measurement apparatus including interferometer addition by Berg. The figure also shows also the video system described in section 5.2.4.

Berg also introduced a cantilever x-y-z-axes fine positioning system (indicated as particle positioner in Figure 5-22) in order to align the particle precisely over the bubble already aligned to the interferometer measurement beam. In the previous design the cantilever could only be moved vertically.

5.2.3 Limitations of the AFM system and modification of the cell

Unfortunately, the AFM device designed at the Chemical Engineering Department of the University of Maine showed some limitations when measurements of the oil-water interface was attempted.

The first essential problem experienced in carrying out AFM experiments was related to the measuring capability of the cantilever movement. According to the original design proposed by Paulsen [109] the cantilever position can be detected with an accuracy of approximately ± 5 nm, which seems quite large for double layer interaction that can be

effective over sub-nanometer distances. This information was not available when the collaboration with the University of Maine was set.

A second major problem was the impossibility of using the interferometric unit in order to detect the deformation of the oil-water interface. The measuring technique of the interferometer is based on the analysis of the reflection signal of a laser beam focused on the apex of the interface (either oil-water or air-water). The reflectivity of an interface, rx, depends on the refractive index of the two phases rx_1 and rx_2 according to the formula:

$$rx = \left(\frac{rx_1 - rx_2}{rx_1 + rx_2} \right)^2 \tag{5.3}$$

The refractive index of air, water and silicone oil are 1.00, 1.33, 1.40 respectively and therefore the reflective index of the air-water interface is 0.02, whilst for the water-oil interface it results in the value of 0.0006, ~30 times lower. Since the interferometer could not spot the position of the oil droplet apex, it was used to focus the bottom of the cell in order to monitor the nominal velocity of the Burleigh TS-300 z-axis stage as driven by the Burleigh motor. Differences between 10% and 15% according to the nominal velocity calculated by (5.2) have been noted for a velocity of 100 nm/s, which were taken into account for the voltage-to-position calibration of the cantilever, as will be detailed in Appendix D.2.

A secondary limit of the AFM apparatus was the impossibility of independently measuring the cantilever spring constant to check the value reported by the vendor. As noted by Cleveland [111], small variations in the cantilever thickness can lead to variations of the spring constant up to 30% of the nominal value. The technique proposed by Cleveland in order to measure the cantilever spring uses the variation of the natural cantilever resonation frequency before and after a known mass has been added to the cantilever [111]. In general, commercial AFMs have the possibility of applying a driving force in order to make the cantilever resonate. Although this facility was not present in the AFM described, the thermal agitation could have been able to

provide large enough oscillations (of order 1 nm) [111] for the technique to be applied. Due to the intrinsic limit of the cantilever position transducer, (± 5 nm), no resonation technique could be applied and, therefore, the cantilever spring constant was assumed according to the value declared by the supplier (Digital Instrument), which was unable to furnish other data about the standard deviation of the value.

The verification of the real capability of the AFM instrument forced the experimental work to deviate from the initial plan of measuring force and interface deformation of the glass-oil-water system before the engulfment the glass in the oil. The investigation was thus focused on the force responsible the engulfment of the particle and how it was enhanced or inhibited by the solution condition. If, during the ballotini to oil approach, the resulting force was attractive the cantilever and the particle experienced a "snapping in" or "jump to contact" motion towards the interface. The resulting force at the moment of the "jump" could be enhanced or completely inhibited by the type of surfactant. This is presented in section 6.3.2.

In order to carry out the experiments with the silicone oil, the cell of the AFM was redesigned (Figure 5-23). The Original cell at the university of Maine was made of Plexiglas walls glued (internally) with sealing silicone. This assembly did not comply with the requirements of the absolute cleanliness of environment, which can highly affect the interaction between the particle and the droplet and overcome the effects of the surfactants and electrolytes present in the solution.

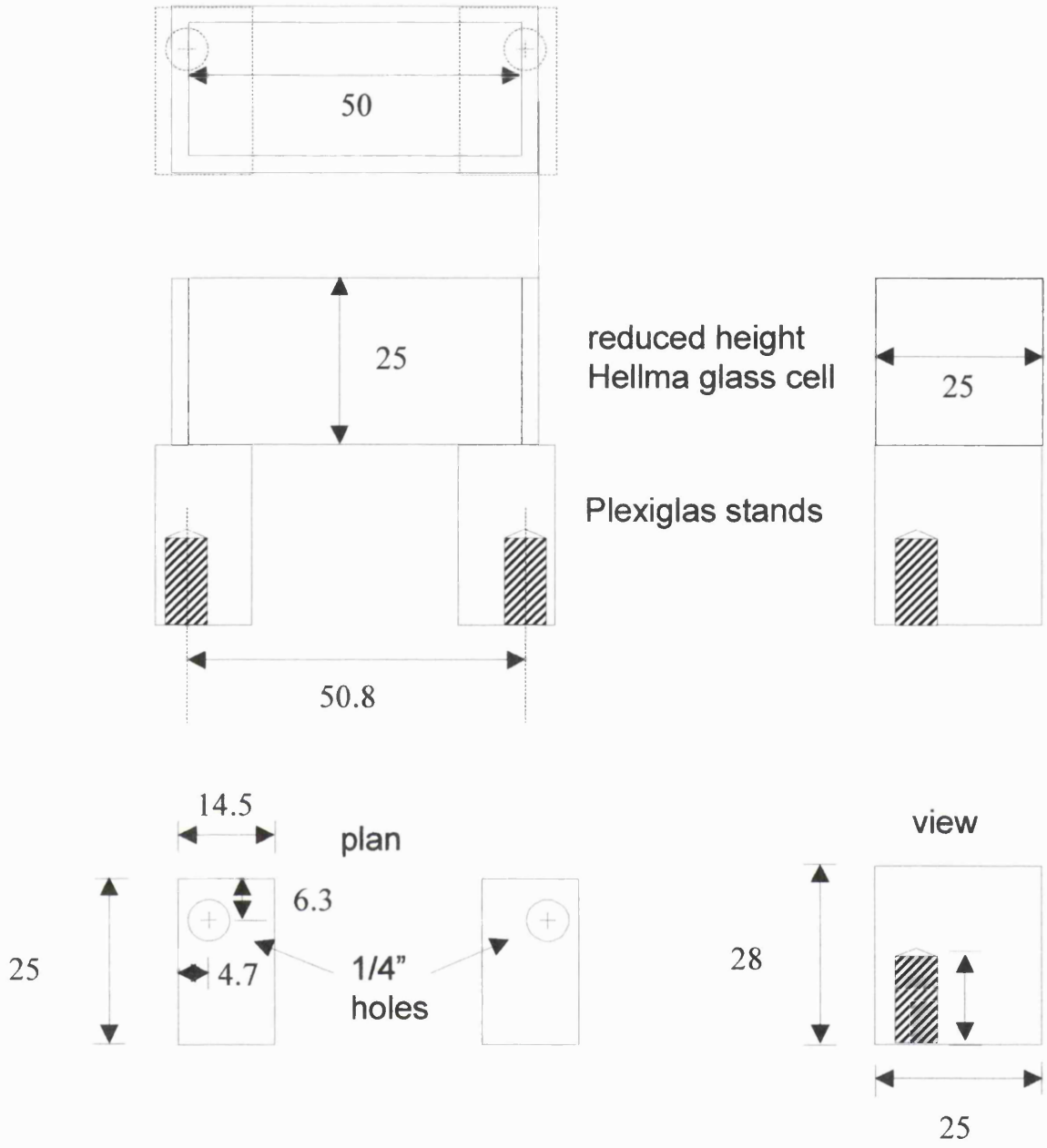

Figure 5-23 Design of the cell used for the AFM experiments. The picture shows the reduced Hellma cell and the Plexiglas stands.

The new cell was derived from a biological optic glass cell available from Hellma Worldwide, measuring 55 mm wide by 25 mm long and 53 mm height. The thickness of the cell is 2.5 mm. The cell height was reduced to 25 mm by means of a diamond saw in order to help with the introduction of the vertical chip holder in the cell. Two Plexiglas stands were used to keep the cell at an appropriate height from the the upper interferometric lens in order to use the Zygo interferometric unit. The stands were

screwed on two drill holes made on the Burleigh TS-300 z-stage and, by means of bi-adhesive tape, the cell was secured on them for the experiment.

5.2.4 Video system

The video system provided the means to visually observe the particle mounting, the alignment procedures and the experiments. It consisted of a Sony XC-75 monochrome CCD camera and an Ultra Zoom 6000 II variable scope with either a 10x or 50x Mitutoyo objective lens supplied by Navitar Inc. The camera was mounted on the scope and images were viewed on a 19-inch monitor and recorded on a Panasonic video recorder.

In order to minimise light disturbances to the cantilever laser signals, experiments were carried out in near darkness and, therefore, a Dolan Jenner Fiber-Lite® illuminator with a single gooseneck cable was used to backlight the water cell. The entire camera assembly was mounted on an x-y-z-axes adjustment. Depending on the objective used (10x or 50x), the focal length of the camera system was either 33 mm or 13 mm, respectively. To accommodate the small working distance, the water cell was designed to place the bubble within a few millimetres of the glass wall having a thickness of 2.5 mm. When viewing an experiment, much of the cantilever laser light was reflected off the cantilever, therefore a coloured glass filter was placed between the water cell and the objective lens to remove the majority of the low-frequency visible light. Figure 5-24 shows a schematic of the high-magnification video system. The variable zoom range was between 0.75-4x, which, once coupled with the 10x objective and shown on a 19-inch monitor, had an overall magnification of approximately 300x to over 1000x. Using the 50x objective increased magnification by approximately five times. The images of the water-oil experiment were recorded on the VCR system by using a 10x objective coupled with the 4x variable zoom setting. The calibration of the images was done with a reference graticule and processed under PowerPoint, which gave a value of 86 μm-real/cm-PowerPoint.

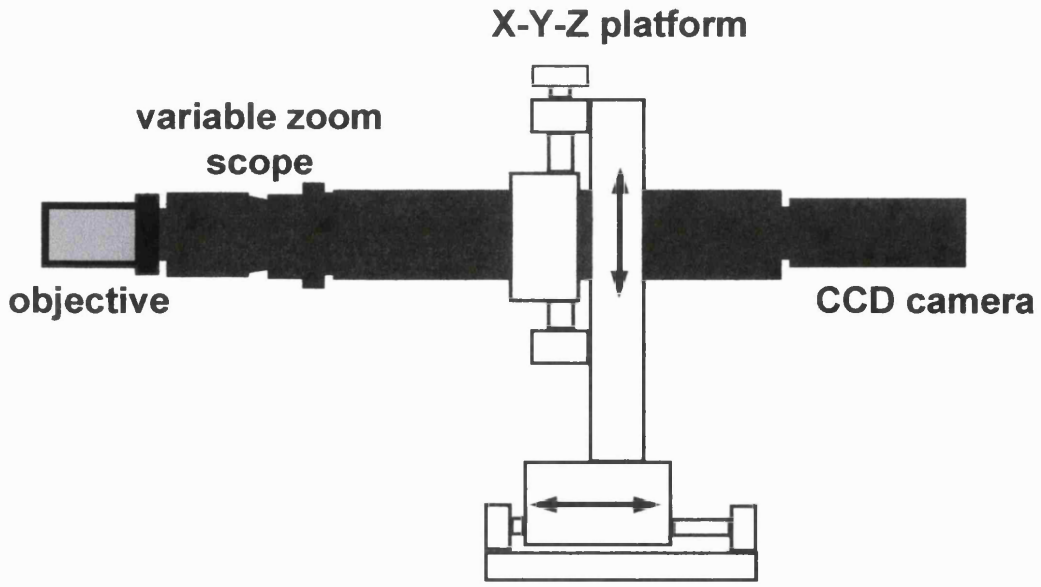

Figure 5-24 Schematic of the video system. The CCD camera was connected to the VCR and monitor to view and record experiments.

5.2.5 Experimental procedures

The investigation of the interaction between a glass particle (~30 microns diameter) and an oil droplet submerged in water can be achieved by means of the AFM through the following steps:

- Mount cantilever chip on chip holder
- Attach glass particle
- Form the oil droplet in the glass cell previously filled with solution
- Focus the laser beam on the back of the cantilever and align the particle with the apex of the oil droplet
- Start the software that checks the laser cantilever alignment
- Run the experiment.

i) Mounting the cantilever chip on chip holder

The chip holder kept the cantilever in position. In order to secure the cantilever to it, the chip holder was first put upside down. The cantilever was held in its seat and secured through a screw that tightens a plate on it. Digital Instruments supplied cantilevers (code name either NP-20 or DNP-20) in wafers of 20. The cantilevers came upside-down in their box and by using tweezers were mounted in this direction to the upside-

down chip holder. the cantilever chips were previously put under a microscope to verify the spring constant. Before attaching a particle, the cantilever was gently blown with compressed air to remove any dust collected in the box in which they were stored.

ii) Attaching a particle to the cantilever

The chip holder was put in its vertical operating position (Figure 5-21) and focused with the video system. To glue the particle, a Loctite product was used (Stick-with-it) that sets in 10 minutes and fully cures after 24h. After 3 hours a good adhesion was reached to perform the experiment. A small portion of glue was spread on a glass slide. The glass with the glue was then placed on the z-stage of the device and the cantilever lowered to within close proximity using the coarse adjustment movement of the cantilever assembly. Using the fine-positioning z-direction adjustment screw, the tip of the cantilever was lowered until contact was made with the glue film. Upon contact with the epoxy, the cantilever tip was immediately withdrawn, transferring a small amount of epoxy to the underside of the tip. Next, the epoxy-covered glass slide was replaced with a clean slide containing a small number of glass beads. Using the camera a properly shaped bead of appropriate size was selected. The epoxy-tipped cantilever was brought into close proximity to the selected bead and the x-y-z adjustment screws were used to position the tip directly over it. The cantilever was then lowered until contact and a small amount of force was applied to ensure strong adhesion. The cantilever was left in place in order to avoid contamination with those in the stocking case.

Figure 5-25 illustrates each of the six steps involved in epoxy application and mounting of a bead to the cantilever.

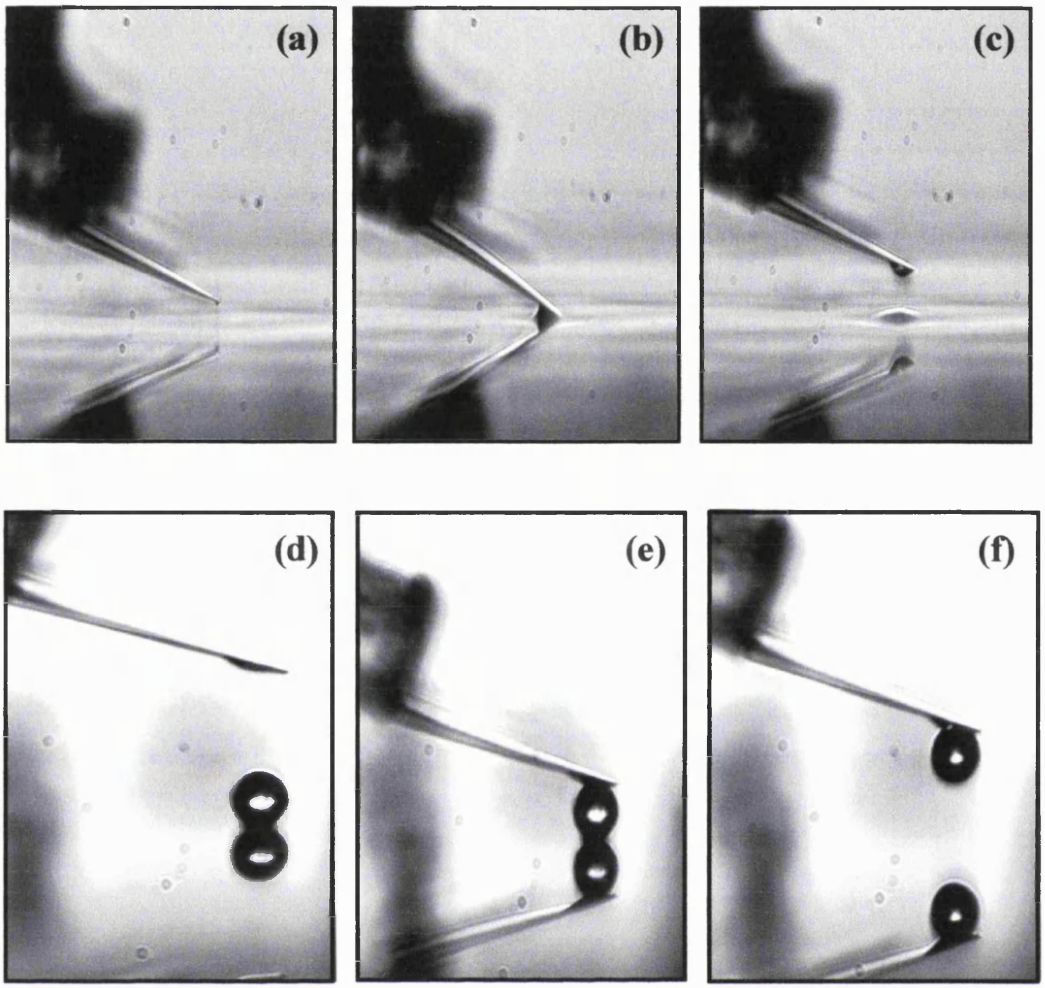

Figure 5-25 Particle mounting procedure: (a) cantilever approaching epoxy film, (b) tip making contact, (c) withdrawing cantilever with attached drop of epoxy, (d) cantilever with epoxy aligned over glass bead, (e) cantilever in contact with bead and slight force applied, and (f) after 2 hours it is ready for the experiment. Note the reflected image on the epoxy and glass slide.

iii) Formation of oil droplet in the glass cell previously filled with solution

The cleaned cell proved to be very hydrophilic and therefore, after being filled with a water solution, a bubble could only be formed with difficulty on its base, especially in solutions of SDS surfactants. In order to avoid this problem, a previously clean silanised cover glass was introduced into the cell at the time of cleaning and care was taken during the rinsing to centre the cover glass on the base of the cell. After drying of the cell containing the silanised cover glass, the oil droplet was much more easily formed on the silanised surface. The bubble was formed with a precision syringe (Hamilton™

10 μl with a 10 cm needle). Oil was sucked into the syringe without using the needle and air mixed with oil was flushed out from the needle after mounting it in order to have an air-free flow of oil. Before forming the oil droplet in the cell the needle was cleaned with a laboratory tissue in order to remove any oil contamination that could be dislodged on the surface of the filled water cell and blot the glass ballotini surface when submerged in the cell. The clean needle was then dipped in the cell in close proximity to the surface of the silanised cover glass and a small bubble was formed. The deposition on the silanised cover glass was achieved by contacting with the needle and by exerting a light pressure on the syringe piston. This method produced stable oil droplets on the glass surface in de-ionised water.. The cell was then put in position under the cantilever chip holder on two Plexiglas supports and secured on them with bi-adhesive tape.

iv) Focusing the laser beam on the back of the cantilever and alignment of the particle with the apex of oil droplet

In order to guarantee the perfect vertical alignment of the laser beam when focusing on the back of the cantilever a simple method was adopted involving the exploitation of the alignment capability of the Zygo interferometer without switching the latter on. The laser beam, through the Oriel beam aligner (see Figure 5-19), could be focused on the centre of the upper lens of the beam splitter until the 90° deviated beams reached the centre of the Zygo laser head turret (see Figure 5-26). At this point the cantilever laser beam was perfectly vertical and the cantilever was then moved under the vertical laser diode through the fine positioning micrometers of the chip holder (see Figure 5-22). The vertical alignment of the chip holder was previously controlled by the bull eye level. The oil droplet was eventually moved into position under the particle via the x-y-axes positioners, which controlled the movable plate on which the Burleigh TS-300 z-stage was mounted (see Figure 5-16). To avoid an involuntary engulfment of the particle with the oil droplet it was better to leave a reasonable gap that would then be reduced by using the piezo electric motor. At this point the Zygo interferometer was switched on in order to use the interferometer measuring capability to focus the base of the cell and have a double check of the Burleigh motor velocity during the particle-to-oil approach. The test voltage on the Zygo board (measured with a digital multimeter) should be 4.15V.

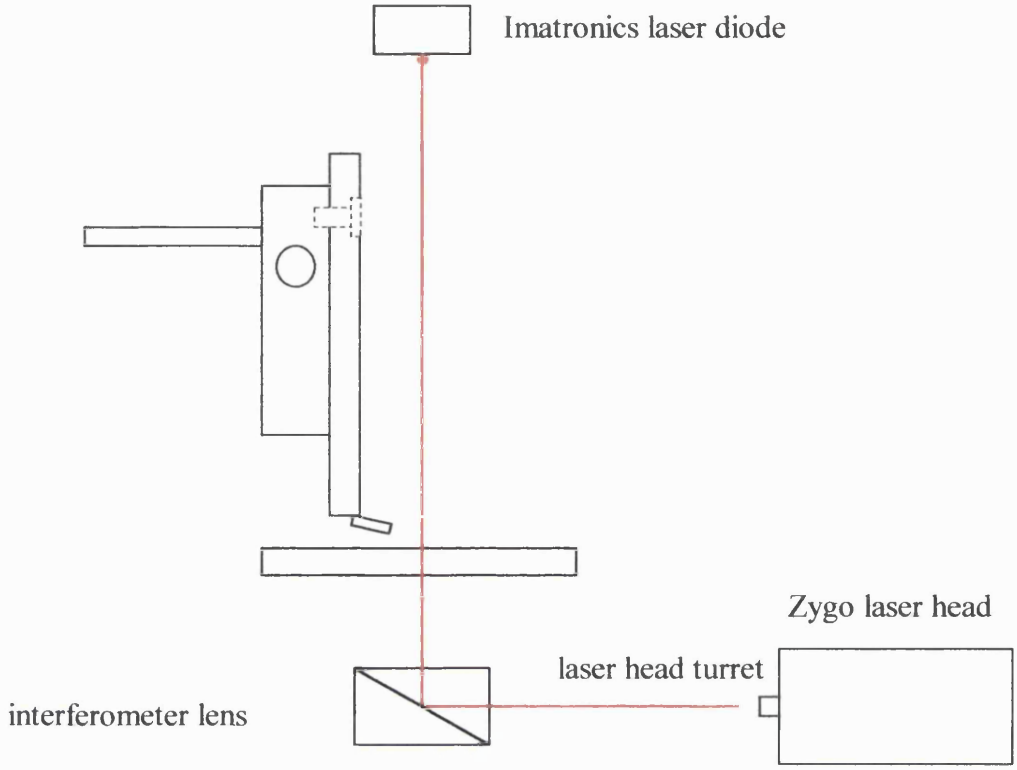

Figure 5-26 Laser diode vertical alignment by exploiting the capability of the Zygo interferometer.

v) Starting the software that checks the laser cantilever alignment

The reflection of the cantilever is detected by the position sensor detector of Figure 5-19 (PSD). By covering the position detector with a piece of paper it is possible to verify the beam light is correctly aligned in the sensitive area of the PSD. In order to be sure that the detector is collecting the cantilever reflection ray, it is suggested to move the cantilever off its position by acting on the micromanipulator and see that the spot, as collected on the paper in front of the position detector disappear. The voltage associated with the position read by the PSD is displayed on video by the program *PSDacq* running under Softwire. This latter program simply displays the PSD voltage as acquired from the CIO-DAS801 board (see Figure 5-19) and write the readings on an Excel file at the inputted logging sequence (either 500Hz or 1000Hz). Rotation of the PSD along its axis allows setting the voltage around 0V that ensures the light spot being collected in the middle of the PSD allowing full extension on the two ends.

vi) Running an experiment

In order to run an experiment, thee different programs were used:

- *motor.vsm*, a Vis Sim program that controls the piezo motor. Vertical upward speed was usually set at 100nm/s.
- *ZMI1000*, the Zygo software that collects the data from the Zygo laser in order to double check the speed of the motor. The frequency of data logging was usually 1000Hz
- *PSDacq*, a program written in a graphical programming enviroment (Softwire) that collects data from the PSD and writes them on an Excel file.

The starting sequence of the programs was first *motor.vsm*, to have the cell moving, followe by *PSDacq* and *ZMI1000*. The data collected by the *ZMI1000* was copied to an excel file for further analysis. All the phases of the experiment were video recorded on tape. The programs were stopped either after the particle was engulfed in the oil droplet or, in the case where no engulfment occurred, after the particle had been considerably moved upward, pushed by the rising oil droplet.

5.3 Materials

Soda lime glass ballotini (Sigmund Lindner type S) were used as model particles as they are spherical, non-elastic and inexpensive. Soda lime glass is principally made of SiO_2 (72% by weight) with the remaining components being divided among Na_2O (13%), CaO (9%), MgO (4%), Al_2O_3 (1%) and Fe_2O_3 (1%). A range of particle sizes below 250μm in diameter were used both in untreated and silanised form. Due to the presence of SiOH groups, the untreated glass surface has a hydrophilic nature, which is readily altered using a silanising agent to produce a hydrophobic surface. The silanising agent was supplied by VWR International (former BDH) as 2% solution of dimethyldichlorosilane in octamethylcyclotetrasiloxane. Of the two, only dimethyldichlorosilane is available for reaction (see Figure 5-27) at room temperature, whilst the latter component only reacts with glass at elevated temperature. In order to silanise ballotini the following method was employed. First to ensure the glass surface was clean and grease free, the ballotini were placed in a 100 ml beaker, soaked in

chromo sulphuric acid (Acros Chimica) for four hours and then thoroughly rinsed with de-ionised water and put in the oven to dry at 70°C.

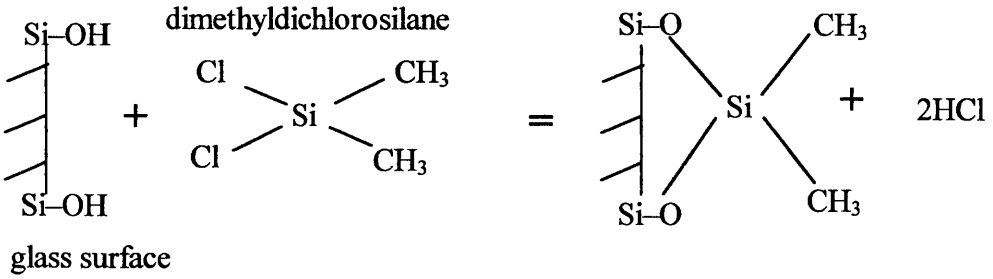

Figure 5-27 Silanisation reaction of the glass surface.

When the ballotini were perfectly dried the silanising agent was added. To ensure an even contact of the agent with all ballotini surfaces a magnetic stirrer was used to agitate the mixture. The reaction was considered to be complete after 30 minutes and again the ballotini were separated from the silanising solution by using a filter funnel and 5 μm filtering paper (both available from Whitman). In order to remove any surplus of silicone residues the ballotini were first washed with toluene (Spectranal, 99.9% pure from Aldrich) and then with methanol (VWR International) before final drying. All the previous operations were carried out in a fume cupboard as recommended by the safety data sheet provided by the vendor.

For the experiment in gaseous medium glycerol was used as the bridging liquid whilst for both the MFB and AFM experiments Analar water (VWR International) and Dow Corning 200 series silicone oil 100 cS (VWR International) were used as the suspending liquid and oil phase (bridging liquid in the MFB experiments), respectively.

Sodium dodecyl sulphate (SDS) especially pure and cetyl trimethilammonium bromide (CTAB) biochemical grade, both available from VWR International, were used as the anionic and cationic surfactant, respectively, for the preparation of the surfactant solution. NaCl (VWR International) was used as the reference electrolyte. All the solution of surfactants and electrolyte were unbuffered.

All the glassware used during the experiment were washed with chromo sulphuric acid, rinsed with de ionised water and dried in the oven.

5.4 The measurement of surface/interfacial tension and contact angles

Measurements of the surface/interfacial tension and contact angles were carried out using a Kruss K12 processor tensiometer, which employs the Du Nouy-ring and the Wilhelmy-plate methods.

The Wilhelmy-plate method (see Figure 5-28) consists of measuring the adhesion force between a liquid and a plate of known dimensions. The liquid adheres to the plate by forming a lamella and the force exerted on the plate is:

$$F = p\,\gamma \cos\theta \qquad (5.4)$$

where F is the force exerted by the lamella on the plate, p is the wet perimeter of the plate, γ the liquid-vapour surface tension of the liquid and θ the contact angle between the plate and the liquid.

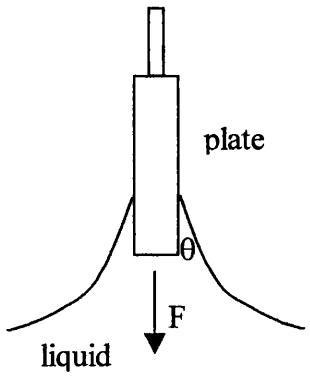

Figure 5-28 Wilhelmy-plate method for surface tension measurement.

By means of equation (5.4), it is possible to calculate the surface tension of a liquid when both the contact angle and the wet perimeter are known. A platinum plate is

commonly used for the Wilhelmy method because the resulting contact angle with all liquids is zero, due to the high surface energy of the platinum plate with respect to that of the liquids.

Once the surface tension of the liquid is known, if the platinum plate is substituted with a sample plate of constant wetting perimeter, (5.4) can be used to calculate the contact angle of the tested liquid toward the sample.

The Du Nouy-ring method, illustrated in Figure 5-30, is substantially similar to the Whilelmy technique, although the measurement element is a platinum ring. The axis of the ring is aligned with the direction of the force measured, which can be written as per equation (5.5):

$$F = \frac{2\pi\gamma Q}{\beta_c} \qquad (5.5)$$

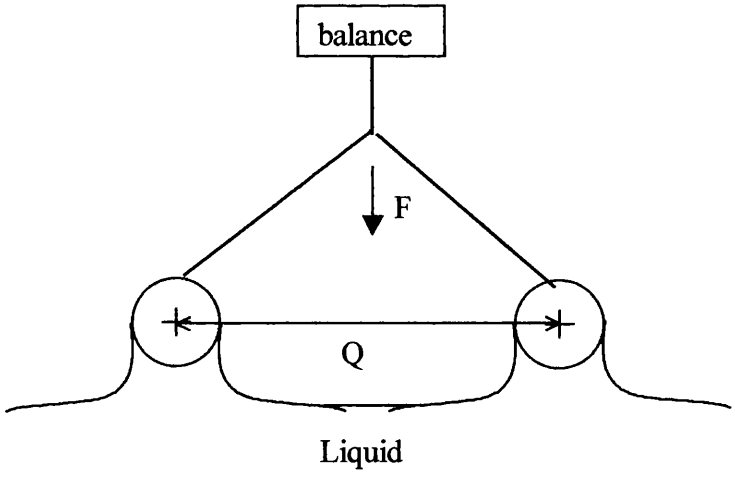

Figure 5-29 Schematic of the Du Nouy-ring method.

where Q is the mean diameter of the ring and β_c is a correction factor that accounts for the complex shape of the liquid lamella around the ring and depends on the geometric parameter of the ring and on the weight of the volume lifted by the ring.

The same techniques can also be applied when the interfacial tension between two immiscible liquid phases has to be calculated, although a measure of the surface tension of the lighter phase must be previously carried out.

5.4.1 The Kruss K12 processor tensiometer and the measuring techniques

The surface tension apparatus (Kruss K12) consists of a measuring unit and a processor unit, which is connected via a serial port to a computer to log data from a dedicated software. A schematic of the measuring unit is shown in Figure 5-30.

The platinum ring and plate are used only for surface/interfacial tensions data. In all the measurements conducted as part of this project they were handled by their shafts to both reduce the chances of damage and to minimise contamination of the measuring surfaces. They were also cleaned after every measurement depending on the type of liquid used for the measurement. After measurement of an aqueous solution the cleaning procedure was as follows; rinsing with warm tap water, rinsing with distilled water, annealing to red hot with a gas torch (RS Components Ltd.) before any subsequent measurements. After measurement of an organic solution the cleaning procedure was as follows; rinsing with a suitable organic solvent, rinsing with acetone, rinsing with distilled water, annealing to red hot with a gas torch. In both cases the ring or plate was allowed to cool to room temperature before carrying out any subsequent measurements. The annealing stage is important to remove any residues (especially organic), which remain after the rinsing procedure. However, care must be taken not to allow the ring or plate to become white hot as this could damage them.

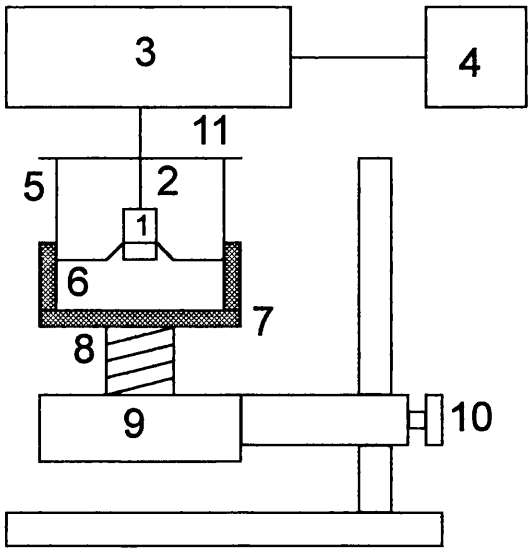

Figure 5-30 Schematic of measuring unit of the Kruss K12 processor tensiometer.

Key for Figure 5-30

(1) Platinum plate - 19.9 mm wide and 0.1 mm thick
(2) Thin rod
(3) Electrobalance (measuring unit)
(4) Processor unit
(5) Beaker
(6) Liquid
(7) Movable platform and thermostatic bath
(8) Screw to allow movement of platform
(9) Motor
(10) Clamp (for coarse adjustment) and support
(11) Lid to minimise evaporation

In order to perform the surface tension measurement the sample liquid was initially poured into the cleaned beaker and placed inside the thermostat vessel. The ring or plate was then inserted into the electrobalance (at this stage the electrobalance was locked). Next, the lock on the electrobalance was loosened and the Plexiglas doors of the tensiometer closed. The tensiometer processor was now loaded. Next, the vessel was moved up until the ring or plate was just above the liquid surface. The processor unit provides the menu for the measurement being started.

In order to determine the interfacial tension between immiscible phases (by means of the plate method) the measurement is carried out in two steps whilst the processor guides the operator through the sequence of operation. Initially the plate is immersed completely in the light phase and the processor unit acquires this first data. At this point, as requested by the processor unit, the light phase must be removed, the platinum plate cleaned and the heavy phase (contained in a second beaker) put in position under the electrobalance. The measuring plate is then positioned above the heavy phase and the measurement starts again. The system starts to dip the plate into the heavy phase and the system stops as soon the latter is detected. At this point the processor unit asks for the plate to be covered with fresh light phase and eventually the measurement of the interfacial tension is carried out.

The measurement of the contact angle on a solid substrate is carried out with the Wilhelmy technique by using a plate made of the material to be investigated. When the surface tension of the liquid is unknown, the contact angle measurement must be preceded by a surface tension measurement using a platinum plate. The testing plate is held in position over the liquid by a clamp whose shaft is fixed to the electrobalance. The beaker containing the liquid to be tested is moved upward using the coarse adjustment until the bottom edge of the sample is a few millimetres above the surface of the liquid. At this point the processor unit and the Kruss tensiometer software is switched on and the measurement is started after selecting the contact angle measurements from the main menu of the software. The tensiometer is driven by the Kruss software to measure advancing and receding contact angles. The software supplied by Kruss allows choice of certain parameters, such as the dimension of the plate used, the surface tension of the liquid and the speed and depth of immersion to be selected.

In Appendix A surface tension, interfacial tension and contact angle measurements taken for the liquids and the solid substrates relevant to the work presented in this thesis are presented.

Chapter 6

6 Results and discussion

The study of liquid bridges formed between particles of either similar or dissimilar surface properties is an important subject affecting agglomeration processes, performed either in the gaseous or in the liquid medium. When different particles are formulated together, which is not unusual during the production of pharmaceutical and agricultural products, surface energy differences can cause preferential agglomeration of some species to occur due to the fact that some particles are selectively wetted at the expense of others [61]. An opposite scenario holds for the selective recovery of particles dispersed in a liquid medium through the addition of an immiscible liquid binder. In this situation it is desirable to enhance the surface discrepancies between the dispersed particles so as the binder can wet preferentially the species to be recovered.

The theoretical and experimental study of force and liquid bridge geometry has always been carried out between pairs of similar and highly wettable particles whilst the situation where the particles have different surface energy has generally been neglected. Particle wettability affects directly the geometry of a liquid bridge and consequences are also reflected in other properties, such as the force of adhesion, the rupture energy and the post rupture liquid distribution. The experimental evidence of these phenomena will be detailed in sections 6.1.2 and 6.2 and the key role of the particle wettability will be recognised regardless of the suspending bulk medium. Section 6.1 analyses the possibilities of applying approximated models (the toroidal model and a new parabolic model) to describe the liquid bridge geometry in relation to the particle wettabilities and to derive a predictive method to determine the post-rupture liquid distribution avoiding the difficulties of solving the Young Laplace equation (3.2). The post-rupture liquid distribution is an important parameter, either in computer simulations where liquid bridges break and reform or for modelling the distribution of liquid in wet granulation processes. It will be shown in the following sections that after liquid bridges break a smaller amount of volume is left on poorly wet particles with respect to that remaining

on more wettable particles, whilst between two similar and well wet particles the binder approximately redistributes according to the volume of the particles.

The more rigorous description of the liquid bridge geometry according to the solution of the Young Laplace equation will be addressed in section 6.2 for the case of glass ballotini of either good or low wettability held by a silicone oil liquid bridge and submerged in water. In section 6.2 it will also be shown that the liquid bridge adhesion is stronger when liquid bridges are formed between particles of good wettability rather than between particles of dissimilar (good/poor) wettabilities. Data of the liquid bridge force and rupture energy for different cases of particle wettabilities will be presented and compared with those predicted from the theory. Higher liquid bridge forces are in general beneficial to particle agglomeration because of their contribution in limiting crack extensions within the agglomerate and therefore reducing the probability of agglomerate breakage. Despite the fact that the experimental evidence of the relationship between particle wettability and the strength of the liquid bridge has been given here only for the case of liquid bridges formed in a liquid medium, the results are independent of the bulk medium, being only related to the particle wettabilities.

On a theoretical basis, in fact, the presence of a suspending liquid phase adds no intrinsic complexity to the physical behaviour of a liquid bridge whilst the possibility of surfactants and electrolytes being present in the bulk can largely modify the nature of the interaction between the particles and the liquid binder and therefore can enhance or inhibit the particle agglomeration. These modifications depend on the nature and concentration of the surfactant, on the pH strength of the solution and on the presence of electrolytes that can increase the surfactant adsorption (see section 4.4.3). The investigation of the strength of silicone oil liquid bridges holding pairs of glass particles has also been examined in aqueous solutions of surfactants and/or electrolytes and will be discussed in section 6.3.

In a different set of experiments carried out at the University of Maine, an atomic force microscope has been used to investigate the DLVO interaction between glass particles and silicone oil droplets suspended in aqueous solutions of surfactant and/or

electrolytes.. The work with the AFM, presented in section 6.3.2, focuses on the interaction between glass and oil before any liquid bridge is formed. The aim of the work was to repeat some of the experiments carried out by Hartley et al. [112] in terms of verification of the water-oil interface deformability under the effects of DLVO forces and to gain an understanding on how the solution conditions influence the interaction between the particle and the binder. Due to the difficulties experienced with the AFM only the second task was achieved.

6.1 Particle wettability in relation to the geometry of a liquid bridge: approximated liquid bridge profiles

In order to describe the geometry of a liquid bridge formed between particles of similar or dissimilar surface energies a new model has been developed using a segment of parabola to approximate the liquid bridge profile. The model has also been compared with the toroidal approximation (see section 3.1.4), but only for the case of similar surface energy particles, as the result of a joint work [59] with the Department of Chemical Engineering of the University of Newcastle (Australia), which provided the calculations for the toroidal method.

Experiments have been carried out using clean glass ballotini in the size range 40 to 130 μm radius. Glycerol liquid bridges were used to hold pairs of ballotini, either silanised or kept in their natural state (see section 5.3 for details of silanisation and cleaning procedures) and the resulting geometry investigated during the liquid bridge separation and rupture. The viscosity and the surface tension of the glycerol were measured as 1630 mPa s and 63 mN/m, respectively, at 20°C. The micro-manipulation technique described in detail in section 5.1, was used to observe the liquid bridge formation and rupture behaviour between spherical particles and to measure directly the liquid bridge geometry. A glycerol droplet was fed onto the surface of one of the particles using a feeding micropipette, which was then withdrawn. The two particles were then brought into contact to form a liquid bridge and then axially separated with a speed of ~1μm/s, continuously. The separation process was recorded with a camera and stills from the video were taken and printed to carry out further image analysis.

The different binder-to-particle interactions allow comparison to be made between the diverse geometries assumed by liquid bridges during particle separation. Glycerol, in fact, exhibits good wettability towards untreated glass and a moderate wettability with respect to silanised glass. During separation, the liquid binder can easily recede from particles exhibiting lower surface energies (poor wettability), which, as separation distance is increased, turns the profile of the liquid bridge from a nodoid geometry to one that is unduloid. This is the case for a liquid bridge formed between an untreated and a silanised glass ballotini (see Figure 6-2). On the contrary, between two untreated glass particles a nodoid geometry is observed throughout separation, which results from a pinning of the 3-phase contact line, leading to a reduction of the contact angle (large hysteresis) whilst the solid-liquid interface is almost constant, as illustrated in Figure 6-1.

The implications such different geometries have on the adhesive force and rupture energy of the liquid bridge will be detailed in section 6.2. Here, the parabolic and toroidal models are presented and then used for predicting the evolution of a liquid bridge from contact through to rupture. In the following derivation of bridge geometry the particles are assumed to be rigid spheres.

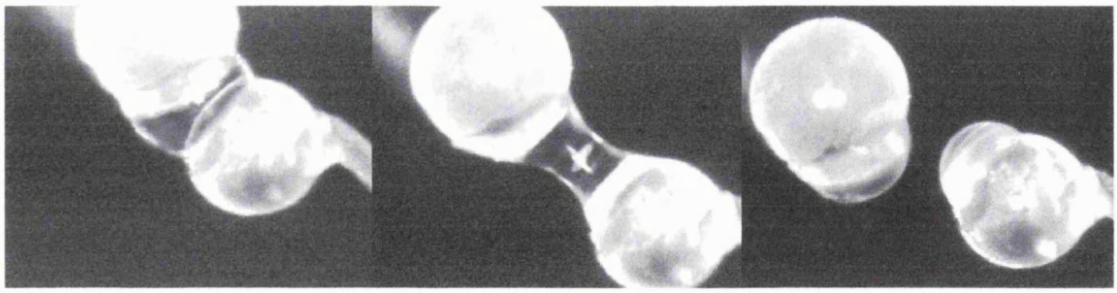

Figure 6-1 Evolution and rupture of a pendular glycerol bridge displaying fixed solid-liquid interfaces. Glass spheres of 125 and 111 microns radii from left to right (exp. A1, see Table 7).

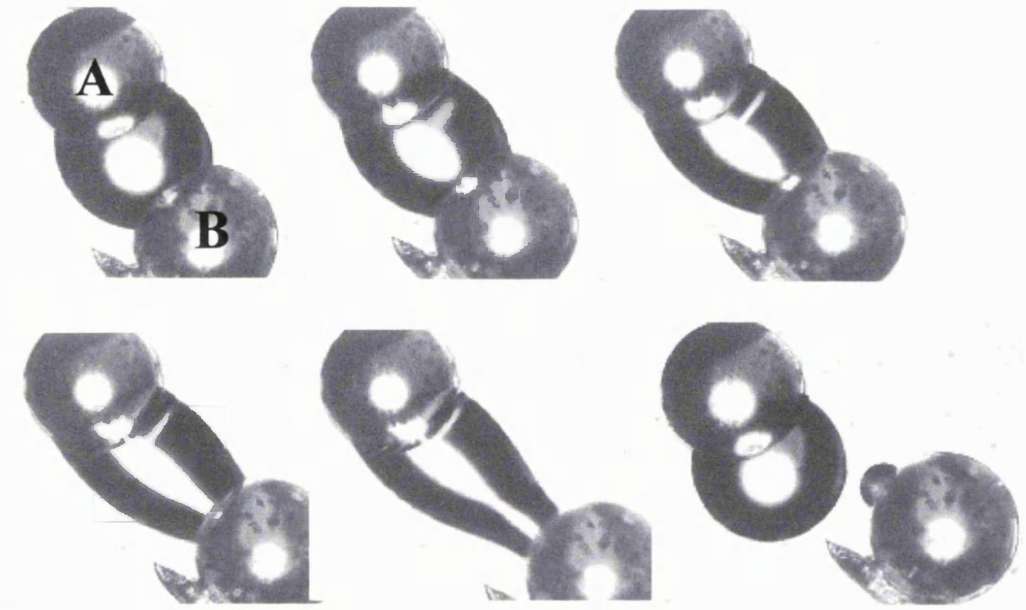

Figure 6-2 Evolution of the shape of a glycerol bridge between two glass spheres with increasing separation distance. The particle A is untreated whereas the particle B is silanised. Glass spheres of 119 and 123 microns radii from left to right (exp. A8, see Table 7).

6.1.1 The toroidal and parabolic models

The toroidal approximation can be split in two categories, whether the meniscus of the liquid bridge assumes a convex or a concave profile. This is not the case for the parabolic approximation, where a single equation can be used to describe both curvatures. Usually in the literature the meniscus is considered to be concave [45, 47, 53] whilst in real cases, according to the volume administered and the binder-to-particle wettability, a convex profile can result.

i) The concave toroidal model

A schematic of the toroidal approximation for a concave geometry is shown in Figure 6-3. The axes reference was chosen in order to simplify the expression of the liquid bridge profile. Two unequally sized spheres of radius R_A and R_B are separated by a distance *a*. The liquid bridge has a constant radius of curvature r_2 in the plane of the page and r_1 (evaluated at the narrowest point of the meniscus) in a plane perpendicular to the page. The x-axis is the axis of symmetry and the origin is taken as the point where the bridge is at its narrowest. The liquid bridge contacts each sphere at the ordinates y_A

and y_B, with a half filling angle of β_A and β_B, respectively, and forms the contact angles θ_A and θ_B on each sphere.

Equating the vertical (y) components of the bridge geometry gives (6.1) and (6.2):

$$R_A \sin\beta_A + r_2 \sin(\theta_A + \beta_A) = r_1 + r_2 \tag{6.1}$$

$$R_B \sin\beta_B + r_2 \sin(\theta_B + \beta_B) = r_1 + r_2 \tag{6.2}$$

Likewise, equating the horizontal (x) components gives (6.3):

$$a = a_1 + a_2 = R_A(\cos\beta_A - 1) + r_2 \cos(\theta_A + \beta_A) + R_B(\cos\beta_B - 1) + r_2 \cos(\theta_B + \beta_B) \tag{6.3}$$

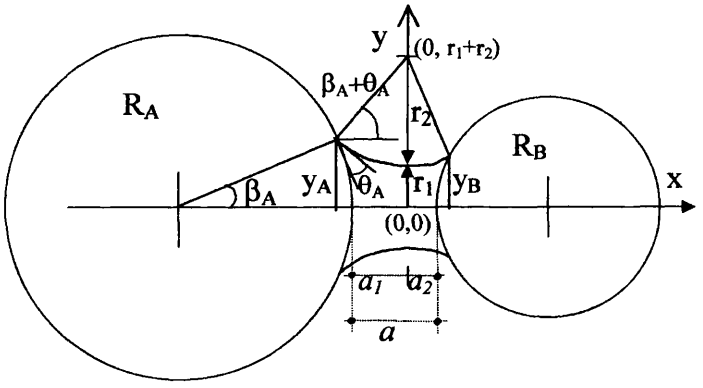

Figure 6-3 Schematic of the toroidal approximation for a concave profile.

The equation for the upper toroidal bridge profile is given by (6.4) for a concave bridge, which occurs when $(\beta_A + \beta_B + \theta_A + \theta_B) < 2\pi$,

$$x^2 + (y - r_1 - r_2)^2 = r_2^2 \tag{6.4}$$

which can be rearranged to give (6.5):

$$y(x) = r_1 + r_2 - \sqrt{r_2^2 - x^2} \tag{6.5}$$

The volume of revolution of the meniscus, $V_{m,A}$, from the point $x = -r_2 \cos(\beta_A + \theta_A)$ (contact with particle A), to the point at which $x = 0$, is given by (6.6):

$$V_{m,A} = \pi \int_{-r_2\cos(\beta_A+\theta_A)}^{0} y^2 \, dx \tag{6.6}$$

By replacing (6.5) in (6.6), equation (6.7) is obtained:

$$V_{m,A} = \pi \int_{-r_2\cos(\beta_A+\theta_A)}^{0} (2r_2^2 + 2r_1r_2 + r_1^2 - x^2 - 2(r_1 + r_2)\sqrt{r_2^2 - x^2}) \, dx \tag{6.7}$$

Integration of (6.7) leads to (6.8):

$$V_{m,A} = \pi \left[(2r_2^2 + 2r_1r_2 + r_1^2)x - \frac{x^3}{3} - (r_1 + r_2)\, x \sqrt{r_2^2 - x^2} - r_2^2(r_1 + r_2) \arcsin\frac{x}{r_2} \right]_{-r_2\cos(\beta_A+\theta_A)}^{0} \tag{6.8}$$

and when the integration limits are substituted, equation (6.9) follows:

$$\frac{V_{m,A}}{\pi r_2^3} = \cos(\theta_A + \beta_A)\left(2 + 2\frac{r_1}{r_2} + \left(\frac{r_1}{r_2}\right)^2 \right) - \frac{\cos^3(\theta_A + \beta_A)}{3}$$

$$-\left(1 - \frac{r_1}{r_2}\right)\left(\cos(\theta_A + \beta_A)\sin(\theta_A + \beta_A) + \frac{\pi}{2} + \theta_A + \beta_A \right) \tag{6.9}$$

A similar expression (6.10) exists for the volume of revolution $V_{m,B}$, obtained from integration of (6.7) from $x = 0$ to $x = r_2 \cos(\beta_B + \theta_B)$, where the profile contacts particle B:

$$\frac{V_{m,B}}{\pi r_2^3} = \cos(\theta_B + \beta_B)\left(2 + 2\frac{r_1}{r_2} + \left(\frac{r_1}{r_2}\right)^2\right) - \frac{\cos^3(\theta_B + \beta_B)}{3}$$

$$-\left(1 - \frac{r_1}{r_2}\right)\left(\cos(\theta_B + \beta_B)\sin(\theta_B + \beta_B) + \frac{\pi}{2} + \theta_B + \beta_B\right) \qquad (6.10)$$

In order to find the exact value of the volume of liquid in the bridge, the volumes of the spherical caps enclosed at each end of the profile need to be subtracted. For the two spheres A and B, characterized by index i, this expression is given by (6.11):

$$V_{cap,i} = \frac{\pi R_i^3}{3}\left(2 - 3\cos\beta_i + \cos^3\beta_i\right) \qquad (6.11)$$

The volume of the bridge is eventually calculated as per (6.12):

$$V_{br} = \sum_{i=A,B}\left(V_{m,i} - V_{cap,i}\right) \qquad (6.12)$$

Equations (6.11) and (6.12) are also valid for the convex model. The area A_{br} of the meniscus interface can be calculated by (6.13):

$$A_{br} = 2\pi\int_{r_2\cos(\beta_A+\theta_A)}^{+r_2\cos(\beta_B+\theta_B)} y(x)\sqrt{1+y'^2(x)}\cdot dx \qquad (6.13)$$

which, after the integration limits are imposed, becomes:

$$A_{br} = \left(1 + \frac{r_1}{r_2}\right)\left(\pi - \theta_A - \beta_A - \theta_B - \beta_B - \cos(\theta_A + \beta_A) - \cos(\theta_B + \beta_B)\right) \qquad (6.14)$$

ii) The convex toroidal model

A convex shape forms when the two spheres are close together and/or when the liquid forms a relatively large contact angle with the two particles, as indicated in Figure 6-4.

The liquid bridge profile is approximated by two arcs of circumference for which r_2 and r_1 represent the radii of curvature in the plane of the page and in a plane perpendicular to it, respectively. In general the centre of the circumference of radius r_2 is not lying on the x-axis. The geometrical condition for the concave shape to occur is $(\beta_A + \beta_B + \theta_A + \theta_B) > 2\pi$ and

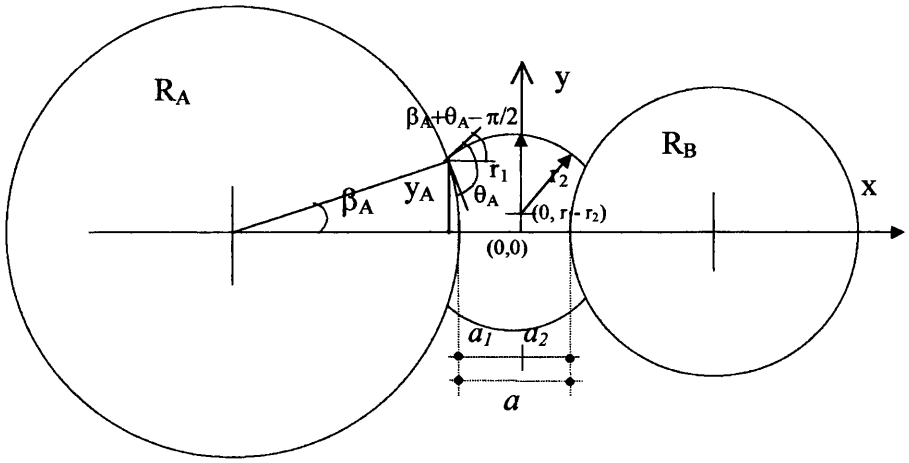

Figure 6-4 Schematic of the toroidal approximation for a convex profile.

The expressions of the volumes and area of revolution can be worked out in the same way as for the concave case by using the expression of the convex profile given in (6.15):

$$y(x) = r_1 - r_2 + \sqrt{r_2^2 - x^2} \qquad (6.15)$$

Similarly to the concave case, the volume of revolution, $V_{m,A}$, is evaluated by integrating (6.6) from the point $x = -r_2 \cos(\beta_A + \theta_A)$ (contact with particle A), to the point at which $x = 0$. When (6.15) is substituted into (6.6), (6.16) results:

$$V_{m,A} = \pi \int_{-r_2\cos(\beta_A+\theta_A)}^{0} (2r_2^2 + 2r_1r_2 + r_1^2 - x^2 + 2(r_1 + r_2)\sqrt{r_2^2 - x^2})\,dx \qquad (6.16)$$

The integration of (6.16) is given in (6.17):

$$V_{m,A} = \pi\left[(2r_2^2 + 2r_1r_2 + r_1^2)x - \frac{x^3}{3} + (r_1 + r_2)\,x\sqrt{r_2^2 - x^2} + r_2^2(r_1 + r_2)\arcsin\frac{x}{r_2}\right]_{-r_2\cos(\beta_A+\theta_A)}^{0}$$

(6.17)

and when the integration limits are substituted, equation (6.18) follows:

$$\frac{V_{m,A}}{\pi r_2^3} = \cos(\theta_A + \beta_A)\left(2 + 2\frac{r_1}{r_2} + \left(\frac{r_1}{r_2}\right)^2\right) - \frac{\cos^3(\theta_A + \beta_A)}{3} - \left(\frac{r_1}{r_2} - 1\right)\left(\cos(\theta_A + \beta_A)\sin(\theta_A + \beta_A) + \frac{\pi}{2} + \beta_A - \theta_A\right) \tag{6.18}$$

A similar expression (6.19) exists for the volume of revolution $V_{m,B}$, obtained from integration of (6.7) from x = 0 to $x = r_2\cos(\beta_B + \theta_B)$, where the profile contacts particle B:

$$\frac{V_{m,B}}{\pi r_2^3} = \cos(\theta_B + \beta_B)\left(2 + 2\frac{r_1}{r_2} + \left(\frac{r_1}{r_2}\right)^2\right) - \frac{\cos^3(\theta_B + \beta_B)}{3} - \left(\frac{r_1}{r_2} - 1\right)\left(\cos(\theta_B + \beta_A)\sin(\theta_B + \beta_B) + \frac{\pi}{2} + \beta_B - \theta_B\right) \tag{6.19}$$

The area A_{br} of the meniscus interface can be calculated from (6.13) by using (6.15) and after the integration limits are imposed (6.20) results:

$$A_{br} = \left(\frac{r_1}{r_2} - 1\right)\left(\theta_A + \beta_A + \theta_B + \beta_B - \pi - \cos(\theta_A + \beta_A) - \cos(\theta_B + \beta_B)\right) \tag{6.20}$$

iii) The parabolic model

Figure 6-5 is the schematic of the parabolic bridge profile approximation. The solid-liquid interface is a spherical cap, which has a maximum height of h_i, L is the length of the liquid bridge and y_{min} is the minimum liquid neck radius of the pendular bridge. The

x-axis is the symmetry axis of the system and the origin is set at the intersection between the x-axis and the half-cord y_A. The liquid to solid contact points are A and B on the two spheres, with co-ordinates of (0, y_A) and (L, y_B), respectively.

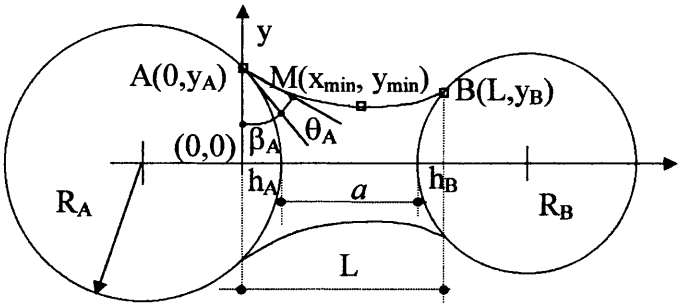

Figure 6-5 Schematic of the parabolic approximation.

The heights of the spherical caps on the particles, h_i, are related to y_i (i = A,B) by (6.21):

$$y_i = \sqrt{R_i^2 - \left(R_i - h_i\right)^2} \tag{6.21}$$

y(x), the function of the upper half of the liquid bridge profile, is approximated by a second order polynomial equation in the form of (6.22):

$$y(x) = \alpha_2 x^2 + \alpha_1 x + \alpha_0 \tag{6.22}$$

in which the values of the three unknown parameters α_2, α_1, α_0, come from the solution of the system given by equation (6.23), the symbols being defined as above:

$$\begin{cases} y(0) = \alpha_o = y_A \\ V_m = \pi \int_0^L y^2(x) \cdot dx = V_{br} + V_{cap,A} + V_{cap,B} \\ y(L) = \alpha_2 L^2 + \alpha_1 L + \alpha_o = y_B \end{cases} \tag{6.23}$$

The area of the liquid bridge, A_{br}, is calculated using (6.24), which leads to (6.25) once equation (6.22) is replaced and integrated between the integration limits:

$$A_{br} = 2\pi \int_0^L y(x)\sqrt{1+y'^2(x)}\cdot dx \tag{6.24}$$

$$\begin{aligned} A_{br} = &-\frac{\pi\left(\alpha_1(1+16\alpha_2\alpha_0-2\alpha_1^2)\sqrt{1+\alpha_1^2}+(-1+16\alpha_2\alpha_0-4\alpha_1^2)\operatorname{arcsin h}(\alpha_1)\right)}{32\alpha^2} \\ &+\frac{\pi\left((2L\alpha_2+\alpha_1)(1+8L^2\alpha_2+16\alpha_2\alpha_0+8L\alpha_2\alpha_1-2\alpha_1^2)\sqrt{1+(2L\alpha_2+\alpha_1)^2}\right)}{32\alpha_2^2} \\ &+\frac{\pi\left((-1+16\alpha_2\alpha_0-4\alpha_1^2)\operatorname{arcsin h}(2L\alpha_2+\alpha_1)\right)}{32\alpha_2^2} \end{aligned} \tag{6.25}$$

In order to approximate the liquid bridge profile using either the toroidal or the parabolic model some geometric quantities must be given or calculated through image analysis from the sequence of liquid bridge separations (see for example Figure 6-1). These quantities are the particle radii $R_{A,B}$, the half filling angles $\beta_{A,B}$, the separation distance a and the volume of the bridge V_{br}.

The application of the toroidal method for both the convex and the concave profile requires the determination of the contact angles θ_A, θ_B and the profile radii of curvature r_1, r_2. These parameters can be calculated iteratively on an Excel® spreadsheet through the solution of equations (6.1)–(6.3) and (6.12). Depending on the volume of the liquid bridge a transition from a convex profile to one that is concave can occur during liquid bridge separation (see Figure 6-1). The toroidal approximation, therefore, involves two different sets of equations to be solved for the same sequence of separation. When the liquid bridge profile changes its configuration from a convex to a concave curvature, it will assume a cylindrical configuration, which cannot be solved by the toroidal model since $r_1 \rightarrow \infty$.

The parabolic approximation is defined by the three parameters α_2, α_1 and α_0, which can be calculated by solving the system (6.23) . It is useful to note that by varying α_2, α_1 and α_0, the single equation (6.22) can be used to approximate both convex and concave menisci. Hence, the parabolic approximation results in a mathematically simpler and much more robust expression than that of the toroid.

Since the circumference and the parabola are not the solution of the Young Laplace equation they do not comply with the constraint on the total mean curvature being constant along the profile of the liquid bridge. However, calculated values of the principal geometric parameters (contact angle, rupture distance) show a fairly close agreement with the experimental data obtained for the experiments, as will be shown in the next section. The curvature of the profile has a role in the evaluation of the liquid capillary pressure and ultimately on the force exerted by the liquid bridge. Mazzone et al. [46] parameterised the dimensionless force versus the normalised bridge volume on the separation distance and compared the toroidal approximation with the numerical solution of the Young-Laplace equation (3.2). They showed that when the particles are nearly in contact only a slight discrepancy is noticed between the two methods throughout the volume range. However, as the separation distance reaches just 10% of the particle radius, the toroidal method significantly underestimates the force as obtained from the numerical solution. The present remark only applies to situations where the force is required to be measured (see 6.2) and not to the results presented in this section where only the geometric quantities are evaluated.

6.1.2 Evolution and rupture of liquid bridges according to the parabolic and toroidal models

Models [47] intended to describe the process of liquid bridge separation always assume the contact angle between the particle and the binder to be fixed and equal to zero throughout separation [45]. However, this assumption is reasonable only for perfectly wettable particles and therefore is not a general case. Predicting the behaviour of real cases is not an easy problem due to the difficulty of modelling the phenomena at the 3-phase contact line. As has been shown in Figures 6–1 and 6–2, the interface can either be pinned or recede depending on whether the wettability between the particle and the liquid binder is good or poor, respectively. This situation can be explained in terms of the contact angle hysteresis. The pinning of a solid-liquid interface can continue until the contact angle between the binder and the particle reaches the receding values. At this point, since no further reduction of the contact angle appears feasible, the solid-

liquid interface reduces. When the difference between the advancing and receding contact angle is large, the 3-phase contact line is pinned and a reduction of the solid-liquid interface is not likely to happen, unless the receding contact angle is reached. The two cases of liquid bridges formed between particles with either good or poor wettability will be discussed separately to better highlight their peculiarities.

i) Liquid bridges formed between particles with good wettability

Some useful simplifications can be made in order to use the parabolic and the toroidal methods to model the configurations assumed by liquid bridges during separation of pairs of particles both exhibiting good wettability toward the binder, as shown in Figure 6-6 where a glycerol liquid bridge is formed between untreated glass particles and the last recorded frames before bridge rupture are the post rupture liquid distribution is shown.

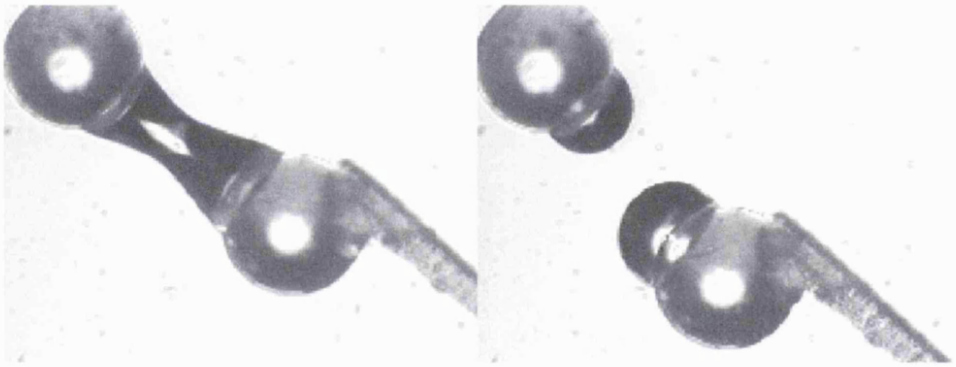

Figure 6-6 Last recorded liquid bridge configuration and post-rupture liquid distribution for the separation of a glycerol liquid bridge (V_{br} = 1383 x 10^3 μm^3) formed between two untreated glass particles of radii R_A=92 μm (left) and R_B=91 (right) μm (exp. A5, see Table 7).

Despite the fact that small reductions of the solid-liquid interface might occur even for particles of good wettability, it can be assumed that these interfaces stay fixed during separation. This condition translates to the fact that the spherical cap heights on the particles, h_i, or equivalently the half-filling angle, β_i, (i=A, B) (Figure 6-3) remain constant during separation whilst the 3-phase contact line is pinned. When the geometry of the particles, the volume and the initial configuration of the bridge are given (or

calculated by image analysis), it is possible to calculate the liquid bridge profiles at different separation distances by solving the system (6.23) for the parabolic approximation or that formed by (6.1)–(6.3) and (6.12) for the toroidal method in which the appropriate equations for the convex and the concave profile must be chosen. The solution of these two systems leads to the determination of the unknown values in (6.22) for the parabolic model and in (6.5) and (6.15) for toroidal concave and convex shapes, respectively. In order to assess the validity of the approximations made (e.g. type of profile and fixed interface) the theoretical profile can be compared with that obtained from experimental observations in terms of the apparent contact angles measured at the liquid contact with particles A and B.

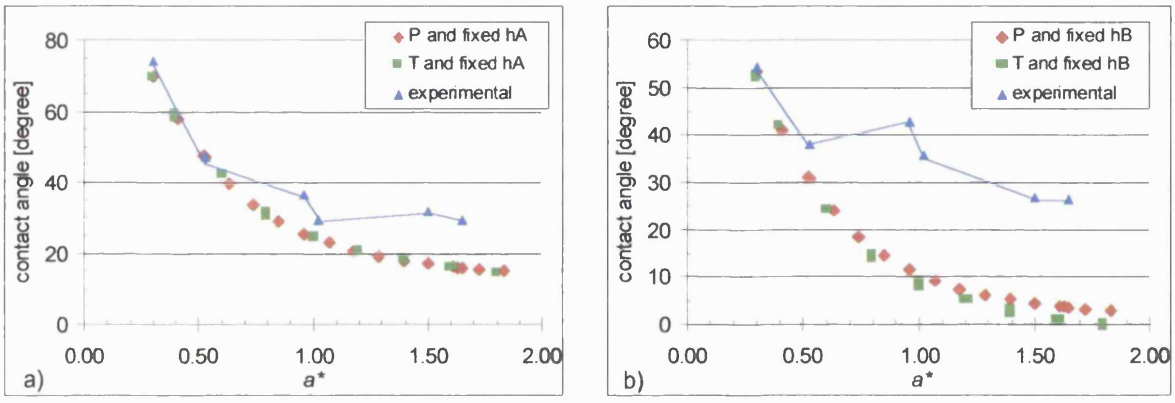

Figure 6-7 Experimental and calculated apparent contact angles for the experiment presented in Figure 6-6 (exp. A5, see Table 7). P refers to the parabolic and T to the toroidal model, both calculated with the approximation of fixed solid-liquid interfaces: a) refers to particle A and b) to particle B.

Figure 6-7 represents a typical situation of the contact angle values for a pair of untreated glass particles (good wettability) held by a glycerol liquid bridge, as shown in Figure 6-1 and Figure 6-6. Data are plotted against a^*, the separation distance normalised with respect to the geometric average radius ($\overline{R} = \frac{2 R_A R_B}{R_A + R_B}$).

The apparent contact angle can be calculated from the approximated liquid bridge profiles by means of (6.26) for spheres A and B, respectively, in which y'_A and y'_B represent the abscissa of the point of contact:

$$\theta_A = \frac{\pi}{2} + \tan^{-1}(y'_A) - \sin^{-1}\left(\frac{y_A}{R_A}\right)$$
$$\theta_B = \frac{\pi}{2} - \tan^{-1}(y'_B) - \sin^{-1}\left(\frac{y_B}{R_B}\right) \qquad (6.26)$$

The previous graphs clearly show that the approximation of keeping the solid-liquid interfaces fixed is not adequate for the untreated glass-glycerol system. The differences between the experimental results and the behaviour predicted by both the parabolic and toroidal models are to be attributed to small reductions of the solid-liquid interface with consequent rearrangement of the 3-phase contact line. From Figure 6-7 it can be seen that initially the contact angles drop quickly, which is well predicted by both profile approximations. However, after a normalised separation of approximately 0.5 for both sphere A (Figure 6-7a) and B (Figure 6-7b) the agreement between theory and experiment is lost. The predicted contact angles drop towards zero whereas the measured contact angles level off at a contact angle value of about 25°. This decrease and then levelling effect of contact angles was observed in all the experiments performed and it proves that the 3-phase contact line was initially pinned whilst the levelling effect shows that after a certain particle separation, the contact line begins to slip on the particle surfaces since the reduction of the solid-liquid area is more favourable than further pinning of the contact angle.

Figure 6-8 and Figure 6-9 show the variation of the height of the spherical cap versus the normalised separation distance between pairs of untreated glass ballotini (A and B) during the separation of glycerol liquid bridges. Except for a few experiments, the curves clearly show that the assumption of fixed solid-liquid interfaces is not respected in most cases. The values indicated at the right hand side of each curve represent the contact angle measured on the liquid bridge configuration observed before rupture. The experimental conditions of the experiments shown in Figure 6-8 are given in Table 7.

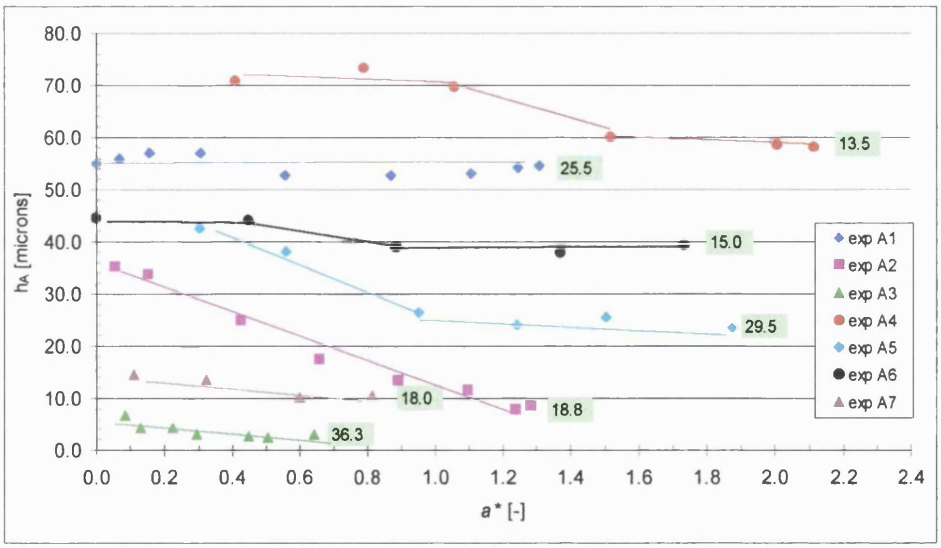

Figure 6-8 Height of spherical cap A versus non-dimensional liquid bridge separation for the experiments of a glycerol liquid bridge holding a pair of untreated glass particles. The values at the right hand side of each profile represent the angle measured on the liquid bridge configuration observed before rupture.

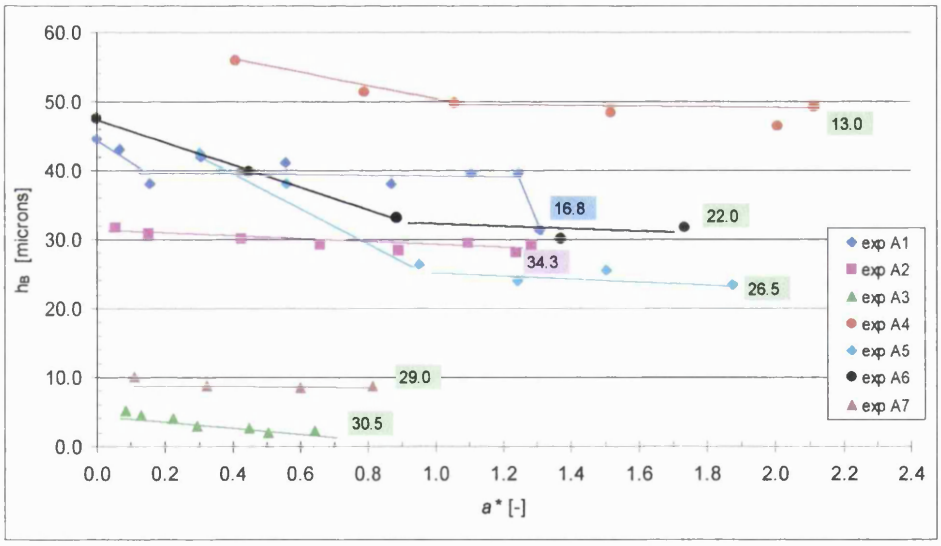

Figure 6-9 Height of spherical cap B versus non-dimensional liquid bridge separation for the experiments of a glycerol liquid bridge holding a pair of untreated glass particles. The values at the right hand side of each profile represent the angle measured on the liquid bridge configuration observed before rupture.

Exp.	R_A	R_B	$\theta_{A,\,initial}$	$\theta_{B,\,initial}$	$h_{A,\,initial}$	$h_{B,\,initial}$	V_{br}
	μm	μm	deg	deg	μm	μm	($\times 10^3$ μm^3)
A1	125	111	70	63	46	45	2175
A2	47	114	66	40	35	32	622
A3	49	44	31	38	6.7	5.1	10
A4	101	100	51	59	71	56	3720
A5	92	91	74	54	31	43	1383
A6	92	91	67	57	45	48	1322
A7	56	103	65	60	14	10	142

Table 7 Experimental conditions for the experiments between untreated glass particles presented in Figure 6-8.

In exp. A2 a large reduction of the solid-liquid interface is observed on particle A, which can be attributed to the difference in size between the two particles. However, this interface reduction can also be influenced by the volume of the binder as seems to be indicated by the results of exp. A7, where the interfaces stay fixed despite the fact thatthe two particles are quite different in size. In this latter experiment though the volume of the liquid bridge is smaller (142 x 10^3 μm^3) than in exp. A2 (622 x 10^3 μm^3). The evolution of the liquid bridge presented in exp. A2 will be further investigated in the next subsection where the reduction of the solid-liquid interface is intentionally promoted by reducing the wettability of one particle by means of silanisation. More contact angle data between an untreated glass slide and glycerol are presented in appendix A.3.

Despite the fact that the fixed interface assumption proved unsuccessful for predicting the contact angles of the liquid bridge, it showed good consistency when used to predict the distance at which rupture of the liquid meniscus occurs, as will be shown later in this section. The model could also be applied to binders that show a nearly 0° receding contact angle towards the particle in order to obtain approximated geometric data of the liquid bridge.

A second approach was then utilized to model the profile of glycerol liquid bridges, still using the toroidal and the parabolic approximation but measuring geometric parameters of the interface at any stage during separation. The new approach, results of which are presented in Figure 6-10 for the prediction of contact angle on both particles, illustrates that both the parabolic and the toroidal approximations are able to give good agreement with the experimental results. However, since the model requires the configuration of the solid-liquid interface in order to be applied, it cannot be considered to be predictive, but rather a model used to approximate a known liquid bridge configuration. The advantages of this latter approach lie in the possibility of calculating the liquid bridge force from an approximated profile (either toroidal or parabolic) without solving the Young Laplace equation (3.2).

The parabolic and the toroidal approximation, however, cannot be applied when the liquid bridge meniscus assumes an unduloid profile instead of a nodoid shape. In this situation, which occurs when the liquid bridge holds at least one poorly wettable particle (see Figure 6-2), both methods fail to accomplish the transition of the profile from concave to convex. Under such conditions the profile can be approximated either with a third order polynomial function or with the numerical solution of the Young Laplace equation (3.1), as will be shown later in this section and in section 6.2, respectively.

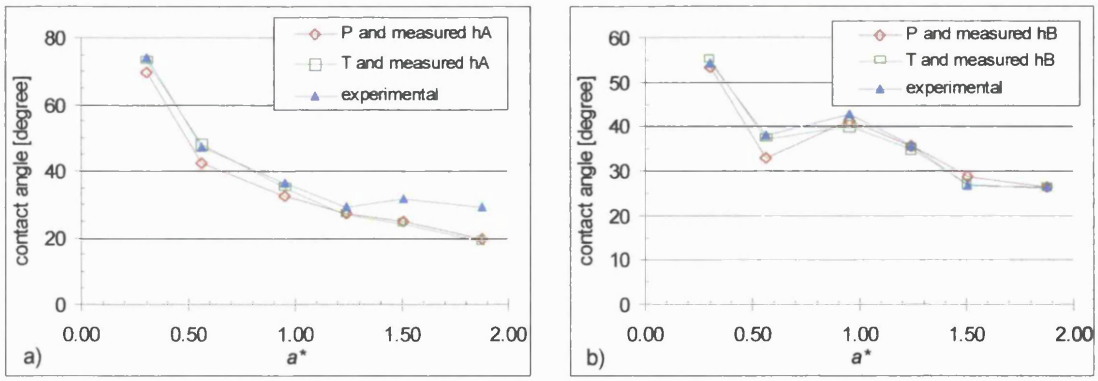

Figure 6-10 Experimental and calculated apparent contact angles for the experiment presented in Figure 6-6 (exp. A5, see Table 7). P refers to the parabolic and T to the toroidal model, both calculated with parameters of solid-liquid interfaces measured during separation: a) refers to particle A and b) to particle B.

Because of the complex phenomena that occur during the rupture of a liquid bridge, a thermodynamic approach incorporating the rupture energy of a liquid bridge (see sections 3.1.6 and 4.2.2) is difficult to apply, as will be shown in section 6.2. In addition to this, the application of the simple criterion proposed by Lian et al. [47] (see section 3.1.3) to evaluate the liquid bridge rupture distance can lead to ambiguous results when a large contact angle hysteresis exists during liquid bridge separation and a discretional judgment is required on deciding whether the advancing or the receding contact angle should to be used in (3.11). A geometric rupture criterion was therefore developed together with the parabolic approximation, which is based on the conservation of the liquid bridge area just before and after rupture. This approximate rupture model has also been tested with the toroidal approximation, which gave the same order of accuracy in the prediction of the bridge rupture distance, as shown in Figure 6-12, Figure 6-13 and Table 8.

The rupture criterion is iteratively applied by assuming a virtual rupture of the liquid bridge at each separation distance during the bridge elongation, which is supposed not to reduce the solid-liquid interfacial area. If we consider a liquid bridge rupture, the liquid binder tends to redistribute on the two particles by forming droplets which can be regarded as perfect caps of spheres (see Figure 6-11) due to the low amount of the liquid binder used during the experimental work ($<10^{-4}$ μm^3), (see the last frame in the sequence of Figure 6-1 and Figure 6-6). In order to quantify the amount of binder left on each particle, it has been assumed that, at each rupture, be it either virtual or real, the volume of the binder distributes between the two droplets in proportion to the amount on either side of the bridge at its thinnest point. For instance, if we consider a virtual rupture for the configuration shown in Figure 6-3, the volume of liquid left on sphere A, V_A, would be calculated according to (6.9) – (6.12).

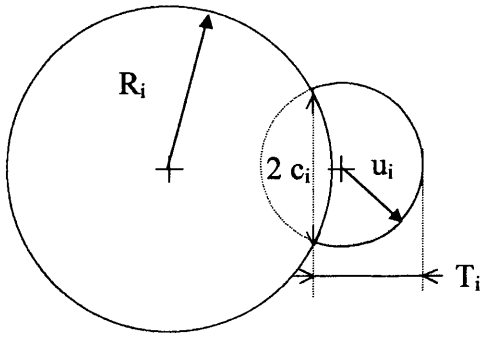

Figure 6-11 Liquid droplet after rupture on a spherical particle i.

Figure 6-11 illustrates the post-rupture droplet shape: u_i is the liquid droplet radius, T_i the liquid droplet cap maximum height and c_i the half cord length, which are all related from (6.27).

$$u_i = \frac{T_i^2 + c_i^2}{2T_i} \tag{6.27}$$

In the proximity of the effective rupture, the area of the liquid bridge A_{br} and the area of the droplets A_{drop} should be almost the same because the liquid bridge cannot absorb any more energy from the surroundings to be turned into new liquid bridge surface. The area rupture criterion assesses that rupture occurs when (6.28) is satisfied, where A_{drop} is calculated by (6.29).

$$A_{drop} - A_{br} = 0 \tag{6.28}$$

$$A_{drop} = \sum_{i=A,B} 2\pi u_i T_i \tag{6.29}$$

In Figure 6-12 the evolution of A_{drop} and A_{br} calculated using both approximations for exp. A4 is plotted versus normalised particle separation. The liquid vapour interfacial area the droplets would have if rupture occurred at a separation well before the observed rupture, is much superior to that of the liquid bridge, which indicates that the liquid bridge is perfectly stable. With elongation, the liquid bridge liquid-vapour interfacial area increases, whilst the droplets interfacial area levels off to a constant value.

Variations in A_{drop} with a^* occur when the solid-liquid interfaces vary and/or the position of the minimum liquid neck on the bridge profile changes. Nevertheless, even though the toroidal and the parabolic approximations have different mathematical expressions, their agreement is excellent in terms of predicted interfacial area, as seen in Figure 6-12.

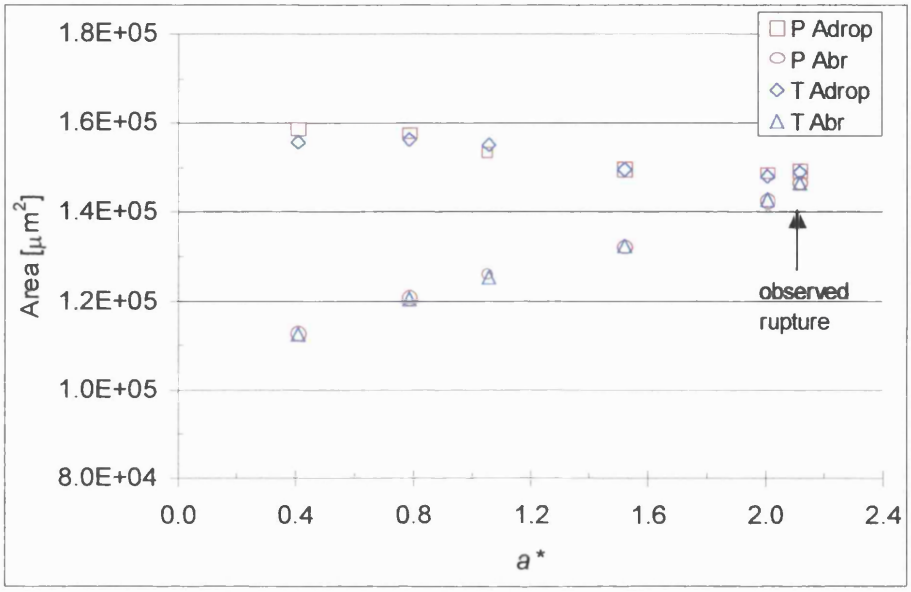

Figure 6-12 Evolution of A_{drop} and A_{br} versus a^* for exp. A4. Results obtained from the toroidal and parabolic models. The arrow indicates the observed rupture distance. P refers to the parabolic and T to the toroidal model, both calculated with the approximation of fixed solid-liquid interfaces.

In Figure 6-13, the normalised experimental rupture distance, as measured from the last liquid bridge configuration recorded on video before rupture occurred, is compared with the values predicted by both the toroidal and the parabolic models (both assuming a fixed interface approximations) and with those calculated from (3.11) using either the advancing or the receding contact angles obtainedfrom the experimental observations. Figure 6-13 indicates that the toroidal model appears to give a very good estimate of the rupture distance except for exp. A1, where no solution could be found for the later stages of separation, which can be attributed to the non perfect axis-symmetry of the liquid bridge, as shown in the sequence of Figure 6-1 relative to this experiment.

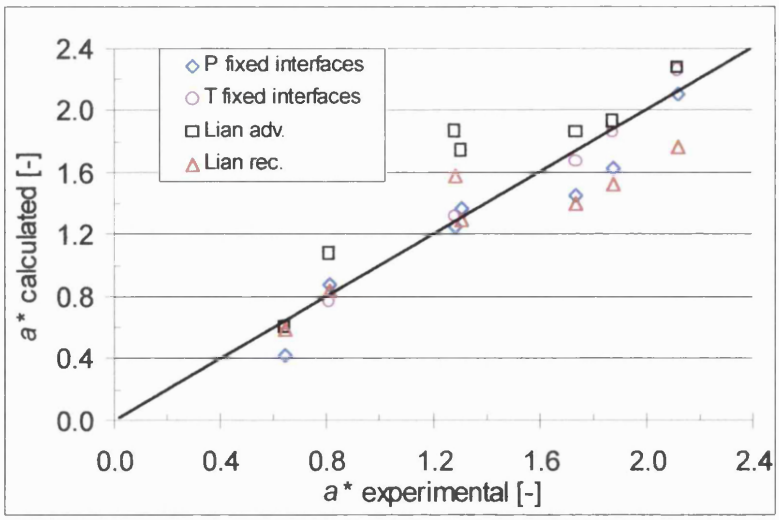

Figure 6-13 Calculated separation distance versus separation distance measured experimentally. The values are normalised with respect to the average geometric radius of the particles. Values presented on the ordinates are calculated according to four models: parabolic (P) and toroidal (T), both calculated with the approximation of fixed solid-liquid interfaces, and from the approach proposed by Lian et al. [47] (3.11) using either the advancing or the receding contact angles.

The parabolic method also offers a good approximation for the separation distance and might be preferred its greater simplicity. The comparison with the predicted rupture distances estimated by the Lian et al. approach seems to show that the use of the receding contact angle in (3.11) is to be preferred with smaller liquid bridge volumes, which leads to shorter separation distances.

In the experiments presented in Figure 6-13 the use of the receding contact angle in (3.11) seems favourable up to an experimental rupture distance, a^*, equal to 1.28, which corresponds to a liquid bridge volume of 622 x 10^3 μm^3. For larger volumes the use of the advancing contact angle leads to rupture distances closer to the value measured experimentally except for exp. A1, whose results could be affected by the non perfect symmetry of the liquid bridge. Table 8 presents the measured and estimated rupture distances using all four approximations.

Exp.	V_{br} x 10 μm^3	a^*(E) [–]	a^*(P) [–]	a^*(T) [–]	a^*(La) [–]	a^*(Lr) [–]
A1	2175	1.31	1.37	no solution	1.74	1.29
A2	622	1.28	1.34	1.32	1.87	1.58
A3	10	0.64	0.43	0.61	0.60	0.59
A4	3720	2.11	2.11	2.22	2.28	1.77
A5	1383	1.88	1.63	1.86	1.93	1.55
A6	1322	1.73	1.67	1.85	1.85	1.40
A7	142	0.81	0.88	0.77	1.08	0.84

Table 8 Normalised rupture distances for pendular liquid bridges: (E) experimental, (T) toroidal and parabolic (P) models calculated from (6.28) with the fixed interface approximation, (La) and (Lr) refer to the Lian approach (3.31) calculated with advancing or receding contact angle respectively.

ii) Liquid bridge formed between particles with good and poor wettabilities

The collaboration with the University of Newcastle (Australia) was limited only to the modelling of glycerol liquid bridges formed between good wettable particles (untreated glass). The study of liquid bridges formed between different wettability particles was an independent work carried out at UCL and is summarised in [60]. From the batch of ballotini used in the work described in the previous subsection a sample was soaked for 30 minutes in a silanising agent, Repelcote VS (2% solution of dimethyldichlorosilane in octamethylcyclotetrasiloxane) in order to modify the surface properties of the particles, according to procedures illustrated in section 5.3. The method of liquid bridge formation as well as the speed of separation (~1 μm/s) stays the same as described in the previous subsection.

The silanisation of the glass particle is intended to reduce the high wetting hysteresis shown by the glycerol on the untreated glass. For pendular liquid bridges, a large or small wetting hysteresis drastically changes the shape adopted by the liquid bridge, as can be seen in Figure 6-2. In this figure a glycerol bridge has been created between a non-silanised glass sphere (A) and a silanised glass sphere (B). With increasing

interparticle distance, the three-phase line is "pinned" on the non-silanised particle A, but reduces on particle B as the liquid recedes from the solid surface.

Table 9 summarises the conditions of the experiments reported in this subsection. It should be noted here that the reduction of one solid-liquid interfacial area occurs also between untreated particles, which show a stronger interaction with glycerol, as it has been observed in the previous subsection for exp. A2 and that was explained by the difference in size between the two particles. Exp. A2 will therefore be included in the analysis presented below due to the experimental conditions that induced dewetting on the solid-liquid interface of the smaller particle. In order to verify the applicability of the parabolic approximation to the case where one particle is silanised, the apparent contact angle of both particles as calculated from (6.26) is compared with the values measured experimentally. Because of the large interface reduction observed on the silanised particle, the parabolic model can only be applied using experimental values of the spherical cap heights, h_i, which are measured at any stage of separation.

Exp.	V_{br} x $10^3 \mu m^3$	R_A μm	R_B μm
A2	622	47	114
A8	6850	119	123*
A9	10500	134*	103

Table 9 Experimental conditions for experiments showing a large reduction of the solid liquid interface. Particles are untreated glass unless marked with *, which indicates that they are silanised.

The prediction of contact angles for exp. A8, which is shown in Figure 6-2, is very good except for the last recorded configuration before rupture, where the parabolic model fails to account for the change in curvature of the liquid bridge in the proximity of particle B. Figure 6-14 shows that the contact angle remains more or less constant on the dewetting particle B, whereas the angle made by glycerol on particle A reduces with increasing particle separation. Additional contact angle data, obtained by a tensiometer unit, between a silanised glass and glycerol are reported in Appendix A.3.

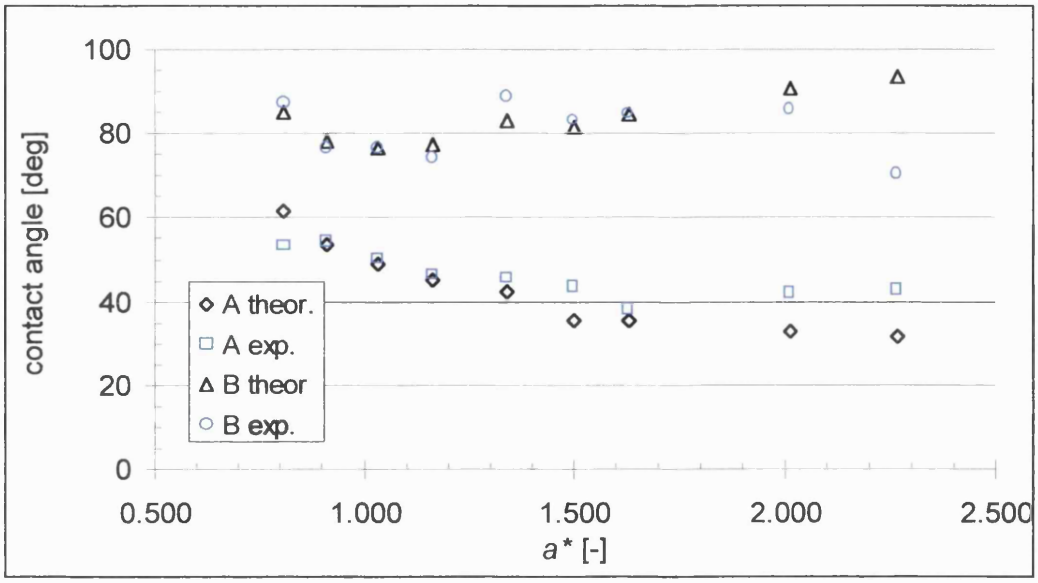

Figure 6-14 Evolution of measured and calculated contact angles versus normalised separation for the case of exp. A8 (see Table 7), which is shown in Figure 6-2. A and B refer to the two particles of which B is silanised.

Figure 6-15 shows the initial and the pre-rupture configurations of the separation sequence recorded from exp. A9. The experimental liquid bridge shape, y(x), plotted versus the bridge length, L, is presented and compared with the parabolic fitting.

The liquid bridge shape shows a clear reduction of the solid-liquid interface on the silanised particle (A), on which the origin of the liquid bridge length is taken. On the contrary, the 3-phase contact line on particle B (untreated) is pinned and the solid-liquid interface stays constant. In order to fit the liquid bridge profile a 4^{th} order polynomial curve has been chosen (Figure 6-17).

This latter choice seems an obvious refinement of the parabolic approximation after a 3^{rd} order polynomial fitting did not show a reasonable agreement with the experimental curve, as shown in Figure 6-16. In Figure 6-17, the 4^{th} order polynomial curve has been used to fit the complete sequence of separation of exp. A9.

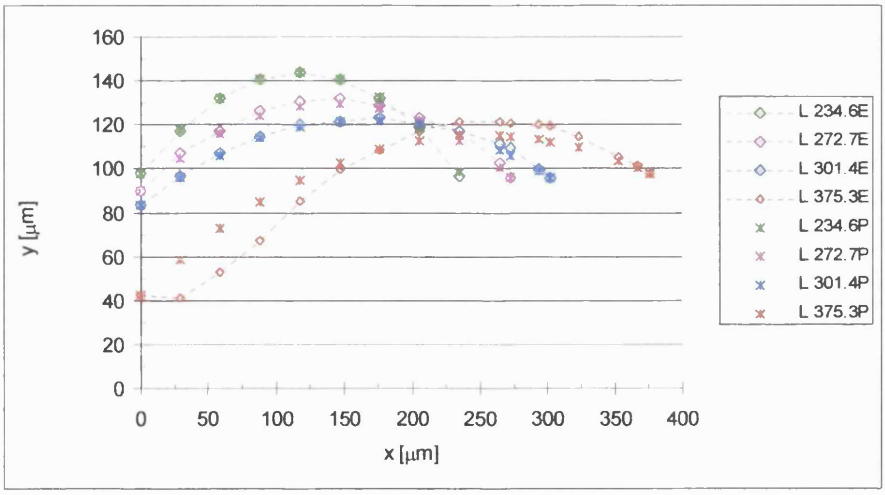

Figure 6-15 Evolution of the bridge profile for exp. A9 (see Table 7). Particle A is silanised, particle B is made of untreated glass. The legend indicates the liquid bridge length, L, in microns, whilst E refers to the experimental curve and P to the parabolic fitting. The shape matching L=375.3 μm corresponds to the last bridge configuration recorded before rupture.

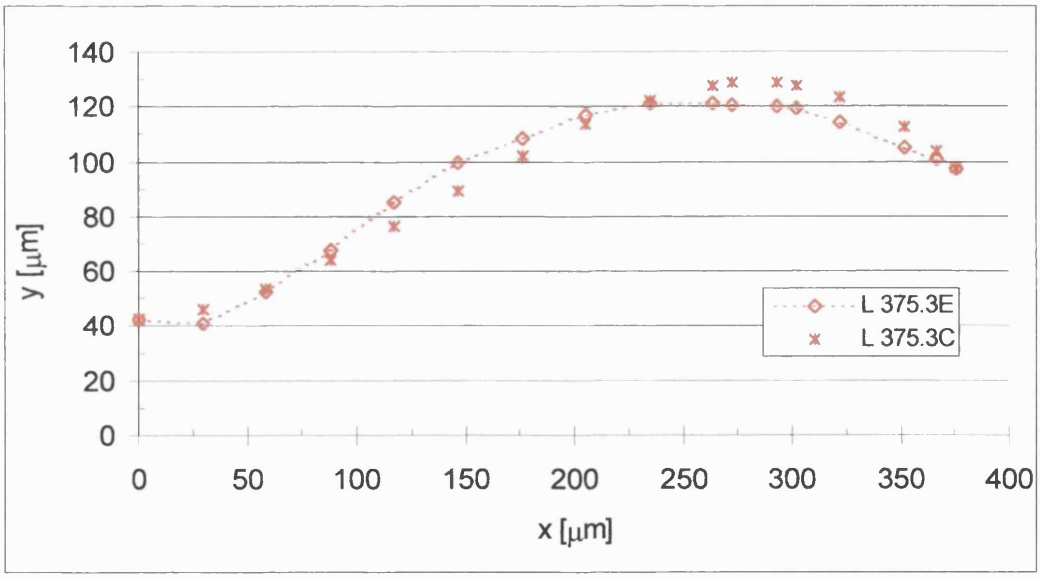

Figure 6-16 Experimental (E) and 3rd order polynomial (C) fittings for the last liquid bridge configuration observed during exp. A9 (see Table 7) at the liquid bridge length L=375.3 μm. The 3rd order polynomial fitting is in the form $y(x)=\alpha_3x^3+\alpha_2x^2+\alpha_1x+\alpha_0$.

The approximation with a 4th order polynomial curve presents more mathematical difficulties than the parabolic model because it requires the determination of the 5 unknown α_i (i=0 to 4) values in (6.30).

$$y(x)=\alpha_4 x^4+\alpha_3 x^3+\alpha_2 x^2+\alpha_1 x+\alpha_0 \tag{6.30}$$

The determination of coefficients α_i is obtained from the solution of system (6.31):

$$\begin{cases} y(0)=y_A \\ y(L)=y_B \\ y'(0)=y'_A \\ y'(L)=y'_B \\ V_m=\pi\int_0^L y^2(x)\cdot dx = V_{br}+V_{cap,A}+V_{cap,B} \end{cases} \tag{6.31}$$

where y'_A and y'_B are the values of the liquid bridge tangent measured on particle A and B at each configuration of separation sequence, respectively. The solution of (6.31) is not trivial and has been achieved by means of the software Mathematica®.

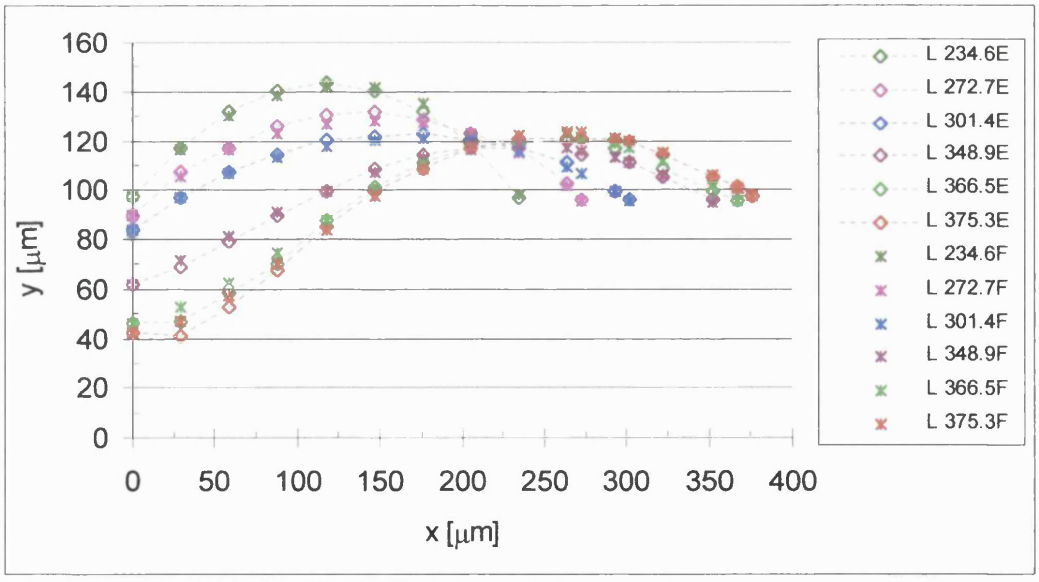

Figure 6-17 Experimental (E) and 4th order polynomial (F) fittings for the separation sequence observed during exp. A9 (see Table 7). L represents the liquid bridge length in microns.

Figure 6-17 compared with Figure 6-15 clearly shows that near the bridge rupture (L~375.3 μm) the profile is better approximated by the 4th order polynomial curve than by the parabola. Furthermore the comparison of Figure 6-15 and Figure 6-17 it can be seen that agreement between the two approximated fittings is observed up to L= 301.4 μm after which (L=348.9 and L=366.5) the parabola curves significantly differed from the corresponding experimental curves. As this is also the case for L=375.3, the curves for L=348.9 and L=366.5 were not plotted in Figure 6-15 simply for clarity.

The 4th order polynomial model cannot be used as a predictive tool, not even for a fixed interface approximation, because it requires too many parameters that cannot be estimated from previous configurations, as for example the values of the tangent of the liquid bridge at the point of contact with the particles, which are not known a priori. Nevertheless, the 4th order polynomial model does allow the verification of a peculiar property of the dewetting phenomena. In all experiments 2, 8 and 9 it resulted that the increase of the liquid bridge area during separation was balanced by the reduction of the dewetting interface. The sum of the two areas, in fact, was almost constant during separation, as shown in Figure 6-18, where A_{dew} is the area of the solid-liquid interface (cap of a sphere) calculated with experimental values from (6.32) either on particle A or on particle B according to where the dewetting occurred.

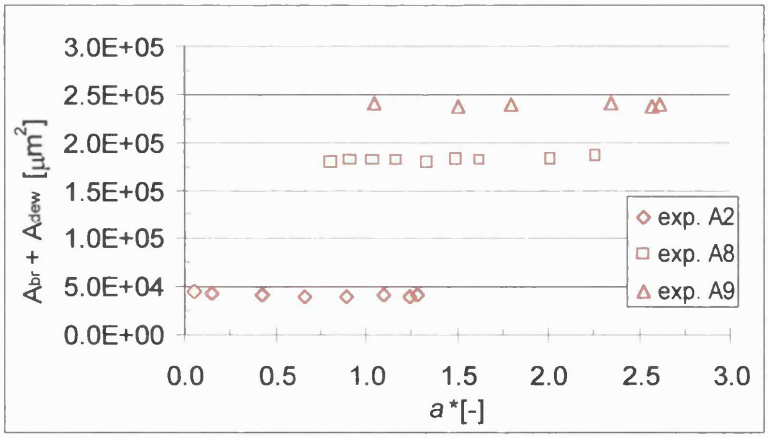

Figure 6-18 Sum of liquid bridge and dewetting areas versus normalised distance for experiments where dewetting of a particle was noticed. The area of the solid-liquid interface is a cap of a sphere. Experimental conditions are reported in Table 7.

$$A_{dew} = 2 \pi R_i h_i \text{ (i= A or B)} \quad (6.32)$$

The area of the liquid bridge was calculated with the 4th order polynomial model for experiments A8 and A9 and with the parabolic model on experiment 2, where, despite the presence of dewetting on the smaller particle, the profile remained unduloid all throughout separation and therefore the parabolic model applied.

iii) Post-rupture liquid distribution

In the previous sections it has been shown that the particle wettability influences significantly the geometry of the liquid bridge. As a consequence, the post rupture liquid distribution is also affected. The liquid left on the particle after a rupture is important in order to understand whether formation of new liquid bridges is favoured or inhibited. Smaller amounts of liquid left on a particle involve less probability of formation of new liquid bridges and this might result in segregation of a specific particle from a mixed formulation. Figure 6-19 represents the volume fraction of liquid binder remaining versus the particle solid fraction on particle A. The particle solid fraction is calculated as the ratio between the volume of particle (A) and the total volume of the two particles, V_s. V_A represents the volume of liquid left on particle A.

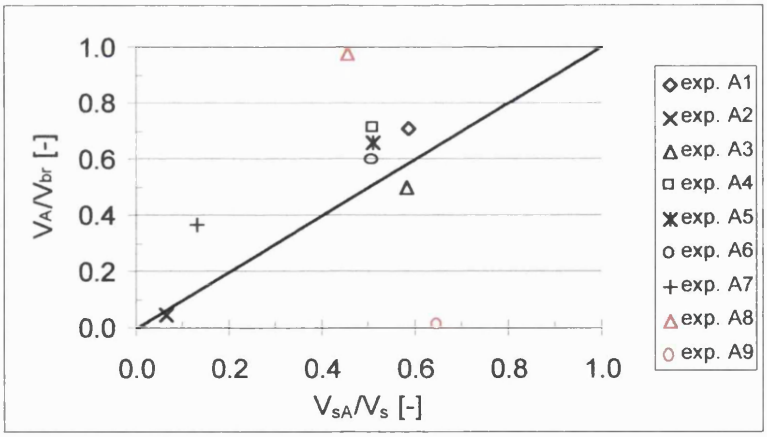

Figure 6-19 Binder volume fraction versus particle solid fraction measured on particle A. In exp. A8 particle A is untreated whilst in exp. A9 particle A is silanised.

On a theoretical basis, it seems reasonable to assume that after rupture the liquid binder distributes roughly proportionally to the volumes of the two spherical particles. The

validity of this assumption, however, must be restricted to cases of similar and well wetted particles and to liquid bridges perfectly symmetrical along the axis of separation. Figure 6-19 illustrates the experimental binder volume distribution versus the solid fraction, as measured on particle A. The graph seems to shows a relation between the solid fraction and the post rupture liquid distribution for liquid bridges formed between well wetted particles (exp. A1 to A7). Discrepancies with the theoretical trend (indicated by the line y=x) can be attributed to the dewetting of the solid liquid interface, which, even when small, can influence the geometry of the liquid bridge and therefore the post rupture liquid distribution. A different situation is noticed for liquid-bridges formed between particles with good and poor wettability. In experiments 8 and 9 the volume of the liquid bridge is almost completely distributed on the untreated particle (particle A on exp. A8 and particle B on exp. A9), which exhibits higher wettability. For the experiments between untreated particles (A1 – A7) , the post-rupture liquid distribution has also been estimated using both the parabolic and toroidal models and the fixed interface approximation. The predictions of both models are presented in Figure 6-20. Both models adequately predict the extent of liquid volume distribution on the particles at rupture. Data presented in Figures 6–18 and 6–19 are shown in Table 10.

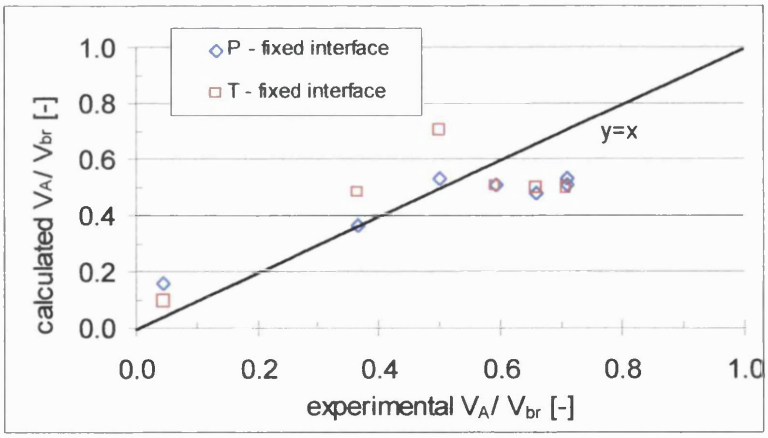

Figure 6-20 Prediction of liquid volume distribution between the two particles using the toroidal T, and parabolic P model with the fixed interface approximation.

Exp.	V_{sA}/V_s [–]	V_A/V_{br} E [–]	V_A/V_{br} P [–]	V_A/V_{br} T [–]
A1	0.588	0.709	0.532	no solution
A2	0.065	0.044	0.160	0.102
A3	0.582	0.499	0.532	0.705
A4	0.511	0.710	0.506	0.500
A5	0.512	0.659	0.479	0.495
A6	0.506	0.593	0.509	0.501
A7	0.132	0.365	0.364	0.477
A8	0.454	0.980	not applicable	not applicable
A9	0.648	0.010	not applicable	not applicable

Table 10 Data presented in the plots of Figure 6-19 and Figure 6-20. E, P, T stand for experimental, parabolic and toroidal, respectively.

6.2 Particle wettability in relation to adhesion force and rupture energy of a liquid bridge

The results presented in this section are concerned with the investigation of silicone oil liquid bridges holding pairs of glass particles submerged in either pure water or aqueous solutions of surfactants and/or electrolytes.

The experiments carried out in water using the MFB, whose methodology has been described in section 5.1, are the natural extension of the project started by Fairbrother [5] for the measurements of liquid bridge force in gaseous bulk medium (air). Despite the fact the experiments here were carried out in a different bulk medium, the results mirror some of the findings reported in section 6.1. However, the investigation was not restricted simply to the geometry of the liquid bridge but also included the measurement of force, capillary pressure and rupture energy in quasi-static conditions (the viscosity effects were negligible). Some preliminary results of the effect of surfactant are also reported in terms of glass wettability and adhesion force of the liquid bridge.

Glass ballotini, either untreated or silanised, of diameter in the range of 90-130 μm have been used as the solid particles whilst silicone oil 100 cS and water have been used as the bridging and suspending liquid, respectively. The cleaning of the particles and the method of silanisation has been discussed in section 5.3. Silanised particles exhibit higher wettability toward the silicone oil than that shown by untreated ballotini, hence, results in this section can be compared with the observations in section 6.1 in terms of the wettability exhibited toward the binder. The surface tension of silicone oil-water interface was measured with the tensiometer according to the procedure described in 5.4 and resulted in the value of 37.8 mN/m. The micro-manipulation technique, adapted to the liquid bulk medium, was employed to form and separate liquid bridges between pairs of particles of different wettability (see section 5.1.1). The separation speed was always kept at ~1μm/s in order to minimize viscous effects. The determination of the liquid bridge adhesion force was made principally by image analysis, which resulted in a more versatile technique, which could adapt to the variation of the liquid bridge volume. However, measurements with the electronic method were also taken and are presented at the end of this section.

The Figures below refer to experiments of liquid bridge separation between either two silanised particles (Figure 6-21) or a silanised and an untreated ballotini, shown in Figure 6-22.

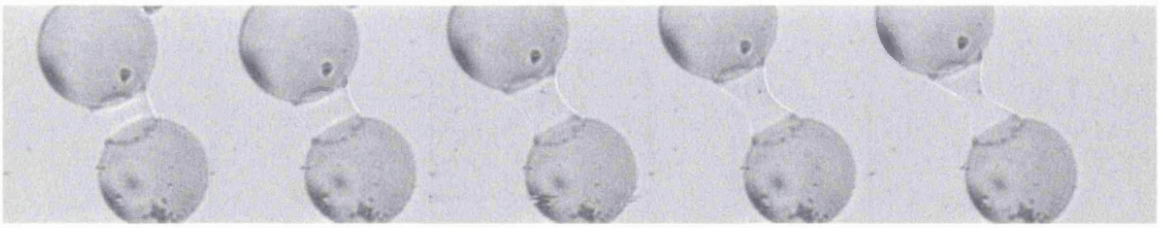

Figure 6-21 Separation sequence of a silicone oil liquid bridge formed in pure water between two silanised glass particles of radii 63.5 μm (left) and 58.9 μm (right), separated at 1 μm/sec. The volume of the bridge is ~ 90500 μm^3, exp. B4 (see Table 11).

The resemblance between the geometries observed in Figure 6-1 and Figure 6-21 is pretty clear and again between well wetted particles a small reduction of the solid liquid

interface is appreciated during separation and a nodoid geometry is observed throughout separation.

On the other hand, as was observed in Figure 6-2, Figure 6-22 shows the reduction of the interface on the poorly wetted particle (untreated ballotini in this case).

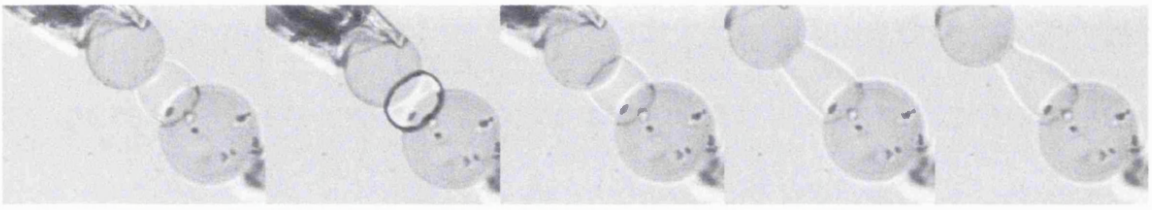

Figure 6-22 Separation sequence of a silicone oil liquid bridge formed in pure water between an untreated glass particle (left) and one that is silanised (right) of radii 44.3 μm and 58.1 μm, respectively. The particle are firsly approached and then separated at 1 μm/sec. The volume of the bridge is ~ 133000 μm^3. The silicone oil bridge poorly wets the untreated particle, exp. B11 (see Table 11).

Exp.	R_A μm	R_B μm	V_{br} ($\times 10^3$ μm^3)	Exp.	R_A μm	R_B μm	V_{br} ($\times 10^3$ μm^3)
B1	47.4	45.9	32.9	**B11**	44.3*	58.1	132.8
B2	52.0	50.1	166.1	**B12**	44.3*	58.1	48.0
B3	52.0	53.5	22.2	**B13**	44.3*	58.1	6.3
B4	63.5	58.9	90.5	**B14**	51.2	50.5*	1200.8
B5	51.0	49.7	31.3	**B15**	58.5	55*	547
B6	51.0	49.7	11.8	**B16**	58.5	55*	72.3
B7	51.0	49.7	5.2	**B17**	46.8*	62.7*	2.7
B8	58.9	48.1*	150.9	**B18**	44.3*	52.7*	5.1
B9	58.9	48.1*	59.8	**B19**	52.7*	52.7*	6.3
B10	44.3*	58.1	170.5	**B20**			

Table 11 Experimental conditions for experiments of liquid bridge separation between untreated (*) and silanised particles submerged in pure water. The silicone oil liquid bridge poorly wets untreated particles.

i) Geometry and adhesive force

Stills of recorded sequences have been analysed using PowerPoint ® (see section 5.1.8) in order to compare the experimental configuration of the liquid bridge with the solution of the Young Laplace equation. For each configuration of the separation sequence, the parameter $\Delta P/\gamma_L$ was determined by (3.6) from image analysis of the experimental geometry and the solution of (3.2) was then obtained numerically using the ordinate y_A and y_B (see Figure 3-1) as the boundary conditions. Figure 6-23a and Figure 6-23b show the good agreement between the experimental and the theoretical profiles for the initial and final configurations of the sequence presented in Figure 6-21. It is useful to note that the x-axis of the geometry profiles is the length of the liquid bridge, indicated as L in Figure 3-1, and not the separation distance *a*. The comparison of the two configurations illustrates that during separation small reductions of the interface occur on both particles (the extreme ends of the profile) whilst an extended pinning of the 3-phase contact line is noticed.

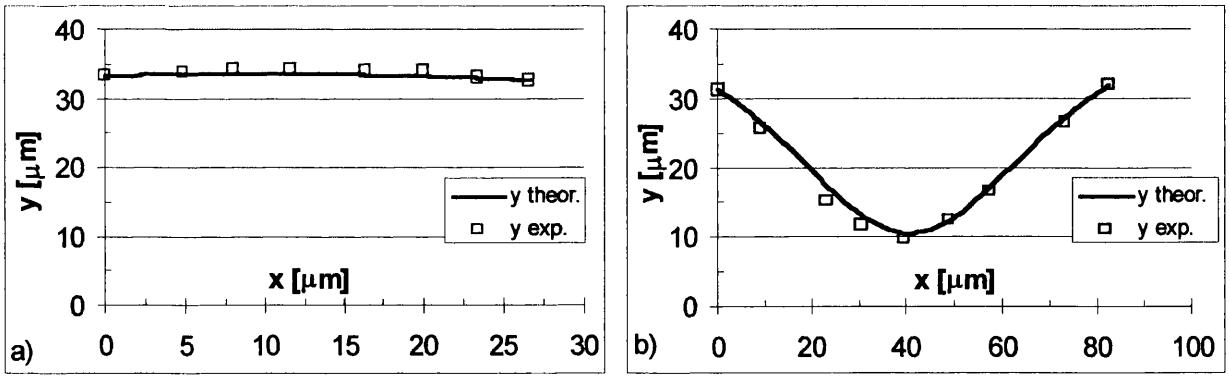

Figure 6-23 Geometry profiles of the liquid bridge shown in Figure 6-21: a) ΔP=1455 Pa, a=7μm; b) ΔP=1540 Pa, a=68μm, exp. B4 (see Table 11).

Figure 6-24 shows the force plot measured during the sequence presented in Figure 6-21 and the comparison with the theoretical values of the liquid bridge adhesion. Equations (3.12) (neck method) and (3.13) (boundary method) have been used to calculate the theoretical force data after the experimental geometry was fitted with the Young Laplace equation in order to determine the pressure variation, ΔP, inside the liquid bridge. The variation of the pressure inside the liquid bridge during separation will be presented in Figure 6-29a.

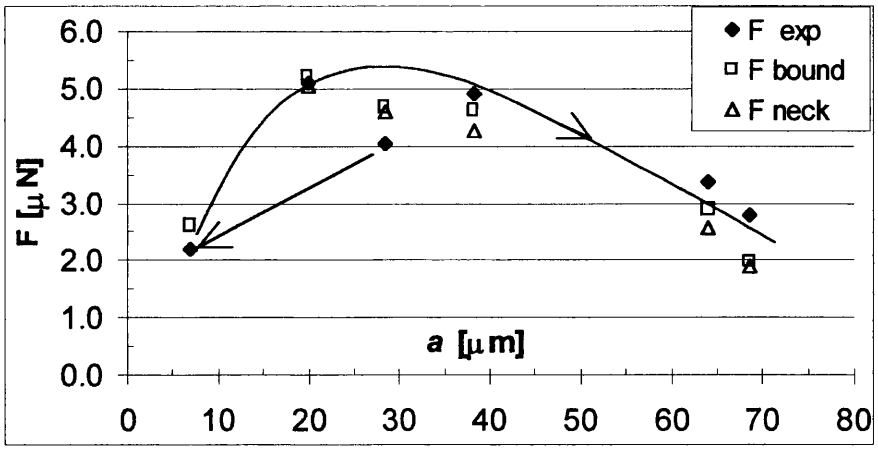

Figure 6-24 Force versus separation distance for liquid bridge shown in Figure 6-21, exp. B4. The plot shows the experimental data and the theoretical values obtained from both the neck and the boundary models.

In Figure 6-24 the arrows reflect the sequence of initial formation, compression and separation of the liquid bridge. It can be noted that the initial force (a~30 μm) is lower than the value obtained at the same abscissa after the liquid bridge has been compressed between the two particles. This fact can be explained by a larger particle-to-binder interface formed upon compression, which leads to higher forces in the following phases of separation, as predicted by (3.13).

Figure 6-25 refers to the separation sequence illustrated in Figure 6-22. The untreated particle, situated on the left of the graph near the x-axis origin, experiences a large dewetting and the liquid bridge ordinate recedes from the initial value of ~30μm (left side on Figure 6-25a) to nearly 15 μm measured on the last observed configuration in Figure 6-25b.

The hysteresis of the liquid bridge force, which follows the initial phase of particle compression, was also observed in the force plot of liquid bridges formed between well and poorly wetted particles, as shown in Figure 6-26. In this latter experiment the compression of the two particles, similar to the previous case, leads to a larger contact area between the particles and the binder, which is followed by the interface receding (on the untreated particle) in the next phase of separation.

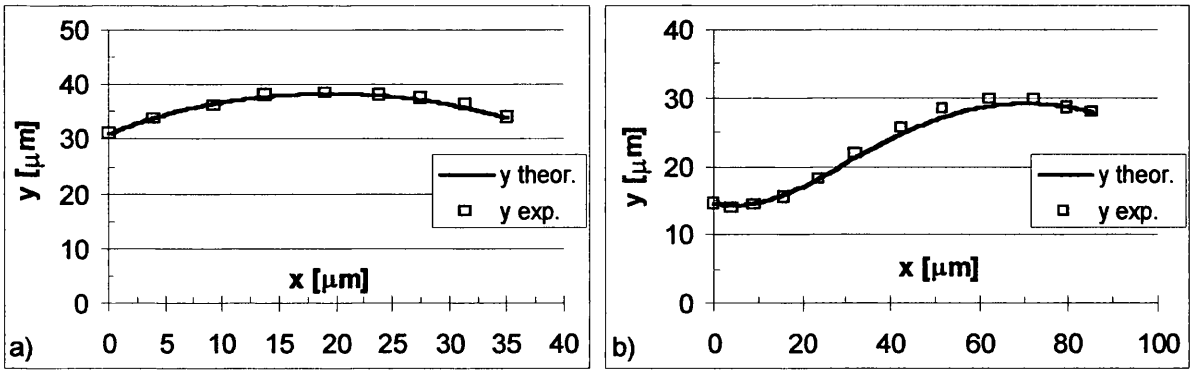

Figure 6-25 Initial and pre rupture configuration of the liquid bridge formed between a silanised and an untreated particle (left side of graphs), shown in Figure 6-22: a) ΔP=2268 Pa, a=12μm; b) ΔP=1758 Pa, a=75μm, exp. B11 (see Table 11).

It is important to make clear that the configurations shown in Figure 6-23b and Figure 6-25b were the last images recorded (with a camera acquiring 25 frames per second) before rupture and are not likely to be the real rupture configurations.

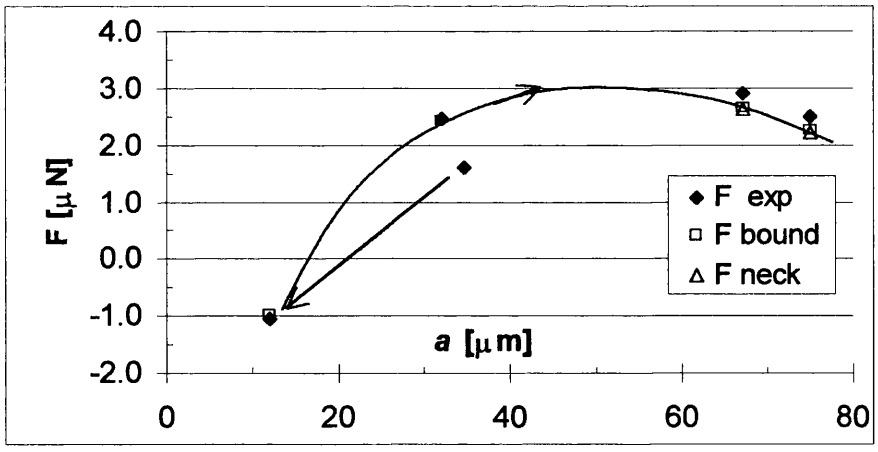

Figure 6-26 Force versus separation distance for a liquid bridge formed between silanised and untreated particles. Sequence is shown in Figure 6-22, exp. B11. The plot shows the experimental data and the theoretical values obtained from both the neck and the boundary models.

The effect of the receding interface on poorly wetted particles (untreated glass) plays an important role in the liquid bridge strength and, as a consequences adhesion forces measured during liquid bridge separation are lower then the case where both particles

present a high wettability toward the binder (silanised particles). The comparison of dimensionless force measured during separation of liquid bridges formed between pairs of particles either both silanised or with different wettabilities (one silanised and the other untreated) in experiments from B1 to B16 shows that the maximum force measured in the silanised-silanised configuration is almost double that determined between silanised and untreated particles (see Figure 6-27).

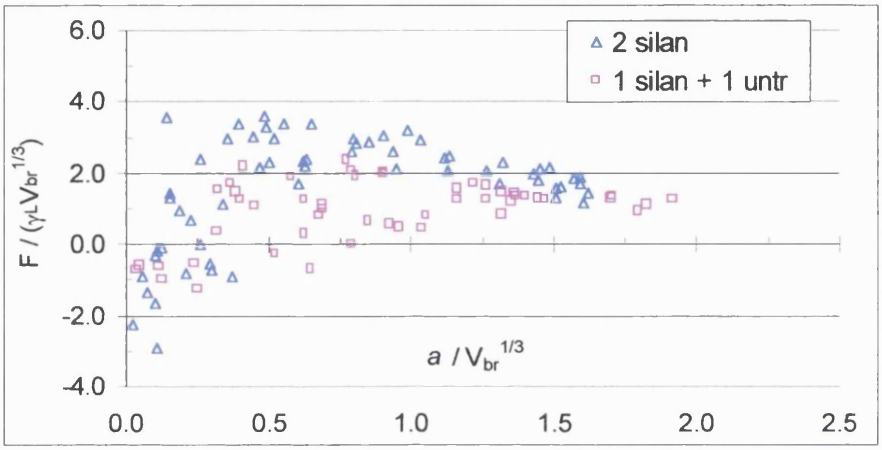

Figure 6-27 Liquid bridge strength versus separation distance in dimensionless form. Untreated particles exhibit a lower wettability toward the silicone oil binder than that revealed by silanised ballotini.

Apart from the force data reported at the end of this section, the liquid bridge adhesion force for experiments B1 to B16 have all been determined via images analysis from the deflection of the flexible pipette recorded during separation.

Viscous forces were also analysed and shown to be negligible for the experimental conditions used. Using (3.15) with the following input data; R=51μm (average value for the experiments B1-B16), η=0.096Pa s, a=2μm, $\frac{da}{dt}$=1μm/s; results in a value of 5.65×10^{-4}μN whilst Ca is 2.5×10^{-6} (see section 3.1.5). The viscous force so calculated is four orders of magnitude lower than the sum of capillary and surface tension forces measured experimentally and verified using either (3.12) or (3.13). In the present set of experiments, (3.15) can be applied rigourosly only to cases the bridge volume is larger

than ~25 x 10^3 μm^3 according to the limiting condition proposed by Ennis et al. [113] on the minimum liquid bridge non-dimensional volume ($V_{br}^* = 0.05$, see also section 3.1.5). The maximum liquid bridge adhesion force for the experiments B1-B16 varied between 2 and 5 μN according to the volume of the bridge and therefore viscous effects have been neglected in the calculations of the liquid bridge energy, which are presented later in this section. Increasing the separation distance and keeping all the other quantities the same, the viscous force reduces even further. This result agrees with [114], in which the stress induced on particle agglomerates deformed at increasing compression speed is studied and the viscous forces contribution to the deformation of the wet mass was found to become predominant only when the capillary number Ca was above a threshold of 10^{-4}.

According to (3.12), the neck size and the capillary pressure of the liquid bridge influence the strength in such a manner that larger sizes and lower pressures favour higher values of strength. The half bridge neck height, plotted versus the volume of the liquid bridge (see Figure 6-28) for all the configurations where the maximum strength was measured, shows that the liquid bridge assumes thicker configurations for the silanised-silanised set of particles.

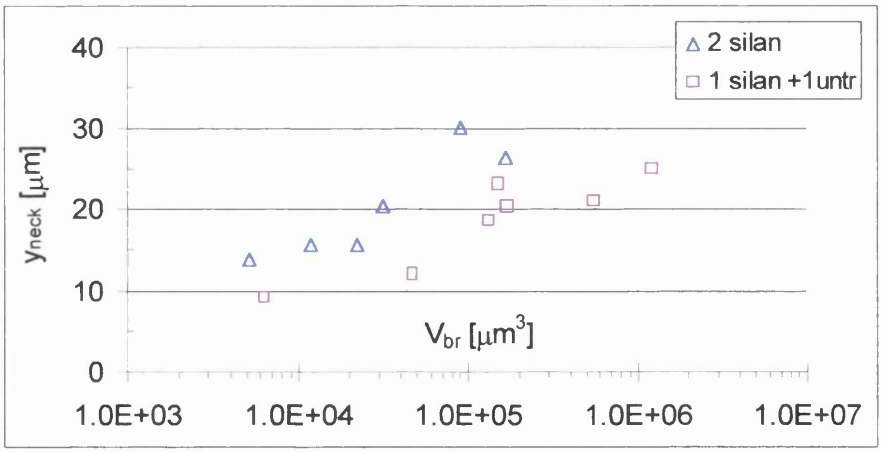

Figure 6-28 Half bridge neck height (y_{neck}) versus volume of the bridge: measurements refers to bridge configurations of maximum strength measured from separation sequence of experiments B1–B16 (see Table 11).

Capillary pressure, which is determined by (3.6) using recorded configurations of the separation sequence, is plotted in Figure 6-29 for a few cases selected from the two sets of experiments. When both particles are silanised (Figure 6-29a), the pressure profile seems to follow a parabolic curve whose concavity decreases as bridge volume increases. Between particles of different surface energy (Figure 6-29b) the parabolic shape exhibited by smaller volume liquid bridges becomes flatter as the volume of the binder increases. Mutual comparison of the non dimensional pressure against the normalised separation distance is presented in Figure 6-30 for the set of experiments B1–B16. The graph generally shows higher values of the capillary pressure in favour of the situation where one particle is untreated and therefore is poorly wetted by the liquid bridge.

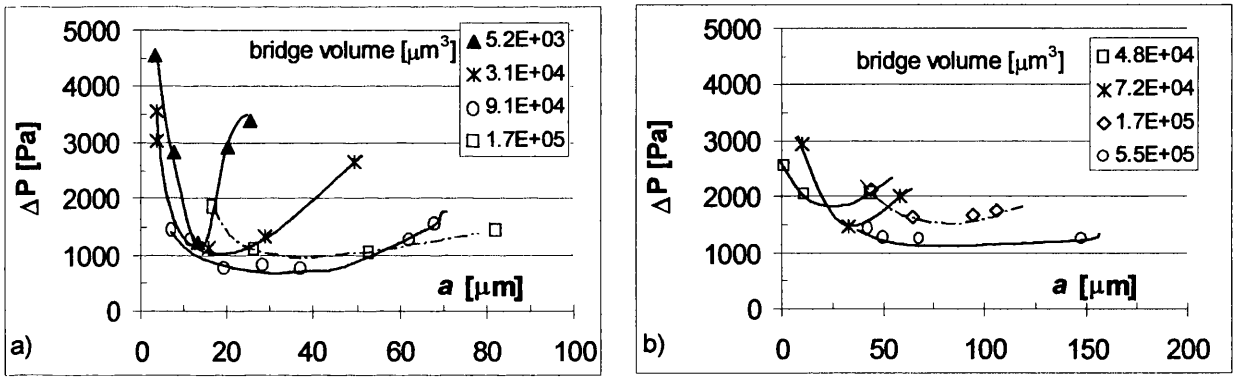

Figure 6-29 Capillary pressure versus separation distance for two silanised (a) and untreated-silanised (b) particles.

From the analysis of Figure 6-28 and Figure 6-30 the lower liquid bridge strength measured between particles with different wettabilities can be explained by the complementary effects presence of thinner bridge necks and higher capillary pressures both working against the bridge strength.

The consequences of the higher strength measured between well wetted particles, is reflected in the higher energies values, W, calculated during particle separation. The calculation of the liquid bridge energy can be easily made from the experimental graph force, as presented in Figure 6-24 and Figure 6-26, which can be fitted with a third order polynomial curve and then integrated through separation distance. The results

obtained from the integration of the force graphs are presented in Figure 6-31 according to the type of wettability exhibited by the particles.

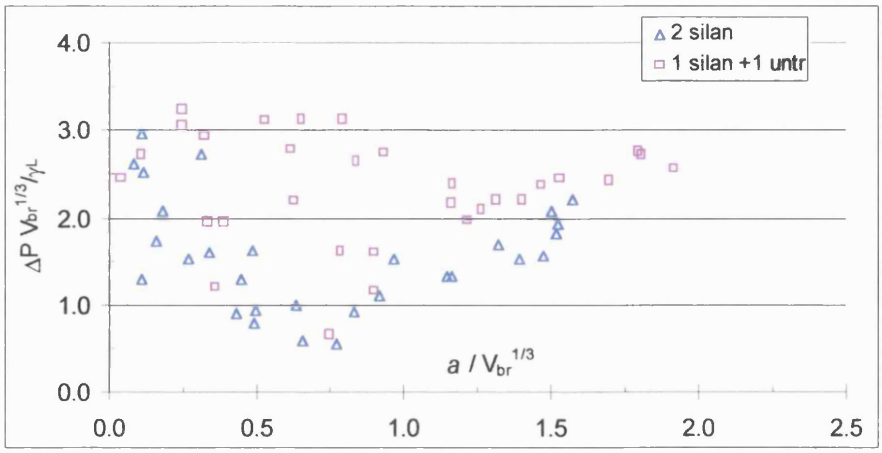

Figure 6-30 Normalised pressure versus non dimensional separation distance calculated from separation sequence of experiments B1–B16 (see Table 11).

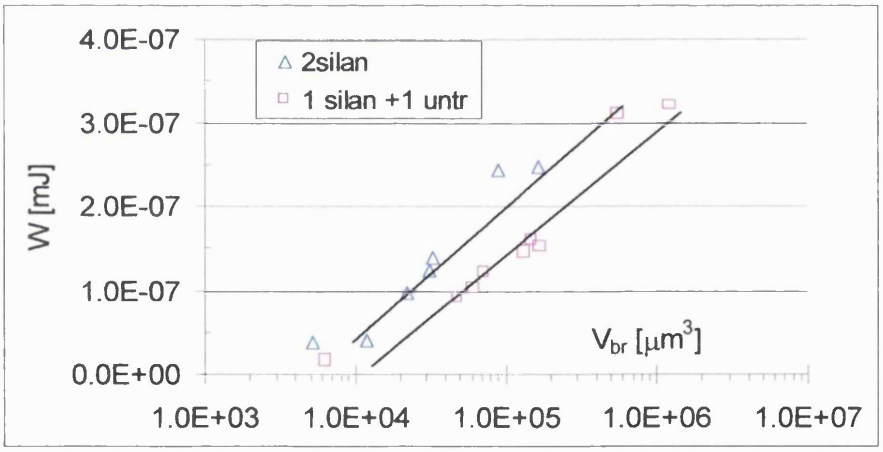

Figure 6-31 Experimental values of liquid bridge energy calculated from the experimental liquid bridge force curves of experiment B1–B16 (see Table 11).

Apart from a few points measured at low liquid bridge volumes that do not fit the general trend of the two set of experiments, the plot shows that more liquid bridge energy is stored between higher wettable particles (silanised) with respect to that measured in configurations where at least one particle is poorly wetted (untreated). The higher liquid bridge energy is beneficial to agglomeration processes in order to

counterbalance the kinetic effect induced by the mixing equipment, which might be able to break the agglomerate. During particles mixing, therefore, agglomerates formed by poorly wetted particles are more likely to be broken. A further effect that hinders the agglomeration of poorly wetted particles is the amount of binder left on the particle after separation. Due to the receding of the particle-binder interface very small amounts of binder will remain available on low wettable surfaces to form new liquid bridges, as can be predicted from the last frame of the sequence in Figure 6-22 and from the analogy with the results in section 6.1.2.

ii) Bridge Rupture energies.

Since the relationship between surface properties and liquid bridge energy can be an important parameter in modelling the behaviour of liquid binders with respect to the agglomeration of a specific product, the theoretical formulae to calculate the deformation energy of a liquid bridge, as proposed by Simons et al. [66] and Pitois et al. [67] in (3.19) and (3.22), respectively, have been compared with the experimental values plotted in Figure 6-31.

Table 12 presents the comparison between the normalised experimental energy data and the values calculated from the two previous models. The normalised energy is defined as $W^* = \frac{W}{\gamma_L \overline{R}^2}$ where $\overline{R}$ is the geometric average radius. Data in Table 12 have been plotted against the binder to particles volume fraction, V_{br}/V_s, (V_s has been calculated as the double of the volume of a particle of radius $\overline{R}$) and are presented in Figure 6-32, except for cases where the error exceeds 50% of the experimental measurement. Both models give reasonably good agreement with the experimental data calculated during the deformation of liquid bridges holding pairs of good wettable particles (silanised). For the case of dissimilar wettabilities, the model of Simons et al., which is based on the assumption of perfectly wetted surfaces, cannot account for the receding phenomena occurring on the untreated particle and, therefore, some of the experimental values are poorly predicted. For the set of experiments between particles of dissimilar wettabilities the model of Pitois et al. shows closer agreement due to the presence of the contact angle parameter, which better describes the dewetting process on the untreated particles.

The contact angles used in (3.22) are the lowest values measured on the particles just before rupture and their averaged readings are shown in Table 12.

Silanised–silanised particles				Averaged receding contact angle 35 ± 3.7 degree			
Exp.	$\overline{R}$	V_{br}/V_s	W^* (E)	W^* (Si)	%err	W^* (Pi)	%err
B1	46.6	0.039	1.70	1.29	-24.0%	1.39	-18.5%
B2	51.0	0.149	2.52	1.39	-45.0%	1.40	-44.6%
B3	52.7	0.018	0.93	0.90	-3.5%	0.87	-6.0%
B4	61.8	0.047	1.73	1.51	-13.0%	1.50	-13.2%
B5	50.3	0.029	1.30	1.25	-3.7%	1.21	-6.9%
B6	50.3	0.011	0.43	0.86	102.0%	0.75	75.4%
B7	50.3	0.005	0.40	0.44	8.2%	0.38	-5.6%

Untreated–silanised particles				Averaged receding contact angle 52 ± 6.2 degree			
Exp.	$\overline{R}$	V_{br}/V_s	W^* (E)	W^* (Si)	%err	W^* (Pi)	%err
B8	52.9	0.122	1.51	0.84	-44.6%	0.95	-37.3%
B9	52.9	0.048	0.97	1.19	23.1%	1.16	20.3%
B10	50.3	0.160	1.59	-0.361	-122.7%	0.391	-75.4%
B11	50.3	0.125	1.53	1.22	-20.6%	1.18	-23.0%
B12	50.3	0.045	0.96	1.55	60.5%	0.99	2.9%
B13	50.3	0.006	0.18	0.16	-10.0%	0.17	-6.6%
B14	50.8	1.091	3.28	-0.56	-117.0%	1.10	-66.3%
B15	56.7	0.358	2.55	0.13	-94.9%	1.18	-53.6%
B16	56.7	0.047	1.00	0.80	-19.2%	0.80	-19.7%

Table 12 Normalised energy to deform a liquid bridge. (E) experimental, (Si) predicted by the Simons et al. model [66] according to (3.19), (Pi) predicted by the Pitois et al. model [67] according to (3.22). Experiments from B1 to B7 are carried out between silanised particles, whilst B8 to B16 concern particles of dissimilar surface energy. Apart from $\overline{R}$ [μm], all the other data are dimensionless.

The models proposed by Simons et al. and Pitois et al., when applied to appropriate cases of liquid bridge deformation, give a satisfactory agreement with the experimental

data considering the fact they are both derived from approximated force laws (see section 3.1.6) and that all the parameters used to calculate (3.19) and (3.22) are determined by image analysis, which will incur some degree of error.

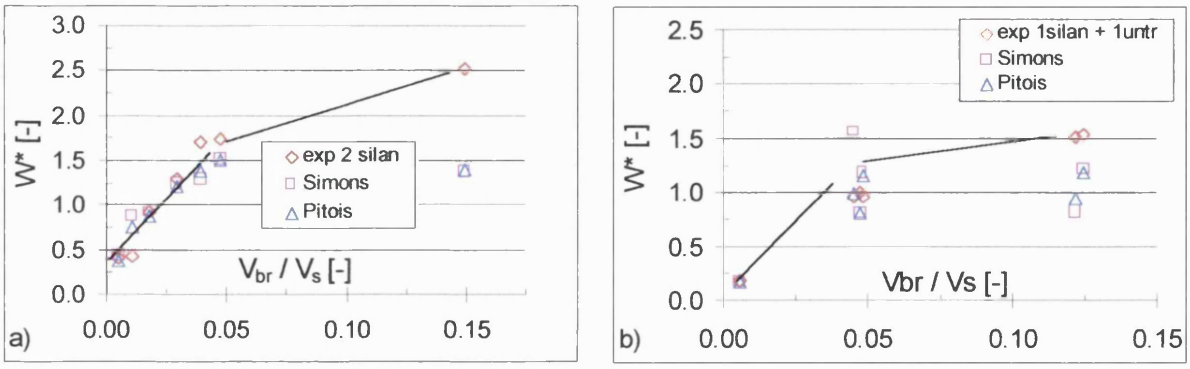

Figure 6-32 Comparison of experimental liquid bridge normalised energy, W^*, with the values obtained from the models proposed by Simons et al. and Pitois et al. according to (3.19) and (3.22), respectively: a) two good wettable particles, b) particles of dissimilar wettabilities. The plot shows data presented in Table 12 apart from those exceeding the 50% error threshold.

The thermodynamic approach described in sections 3.1.6 and 4.2.2 is presented in Figure 6-33 for the set of experiments from B1 to B16. The Helmholtz free energy, ΔA, is calculated using (4.11) between two configurations of the liquid bridge deformation and is compared with the corresponding energy W gained during the liquid bridge deformation between the same configurations.

Exp.	W	ΔA	%err	Exp.	W	ΔA	%err	Exp.	W	ΔA	%err
B1	1.40	0.95	-32%	**B7**	0.38	0.03	-91%	**B13**	0.17	0.14	-19%
B2	2.48	1.46	-41%	**B8**	1.60	2.46	54%	**B14**	3.20	1.35	-58%
B3	0.97	1.75	82%	**B9**	1.02	1.06	4%	**B15**	3.10	2.59	-17%
B4	2.45	2.38	-3%	**B10**	1.52	1.62	6%	**B16**	1.21	0.94	-22%
B5	1.24	0.52	-58%	**B11**	1.47	1.86	27%				
B6	0.40	0.38	-5%	**B12**	0.92	1.14	24%				

Table 13 Experimental energy of liquid bridge deformation, W, compared with the Helmholtz free energy, ΔA calculated using (4.11). Both W and ΔA are expressed in mJ $x10^{-7}$.

Figure 6-33 shows only the data whose relative error is below the 50% threshold. Since values used to calculate (4.11) are determined from image analysis, the same limitations to the method apply, as illustrated for the data presented in Table 12.

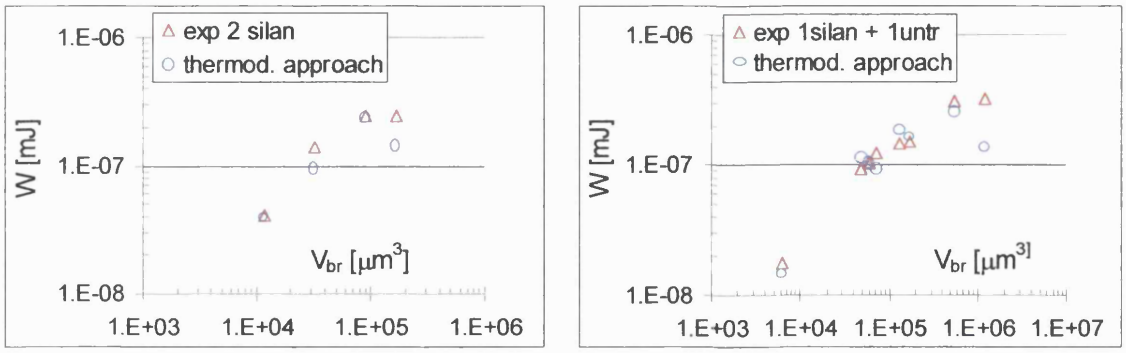

Figure 6-33 Comparison of experimental liquid bridge energy, W, with the values of the Helmholtz free energy ΔA calculated from (4.11): a) two silanised particles, b) untreated-silanised particles. The plot shows data presented in Table 13 apart from those exceeding the 50% error threshold.

The data shown in Figure 6-33 seems to confirm that during a quasi-static separation the energy stored by a liquid bridge can be calculated in terms of the capillary pressure variations, increase of the interfacial bridge area and variation occurring at the 3-phase contact line in terms of solid-liquid interfacial area and contact angles between the liquid meniscus and the particle. Unfortunately the comparison between correspondent experments presented in Table 12 and Table 13 show disagreement of cases where 50% of error is exceeded and further experiments are needed to assess the validity of this thermodynamic approach.

Data presented so far in this section have been summarised in [115].

In a different set of experiments reported in [116] the liquid bridge force between two untreated particles submerged in water and held by a silicone oil bridge has been measured and compared with the theoretical values obtained from the neck and the boundary models using (3.12) and (3.13), respectively. Since smaller volumes of silicone oil have been administered to form the liquid bridge, the deflection of the

flexible particle was acquired via the piezo electric follower, according to the procedures illustrated in section 5.1.1 and in Appendix C. The capillary pressure inside the liquid bridge was determined after an observed geometry was fitted with the profile resulting from the solution of the Young Laplace equation.

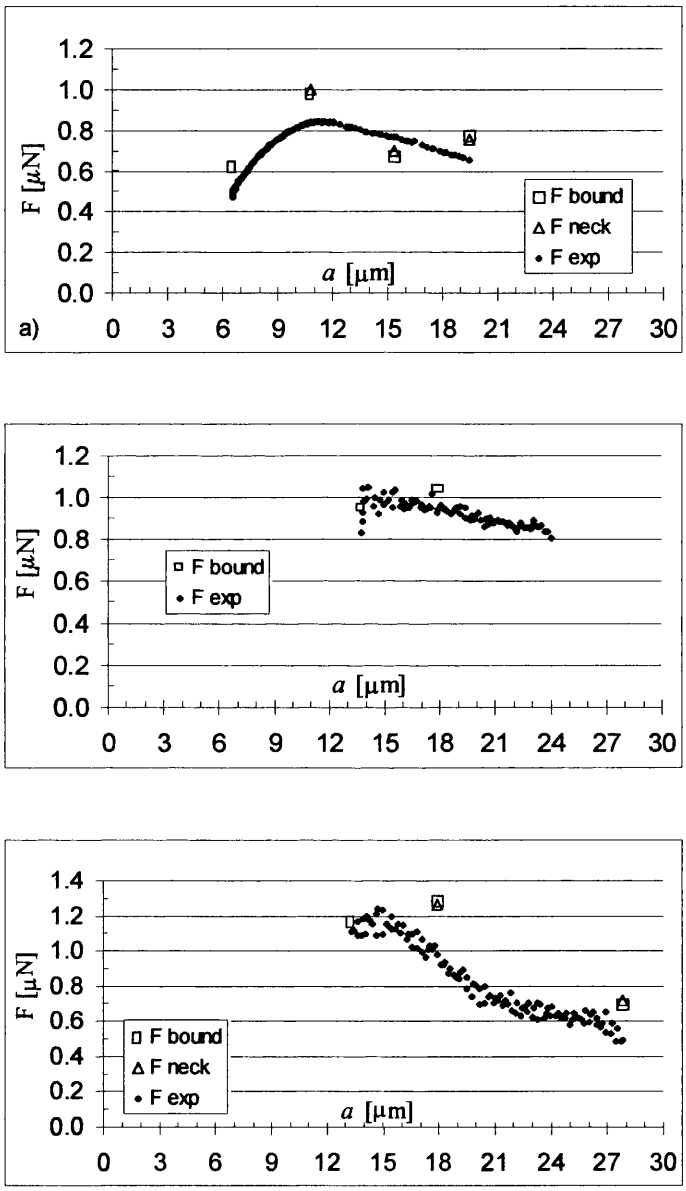

Figure 6-34 Force versus separation distance a: a) exp. B17 F_{max}=0.84μN, a_{rup}=19.4μm; b) exp. B18, F_{max}=1.02μN, a_{rup}=25.2μm; c) exp. B19, F_{max}=1.23μN, a_{rup}=27.7μm, (see Table 11 for experimental conditions).

The experimental data presented in Figure 6-34 show good agreement with the theoretical values predicted by both the neck and the boundary models.

The increase in F_{max} from Figure 6-34a to Figure 6-34c reflects the increase in the binder volume. As in the previous cases, the separation speed was 1μm/s and the viscous forces were negligible when compared with the capillary and surface energy terms. Using (3.15) with the following input data (exp. B18): R=44μm (smaller of the particles), η=0.096Pa s, a=2μm, $\frac{da}{dt}$=1μm/s, the value of 4.38×10^{-4} μN for the viscous force results, whilst the maximum capillary and surface tension force was correctly calculated from (3.13) in the value of 1.03 μN. In this set of experiments the condition on the minimum liquid bridge dimensionless volume is not respected ($V_{br}^{*} = 0.05$, see also section 3.1.5) and therefore (3.15) should be only used to give an indicative value of the viscous force magnitude, which results much lower than the static liquid bridge components.

The electronic technique for measuring the liquid bridge adhesion force (Appendix C) presents some limitations in terms of the maximum distance at which the particles can be separated (~15 μm in addition to the initial separation distance), which restricts the maximum liquid bridge volume that can be administered between the particles (~6500 μm^3). The technique of liquid bridge formation and force measurements has been reviewed in section 5.1.1, where it has been shown that the problems of determining the initial values of both the adhesion force and the interparticle distance limit the investigation of liquid bridges holding particles in contact. In chapter 8 some improvements will be proposed to solve this problem.

The electronic technique is also very sensitive to any asymmetry of the liquid bridge, as can be seen from the force data recorded in Figure 6-34c.

6.3 Influence of surfactants on the liquid bridge adhesion and particle-to-binder interaction in the liquid bulk medium

The present section focuses on the influences that the presence of dissolved surfactants in the suspending liquid bulk medium might have on both the liquid bridge adhesion and on the interaction between the binder and the particles. In many technological processes, such as flocculation, froth flotation and spherical agglomeration (see section 4.4.3), it is well established that the use of surfactants can favour the agglomeration of particles dispersed in a liquid medium and their selective recovery or separation. In the spherical agglomeration process, questions arise as to whether the beneficial use of surfactants reflects an increase of the adhesive strength exhibited by single liquid bridges or from improvement in the affinity between the liquid binder and the suspended particles. In the former case, agglomeration would be driven by liquid bridge (static) forces, whilst DLVO forces would be the predominant interaction in the latter situation. Common sense would suggest that DLVO forces must be responsible for agglomeration since the use of surfactants decreases the surface tension of the liquid binder and as a consequence the total liquid bridge adhesion decreases. Surfactants, however, are usually employed at very small concentrations and are also combined with the use of electrolytes that have minimal effect on the binder surface tension yet increase the adsorption of the surfactant on the particles at a specific concentration (see section 4.4.2). As a result of the combined use of both surfactants and electrolytes, the concentration of the latter reagent can be chosen as low as 10^{-5}M, which does not make a significant change to the surface tension of a liquid binder.

In aqueous solutions of surfactants and/or electrolytes, silicone oil (100 cS) has been used to form either a liquid bridge between glass particles or small droplets in a glass cell in order to either measure the bridge strength or the DLVO interaction towards an approaching glass particle. The adhesion of liquid bridges has been studied using the MFB (see section 5.1) from image analysis observations, whilst the AFM described in section 5.2 has been employed for the experiments involving DLVO interactions. Soda lime ballotini of diameter in the range of 40-110 μm has been used for the liquid bridge experiments whilst particles of the same material but not larger than 40 μm diameter

have been used for the AFM experiments, either untreated or silanised. Cleaning of the particles was done with chromo sulphuric acid according to the procedure described in section 5.3. NaCl has been used as the reference electrolyte and SDS and CTAB as the anionic and cationic surfactants, respectively. Suppliers and grade of the reagent has been indicated in section 5.3.

6.3.1 Liquid bridge adhesion

As shown in section 6.2, the contact angle formed between the particle and the binder during the liquid bridge separation largely influences the profile and the adhesive strength of the liquid bridge. From the comparison of Figure 4-13 and Figure 4-14 it results that the zeta potential of both glass and silicone oil is modified by the adsorption of CTAB according to the concentration of the solution. When the aqueous solution is more diluted than 10^{-4} M the potential of glass and silicone oil have opposite signs and this could lead to a more stable glass-oil interface explained by the attraction of the two oppositely charged areas. This relatively strong interaction should be reflected by a decrease of the receding contact with respect to a situation where no surfactant is used. The receding contact angle that can be used as a measure of glass oleophilicity, by assuming that lower receding angles at the glass-oil interface correspond to a higher grade of oleophilicity. SDS, on the contrary, makes the zeta potential of both the oil and the glass particles increasingly negative (see potential determining ion effect in section 3.3.3 and Figure 4-13 and Figure 4-14) and its use should lead to higher contact angle than that of CTAB. The results of the advancing and receding contact angle for different bulk solutions are presented in Table 14.

Contact angle degree	AnalaR water pH5.6	SDS 10^{-3}M	SDS 10^{-2}M	CTAB 10^{-4}M
Advancing	93±3	100±2	180	105±2
Receding	77±4	96±1	180	49±1

Table 14 Advancing and receding contact angles of a 100 cS silicone oil droplet deposited on glass ballotini submerged in different aqueous solutions. The oil and the ballotini have been left to equilibrate separately for 15 minutes in the bulk medium before contact takes place.

As expected from zeta potential data presented in section 4.4.2 the affinity of glass and oil decreases as the SDS concentration is increased up to a value of 10^{-2}M where the contact angle is 180 degree and glass becomes completely unwettable. The addition of CTAB reduces moderately the receding contact angle of the oil (49 degree) if compared with the value measured in pure water (77 degree). The variation of the contact angle should lead to differences in the adhesive strength of the liquid bridge, as will be illustrated in Figure 6-39.

Figure 6-35 shows the advancing and the receding contact angle of a silicone oil droplet deposited on a glass particle in a CTAB solution 10^{-4} M. Prior to the oil deposition, both the glass and the oil droplet (formed on the feeding micropipette) have been left to equilibrate separately for 15 minutes inside the bulk medium.

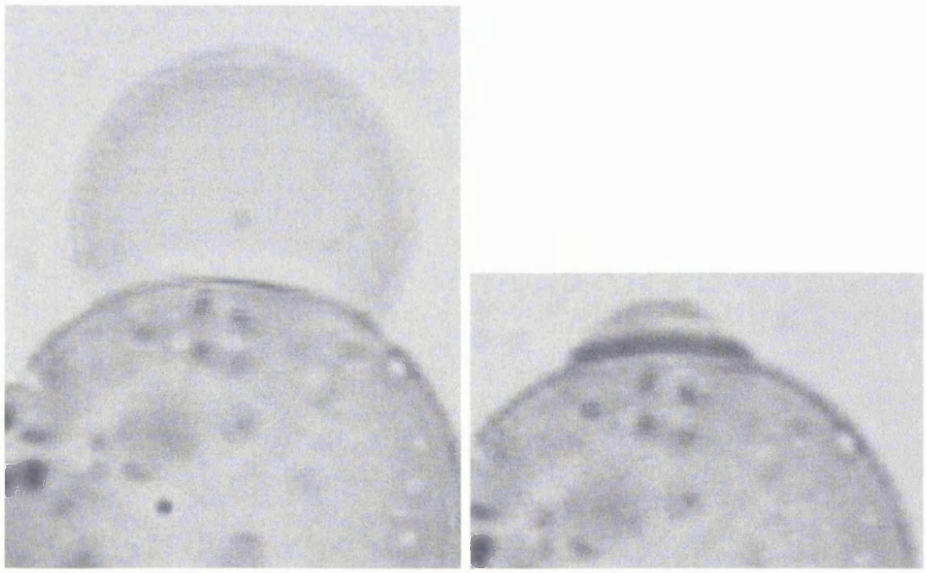

Figure 6-35 Advancing (left) and receding contact angle (right) of silicone oil on a glass ballotini in a solution of CTAB 10^{-4} M. The angles are measured in the organic phase and are 93.4 deg. and 49.7deg. from left to right, respectively.

The oil volume on the glass ballotini was first increased and then subtracted in order to measure the advancing and receding contact angles. Before any oil addition or withdrawal the droplet has been left for five minutes to reach a stable configuration, after which the image was recorded.

Figure 6-36 shows the receding contact angle of the glass-oil interface in a solution of 10^{-3} M SDS where both the ballotini and the oil droplet have been equilibrated (for 15 minutes) in the solution.

Figure 6-36 Receding contact angle of silicone oil on glass ballotini in a solution of SDS 10^{-3} M. The oil and the ballotini have been left to equilibrate separately for 15 minutes in the bulk medium before the contact takes place. The receding angle is 96.6 deg.

The time of equilibration seems to play a very important role in the wettability process. In Figure 6-37 the bulk conditions are the same as for Figure 6-36, but in this case only the ballotini has been left to equilibrate in the solution for 15 minutes whilst the feeding micropipette was kept outside the solution.

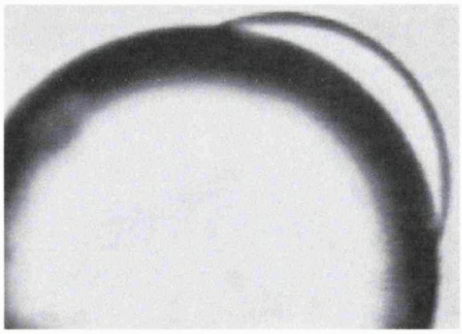

Figure 6-37 Receding contact angle of silicone oil on glass ballotini in a solution of SDS 10^{-3} M. Only the ballotini has been left to equilibrate for 15 minutes in the bulk medium before the contact takes place. The receding angle is 27.1 deg.

When the oil droplet was formed and retracted, surprisingly, a much lower contact angle was measured in comparison to the value observed in the case shown in Figure 6-36. The difference can be explained by the differences in surface charge between a

surfactant covered surface and the fresh oil surface. However, in the experiments regarding the measurements of liquid bridge adhesive forces, presented later in this section, only the case where both the particles and the oil were equilibrated for 15 minutes with the bulk solution prior to the liquid bridge formation has been considered. Because surfactants adsorb very quickly on to surfaces, 15 minutes seems a large enough time to have complete adsorption. According to Atkin [106], in fact, the adsorption of CTAB on glass takes place in ~30s.

Table 15 presents the data of surface tension used for the liquid bridge measurements. The interfacial tension values were calculated using the Kruss K12 tensiometer.

	AnalaR water pH5.6	[1]SDS 10^{-3}M	SDS 10^{-2}M	[2]CTAB 10^{-4}M	CTAB 10^{-5}M + NaCl 10^{-3}M
Interfacial tension γ_L [mN/m]	37.8	33.8 *35.7	11.1 *9.8	28.2 *26.3	38.1

Table 15 Interfacial tension of silicone oil in different aqueous solutions. [1]CMC 8.1×10^{-3} M, [2]CMC 9.1×10^{-4} M. Superscripts *[1,2] refers to data taken from [108].

Figure 6-39 illustrates the data of the maximum normalised adhesive force versus the liquid bridge volume. Figure 6-38 shows the configuration of a liquid bridge at which the maximum force was recorded.

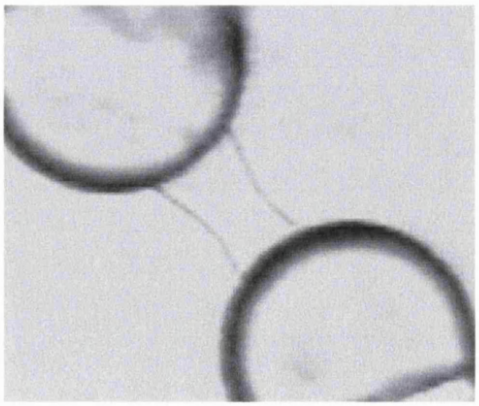

Figure 6-38 Configuration of maximum liquid bridge strength. Glass ballotini of ~50 μm diameter are held together by a silicone oil liquid bridge in a solution of 10^{-5} M CTAB and 10^{-3} M NaCl.

The quasi-static separation (~1 μm/s) made the viscous effects negligible. Figure 6-39 seems to show that there are some conditions (specifically, for both the solution containing CTAB) where the liquid bridge strength increases, reflecting the higher oil-ballotini wettability. Although contact angle measurements have not been carried out for the solution containing both CTAB 10^{-5}M and NaCl 10^{-3}M, the kinetics of adsorption of CTAB on to glass, which is favoured by the presence of salts [106] (see section 4.4.2), seems to suggest that this solution might be favourable for the increase of the liquid bridge strength. The highest value measured for the maximum force (~2.2), however, are lower than that measured between pairs of silanised particles in pure water (~3.6), which seems to show that CTAB can increase the affinity of glass towards oil only moderately. Due to the large spread of the data obtained for the mixed solution of CTAB and NaCl, more observations would be required to determine an average value of the maximum force. Table 16 summarizes the experimental conditions for the experiments presented in Figure 6-39.

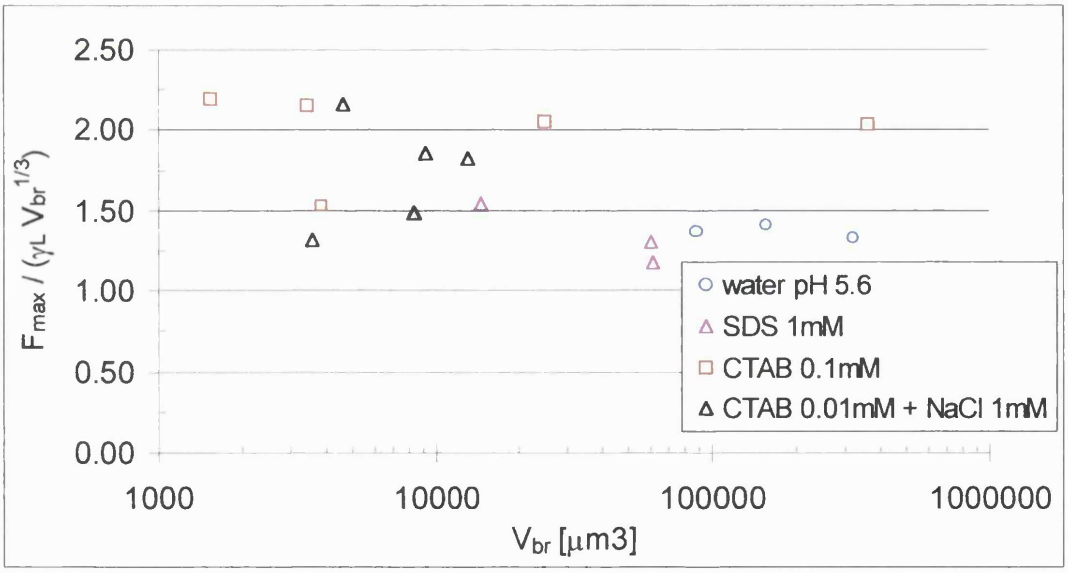

Figure 6-39 Maximum liquid bridge force between glass ballotini held by a 100 cS silicone oil liquid bridge in different aqueous solutions.

Exp.	R_A μm	R_B μm	V_{br} ($\times 10^3$ μm^3)	bulk medium	Exp.	R_A μm	R_B μm	V_{br} ($\times 10^3$ μm^3)	bulk medium
C1	53.5	52.8	87.4	a	**C9**	30.6	35.2	1.5	c
C2	55.4	56.6	156.3	a	**C10**	38.2	42.9	3.9	c
C3	50.5	52.8	60.4	b	**C11**	29.8	41.3	3.4	c
C4	49.3	52.8	61.1	b	**C12**	26.8	26	9.1	d
C5	43.6	39.0	14.4	b	**C13**	29.2	27.9	8.3	d
C6	48.2	40.5	319.4	a	**C14**	26.6	25.9	13.1	d
C7	48.2	49.3	359.7	c	**C15**	21.1	20.3	3.6	d
C8	48.2	49.3	24.9	c	**C16**	25.9	23.7	4.6	d

Table 16 Experimental conditions for the experiments presented in Figure 6-39: a) Analar water pH 5.6, b) SDS 10^{-3} M, c) CTAB 10^{-4} M, d) CTAB 10^{-5} M and NaCl 10^{-3}M.

6.3.2 The DLVO interaction

When an aqueous solution contains solid particles it is likely that various species will have different surface charges. The total free energy of the colloidal system can be lowered by reduction of the interfacial area, which leads to a more stable configuration. This reduction in area can occur by coalescence, or for solids dispersed in liquids, by coagulation. The degree of stability of a dispersed system is controlled by the rate of coagulation: the slower the rate the higher the stability. Reduction in the rate of coagulation is due to the formation of an electrical double layer at the particle-fluid interface. When two particles with the same charge approach one another their double layers interact giving rise to repulsive forces which oppose coagulation, as summarised in section 3.3.3. In some industrial applications where a particle must be recovered or separated from a solution (spherical agglomeration, froth flotation, flocculation) the coagulation is beneficial to the process and therefore its enhancement is sought.

The double layer interaction between a glass particle and a droplet of oil both submerged in an aqueous solution cannot be studied using the micro-force balance. The limitations of the MFB concern the possibility of getting a stable approaching velocity down to 50 nm/s, of determining the movement of the mobile oil-water interface near

contact, and on acquiring a stable electrical signal from the measuring micropipette. The variation of the MFB follower signal can lead to uncertainty on the position of the particle up to 75 nm, which is negligible for liquid bridge separation experiments but significant when testing double layer and van der Waals forces. The measuring resolution of the MFB will be discussed in Appendix C.1 together with all the relevant parameters of the equipment. The possibility of overcoming the limitations of the MFB have been described in section 5.2.

The experimental work with the AFM intended to measure the DLVO forces between glass and oil in water following the approach proposed by Hartley et al. [112], in which the interaction between a colloidal silica particle and a n-decane oil droplet submerged in a solution of a 1:1 electrolyte ($NaNO_3$) induced, according to the authors, the deformation of the oil-water interface. The evaluation of the interparticle distance between the colloidal probe and the apex of the droplet is usually a delicate and disputed matter. The evaluation of this distance involves the simoltaneous measurement of both the particle and the oil droplet apex positions. The latter value is quite difficult to measure due to the deformability of the oil droplet under the interaction with the rigid particle. Therefore, approximated methods are mostly used. Hartley et al. [112] proposed to assume the zero relative separation distance at the point where the value of 0.01 mN/m for the normalized force was first measured. Since the particle-to-droplet relative distance diminishes as long as the particle and the droplet are brought closer together, the relative separation becomes negative until the engulfment between the particle and the oil droplet occurs. In Figure 6-40 the results from [112] are presented. The downward arrows correspond to the position at which the colloid probe becomes engulfed by the n-decane droplet, at which point deflection data became unmeasurable. F_{def} corresponds to the onset of the droplet deformation with a consequent deviation from the theoretical force law (3.27). Figure 6-40 shows that the onset of the oil deformation occurs at larger relative separation when more diluted solutions are used. This behaviour follows the increase of the Debye length.

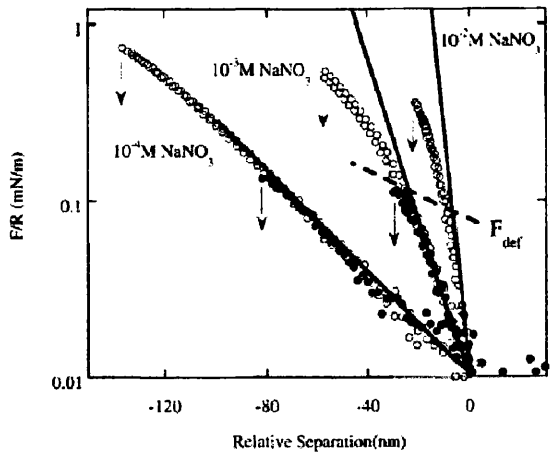

Figure 6-40 Measurement of surface forces between a silica colloid probe and an *n*-decane-aqueous interface in various concentrations of $NaNO_3$, pH 5.6. The filled and open symbols denote separate experiments. The solid lines associated with each 1:1 electrolyte concentration represent the predicted decay length for the interactions calculated from the theoretical Debye lengths (κ^{-1}) for the solutions: 10^{-4} M (30.52 nm), 10^{-3} M (9.65 nm), 10^{-2} M (3.05 nm). F_{def} is the normalised force at which the oil interface starts deforming (after [112]).

Hartley et al. [112] also studied the behaviour of the anionic surfactant (sodium dodecyl sulphate) SDS added to an electrolyte solution. It is interesting to note that with or without surfactant addition the force plot differs from the theoretical behaviour of a 1:1 electrolyte ($NaNO_3$), which was been introduced in the bulk solution as the reference for the measurements. The plot bifurcation increases with the SDS concentration, which the authors explained by an increasing deformation of the oil-water interface due to the charge interaction with the particle. Figure 6-42 shows a magnification of this phenomenon.

Mulvaney et al. [117] measured the interaction between a silica particle and an n-decane droplet in a solution of SDS and electrolyte (NaCl). They found that the interaction was always repulsive at any separation distance and compared it with the prediction from the DLVO theory. SDS is not adsorbed significantly on glass but plays a potential determining role. From electrophoresis measurements it resulted that the zeta potential of both surfaces was negative and, since the van der Waals interaction is attractive, the repulsion of the surfaces can be explained from the double layer effects acting under a constant charge model, as illustrated in Figure 6-43.

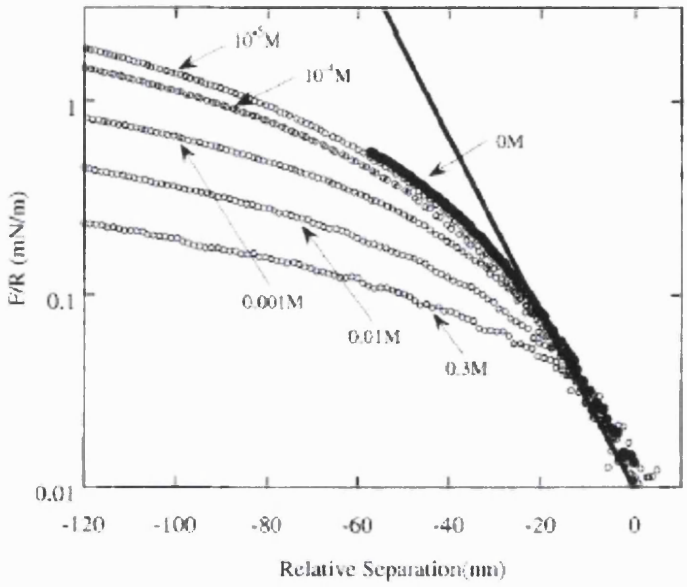

Figure 6-41 Measurement of surface forces between a silica colloid probe and the n-decane-aqueous interface in 10^{-3} M $NaNO_3$, pH 5.6, at different concentrations of SDS. Solid symbols represent data recorded in the absence of SDS for comparison. The solid line represents the predicted decay length for a 1:1 electrolyte (concentration of 10^{-3} M, k^{-1} 9.65 nm).

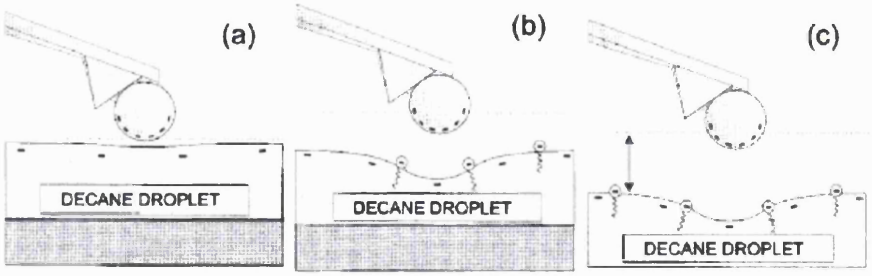

Figure 6-42 Magnification of the deformation of a n-decane-water interface due to charging effects; a) without surfactant, b) – c) at increasing SDS concentration (after [112]).

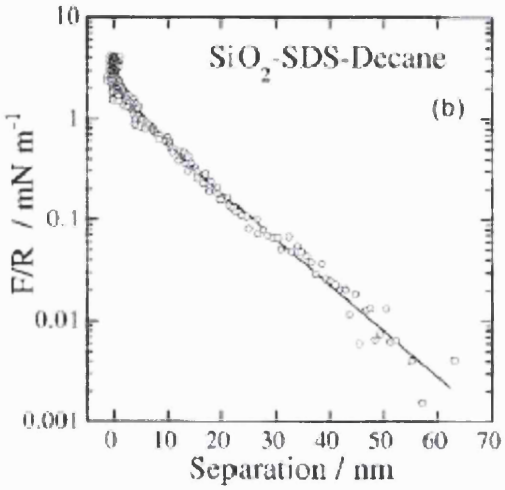

Figure 6-43 Force–separation curve for silica–water–n-decane in the presence of 1.0 mM SDS and 10 mM NaCl. The approach is repulsive at all separations and there is no adhesion during retraction in the presence of surfactant. The force curve was fitted using a Hamaker constant of 0.6 x 10^{-20} J, Ψ_0 (silica) –60 mV, Ψ_0 (oil) –30mV, κ^{-1} 10 nm. Interaction under constant surface charge conditions. The pH was 5.6 (after [117]).

Unfortunately the AFM device designed at the Chemical Engineering Department of the University of Maine for the interaction between a particle and an air bubble in a liquid medium could not detect the deformation of the oil-water interface, as has been described in 5.2.3.

The verification of the real capability of the AFM instrument resulted in deviation from the initial plan. Figure 6-44 represents a typical AFM experiment between a glass ballotini and a silicone oil droplet. The ballotini attached to the cantilever eventually gets engulfed in the droplet, which is moved upwards typically at a speed of either 50 or 100 nm/s. Since the radius of the ballotini is ~50 times smaller than that of the oil droplet, the latter is usually considered a planar surface.

The interaction between the glass ballotini and the silicone oil-water interface is determined through the analysis of the raw voltage data acquired after a laser signal is reflected back by the cantilever on which the particle is mounted (see chapter 5 for the experimental set-up).

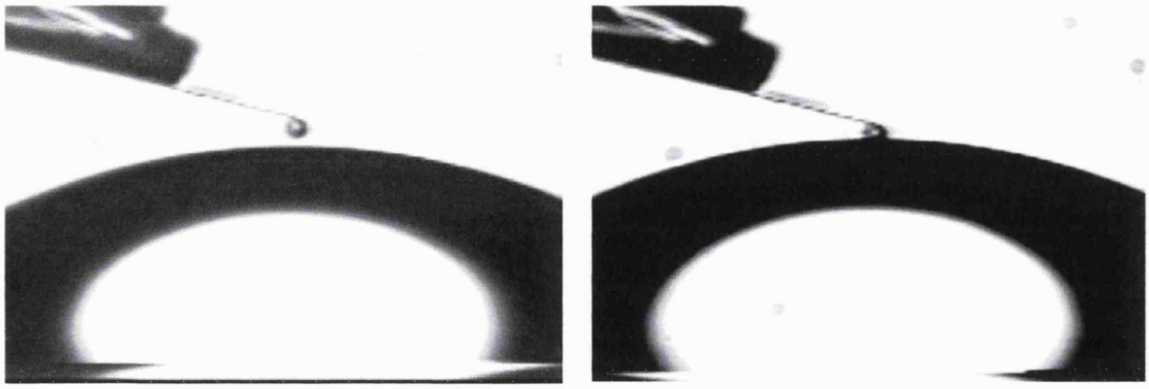

Figure 6-44 AFM experiment between a glass ballotini (R= 16.4 μm) and silicone oil droplet in a solution of NaCl 10^{-4} M. The cantilever flexibility is 0.12 N/m. The oil droplet is moved upward at 100 nm/s until the ballotini becomes engulfed in it (right picture).

In Figure 6-45 the raw data of the interaction between a glass ballotini and a silicone oil droplet in a 10^{-3} NaCl solution are presented. The graph shows three regions:

- A, where the cantilever is undisturbed
- B, where the cantilever is first displaced away and then engulfed in the silicone oil droplet due to the DLVO interaction
- C, where the ballotini and the cantilever are coupled with the upward movement of the oil droplet.

The most important region is clearly B.

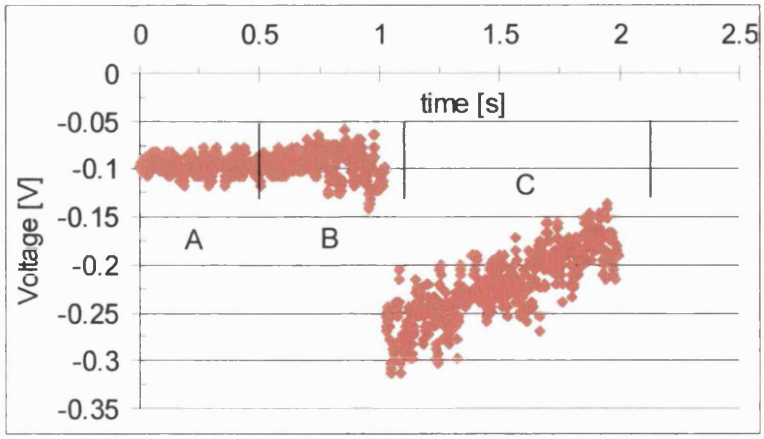

Figure 6-45 Cantilever voltage raw data acquired during the interaction between a glass ballotini (R = 16.8 μm) and a silicone oil droplet in a 10^{-3} M solution of NaCl. Data are acquired at 500 HZ. A) particle and cantilever at rest, B) DLVO interaction region, C) Cantilever moved by the upward movement of the oil droplet.

In the absence of both the cantilever and the droplet apex positions it is impossible to determine the real separation between the oil droplet and the glass ballotini. An assumption has to be made in order to determine the experimental force-separation curve and therefore the separation distance just before contact when the ballotini jumps onto the oil droplet is set to 1nm. This hypothesis seems reasonable in view of the distance at which solid bodies are considered in contact that is usually set to 0.165 nm [74]. This assumption, however, did not take into account the roughness of the particle which was not measured and which can influence the separation distance of closest approach between the particle and the oil droplet. From the raw data of Figure 6-45 it is possible to determine the experimental curve for the normalised force versus the separation distance and to compare it with the value predicted from the DLVO theory as per Figure 6-46. The determination of the experimental curve is explained extensively in Appendix D.2.

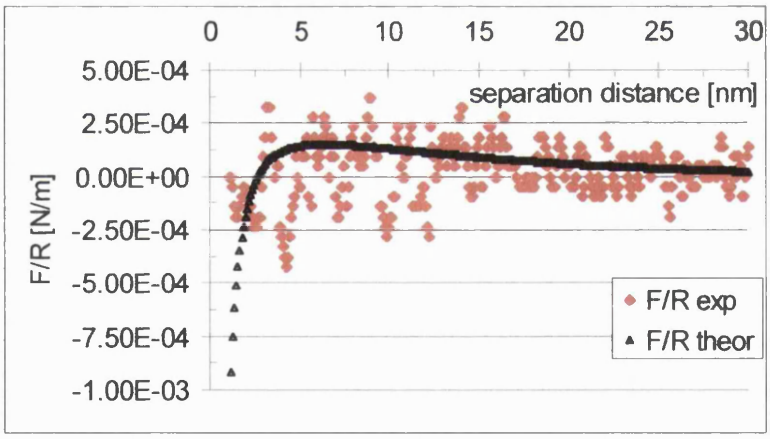

Figure 6-46 Normalised force versus separation distance for the raw data presented in Figure 6-45. The theoretical curve is calculated by the DLVO theory according to Derjaguin approximation (3.28); the Hamaker constant is set to 1x 10^{-20} J. The double layer interaction is based on a constant potential model according to [81], the potential of glass is –24.5 mV [84], that of oil is –25.2 mV [83], κ^{-1} = 9.6 nm.

In order to fit the experimental data with the DLVO prediction a value of 1 x 10^{-20} J has been set for the Hamaker constant. Unfortunately, due to lack of literature data for the silicone oil–water–glass system, it was impossible to verify the accuracy of this assumption. This value seems reasonable, however, considering that other authors [117] estimated a value of 0.6 x 10^{-20} J for the n-decane–water–silica system. For the double layer interaction the approximate solution proposed by Hogg et al. [81] has been used according to a constant potential model. The physical data used for the fitting are presented in Figure 6-46. In all the experiment the solution were not buffered with the pH varying in a narrow range between 5.6 and 5.8.

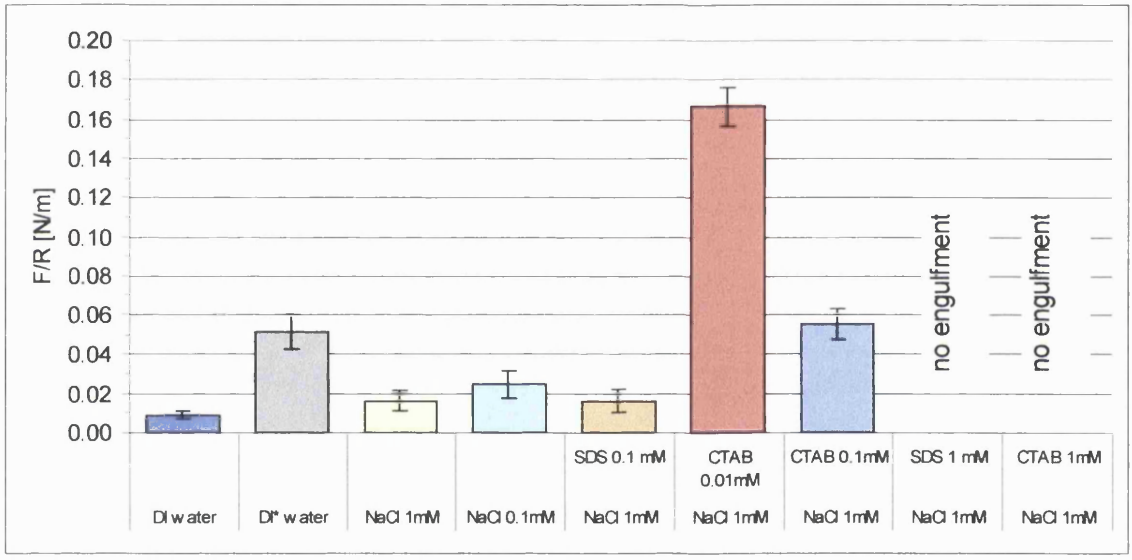

Figure 6-47 Glass ballotini to silicone oil normalised force for different solutions of electrolyte and surfactants. The interaction, if any, is measured just before the particle engulfment. DI stands for de-ionised and the asterisk refers to silanised ballotini.

The only type of analysis that seemed feasible with the AFM at the University of Maine was the evaluation of the force between the oil and the ballotini measured by the discontinuity of the cantilever voltage signal as seen in region B of Figure 6-45. The normalised force presented in Figure 6-47 can be correlated to the stability of the colloidal dispersions. These interactions can be interpreted in terms of the DLVO theory by assuming that the double layer effect is giving the major contribution to the interaction whilst the van der Waals effects stays almost constant as the solution conditions vary.

Because no zeta potential values were found in literature for the specific system of glass and silicone oil submerged in a solution of both electrolyte and surfactants, an attempt was made to measuring experimentally by electrophoresis (measurement of the movement of charged surface relative to stationary liquid by an applied electrical field) but the relative large size of the particles (40 μm diameter) prevented the measurement due to quick particle settlement due to gravity. For this reasons only qualitative investigations can be made on the zeta potential of the system of interest based on the data reported by Gu and Li [83, 84], who investigated only the effects of the CTAB and SDS surfactants. The potential data (mV) are presented in Table 17 as retrieved from their graphs (see Figure 4-13 and Figure 4-14).

As the concentration of CTAB is increased the glass surface becomes less negatively charged and eventually positive whilst the oil is increasingly positive.

The concentration for which the two surfaces have opposite signs must lead to an attractive force at any interparticle separation distances. This is shown by Figure 6-48 for a solution of 10^{-4} M CTAB, in which the potential of glass and oil are respectively –4.9 and 79.6 mV as indicated from Table 17.

CTAB	10^{-5}M	10^{-4}M	10^{-3}M	10^{-2}M
glass	-24.4	-4.9	7.3	
silicone oil	39.3	79.6	82.1	

SDS	10^{-5}M	10^{-4}M	10^{-3}M	10^{-2}M
glass		-84.4	-89	
silicone oil		-46.8	-57.1	

Table 17 Zeta potential data for glass and silicone oil submerged in solutions of SDS and CTAB as retrieved from the graphs of Gu and Li [83, 84]. The units are mV.

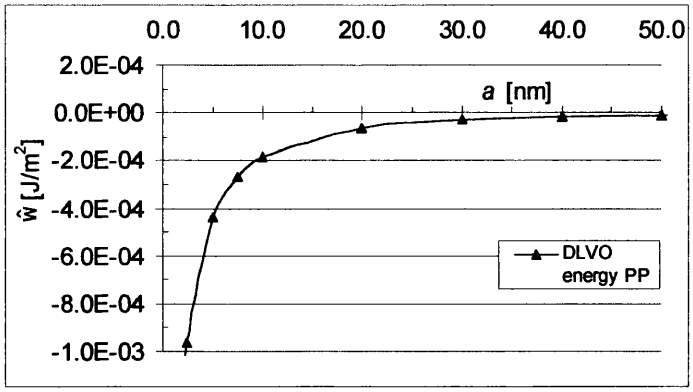

Figure 6-48 Theoretical DLVO energy per unit area versus separation distance for the interaction of a planar glass and a silicone oil surface in a solution of 10^{-4} M CTAB. The van der Waals component has been calculated by setting the Hamaker constant to 1x 10^{-20} J. The double layer interaction is based on a constant potential model according to (3.41) [81], the potential of glass Ψ_1 is –4.9 mV [84], that of oil Ψ_2 is 79.6 mV [83], κ^{-1} = 30.37 nm.

Despite the fact that the presence of the electrolyte increases the adsorption of CTAB on both the glass [106] and the oil and makes the surface potentials differ from those presented in Table 17 (yet maintain an increasing trend as the concentration of CTAB is increased), the maximum of the attraction must be still related to the presence of oppositely charged surfaces. This situation is confirmed by the graph in Figure 6-47, where the highest interaction is measured for a solution of 10^{-5} M CTAB and 10^{-3} M NaCl. As the concentration of CTAB is increased the oil and the glass become increasingly positive and the force gradually reduces until it disappears for the 10^{-3} M CTAB and 10^{-3} M NaCl solution.

Different conditions apply for the case of the anionic surfactant SDS. Because it is not significantly adsorbed on either of the two surfaces and the electrolyte does not change the kinetics of adsorption, the particle and oil potentials can be assumed, in first approximation, to be the sum of the potential induced by the SDS and the NaCl acting separately. The values for the potential are then retrieved from [83, 84] and the total DLVO interaction is calculated and presented in Figure 6-49 and Figure 6-50, which differs by a factor 2π from the normalised force F/R.

In Figure 6-49 the DLVO energy per unit area is calculated by using an approximated constant potential method [81], as per (3.41). From Figure 6-47 the normalised force F/R for the solution of 10^{-3} M NaCl and 10^{-4} M SDS is still attractive despite the potential of glass and oil being both negative (from [83, 84] these are –44.4 mV and –26.4 mV respectively).

As the concentration of SDS is increased to 10^{-3} M both the surface potentials become more negative (from [83, 84] they have values of –49 mV and –40.1 mV for the glass and the oil, respectively) and thus the force law cannot be described by the constant potential model as in Figure 6-49. In these circumstances a constant charge model is more appropriate to study the interaction during the approach.

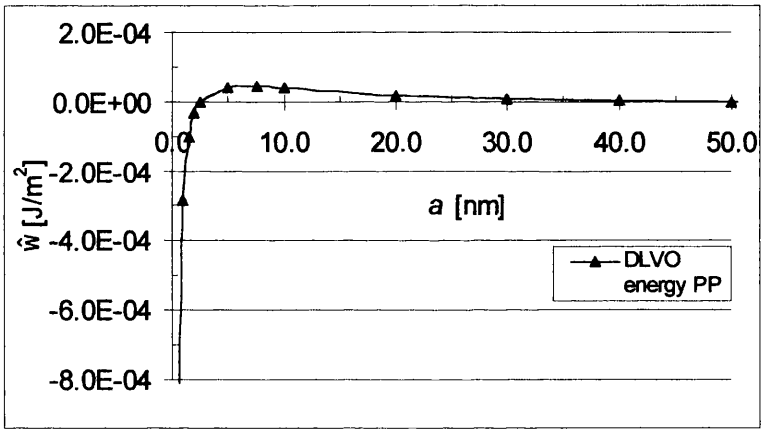

Figure 6-49 Theoretical DLVO energy per unit area versus separation distance for the interaction of a planar glass and a silicone oil surface in a solution of 10^{-3} M NaCl and 10^{-4} M SDS. The van der Waals component has been calculated by setting the Hamaker constant to 1x 10^{-20} J. The double layer interaction is based on a constant potential model according to (3.41) [81], the potential of glass Ψ_1 is –44.4 mV [84], that of oil Ψ_2 is –26.4 mV [83], κ^{-1} = 9.16 nm.

Figure 6-50 is based on the approximated constant charge solution (3.42) proposed by Gregory [82]. Because this solution is valid for surfaces of the same potential a value of –50 mV has been arbitrarily chosen. Figure 6-50 shows that the DLVO interaction is always positive down to ~0.8 nm at which point it starts to decrease slightly due to the increasing attractive effect of the van der Waals component. Similarly, a constant

charge model could be used to explain the repulsion (Figure 6-47) exhibited by oil and glass in a solution of 10^{-3} M NaCl and CTAB.

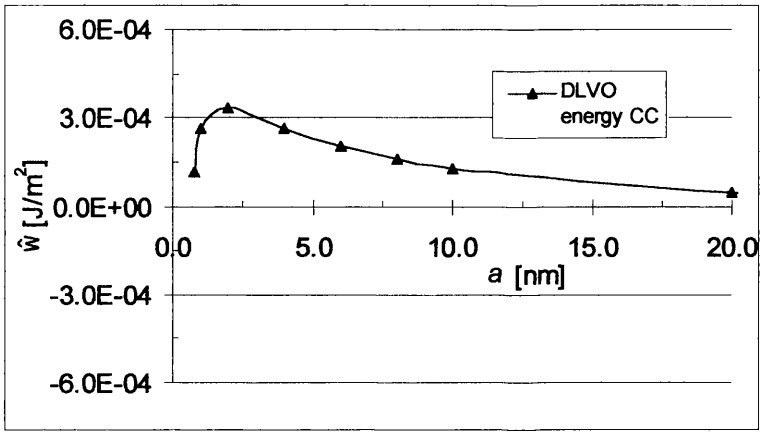

Figure 6-50 Theoretical DLVO energy per unit area versus separation distance for the interaction of a planar glass and a silicone oil surface in a solution of 10^{-3} M NaCl and 10^{-3} M SDS. The van der Waals component has been calculated by setting the Hamaker constant to 1x 10^{-20} J. The double layer interaction is based on a constant charge model according to (3.42) [82], the potentials of glass and oil are set to –50 mV, κ^{-1} = 10 nm.

Both the plots in Figure 6-49 and Figure 6-50 are calculated by assuming the value of 1 x 10^{-20} J for the Hamaker constant.

The comparison of Figure 6-47 with Figures 6–26 and 6–38 shows that the highest DLVO interaction between particles and binder does not necessarily lead to a maximum in the liquid bridge adhesion force. The adhesion of a silicone oil liquid bridge resulted higher between silanised particles (see section 6.2) rather than between untreated particles submerged in a mixed solution of 10^{-5}M CTAB and 10^{-3} M NaCl (see section 6.3.1). On the contrary the DLVO interaction of oil and a silanised particle in pure water is not as large as the case of untreated glass ballotini and silicone oil in a solution of 10^{-5}M CTAB and 10^{-3}M NaCl.

The mechanisms that influence the liquid bridge adhesion and the particle-binder DLVO interaction when the conditions of the aqueous solution vary, are very complex and have not been ascertained during the work reported here. Although the adhesive

force of a liquid bridge seems to depend on the surface energy ratio between the particle and the binder, whilst the DLVO interaction depends on the surface charges of both the particle and the binder, their mutual influence is not clear.

To elucidate which of the two effects, either liquid bridge adhesion forces or DLVO interactions, is more important in the spherical agglomeration process, experimental work should be focused on an agglomerator device to measure the grade of recovery of particles initially dispersed in an aqueous solution liquid once an organic phase is added. Monitoring the grade of particle recovery against different solution conditions and measuring the liquid bridges strength and DLVO interaction between particle/binder can explain the mutual role the basic particle interactions.

6.4 General discussion

In this chapter it has been shown that particle surface properties are of fundamental importance for processes involving the agglomeration of particles dispersed either in a gaseous or liquid bulk medium.

Surface properties affect both the strength of liquid bridges formed between particles and, in a liquid suspending medium, the DLVO interaction between the particle and the liquid binder.

The evolution and rupture of pendular liquid bridges subjected to elongation and large or moderate contact angle hysteresis have been modelled either by using simple approximations (parabolic or toroidal method) or the Young Laplace equation. The approximated models exhibited a fairly good agreement with the experimental data when used to predict geometric parameters of the liquid bridge formed between particles of good wettabilities.

The surface properties of the particles have been modified either artificially, by means of silanisation, or, for the case of a liquid suspending medium, by addition of specific

surfactants and electrolyte, which, industrially, is the only viable way to modify the particle surface properties.

The experimental results with silanised and untreated particles clearly showed that the strength of a liquid bridge is controlled by the receding contact angle between the liquid bridge and the particle. During particle separation, in fact, the liquid bridge can either recede from poorly wetted particles or stay almost fixed on well wetted particles leading to a slipping or a pinning of the contact angle, respectively. These two effects ultimately influence the profile of the liquid bridge. For the silicone oil–water–glass system the pinning resulted on silanised ballotini. When the contact angle is pinned the capillary pressure inside the bridge is comparatively lower and the liquid bridge neck is larger than the case where it recedes. The complementary effects of lower capillary pressure and thicker liquid bridges explain the higher force measured between well wetted particles.

When the particles are suspended in a liquid bulk medium, the adsorption of surfactant on the surface of both the particle and the droplet of liquid binder modifies their surface charge and therefore their electrical interaction. Particles and binder droplets that are oppositely charged lead to stronger interactions, which can be explained By the DLVO theory.

The use of surfactants decreases the interfacial tension between the suspending medium and the liquid binder, which is unfavourable for the strength of the liquid bridge. In order to obtain appropriate surfactant adsorption without affecting the binder-medium interfacial tension the use of electrolyte is advised. Electrolytes do not affect the interfacial tension but can increase the adsorption of the surfactant on both the particle and the binder droplets. The selection of the surfactant suitable for the agglomeration of specific particles through a liquid binder can be achieved via contact angle, zeta potential or AFM measurements between the particle and the binder.

Chapter 7

7 An industrial case study: predicting pharmaceutical granulation performance from micro-scale measurements

Throughout the course of the work reported in this thesis, additional investigations have been carried out in collaboration with Merck Sharp & Dohme (Hoddesdon, UK) in order to determine whether or not the MFB apparatus could be employed to test the performance of two different binders, hydroxypropyl methylcellulose (HPMC) and polyvinylpyrrolidone (PVP), commonly used to agglomerate paracetamol. The objective of this experimental investigation carried out in the gaseous bulk medium (air) was to have a technique for selecting the most appropriate binder-particle systems for optimal granulation performance. In this chapter preliminary results are illustrated and discussed.

Formulated particles are commonly agglomerated using a liquid binder, which forms liquid bridges between particle and leads to formation of larger granules. Upon drying of the granulated material, the bridges holding the granules together form strong adhesive bonds containing the polymer used to prepare the binder solution. In order to minimize formulation development time, it is desirable to make an early decision on the most suitable binder for a particular drug/excipient mixture, based on the binder's intrinsic ability to adhere the drug into granules.

In principle, the easier the liquid binder is able to redistribute among the particles during the mixing phase, the better the mechanical properties of the agglomerate resulting from formation of solid bridges during the drying phase, as indicated in Figure 7-1. The ability for a binder to distribute between particles can be seen as the result of the competitive effect between the adhesion of the binder with the particle and the cohesion

for itself. When the adhesion energy is larger then the cohesion energy, the particle is able to retain some binder after a liquid bridge is broken between particles. In the opposite condition, a particle can recede from the binder and remain unwetted. The tendency for the liquid to spread across a particle is determined by the spreading coefficient S_p introduced in (4.15) which turns into:

$$Sp = \gamma_L (1+\cos\theta) A_{SL} - 2 \gamma_L A_{br} \qquad (7.1)$$

in which the apparent contact angle, θ, should be calculated for the configuration in which the liquid bridge is under tension. The more the liquid binder is able to adhere to a particle (favoured by a high work of adhesion W_{adh}, see also (4.12)), compared to its tendency to self-associate (favoured by a large value W_{coh}, see also(4.14)) the better the redistribution of liquid on the particles.

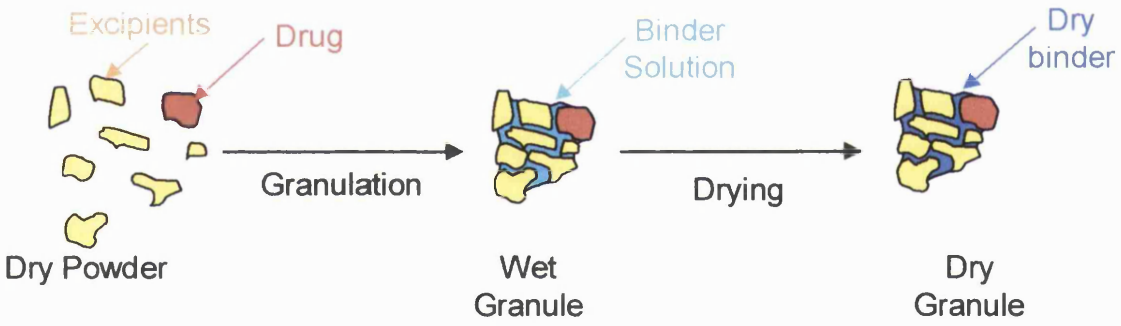

Figure 7-1 Schematic representation of the action of binder during the processes of granulation and drying.

The spreading coefficient can be qualitatively investigated by observing the amount of binder left on a particle after engulfment and withdrawal of the particle in a binder reservoir.

Possibly a direct approach to determining the relevant interactions between the liquid and solid is to measure the forces experienced between two drug particles separated by a liquid bridge using a micro-manipulator. This latter approach and the investigation of distribution coefficients, both applied to the case of HPMC and PVP solutions, is reported in the following sections.

7.1 Materials and methods

The MFB apparatus has been used to manually elongate, along their axis, liquid bridges (of either HPMC or PVP solution) formed between paracetamol crystals previously attached to the tip of elongated micropipettes similar to those presented in Figure 5-8. The movement of the flexible pre-calibrated micropipette was recorded and analysed to determine the maximum adhesion force exerted by the liquid bridges.

Paracetamol crystals and polymeric binders HPMC and PVP, in their solid state, were supplied by MSD™, which also indicated the concentrations at which the binders are normally dissolved in water for agglomeration (2.5% – 12.5% wt $_{binder}$/wt $_{H2O}$).

Liquid binder was prepared with Analar water (VWR International). In the preliminary experiments reported here, several liquid bridge separations were performed for each binder concentration. Three different concentrations (wt $_{binder}$/ml $_{H2O}$) were prepared: PVP 4%, PVP 10% and HPMC 4%. The aim was to have some comparable data between the two PVPs, with the expectation that larger forces would be measured with the higher binder concentrations. Experiments were also performed with HPMC 4%, in order to have a comparison of the performances of the two binders at the same concentration. It was not possible to use higher concentrations of HPMC, due to the very fast drying rate.

Paracetamol was supplied as small needle-shaped crystals, which could not be stuck on to the pipette tips due to their very small (<10microns) dimensions. However, amongst them were a few larger crystals, as shown in Figure 7-2 and it was these that were used in the experiments. Due to the irregularity of the crystals it was not possible to calculate their volumes from 2D images.

Two methods were used to manipulate the particle as described in Figure 7-3. Method 1 (see Figure 7-3 from stage 1 to 8) involved measurements on liquid bridges between two drug particles according to the technique already used with the ballotini.

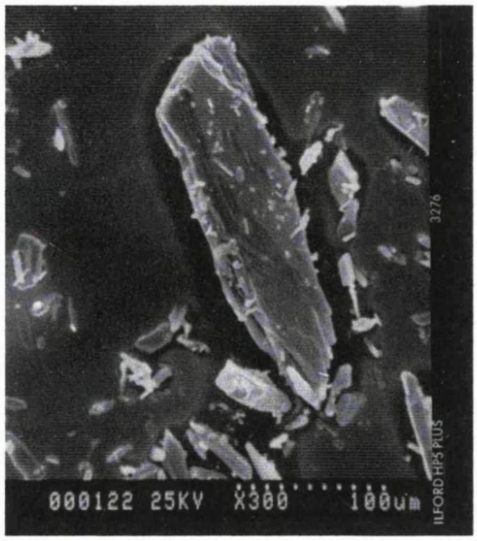

Figure 7-2 An SEM image of a crystal of paracetamol.

Because of the difficulties of forming a liquid bridge between fresh crystal surfaces and the high evaporation rate of the polymeric solutions (see later in this chapter) not all the experiments were successful and, therefore, method 1 was modified to carry out further experiments. The modification to the experimental procedure (method 2, see Figure 7-3 from stage 1 to 4) was to replace the second particle on the flexible pipette with the straight section of the feeding pipette, which was mounted at right angle with the pipette on which the crystal was attached. After a droplet of binder was formed on the feeding pipette, the crystal was then brought into contact with the droplet and, once a bridge had formed between the particle and the pipette, was pulled away, causing the straight feeding pipette to deflect. This deflection was measured directly from the images and used to calculate the adhesion force. Method 2 was also less susceptible to drying effects of the binders because of the large volume of the liquid used.

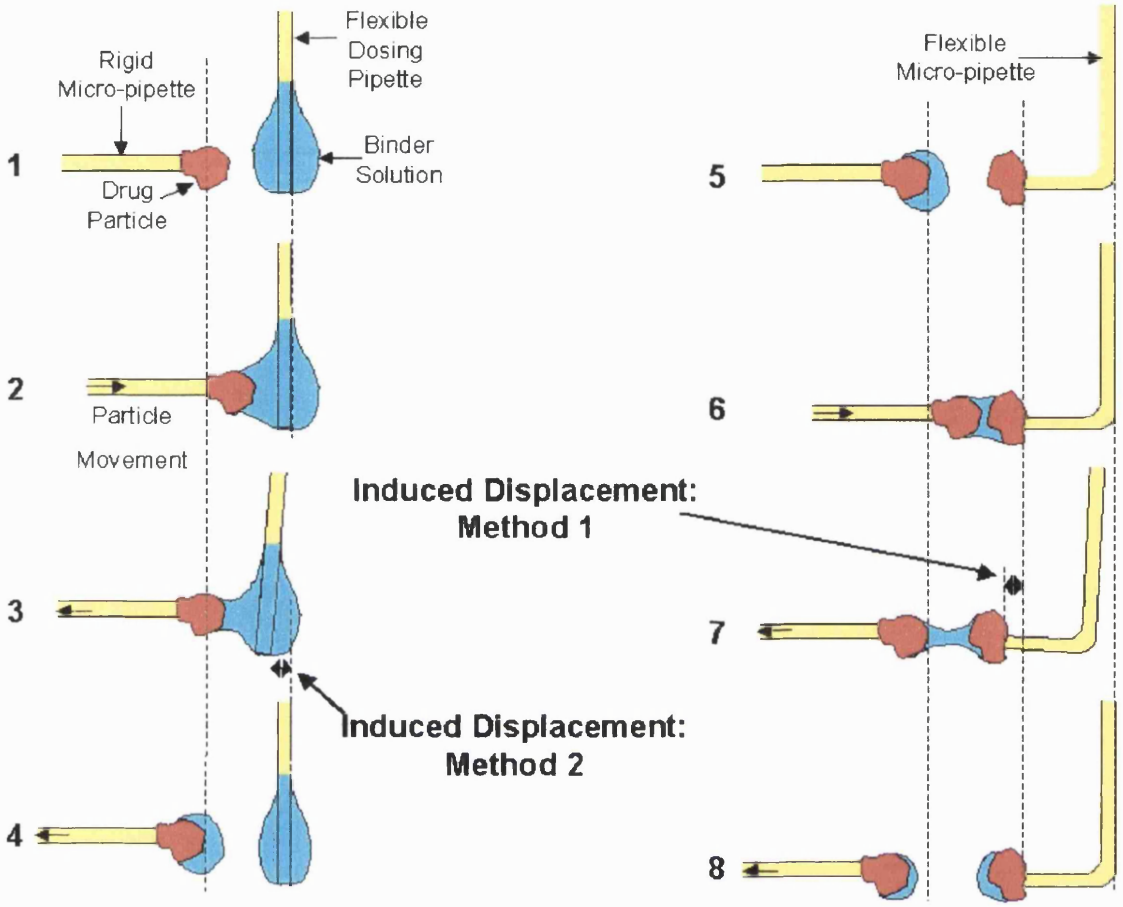

Figure 7-3 Schematic sequence of events for experiments with the micro-force balance. Two types of measurements were made, both involving measurement of the displacement of a flexible micro-pipette through movement of the rigid micro-pipette. Method 2 involved stages 1 to 4 only. In method 1, stages 1 to 4 were also used for wetting the first particle before withdrawing the dosing pipette, followed by stages 5 to 8 to contact the wet particle with a dry particle.

A common problem for the experiment carried out using method 1 and PVP was the extreme difficulty in dosing small quantities of polymeric solution onto the particles in order to form discrete liquid bridges. The small amount of liquid binder left on the crystal at each attempt of droplet formation tended to evaporate (reasonably, the solution fraction), leaving a very concentrated polymeric substrate to adhere on the paracetamol. This phenomenon can be ascertained from the last frame of Figure 7-4, where the shape of the crystals, recorded after a few contacts with the binder is much more rounded than in the initial frame.

As will be discussed in the next section, the possibility of forming a binder droplet onto the paracetamol crystals is related to the magnitude of the surface energies of the pair, which favours deposition of HPMC binders and hinders that of the PVP solutions.

The volume of liquid binder administrated between two particles (method 1) has been calculated by processing the images captured during the experiment. The technique used was to focus the feeding micro-pipette before and after the attempt to form a liquid bridge, as shown in Figure 7-4.

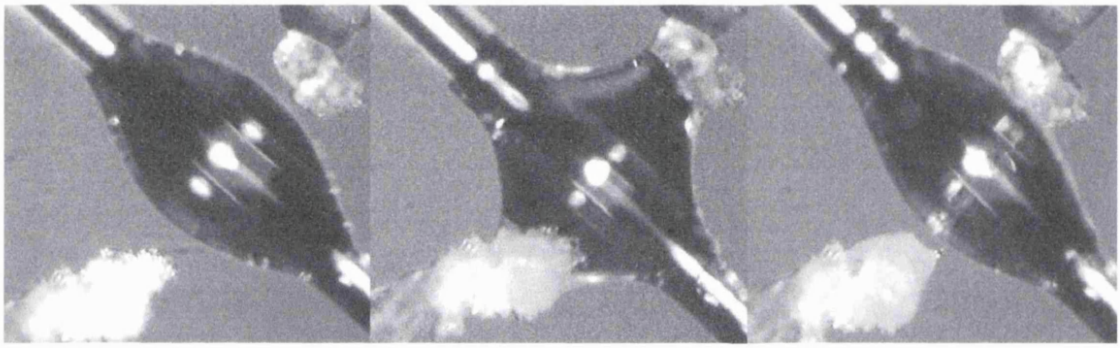

Figure 7-4 Attempt to form a liquid bridge of PVP 10% (method 1).

The profile of the liquid bridge on the feeding micro-pipette can be well approximated by a segment of a parabola and through geometric revolution it is possible to calculate the variation of volume between the two configurations. Similarly, the volume formed on the feeding pipette for experiments carried out using method 2 has been determined by calculating the integral of revolution of the segment of parabola approximating the droplet and by subtracting from it the volume of the pipette (segment of a cylinder). The axis of the pipette has been assumed as the axis of revolution for volume calculations (see Figure 7-6).

7.2 Result and discussions

Using the technique described above it was possible to take force measurements using either of the two methods. Method 2 also allowed qualitative differences between

spreading coefficients exhibited by the two polymers with respect to the paracetamol crystals to be appreciated.

7.2.1 Spreading coefficient

Figures 7–5 and 7–6 show that, on contact with the crystals, PVP solutions rapidly spread over the crystal surfaces (Figure 7-5b and d and Figure 7-6b and d).

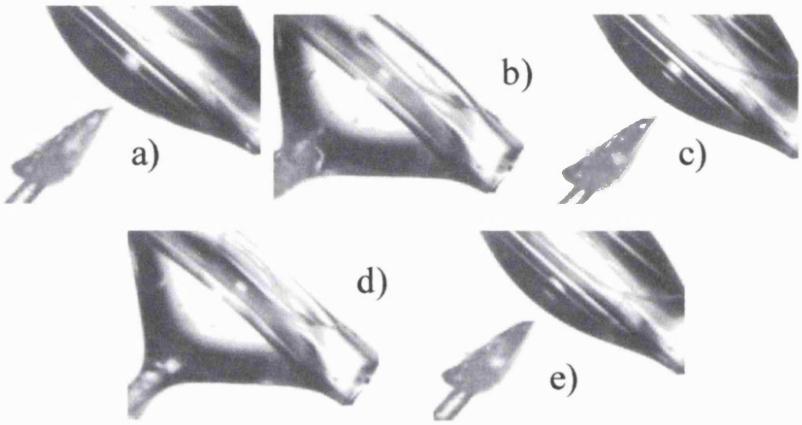

Figure 7-5 PVP 4% (a) initial approach of crystal to liquid, (b) crystal engulfed in liquid, (c) removal of crystal from liquid, (d) second contact with liquid and (e) second withdrawal from liquid.

However, on withdrawing the crystals, the liquid de-wetted the surfaces (Figure 7-5c and e and Figure 7-6c and e) leaving the profile of the paracetamol surface smoother than before wetting.

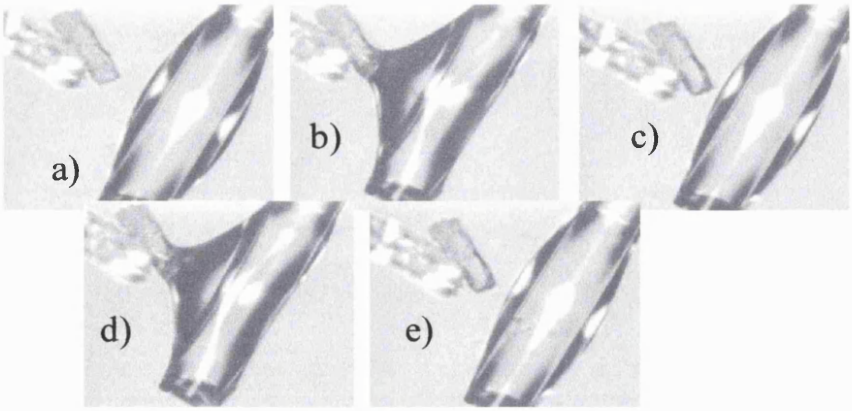

Figure 7-6 PVP 10% (a) initial approach of crystal to liquid, (b) crystal engulfed in liquid, (c) removal of crystal from liquid, (d) second contact with liquid and (e) second withdrawal from liquid.

Only after the surface profile had been changed through wetting and withdrawal, was it possible to deposit liquid of sufficient volume to form a bridge between the crystals (see Figure 7-7b). In these repeated contacts it is plausible that some PVP may have become deposited on the surface (see Figure 7-7a), improving the spreading coefficient of the coated substrate. It cannot be excluded that in the experiment shown in Figure 7-7, during the time spent to repeat the contacts between the crystals and the binder (~90s), the property of the liquid binder will have changed due to partial evaporation of the water fraction, which leaves a more concentrated reservoir of binder. This latter effect reduces the surface tension of the binder and therefore the cohesion energy in favour of the spreading coefficient adhesion energy.

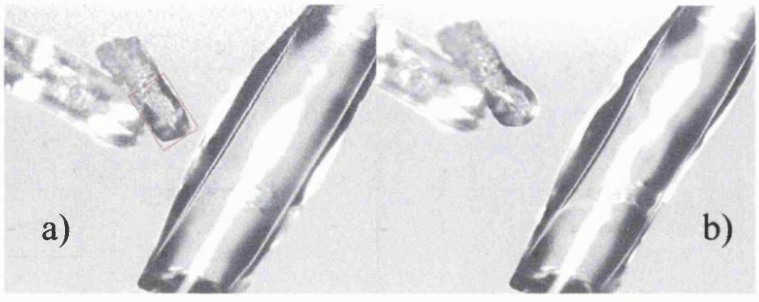

Figure 7-7 PVP 10% experiment presented in Figure 7-6 after a few contacts between the crystal and the binder; (a) dried binder has partially coated the crystals (red box) increasing the distribution coefficient , (b) some liquid binder is left on the crystal.

With the HPMC solution, the spreading coefficient was greater than for PVP, as shown in Figure 7-8, where some liquid is captured by the paracetamol crystal as shown in frames c and e. This effect can be explained by a lower lower surface tension exhibited by the HPMC 4% solution if compared with those of the PVP solutions.

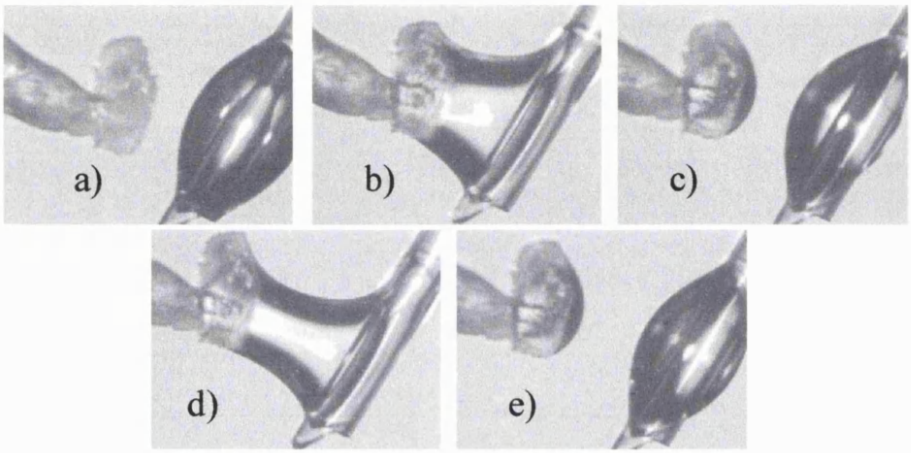

Figure 7-8 HPMC 4% (a) initial approach of crystal to liquid, (b) crystal engulfed in liquid, (c) removal of crystal from liquid, (d) second contact with liquid and (e) second withdrawal from liquid. Some binders is left on both frame (c) and (e).

The decrease of the the surface tension in (7.1) leads to an increase of the spreading coefficient S_p, assuming that the contact angle remains approximately unchanged for the two polymeric solutions. Both the liquid binders, in fact, exhibit a good wettability towards the crystal, as results from the images where the liquid bridges are under tension (Figure 7-6d and Figure 7-8d). In both configurations the liquid meniscus is very pinned and the contact angle with the crystal base line is almost zero. Contact angles, however, were only analysed qualitatively due to the irregularity of the crystal shape, which did not allow the experimental value to be calculated exactly.

For the PVP solution (Figure 7-6) the cohesive energy of the binder is higher then the crystal-to-binder interfacial energy and therefore it is thermodynamically more favourable the receding of the interface rather than the breakage of the liquid. On the contrary, for the HPMC solution (Figure 7-8), the complementary effects of interfacial

(crystal-to-binder) and cohesive (binder) energy, favour the liquid binder breakage instead of its withdrawal the crystals surface.

From a thermodynamic point of view, the rupture of the liquid meniscus, which occurs only with the HPMC solution, should be favoured by a higher spreading coefficient (7.1) exhibited by HPMC in comparison to that of the PVP solutions. As results from (7.1), the spreading coefficient, S_P, increases as the surface tension decreases, assuming the binder solutions to have a receding contact angle toward the crystal close to 0 degree. The surface tensions of the HPMC 4% and PVP 4% solutions were obtained from [118] and [119] resulting in the values of 42.4 and 62 mN/m, respectively, whilst the surface tension of the PVP 10% solution was measured with the tensiometer technique and the value 56.7 mN/m was obtained, which explains the highest S_p exhibited by the HPMC solution.

Questions arise as to whether or not the better spreading coefficient exhibited by the HPMC solution in Figure 7-8 is the result of a more favourable geometry when compared with the needle-shaped crystals used in the PVP experiments shown in Figures 7–5 and 7–6. The wetting behaviour is indeed a matter of surface properties and is not influenced by the geometry of the crystal, as can be seen in Figure 7-9, where a crystal engulfed in a PVP 10% solution is engulfed without formation of a binder droplet upon withdrawal.

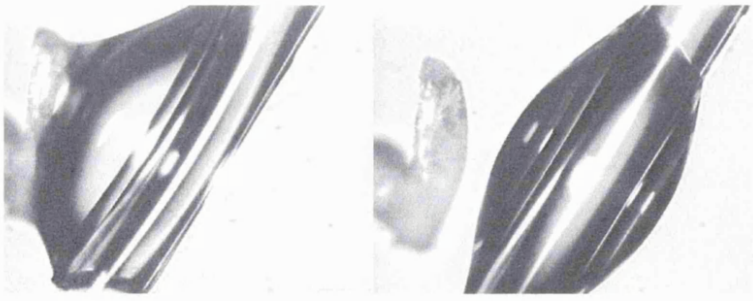

Figure 7-9 PVP 10% (left) crystal engulfed in the binder and after withdrawal (right).

7.2.2 Force of adhesion

Forces were calculated using both methods 1 and 2, and employing the techniques described in section 7.1. The volume of the liquid bridge was often quite large with respect to the volume of the crystals (see Figure 7-10).

For each sequence of separation the force was evaluated at different distances. The values plotted in Figure 7-11 were the maximum values that were measured during separation. These measurements were only made when the binder was in the liquid phase (i.e. as soon as the bridges were formed). With the present set-up it is not possible to measure the change in adhesion force with time as the bridge dries to a solid. This is principally due to the use of the deflection of the flexible micro-pipette in the calculation of the force. With solid bridges, this deflection is so great prior to rupture that it moves beyond the field of view of the microscope and therefore cannot be observed.

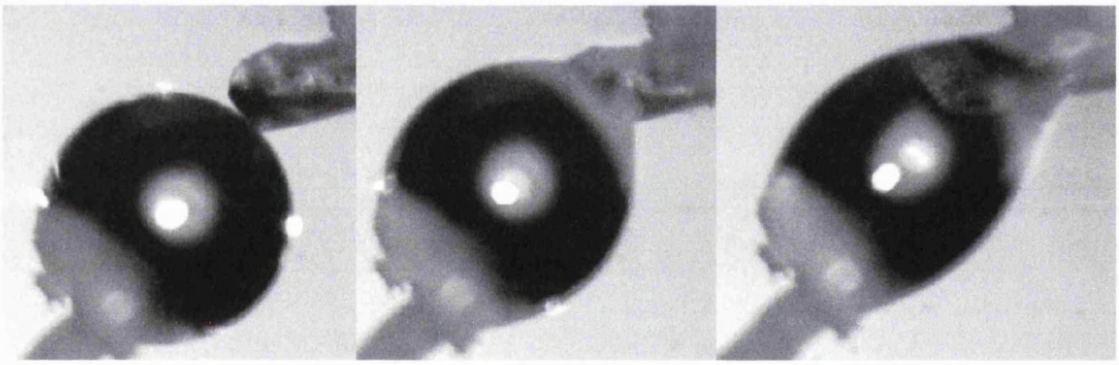

Figure 7-10 Method 1 force measurement using a PVP4% binder. Both crystals were repeatedly engulfed in the liquid binder before a liquid bridge could be formed.

Figure 7-11 shows that the two measurement methods present a reasonably good agreement only for PVP 10% and HPMC 4% solutions. Due to the difficulties experienced during the experiments carried out between two crystals (method 1), results from method 2 should be preferred for the PVP 4% solution, where significant disagreement between the two methods is observed.

A comparison of the binders' adhesive strength could be achieved by considering a dimensionless force obtained by dividing the normalised force in Figure 7-11 by the wetting perimeter of the crystal. This approach has not been used due to the difficulty of measuring the wetting perimeter of the crystals.

The plot in Figure 7-11 seems to show that the PVP 10% solution presents the highest normalised values compared with the other two binders. Table 18 shows the fitting curve for the data of the PVP 10% and HPMC 4% solutions according to method of measurement.

The selection of the optimum binder, however, should not be based only on seeking the highest value of the liquid bridge strength, but also on the wetting behaviour of the two binders toward the crystal, as will be discussed in the next section.

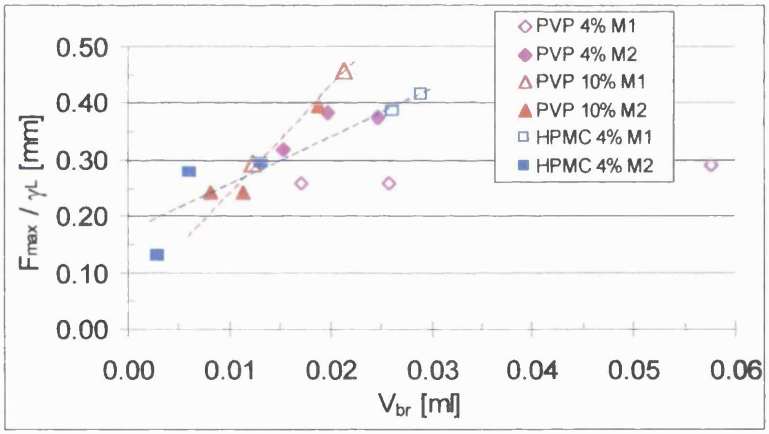

Figure 7-11 Max liquid bridge force (normalised with surface tension) versus volume of different binders for experiments of liquid bridge separation carried out using the technique indicated as method 1 (crystal-binder-crystal, M1) and method 2 (crystal-binder-pipette, M2). The trend lines for the HPMC 4% and PVP 10 % solutions fit the data obtained using both methods.

Solution	Fitting curve	R-squared value	Methods
PVP 10%	y = 17.06x +0.08	0.95	M1 + M2
HPMC 4%	y = 8.75x + 0.16	0.85	M1 + M2
PVP 10%	y = 18.04x +0.07	1	M1
HPMC 4%	y = 10.55x + 0.10	1	M1
PVP 10%	y = 15.25x + 0.09	0.91	M2
HPMC 4%	y = 13.66x + 0.16	0.62	M2

Table 18 Fitting curves for the data presented in Figure 7-11.

7.2.3 General discussion on binder selection

The work reported in this chapter has shown that the MFB device can indeed detect differences in wetting behaviour of the three binder systems investigated, which leads to differences in adhesion force. The relative importance between the spreading coefficient and the normalised adhesive strength of a single liquid bridge seems to lie in favour of the former parameter. The spreading coefficient, in fact, is responsible for the distribution of liquid binder during particle-binder mixing. The difficulty exhibited by the PVP solutions in depositing on the paracetamol crystals (see Figure 7-5 and Figure 7-6) seems to indicate that during granulation the binder would not be uniformly distributed between the paracetamol particles. Moreover, the high evaporation rate exhibited by the PVPs can rapidly increase the viscosity of the binder and contribute to enhanced differences in the binder distribution. These differences can lead to problems during the drying phase because areas of fragility result within the agglomerate.

A different scenario holds for the HPMC solution. Due to the lower value of the surface tension, a diminished adhesion results, which favours the increase of the spreading coefficient and a better wetting behaviour. The ability of the paracetamol crystals to be wetted by HPMC involves a better distribution of liquid during the particle binder mixing. In this scenario the binder is more evenly distributed within the bulk mass forming a more homogeneous mixture of particles and binder. Since the mechanical

strength of agglomerates is the result of the adhesive force of single *solid* bridges formed during the drying phase, the distribution of binder just before drying is a fundamental parameter to achieve uniform mechanical properties. Both PVP and HPMC solid bridges exhibit a very strong adhesion that was outside the measuring capability of the MFB equipment.

The wet granulation phase should promote a homogeneous binder distribution, which is a prerequisite to the final mechanical properties of the agglomerate after drying. Therefore a binder should be chosen due to its spreading ability rather then in terms of the adhesive force of single liquid bridges. This conclusion is in agreement with the work of Rowe [13] who found paracetamol to give lower granule friability, lower tablet capping index and higher tablet strength when granulated with HPMC than with PVP. Rowe explained this result in terms of the spreading coefficient of the polymer binder and based his assumption on the fact that the better the spreading of the polymer among the particle the greater the strength of adhesion within the granule. The spreading coefficient, which he measured as increasing in the order; Starch < PVP < Acacia < HPMC, can be predicted from the surface free energies of both the dry binder and the drug, usually derived from contact angle measurements of probe liquids, such as water and diiodomethane. The results presented in this work, achieved by observations of fundamental particle behaviour, suggest that the advantage of the HPMC solution can also be explained by a better distribution of the binder in the wet phase of agglomeration than that achieved by using PVP solutions.

Chapter 8

8 Conclusions and future work

This thesis has focused on has improving the understanding of the relationship between particle surface properties and liquid bridges characteristics and has discussed the consequences these phenomena may have on agglomeration processes, performed either in a gaseous or a liquid medium.

In many industrial processes particles of different surface properties are agglomerated together through the addition of a liquid binder and the resultant differences in the (particle) wetting behaviour can cause problems in the final composition of the product, since some species can be agglomerated at the expense of others.

Despite the fact that the wetting behaviour of a species can be thoroughly investigated and many studies have been concentrated on the geometry and adhesiveness of liquid bridges formed between well-wetted particles, similar studies regarding particles exhibiting differences in wetting behaviour have not received the same interest in literature. The experimental work of this thesis has therefore concentrated on the geometry (investigated in the gaseous and liquid media) and on both the force and the energy (only in the liquid bulk medium) of a liquid bridge holding pairs of particles of similar/dissimilar wetting behaviour. Differences between the two cases have been presented and the consequences on agglomeration phenomena discussed.

In the liquid bulk medium the DLVO interaction between particles and the liquid binder before their contact becomes as important as the formation of liquid bridges. In a different set of experiments conducted via an AFM, the particle-to-binder interaction has been investigated and the conditions (addition of salts/surfactants) that may favour or prevent the contact were observed and explained according to the DLVO theory.

This thesis offers a detailed investigation of liquid bridges and experimentally examines some cases that may be relevant to industrial agglomeration processes, as illustrated in the industrial case study presented in chapter 7.

8.1 Conclusions

Liquid bridge investigations, independent of the suspending phase, have been concentrated on the effect that the particle surface energy has on the geometry assumed by the liquid bridge during particle separation. Some similarities can be drawn between the two cases. It was noticed, in fact, that when a liquid bridge is formed between a good and a poorly wet particle, the liquid bridge dewets on the particle exhibiting the lower adhesion with the binder. The wettability properties of a particle clearly depend on both the suspending medium and the liquid binder used. In air, untreated glass has higher wettability than silanised glass towards glycerol, whilst in water, using silicone oil as a binder, the opposite occurs.

Between highly wettable particles liquid bridges of nodoid profiles were always observed, whilst when a good and a poorly wet particle were paired, the resulting profile, as the interparticle distance increased, switched from nodoid to unduloid, induced by binder dewetting of the poorly wet particle.

The nodoid profile of a liquid bridge can be approximated by a segment of circumference (toroid approximation) or with a new approximation based on a segment of parabola (parabolic approximation), which results in a mathematically simpler expression than that based on the toroid. In a gaseous suspending medium, toroid and parabolic approximations where compared for the prediction of the liquid bridge rupture distance based on a new geometric method that predicts the rupture of the liquid bridge to occur when the area of the bridge is equal to that of the droplets formed after bridge rupture and volume redistribution on the solid particles. This new rupture method showed good agreement with the experimental results and with the more traditional method proposed by Lian et al. [47]. However, neither of the two approximated methods was able to describe appropriately the liquid bridge transition from a nodoid to

an unduloid configuration occurring between particles of different surface energies. In this situation, polynomial curves of higher order (fourth) were used.

The profile assumed by a liquid bridge during separation is very important to the understanding of how the binder distributes on the particles after rupture, which can influence further stages of agglomeration. When dewetting occurs the post rupture binder distribution is largely in favour of the particle with higher wettability and therefore, in a mixture of powders, particles exhibiting lower wettabilities can easily segregate due to binder depletion.

Following on from the analysis of liquid bridge geometries in relation to particle surface energies in air, experimentation was also extended to the liquid bulk medium. Results similar to the situation depicted for experiments carried out in air were obtained, with dewetting always affecting the particle exhibiting lower wettability. For the experiments carried out in a liquid medium the profile of the liquid bridges has been determined using the solution of the Young Laplace equation. It was noted that higher liquid bridge forces occurred between pairs of highly wettable particles where the configuration remained nodoidal throughout separation. Conversely, when dewetting occurred on a particle and the profile turned unduloidal, higher values of the capillary pressure and thinner liquid bridge necks (both measured experimentally) led to lower bridge adhesion. The force curve during liquid bridge separation was integrated through the distance and the energy stored by the liquid bridge was calculated. As a result of these investigations, particles with lower wettability towards the binder were seen to be a disadvantage in particle agglomeration due to the formation of weaker bridges which store less energy to resist external perturbations and which, when broken, leave only a small amount of liquid binder on the particle to form other liquid bonds. The determination of the liquid bridge profile obtained from the solution of the Young Laplace equation allows the capillary pressure inside a bridge to be calculated for each configuration. This value has been used to calculate, from a thermodynamic point of view, the variation of the energy stored inside a liquid bridge between two configurations. The method, which also accounted for the pinning or the slippage of the three phase contact line at the solid-binder-suspending medium interface, gave good

agreement with values measured experimentally from integration of the force-separation curves. The results of the liquid bridge investigations obtained in a liquid medium are fully extendable, qualitatively, to the case of a gaseous suspending phase.

The interaction of particles suspended in a liquid medium is not only restricted to the formation of liquid bridges. An important aspect is also the interaction of particle and liquid binder through DLVO forces, which are very influenced by the presence of surfactants or electrolytes dissolved in solution. Questions arise on which of these two types of forces (liquid bridge or DLVO) are dominant in the mechanisms of agglomerate formation. The interaction of particles and liquid binder in an aqueous solution of different surfactants/electrolytes as well as in pure water, has been investigated using an AFM. Results showed that this interaction could be either depleted or increased according to the type and concentration of surfactant present in the solution. Both SDS and CTAB at concentrations close to the CMC prevented the contact between the binder and the particle, whilst in a more diluted solution of CTAB (also in the presence of NaCl, which increases the adsorption of surfactant onto the particle) the interaction between the particle and the binder was greately increased. This different behaviour has been explained in terms of the effect surfactant addition has on the zeta potential of the particle and the binder, which ultimately affects their double layer interaction. The comparison of the two sets of force measurements (liquid bridge and DLVO) showed that conditions favouring the liquid bridge adhesion do not necessarily maximise the DLVO interaction, whilst for the conditions where the DLVO interaction was maximised the liquid bridge adhesion did not show a maximum. Since an early decision made on the selection of process conditions ultimately influences the degree of recovery in any spherical agglomeration process, the combined effect of DLVO and liquid bridge forces is very important and more investigation is required to understand which of the two has to be sought to favour particle agglomeration.

The case study presented in chapter 7 has given some useful indications for liquid binder selection in a real process process performed in a gaseous bulk medium. Liquid bridge forces, wettability and post rupture binder distribution were tested between paracetamol crystals and different liquid binders commonly used in the pharmaceutical

industry (PVP, HPMC). Both the binders have high wettability towards paracetamol, with PVP exhibiting the highest liquid bridge forces, whilst HPMC produced a better binder distribution. Data presented in literature [13] on the final strength of paracetamol crystals either granulated with PVP or HPMC showed better mechanical properties in favour of HPMC. In the light of the observations obtained using the MFB, it seems that the liquid binder distribution inside a granule is a much more important parameter than the particle-particle adhesion. It can be concluded that the better distribution of the HPMC liquid binder confers at the moment of drying, a more homogeneously distributed net of solid bridges, which ultimately increases the mechanical properties of the agglomerate.

8.2 Future work

The work reported in this thesis has shown that fundamental investigations of particle binder interaction are a very powerful tool to improve agglomeration process performance in either liquid or gaseous media. Direct observations of the mechanisms responsible for particle interactions (obtained at the same size scale of a technological process) help in the understanding of the phenomena behind agglomeration without introducing side effects, such as gravity. Among the mechanisms that can be investigated using the MFB, the measurements of the liquid bridge strength (either axial or of shear), the post rupture liquid binder distribution, the advancing and receding contact angles (binder-to-particle), the binder drying rate and the particle shape and porosity all have an impact on the final performance of an agglomeration process. Some of these quantities can also be measured using more traditional techniques. Investigations of wettability and post rupture binder distribution can be successfully obtained on samples of larger dimensions in the cm scale. Contact angle measurements can be achieved by either using the Wilhelmy-plate technique or by direct observations of liquid binder deposited on large samples. Solid-particle adhesiveness can be measured using a processor tensiometer. These types of measurement can integrate data obtained using the MFB to have a clear picture of the phenomena behind agglomeration both at a macro (surface chemistry) and micro (particle interactions) scale.

The use of the MFB is not restricted only in investigating agglomeration problems, but can be used for example to determine the adhesiveness of particles (dirt or dust) to a cleaning cloth or to fabrics either in a gas or in a liquid bulk medium which condition can be changed by the presence of surfactants. This explains the growing interest the MFB is receiving from the industry.

The MFB used in this work, however, presents some drawbacks. It requires lots of dexterity and skills in preparing the micropipettes and performing the experiments and a considerable amount of time is also spent in forming and calibrating micropipettes. These limits are overtaken by the new generation of MFB designed to improve the original unit. In the new design, the micropipette is connected to a flexo-strip assembly, which deflects according to the force sensed by the micropipette. In this new unit the micropipette does not need to be calibrated and the measurements relies on the spring constant of the flexo-strip assembly.

Another limit of the MFB used in this work is the difficulty experienced in measuring the adhesive force using the control electronics and this limit directed most of the investigations of liquid bridge adhesion toward the image analysis technique. The control electronics can in theory drive particle separations up to 36 μm. However, when the piezo electric crystals approach their limits of contraction and expansion unpredictable behaviour has been noted. Thus to ensure accurate readings it is recommended that the crystals are operated 10% either side of the manufacturers quoted travel distances, thereby giving the electronics the capability of driving particle separation up to ~30 μm (see Figure 5-4). This limitation translates to a maximum volume administered between pairs of particles of ~6500 μm^3, as has been estimated from image analysis observation. To make the control electronics more useful for force data acquisition the measuring technique should be modified as shown in Figure 8-1.

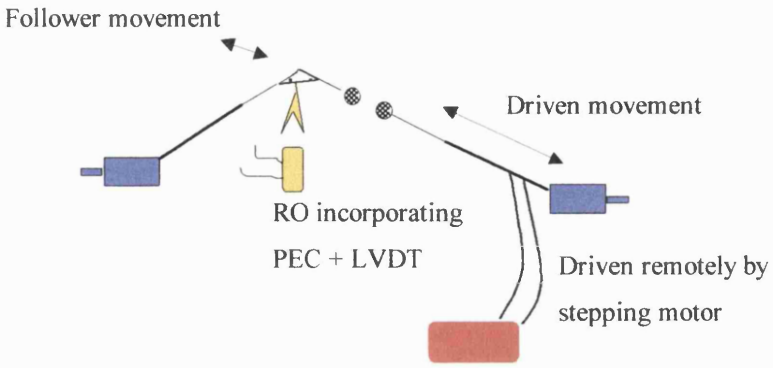

Figure 8-1 Modifications to the control electronics of the MFB in order to improve liquid bridge force adhesion.

Basically the driven movement, which controls particle separation and the follower movement, used to acquire the flexible pipette, should be separated (compared with the present configuration presented in Figure 5-3) and put on different micropipettes in order to ease the calculation of the bend deformation. The piezo electric crystals for the driven movement should be substituted by a stepping motor, which provide a better control of the speed of separation in cases where the viscosity effects on the liquid bridge adhesion are to be investigated. In this case the piezo electric crystals on the follower should be substituted with one of larger expansion. The actual value of the follower piezo expansion is 15 μm, which limits the maximum force measurable according to the flexibility and the volume of the liquid bridge dispensed between two particles. Since these two parameters are only coarsely controllable, a larger extension of the piezo follower (30 μm) would prevent maximum extension to be reached before the liquid meniscus is broken.

Future works should be directed to laboratory-scale agglomeration units to verify the properties of agglomerates in relation to the surface chemistry essays carried out on the specific binder-particle system. To achieve this both traditional surface chemistry measurements and the use of the MFB will provide a better understanding of the results obtained with the agglomeration unit. For the spherical agglomeration process measurement of particle recovery from a lab-scale mixer will help in the understanding of whether agglomeration in liquid is driven by liquid bridge adhesion or DLVO interactions.

Measurements of liquid bridges shear forces, rate of binder drying, dynamic effects induced by the viscosity of the binder, and investigations of agglomerate porosity seem to have an important role in the phenomena of agglomeration, which have not been investigated in the work reported in this thesis. Therefore they represent an interesting matter of study for future works.

Chapter 9

9 References

[1] Sherrington P.J. and Oliver R., Granulation. 1981, London, Heyden

[2] Ennis, B. J., Tardos, T. and Pfeffer, R., A Microlevel-based characterization of granulation phenomena. *Powder Technol.* **65**, 257-272 (1991).

[3] Schaafsma, S. H., Vonk, P., Sagers, P. and Kossen, N. W. F., Description of agglomerate growth. *Powder Technol.* **97**(3), 183-190 (1998).

[4] Iveson, S. M., Litster, J. D., Hapgood, K. and Ennis, B. J., Nucleation, growth and breakage phenomena in agitated wet granulation processes: a review. *Powder Technol.* **117**(1-2), 3-39 (2001).

[5] Fairbrother, R. J. A microscopic investigation of particle-particle interactions in the presence of liquid binders in relation to the mechanisms of 'wet ' agglomeration processes. 1998. London (UK), PhD thesis, University of London.

[6] Ennis, B. J. and Litster, J. D., *in* "Perry's chemical engineers' handbook." p. 20-56, New York, 1997. R. H. Perry and D. W. Green Eds.,

[7] Capes, C. E. and Danckwerts, G. C., Granule formation by the agglomeration of damp. *Trans. Inst. Chem. Eng.* **43**, T116-T130 (1965).

[8] Padday, J. F., The equilibrium and stability properties of menisci: the measurement of surface tension by exact method. *Pure & App. Chem.*, 485-494 (1976).

[9] Johnson, K. L., Contact Mechanics. 1985, Cambridge, Cambridge University Press

[10] Schubert, H., Principles of agglomeration. *Int. Chem. Eng.* **21**(3), 363-377 (1981).

[11] Lian, G., Thornton, C. and Adams, M. J., Discrete particle simulation of agglomerate impact coalescence. *Chem. Eng. Sci.* **53**(19), 3381-3391 (1998).

[12] Tardos, I. G., Khan, M. I. and Mort, P. R., Critical parameters and limiting condition in binder granulation of fine s granulation. *Powder Technol.* **94**, 245-258 (1997).

[13] Rowe, R. C., Correlation between predicted binder spreading coefficients and measured granule and tablet properties in the granulation of paracetamol. *Int. J. Pharm.* **58**(3), 209-213 (1990).

[14] Schaefer, T. and Mathiesen, C., Melt pelletization in a high shear mixer .9. Effects of binder particle size. *Int. J. Pharm.* **139**(1-2), 139-148 (1996).

[15] Plateau, J., *The figures of equilibrium of a liquid mass*, Annual report of the Smithsonian Institution, 338-369 (1864) Washington D.C.

[16] Adetayo, A. A., Litster, J. D., Pratsinis, S. E. and Ennis, B. J., Population balance modeling of drum granulation of materials with wide size distribution. *Powder Technol.* **82**(1), 37-49 (1995).

[17] Abdel-Ghani, M., Petrie, J. G., Seville, J. P. K., Clift, R. and Adams, M. J., Mechanical-properties of cohesive particulate solids. *Powder Technol.* **65**(1-3), 113-123 (1991).

[18] Pietsch, W., Size enlargement by agglomeration. 1991, Chichester, John Wiley

[19] Capes, C. E. and Darkovich, K., *in* "Encyclopedia of chemical technology." p. 222, 1997. Kirk-Othmer Eds.,

[20] Iveson, S. M. and Litster, J. D., Growth regime map for liquid-bound granules. *AIChE J.* **44**(7), 1510-1518 (1998).

[21] Mort, P. R. and Tardos, G., Scale-up of agglomeration processes using transformations. *Kona* **17**, 64-75 (1999).

[22] Kristensen, H. G., Holm, P. and Schaefer, T., Mechanichal properties of moist agglomerate in relation to granulation part 1: Deformability of moist, densified agglomerates. *Powder Technol.* **44**, 227-237 (1985).

[23] Kristensen, H. G., Holm, P. and Schaefer, T., Mechanichal properties of moist agglomerate in relation to granulation part 2: Effects of particle size distribution. *Powder Technol.* **44**, 239-247 (1985).

[24] Knight, P. C., Instone, T., Pearson, J. M. K. and Hounslow, M. J., An investigation into the kinetics of liquid distribution and growth in high shear mixer agglomeration. *Powder Technol.* **97**(3), 246-257 (1998).

[25] Keningley, S. T., Knight, P. C. and Marson, A. D., An investigation into the effects of binder viscosity on agglomeration behaviour. *Powder Technol.* **91**, 95-103 (1997).

[26] Ritala, M., Jungersen, O., Holm, P., Schaefer, T. and Kristensen, H. G., A comparison between binders in the wet phase of granulation in a high shear mixer. *Drug. Dev. Ind. Pharm.*, 1685-1700 (1986).

[27] Iveson, S. M. and Litster, J. D., Foundamental studies of granule consolidation: Part2. Quantifying the effects of binder surface tension. *Powder Technol.* **99**(3), 243-250 (1998).

[28] Eliasen, H., Kristensen, H. G. and Schaefer, T., Growth mechanisms in melt agglomeration with a low viscosity binder. *Int. J. Pharm.* **186**(2), 149-159 (1999).

[29] Kelsall, G. H. and Pitt, J. L., Spherical agglomeration of wolframite ((Fe, Mn)WO4) mineral particles. *Chem. Eng. Sci.* **42**(4), 677-689 (1987).

[30] Aplan, F. F., Coagulation and flocculation: theory and applications. 1993, New York, Dekker M

[31] Aplan, F. F., *in* "Handbook of separation techniques for chemical engineers." p. 5-33, New York, 1997. P. A. Schweitzer Eds.,

[32] Bos, A. S. and Heerens, J. J., Light backscattering as a technique to measure solids particle-size and concentration in suspension. *Chem. Eng. Commun.* **16**(1-6), 301-311 (1982).

[33] Capes, C. E. and Darkovich, K., A survey of oil agglomeration in wet fine coal processing. *Powder Technol.* **40**, 43-52 (1984).

[34] House, C. I. and Veal, C. J., *in* "Colloid and Surface Engineering: Application in the Process Industries." p. 189, London, 1992. R. A. Williams Eds.,

[35] Good, R. J. and Islam, M., Liquid bridges and the oil agglomeration method of coal beneficiation: an elementary theory of stability. *Langmuir* **7**, 3219-3221 (1991).

[36] Sadowski, Z., A study on hydrophobic aggregation of calcite aqueous suspensions. *Powder Technol.* **80**, 93-98 (1994).

[37] Sadowski, Z., Selective spherical agglomeration of fine salt-type mineral particles in aqueous solution. *Colloid. Surface.* **96**, 277-285 (1995).

[38] Sparks, B. D., Meadus, F. W., Kumar, A. and Woods, J. R., The effect of asphaltene content on solvent selection for bitumen extraction by the SESA process. *Fuel* **71** , 1349-1353 (1992).

[39] Grant, J. and Blain, T., Short sequence recycling: the factors affecting ink agglomeration and stability. *Pulp Pap-Canada* **98**(1), 51-56 (1997).

[40] Morishima, K., Kawashima, Y., Takeuchi, H., Niwa, T., Hino, T. and Kawashima, Y., Tabletting properties of bucillamine agglomerates prepared by the spherical crystallization technique. *Int. J. Pharm.* **105**(1), 11-18 (1994).

[41] Morishima, K., Kawashima, Y., Kawashima, Y., Takeuchi, H., Niwa, T. and Hino, T., Micromeritic characteristics and agglomeration mechanisms in the

spherical crystallization of bucillamine by the spherical agglomeration and the emulsion solvent diffusion methods. *Powder Technol.* **76**(1), 57-64 (1993).

[42] Ikegami, K., Kawashima, Y., Takeuchi, H., Yamamoto, H., Isshiki, N., Momose, D. and Ouchi, K., Primary crystal growth during spherical agglomeration in liquid: designing an ideal dry powder inhalation system. *Powder Technol.* **126**(3), 266-274 (2002).

[43] Kawashima, Y., Okumura, M. and Takenaka, H., Spherical crystallization - direct spherical agglomeration of salicylic-acid crystals during crystallization. *Science* **216**(4550), 1127-1128 (1982).

[44] Orr, F. M., Scriven, L. E. and Rivas, P., Pendular rings between solids: meniscus properties and capillary forces. *J. Fluid Mech.* **67**(4), 723-742 (1975).

[45] De Bisschop, F. R. E. and Rigole, W. J. L., A physical model for liquid capillary bridges between adsorptive solid spheres: the nodoid of Plateau. *J. Colloid Interface Sci.* **88**(1), 117-128 (1982).

[46] Mazzone, D. N., Tardos, G. and Pfeffer, R., The effect of gravity on the shape and strength of a liquid bridge between two spheres. *J. Colloid Interface Sci.* **113**(2), 544-556 (1986).

[47] Lian, G., Thornton, C. and Adams, M. J., A theoretical study of the liquid bridges forces between two rigid spherical bodies. *J. Colloid Interface Sci.* **161**, 138-147 (1993).

[48] Erle, M. A., Dyson, D. C. and Morrow, N. R., Liquid bridge between cylinders, in a torus, and between spheres. *AIChE J.* **17**(1), 115-121 (1971).

[49] Simons, S. J. R. and Fairbrother, R. J., Direct observations of liquid binder-particle interactions: the role of wetting behaviour in agglomerate growth. *Powder Technol.* **110**(1-2), 44-58 (2000).

[50] Pepin, X., Simons, S. J. R., Blanchon, S., Rossetti, D. and Couarraze, G., Hardness of moist agglomerates in relation to interparticle friction, granule liquid content and nature. *Powder Technol.* **117**(1-2), 123-138 (2001).

[51] Ortega, J. M. and William, G. P., Numerical methods for differential equations. 1981, Boston, Pitman

[52] Padday, J. F., The shape, stability and breakage of pendant liquid bridges. *J. Fluid Mech.* **352**, 177-204 (1997).

[53] Fisher, R. A., On the capillary forces in an ideal soil; correction of formulae given by W.B. Hines. *J. Agric. Sci.* **16**, 492-505 (1926).

[54] Mehrotra, V. P. and Sastry, V. S., Pendular bond strength between unequal-sized spherical particles. *Powder Technol.* **25**, 203-214 (1980).

[55] Pitois, O., Moucheront, P. and Chateau, X., Liquid bridge between two moving spheres: An experimental study of viscosity effects. *J. Colloid Interface Sci.* **231**(1), 26-31 (2000).

[56] Willett, C. D., Adams, M. J., Johnson, S. A. and Seville, J. P. K., Capillary bridges between two spherical bodies. *Langmuir* **16**(24), 9396-9405 (2000).

[57] Wolfram, M. and Pinter, J., Mechanical stability of liquid bridges immersed in a second liquid. *Acta Chim. Hung.* **100**, 433-448 (1979).

[58] Mason, G. and Clark, C. G., Liquid bridges between spheres. *Chem. Eng. Sci.* **20**, 859-866 (1965).

[59] Pepin, X., Rossetti, D., Iveson, S. M. and Simons, S. J. R., Modelling the evolution of pendular liquid bridges in the presence of large wetting hysteresis. *J. Colloid Interface Sci.* **232**, 289-297 (2000).

[60] Pepin, X., Rossetti, D. and Simons, S. J. R., Modelling pendular liquid bridges with a reducing solid-liquid interface. *J. Colloid Interface Sci.* **232**, 298-302 (2000).

[61] Schildecrout, S. A., Rheology of pharmaceutical granulations. *J. Pharm. Pharm. Sci.* **36**(8), 502-505 (1984).

[62] Schubert, H., Kapillaritat in porosen feststoffsystemen. 1982, Heidelberg, Springer-Verlag Berlin

[63] Chan, D. Y. C. and Horn, R. G., The drainage of thin liquid films between solid surfaces. *J. Chem. Phys.* **83**(10), 5311-5324 (1985).

[64] Cameron, A., Basic lubrication theory. 2nd ed., 1976, Chichester, John Wiley

[65] Pepin, X., Blanchon, S. and Couarraze, G., Power consumption profiles in high-shear wet granulation. II: Predicting the overwetting point from a spreading energy. *J. Pharm. Sci.* **90**(3), 332-339 (2001).

[66] Simons, S. J. R., Seville, J. P. K. and Adams, M. J., An analysis of the rupture energies of pendular liquid bridges. *Chem. Eng. Sci.* **49**(14), 2331-2339 (1994).

[67] Pitois, O., Moucheront, P. and Chateau, X., Rupture energy of a pendular liquid bridge. *Eur Phys J B* **23**(1), 79-86 (2001).

[68] Fisher, L. R. and Israelachvili, J. N., Direct measurement of the effect of menisci on adhesion: a study of the applicability of macroscopic thermodynamics to microscopic liquid interfaces. *Colloid. Surface.* **3**, 303-319 (1981).

[69] Adams, M. J., Williams, D. and Williams, J. G., The use of linear elastic fracture-mechanics for particulate solids. *J. Mater. Sci.* **24**(5), 1772-1776 (1989).

[70] Pepin, X., Blanchon, S. and Couarraze, G., Power consumption profiles in high-shear wet granulation. I: Liquid distribution in relation to powder and binder properties. *J. Pharm. Sci.* **90**(3), 322-331 (2001).

[71] Holm, P., Schaefer, T. and Kristensen, H. G., Granulation in high-speed mixers part V. Power-consumption and temperature-changes during granulation. *Powder Technol.* **43**(3), 213-223 (1985).

[72] Berbner, S. and Loffler, F., Influence of high temperature on particle adhesion. *Powder Technol.* **78**, 273-280 (1994).

[73] Seville, J. P. K., Willett, C. D. and Knight, P. C., Interparticle forces in fluidisation: a review. *Powder Technol.* **113**(3), 261-268 (2000).

[74] Israelachvili, J. N., Intermolecular & Surface Forces. 2nd ed., 1992, S. Diego, Academic Press

[75] Hamaker, H. C., The London-van der Waals attraction between spherical particles. *Physica* **4**, 1059-1072 (1937).

[76] Medout-Marere, V., A simple experimental way of measuring the Hamaker constant A_{11} of divided solids by immersion calorimetry in apolar liquids. *J. Colloid Interface Sci.* **228**, 434-437 (2002).

[77] Hunter, R. J., Foundation of colloid science. 1st ed., 1987, Oxford, Oxford Science Publications

[78] Grahame, D. C., The electrical double layer and the theory of electrocapillarity. *Chem. Rev.* **41**, 441-501 (1947).

[79] Shaw, D. J., Introduction to colloid & surface chemistry. 4th 1992, Oxford, Butterworth-Heinemann

[80] Mc Cormack, D., Carnie, S. L. and Chan, D. Y. C., Calculation of electric double-layer force and interaction free energy between dissimilar surfaces. *J. Colloid Interface Sci.* **169**, 177-196 (2002).

[81] Hogg, R., Healy, T. W. and Fuerstenau, D. W., Mutual coagulation of colloidal dispersions. *Trans Faraday Soc* **62**, 1638-1651 (1966).

[82] Gregory, J., Approximate expression for the interaction of diffuse electrical double layer at constant charge. *J. Chem. Soc. Faraday Trans. 2* **69**, 1723-1728 (1973).

[83] Gu, Y. G. and Li, D. Q., The zeta-potential of silicone oil droplets dispersed in aqueous solutions. *J. Colloid Interface Sci.* **206**(1), 346-349 (1998).

[84] Gu, Y. G. and Li, D. Q., The zeta-potential of glass surface in contact with aqueous solutions. *J. Colloid Interface Sci.* **226**(2), 328-339 (2000).

[85] Zajac, J., Trompette, J. L. and Partyka, S., Adsorption of cationic surfactants on a hydrophilic silica surface at low surface coverages: effects of the surfactant alkyl chain and exchangeable sodium cations at the silica surface. *Langmuir* **12**, 1357-1367 (1996).

[86] Chan, D. Y. C., Healy, T. W. and White, L. R., Electrical double layer interaction under regulation by surface ionization equilibria. Dissimilar amphoteric surfaces. *J. Chem. Soc. Faraday Trans. 1* **72**, 2845-2865 (1976).

[87] Fowkes, F., Attractive forces at interfaces. *Ind. Eng. Chem.* **56**, 40-52 (1964).

[88] van Oss, C. J., Good, R. J. and Chaudhury, M. K., Additive and non additive surface tension components and the interpretation of contact angles. *Langmuir* **4**, 884-891 (1988).

[89] Kwock, D. Y., Li, D. and Neumann, A. W., Evaluation of the Lifschitz-van der Waals/acid-base approach to determine interfacial tensions. *Langmuir* **10**, 1323-1328 (1994).

[90] Della Volpe, C. and Siboni, S., Some reflections on acid-base solid surface free energy theories. *J. Colloid Interface Sci.* **195**, 121-136 (1997).

[91] Murmur, A., Line tension effect on contact angles: axisymmetric and cylindrical systems with rough or heterogeneous surfaces. *Colloid. Surface.* **A 136**, 81-88 (1998).

[92] Li, D., Drop size dependance of contact angles and line tensions of solid-liquid systems. *Colloid. Surface.* **A 116**, 1-23 (1996).

[93] Drelich, J., The significance and magnitude of the line tension in three-phase (solid-liquid-fluid) systems. *Colloid. Surface.* **A 116**, 43-54 (1996).

[94] Li, D. and Steigmann, D. J., Positive line tension as a requirement of stable equilibrium. *Colloid. Surface.* **A 116**, 25-30 (1996).

[95] Scheludko, A. D., Condensation of vapors on spherical nuclei and the line tension effect. *J. Colloid Interface Sci.* **104**(2), 471-488 (1985).

[96] Murmur, A., The actual contact angle on a heterogeneous rough surface in three dimensions. *Langmuir* **14**(18), 5292-5297 (1998).

[97] Joanny, J. F. and De Gennes, P. G., A model for contact angle hysteresis. *J. Chem. Phys.* **81**(1), 553-562 (1984).

[98] Schwartz, L. W. and Garoff, S., Contact angle hysteresis on heterogeneous surfaces. *Langmuir* **1**, 219-230 (1985).

[99] Adamson, A. W., Physical chemistry of surfaces. 6th ed., 1997, New York

[100] Extrand, C. W., A thermodynamic model for contact angle hysteresis. *J. Colloid Interface Sci.* **207**, 11-19 (1998).

[101] Quere, D., Azzopardi, M. J. and Delattre, L., Drops at rest on a tilted plane. *Langmuir* **14**(8), 2213-2216 (1998).

[102] Hough, D. B. and Rendall, H. M., *in* "Adsorption from solution at the solid/liquid interface." p. 247, London, 1983. G. D. Parfit and C. H. Rochester Eds., Academic Press

[103] Fuerstenau, D. W., Streaming potential studies on quartz in solution of aminium acetate in relation to the formation of hemicelles at the quartz-solution interface. *J. Chem. Phys.* **60**, 981-985 (1958).

[104] Somasundaran, P. and Krishnakumar, S., Adsortion of surfactants and polymers at the solid-liquid interface. *Colloid. Surface.* **123-124**, 491-513 (1997).

[105] Rosen, M. J., Surfactants and interfacial phenomena. 1978, New York, John Wiley

[106] Atkin, R., Craig, V. S. J. and Biggs, S., Adsorption kinetics and structural arrangments of cationic surfactants on silica surfaces. *Langmuir* **16**, 9374-9380 (2000).

[107] Pagac, E. S., Prieve, D. C. and Tilton, R. D., Kinetics and mechanisms of cationic surfactant adsorption and coadsorption with cationic polyelectrolytes at the silica-water interface. *Langmuir* **14**(2333), 2342 (1998).

[108] Gu, Y. G. and Li, D. Q., Measurments of contact angles between an oil-water interface and a fiber by the ACDPAC technique. *J. Colloid Interface Sci.* **206**, 288-296 (1998).

[109] Paulsen, F. G. Modeling and experimental studies of particle-bubble attachment in flotation systems. 1996. Orono (ME) US, PhD thesis, University of Maine.

[110] Berg, S. R. Measurement of long-range hydrophobic attraction forces during bubble/particle attachment. 2000. Orono (ME) US, PhD thesis, University of Maine.

[111] Cleveland, J. P., Manne, S., Bocek, D. and Hansma, P. K., A non destructive method for determining the spring constant of cantilevers for scanning probe microscopy. *Rev. Sci. Instrum.* **64**(2), 403-405 (1993).

[112] Hartley, P. G., Grieser, F., Mulvaney, P. and Stevens, G. W., Surface forces and deformation at the oil-water interface probed using AFM force measurement. *Langmuir* **15**(21), 7282-7289 (1999).

[113] Ennis, B. J., Jinlang, L., Tardos, G. I. and Pfeffer, R., The influence of viscosity on the strength of an axially strained pendular liquid bridge. *Chem. Eng. Sci.* **45**, 3071-3088 (1990).

[114] Iveson, S. M., Page, N. W. and Litster, J. D., The importance of wet powder dynamic mechanical properties in understanding granulation., *Proc. 7th Int. Simp. Agglom. 2, 541-547* Albi, France, 29th - 31st May (2001).

[115] Rossetti, D., Pepin, X. and Simons, S. J. R., Rupture energy and wetting behaviour of pendular liquid bridges in relation to the spherical agglomeration process. *J. Colloid Interface Sci., Accepted for publication*

[116] Rossetti, D. and Simons, S. J. R., A micro-scale investigation of liquid bridges in the spherical agglomeration process. *Powder Technol.* **130**((1-3)), 49-55 (2003).

[117] Mulvaney, P., Perera, J. M., Biggs, S., Grieser, F. and Stevens, G. W., The direct measurement of the force of interaction between a colloid particle and an oil droplet. *J. Colloid Interface Sci.* **183**, 614-616 (1996).

[118] Chang, S. A. and Grey, D. G., The surface tension of aqueous hydroxypropyl cellulose solutions. *J. Colloid Interface Sci.* **67**(2), 255-265 (1978).

[119] Huang, Q. R. and Wang, C. H., Surface laser light scattering studies of the air/poly(N-vinyl- 2-pyrrolidone)-water solution interface. *J. Chem. Phys.* **105**(15), 6546-6552 (1996).

Appendix A: Surface chemistry data

The present section is divided in to three parts and shows surface tension (with or without addition of surfactant), interfacial tension and contact angle readings which were relevant to the experimental work reported in the main body of the thesis.

A.1 Surface tension measurements

Surface tension data were measured with the Kruss K12 tensiometer according to (5.4) using a platinum plate 19.9 mm wide and 0.2 mm thick with a wetting perimeter, p, of 40.2 mm. Platinum presents high wettability towards all liquids and therefore the resulting contact angle is zero. Equation (5.4) modifies into (A.1).

$$F = p\,\gamma \qquad \text{(A.1)}$$

The surface tensions of Analar water, glycerol diiodomethane and a few silicone oils of different viscosities have been measured at room conditions (23 °C) and are presented in Table 19. The data agree with values declared by the material supplier (VWR International).

Test liquid	Surface tension [mN/m]	[1]Surface tension [mN/m]
Analar water	72.65	72.7
Glycerol	63.11	63.2
Diiodomethane	51.1	50.8
Silicone oil cS 50	20.80	20.8
Silicone oil cS 100	20.87	20.9
Silicone oil cS 200	20.94	21

Table 19 Surface tension values of liquids. [1]Data from supplier. The viscosity of the silicone oil is expressed in cS = mm^2/s, (kinematic viscosity).

The Kruss K12 tensiometer has also been used to measure the surface tension of water at increasing concentration of an anionic surfactant (SDS), presented in Figure A–1. The surface tension of the solution decreases until the formation of micelles prevents further reduction. The critical micelles concentration (CMC) has been calculated to occur at 8.6 x 10^{-3} M, in agreement with data available from [108] (8.1 x 10^{-3}M).

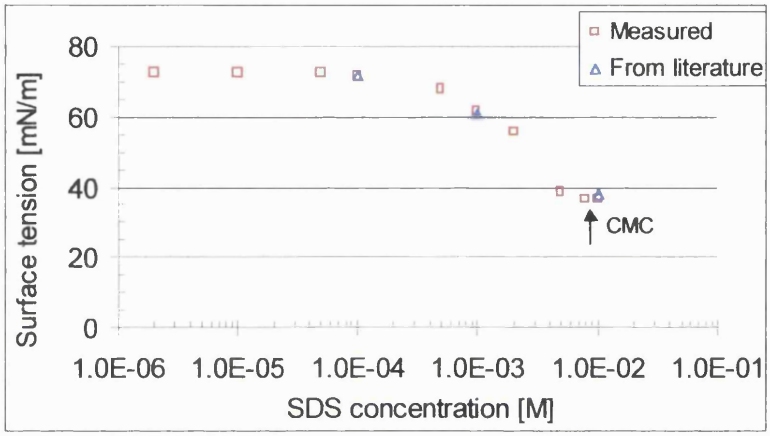

Figure A–1 Measured surface tension of water at increasing concentration of an anionic surfactant (SDS). Literature data are available from [108]. CMC occurs at ~8.6 x 10^{-3} M.

A.2 Interfacial tension measurements

The interfacial tension between two immiscible liquids or between a liquid and a solid can be determined by applying the polar-dispersive surface tension decomposition introduced in (4.3). It is legitimate to generalize (4.4), introduced to calculate the interfacial tension between two phases of which at least one has a complete dispersive nature, with (A.2), where no restriction is imposed on the nature of the two phases, having a surface tension which can be a combination of polar and dispersive molecular effects.

$$\gamma_{12} = \gamma_1 + \gamma_2 - 2\sqrt{\gamma_1^d \gamma_2^d} - 2\sqrt{\gamma_1^p \gamma_2^p} \qquad (A.2)$$

Equation (A.2) has been used to calculate the interfacial tension of a water-oil interface. In order to do so the polar and dispersive components of the surface tension of both oil and water are required. The case of water is well detailed in literature [89] and γ^d and γ^p result in the value of 21.7 and 51 mN/m, respectively. The components of silicone oil (100cS) were determined experimentally using the technique proposed by van Oss et al. [88]. By measuring the equilibrium contact angle between a dispersive solid and the silicone oil, it is possible to rearrange (4.4) and (4.7) into (A.3) to obtain the expression for the dispersive component of the silicone oil surface tension, γ_L^d , as a function of the surface energy of the solid (dispersive only), γ_S, the equilibrium contact angle, θ, and the total surface tension of the silicone oil, γ_L:

$$\gamma_L^d = \frac{\gamma_L^2 (1+\cos\theta)^2}{\gamma_S} \qquad \text{(A.3)}$$

Using a paraffin film (parafilm M, obtained from American National Can^{TM}) as the totally dispersive substrate (γ_S = 22.6 mN/m, obtained from private communication) the advancing contact angle with silicone oil 100 cS (γ_L = 20.9 mN/m) was calculated and resulted in the value of 31.0 degrees. Using (A.3), the dispersive component of the silicone oil surface tension resulted in the value of 16.6 mN/m, which, by means of (4.3), allowed the calculation of the value 4.3 mN/m for the polar component, γ_L^p.

Using (A.2) the water-oil interfacial tension was calculated as of 27.6 mN/m, which is quite different from the value of 37.8 mN/m measured experimentally with the Kruss K12 tensiometer and from that available in the literature [108] (39.3 mN/m), obtained between de-ionised water and a silicone oil 200 cS. Disagreement with experimental data may be due to inaccuracy of (A.2) for modelling the interfacial tension. A more accurate approach would require the use of (4.6), which uses a different definition for the polar part of the surface tension made according to Lewis acid/base components. This method , however, does not guarantee the value of the silicone oil-water interfacial tension to be determined, hence, experimental interfacial tension data were always

obtained using the Kruss K12 tensiometer. Data of the water-oil interfacial tension in presence of surfactants/electrolytes have been reported in section 6.3.1, Table 14.

A.3 Contact angle measurements

During the work reported in this thesis, contact angle measurements were taken in many different ways. Images analysis has been used to obtain readings, in both liquid and gaseous media, either from liquid binder menisci at the 3-phase contact line or from a binder droplet deposited on a particle. These measurements have already been shown in chapter 6 for both suspending media. The Kruss K12 tensiometer together with dedicated software was also used to take measurements of advancing and receding contact angles between plate samples and test liquids. These measurements are reported in Table 20. During all the following measurements the plate was immersed in the test liquid at 0.15 mm/s.

Solid	Test liquid	Adv. contact angle [degree]	Rec. contact angle [degree]
Glass	Analar water	0	0
	Glycerol	60.2	0
Silanised glass	Analar water	95.8	84.9
	Glycerol	92.9	80.9
	Diiodomethane	68.5	–
Paraffin (Parafilm)	Silicone oil cS 100	31.0	13.3

Table 20 Advancing and receding contact angle measurements obtained using the the Kruss K12 tensiometer.

Diiodomethane adhered very strongly to the silanised glass slide (during the immersion phase of the experiment when the advancing angle is measured) and left an oily film which prevented accurate measurements of the receding angle. After the sample is dipped in the liquid the movement of the electrobalance is inverted and the sample is retracted from the liquid while the receding contact angle is measured. During this phase, the meniscus of diiodomethane slid on the oil film formed during the advancing

phase instead of receding from the solid. The receding phase contact angles where therefore higher than the advancing angles and thus have not been presented in Table 20. Data between glass (either untreated or silanised) and glycerol are in agreement with values obtained by image analysis between glass ballotini and glycerol and presented in section 6.1.2. The lower receding contact angle measured using untreated glass and the tensiometer in comparison to data presented in Figure 6-8 maybe caused by a different finishing of the two surfaces and different method of liquid meniscus deformation, in one case with the electrobalance and in the other by particle separation.

Appendix B: Micropipette calibration

This section explains the technique used to calculate the micropipette flexibility, which is used to convert the deflection of the micropipette (during liquid bridge separation) into the force exerted by the liquid bridge. This method can be used to calibrate pipettes of different geometries for both the liquid and the gaseous bulk media experiments.

To measure the micropipette spring constant, the pipette is mounted in the micromanipulator (Figure B–1, left). The thin pipette is then brought into focus and the value on the microscope's fine focus micrometer noted.

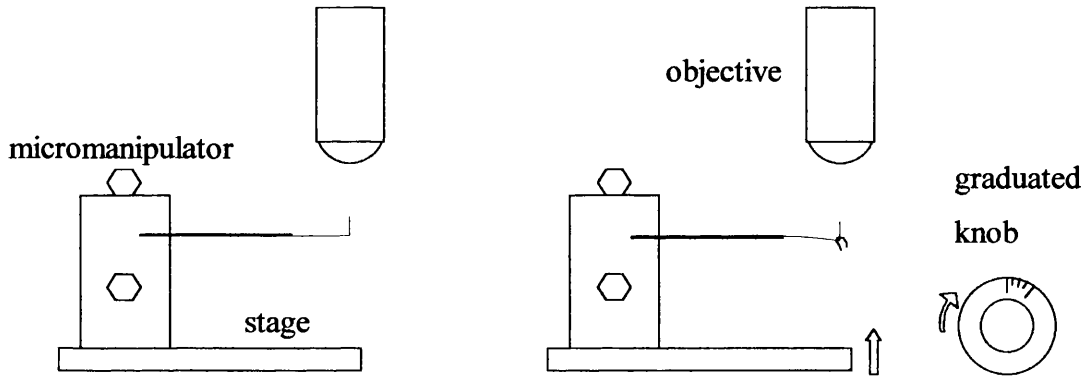

Figure B–1 Left, flexible micropipette mounted in the micromanipulator and right, weight hung on the micropipette.

A series of weights are hung over the 90° bend in the flexible micropipette (Figure B–1, right) and the resulting displacement measured by bringing the pipette tip back into focus and noting the new micrometer reading. The knob scale is divided into 100 parts and a full rotation of the knob drives a vertical movement of 0.1 mm of the stage. One graticule on the knob, therefore, resolves 1 μm. The weights are small lengths of electrical nichrome wire bent into horseshoe shapes. Their mass was measured to the nearest one thousandth of a gram using a balance. Their addition and removal is facilitated using long nosed tweezers.

For each weight the reading is repeated three times and an average taken. A force displacement table is then produced (Table 21). The spring constant is calculated for each weight and an average value is taken.

Weight (μN)	Deflection (μm)	Spring constant (μN/μm)
0	0	
31.3	96	0.326
48.0	150	0.320
66.6	205	0.325
75.4	230	0.328
90.1	277	0.325
Average		**0.325**

Table 21 Weight-deflection data for glass micropipette calibration.

Appendix C: Additional MFB data for electronic force measurements

This section helps with measuring the adhesiveness of liquid bridges using the electronic control provided with the MFB. This section focuses on the control electronic, on the code used for the data acquisition, on the calibration of voltage data into readings of pipette movement and in the spreadsheet used to determine the liquid bridge force-separation plot data.

C.1 Control Electronics

The electronic equipment (Figure C–1), which controls the linear variable differential transformers (LVDT) and the piezoelectric crystals (PEC) on the adapted stage and provides the interface for the A/D board in the computer, was designed and built by Roger Murphy of the Department of Physics at the University of Bristol. It consists of a driven channel and a follower channel.

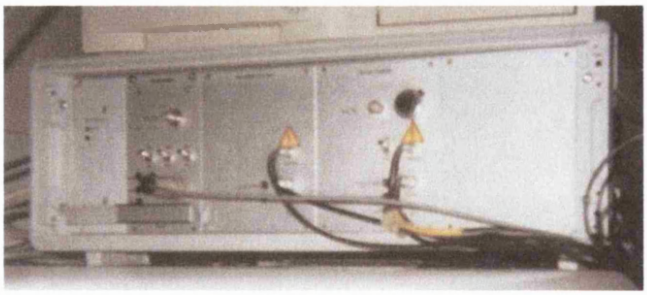

Figure C–1 Photograph of the control electronics.

The driven channel drives a Physic Instrument (PI) P810.30 (30μm expansion) PEC, its expansion monitored by a PI E115.21 (±0.5mm) LVDT. A single channel control module PI E810.10, which provides LVDT conditioning, error control amplification, HV (high voltage) drive amplification and a DC/DC converter, is used to control the

driven channel. It is due to the non linearity and hysteresis associated with PECs that such a control system is required.

Local control of this driven channel is provided by means of a front panel potentiometer. Alternatively, signal control may be exerted via either the BNC socket on the front panel or via the multiway signal I/O (input/output) "D" connector on the rear panel. A ±5V signal level change causes full expansion and contraction of the PEC. Note that all input and output signals have alternative access via the 15way "D" socket on the rear panel. Pin allocation is shown in Table 22. These are linked to the A/D board in the computer.

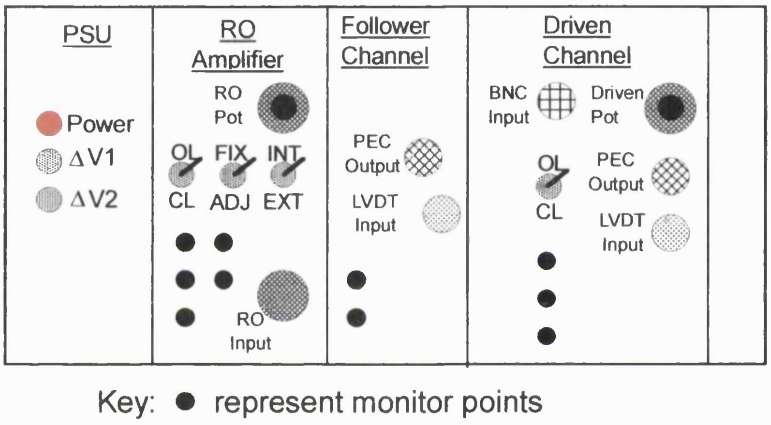

Figure C–2 Schematic of front panel of control electronics.

PIN	SIGNAL	PIN	SIGNAL
1	RO MON 1 (reflecto-optical monitor)	9	GROUND
2	RO MON 2 (reflecto-optical monitor)	10	GROUND
3	RO EXTERNAL INPUT	11	GROUND
4	LVDT SENSE FOLLOWER CHANNEL	12	GROUND
5	V_{OUT}/100 FOLLOWER CHANNEL	13	GROUND
6	LVDT SENSE DRIVEN CHANNEL	14	GROUND
7	V_{OUT}/100 DRIVEN CHANNEL	15	GROUND
8	V_{IN} DRIVEN CHANNEL		

Table 22 Pin allocation for 15 way "D" socket on rear of control electronics.

The movement of a pipette attached to the driven assembly can be measured by attaching a small mirror at the point of interest, in this case at the bend. The follower channel can then be set up to follow the movement of the edge of the mirror. A schematic of the overall control circuit configuration is shown in Figure C–3.

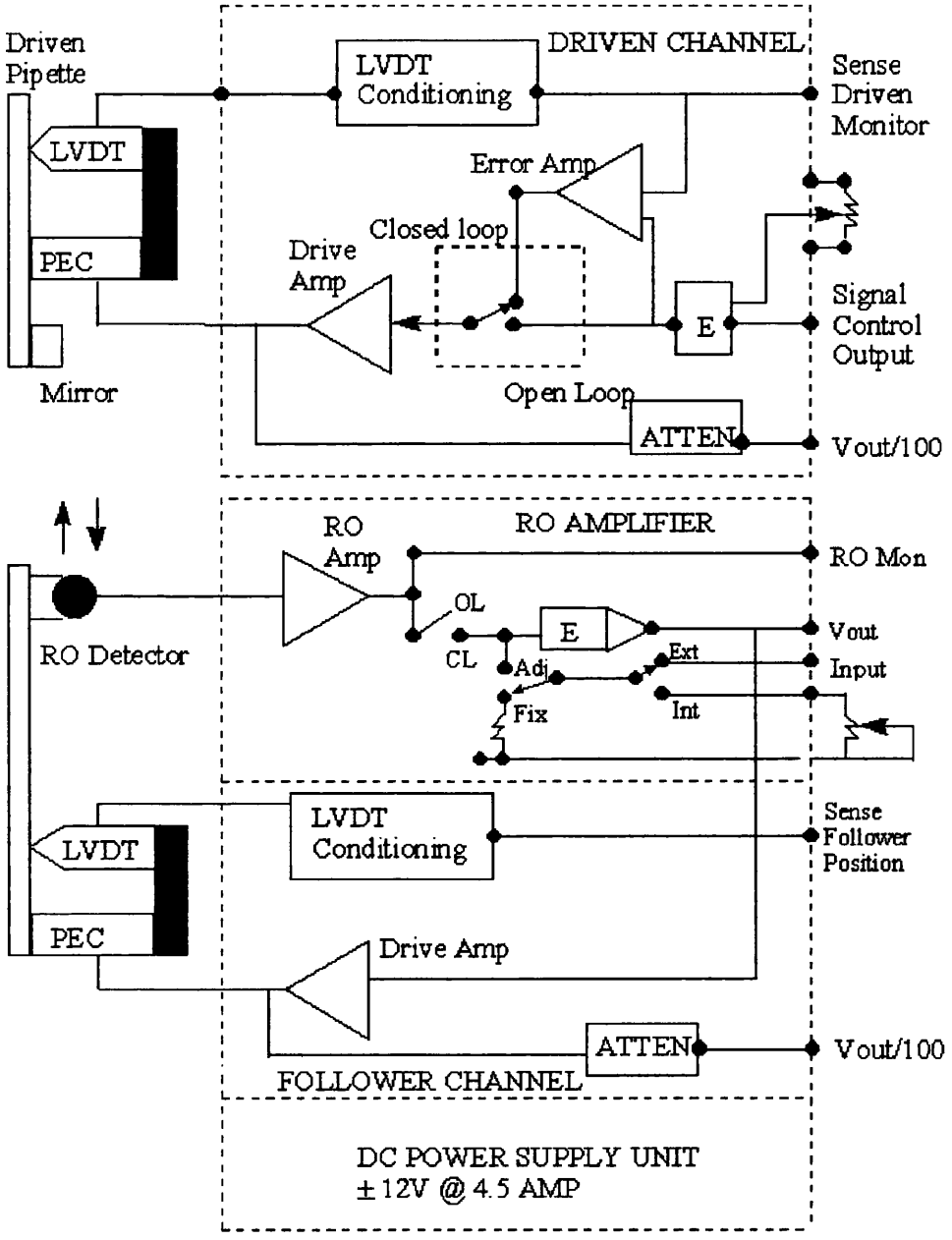

Figure C–3 Circuit diagram of control electronics.

To control the follower a reflecto-optic (RO) sensor is used to linearly detect the position of the edge of the mirror in its field. This signal is used to drive the RO amplifier.

The amplifier output provides the input to the drive amplifier on a second single channel control module E810.10. The follower drives a PI P810.10 (15μm expansion) piezo electric crystal and the position is measured by a PI E115.21 LVDT.

The equipment is 240V AC (alternate current) mains powered via a fused IEC mains socket on the rear panel together with a power on switch. Internally the equipment is provided with a modular power supply type HSU 100-32, manufactured by Contact Lambda providing 12V @ 5amps and –12V @ 0.5 amps.

PI Operating manual PZ54E describes the set up and operation of the E810.10 module. All jumper links are placed for standard settings.

C.1.1 Equipment set-up

Figure C–4 is a schematic of the electronically controlled mechanical assembly on the microscope stage as viewed from above. The optically clear dish is not represented to simplify the schematic.

The driven movement of both the driven PEC and the follower PEC is in a left and right horizontal plane. Movement in other directions is achieved by manual manipulation of the micrometers. The cylindrical body of the RO sensor has its major axis perpendicular to the horizontal and optically senses objects 4.5 mm above its face when the external medium is air and 1.5 mm when the pipette is submerged in water.

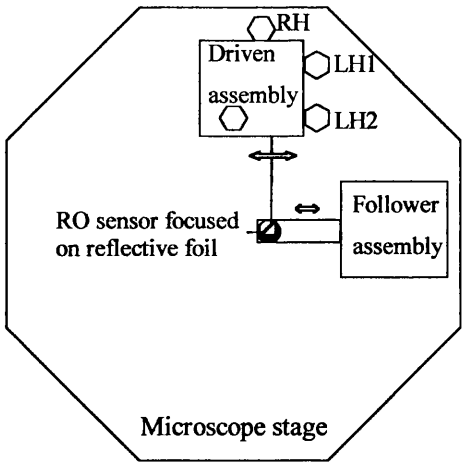

Figure C–4 Schematic of electronically controlled stage parts. LH and RH stand for left and right hand manipulator, respectively.

Often the set-up depends on the experiment to be carried out. However, in most cases it is necessary for the movement of the follower to be located about at the centre point of the driven movement. i.e.,

Driven channel's range (30μm) ⟷ P810.30

Follower channel's range (15μm) ⟷ P810.10

This allows non-invasive control over the whole range of the follower.

C.1.2 Driven channel set-up

To set up the driven channel the control unit must first be switched off before the leads are connected. The control unit can then be switched back on again. At all times, it is important to note that output voltages of up to 120V occur on the central pin of the connectors to the PECs on the front panel of the equipment. The mode of operation is then switched to open loop (switch on front panel), and the driven potentiometer set to 5.0 (if travel is required only in one direction they are set 15% away from limit of the potentiometer). Alternative the potentiometer is left to 0.0 and the value 5.0 is inputted via software (see section C.1.5). With the LVDT in an uncompressed condition, the

voltage on the driven sensor test point is monitored, and the LVDT is then slowly compressed. Figure C–5 shows the output voltage characteristics of a LVDT with compression, and the set-up point is indicated (here further compression results in an increase in the output of the LVDT above 5 volts and vice-versa). Compression can be achieved either with the LVDT grub screw (mounted against the LVDT on the micromanipulator assembly) or by the LH1 (left hand) micrometer of the micromanipulator (Figure C–4). The sensed voltage is adjusted to +5.0 ± 0.05V (point indicated on Figure C–5 as set-up). The LVDT electronics are set up so that full PEC expansion results approximately in a 10 volt change from the LVDT sense output. The mode of operation is then switched to closed loop (CL), if the set-up is correct the sensed voltage should remain at +5.0 ± 0.5V.

The driven channel is now set up to follow an input signal, provided that it is within the range ±5.0V and frequency <10Hz. From this point no alterations of the grub screw or the LH1 micrometer are required. The RH (right hand) and LH2 micrometer are used to move the whole driven assemble without altering the set-up conditions.

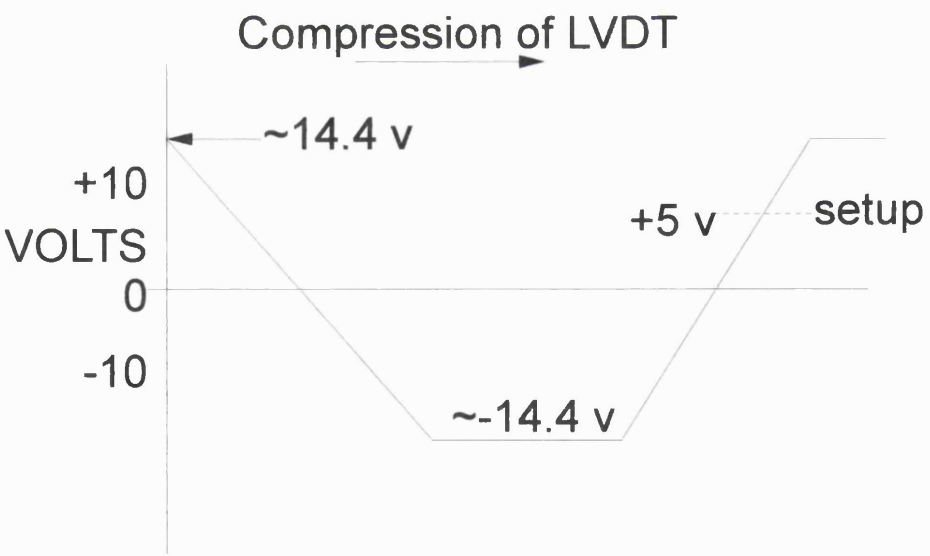

Figure C–5 Voltage output characteristics of a LVDT.

C.1.3 Follower channel set-up

Before starting the follower set-up, the driven channel has been set to CL and 5.0 on the potentiometers and have no input signal (section D.4). The three front panel switches (on the RO amplifier board) are then set to OL, FIX and INT. The RO sensor is positioned for total reflection from the mirror with a separation of approximately 4.5mm for gas (air) phase work and 1.5 mm for liquid (water) phase work. The output of MON1 is monitored and by vertical adjustment of the RO sensor, the most negative signal in the range 0 to –5V is sought (if the mirror is too good the sensor becomes over sensitive). The RO device is then moved to the edge of the mirror (either by moving the driven or the follower assemblies) until the voltage at MON2 is 0.0 ±0.05V. The light spot from the RO sensor is now on the edge of the mirror.

The FIX setting demands a 50% open loop expansion (alternative starting positions are possible by selecting ADJ and using the potentiometers). The mode of operation is now switched to closed loop (CL), if correctly set up the PEC stays at 50% expansion. The uncompressed follower LVDT, should now be compressed (as with the driven channel) until the set up point is reached and measures 5.0 ± 0.05V.

A variation of the driven channel should now result in a corresponding change in the follower channel, subject to compatibility with its smaller range.

C.1.4 Adjustments and calibration

The driven and follower side have different internal amplifications. Thus this has to be allowed for in their voltage change against distance moved calibration (see section C.1.6).

The switch positions work as follows. When the fix/adj. switch is on 'fix', the int/ext switch is inoperative. With the fix/adj switch on 'fix', the electronics are set so that when the LVDT and PEC are set up in the open loop state, the PEC is half-way through its total travel (i.e. at 50% expansion). Closing the loop should introduce only a small error demand, so that it is stable.

If set up at one end of the PECs travel is required, the fix/adj. switch is set to 'adj'. The voltage output to the PEC can then be adjusted. With the int/ext switch on 'int', the potentiometer on the front will adjust the position. With the int/ext switch on 'ext', the potentiometer is inoperative. Instead, an external voltage (e.g. from a computer output) can be used to control the position.

C.2 Code for data acquisition

To convert the analogue voltage values of the LVDTs to digital values capable of being logged, an IBM PC compatible Advantech PCL-818HD data acquisition card is fitted to the computer. It incorporates 12-bit A/D conversion with a ± 10 volt input range, D/A conversion with an output range of 0 to 10 volts and a timer / counter with a maximum time base of 100MHz.

To control the functions of the data acquisition card, it was necessary to write a computer program. This program, written originally by Fairbrother [5] in the computer language C, was modified during the course of the present research to control the rate of particle separation (usually 1 μm/s) and to set the driven voltage without using the potentiometer on the front panel of the control electronic. The software code is given in the following pages. The program works with a software driver (supplied by Advantech), which allows all the user defined options to be specified in a common parameter table.

The code was written and compiled using a Borland Turbo C environment. Where possible ANSI C code was used. A full explanation of the programming of the board can be found in the Advantech PCL-818HD user's manual.

When the program is started the keys F1, ↓, ESC are used to start recording data, to start the separation sequence and to exit the program, respectively. It is important to record start recording data before the separation is fired in order to acquire data during the formation of the liquid bridge.

```
/*****************************************************************/
/*                Channel 0 and 1 monitoring and driving program              */
/* Modified by D. Rossetti September 2001from Fairbrother's original source */
/*****************************************************************/

#include <stdio.h>
#include <conio.h>
#include <stdlib.h>
#include <dos.h>
#include <time.h>
#include <bios.h>

/* key definition */
#define UPARR        0x4800
#define DNARR        0x5000
#define ESC          0x11b
#define F1           0x3b00

extern pcl818HD(int, unsigned int *);
FILE *results;
unsigned int param[60];              /* Parameter array */
unsigned int AD_data[100];           /* Buffer for A/D data */
unsigned int DA_data[100];           /* Buffer for D/A data */
void board_error(void);              /* board_error function prototype */
void displaydata (void);             /* display data function prototype */

/* Pointer to get the segment and offset of arrays */
unsigned int far * dataAD;
unsigned int far * dataDA;

void displaydata (void);
```

```
int exitloop=0;
int readkey;
int sci=0;              /* signal control input via the computer */

int record_LVDTs;

float upvolt;           /* set the up voltage for separation via computer*/
float up12volt;         /* convert upvolt to 12 bit number */
float a=14.011;         /*constant for speed separation */
float k;                /*speed of separation */

float Follower;         /*****************************************************/
float Driven;           /*                                                   */
float Follower_Vout;    /* Holds data during conversion to a voltage value */
float Driven_Vout;      /*                                                   */
float RO_Mon1;          /*                                                   */
float RO_Mon2;          /*****************************************************/

/* local time code */

time_t timer;
struct tm *tblock;

int main()
{
/* print top of screen */

clrscr();
printf("\n************************************************************");
printf("\n*                                                          *");
printf("\n* Great Channel Monitoring And Driving Program             *");
printf("\n*                                                          *");
```

```
printf("\n*****************************************");
printf("\n\n      F1-start  ESC-quit program ");
gotoxy(17,10);
printf("Results file is RESULTS.CSV load in Excel");

/* ask for and set initial voltage output */
gotoxy(17,15);
printf("Input the up voltage to drive separation");
gotoxy(17,16);
printf("Range 0 - 10 volts:");
scanf("%f", &upvolt);          /* Get initial up voltage */
up12volt = upvolt * 409.6;     /* Convert up voltage to 12bit number */
gotoxy(17,18);
printf("Input the speed of separation [microns/sec]:");
scanf("%f", &k);               /* Get the speed of separation     */
gotoxy(17,19);
printf("Do you want to record LVDTs data [1/0]?:");
scanf("%d", &record_LVDTs);        /* Get the flag to record LVDTs data */

/* PARAMETER TABLE */

param[0] = 0;          /* Board no. for this parameter table. 0: 1st board */
param[1] = 0x320;      /* Card base I/O address */
        /* This is set on the card by switch SW1 */

/* Trigger pacer rate = (card base frequency) / (C1 * C2)*/
/* = base freq. / (param[5] * param[6])*/
param[5] = 1000;       /* Pacer divider constant C1 */
param[6] = 100;        /* Pacer divider constant C2 */
param[7] = 0;          /* Trigger mode, 0: pacer trigger */

dataAD = AD_data;                  /* Get the address of the A/D data buffer */
```

```
param[10] = FP_OFF(dataAD);        /* Offset of A/D data buffer A */
param[11] = FP_SEG(dataAD);        /* Segment of buffer A */
param[12] = 0;          /* Offset of A/D data buffer B. If B not used, set to 0 */
param[13] = 0;          /* Segment of A/D data buffer B. If B not used, set to 0 */
param[14] = 6;          /* Number of A/D conversions */
param[15] = 0x0;        /* A/D conversion start channel */
                        /* Follower piezo is measured on channel 0 */
param[16] = 0x5;        /* A/D conversion stop channel */
                        /* Driven side piezo is measured on channel 1 */
param[17] = 8;          /* Overall gain. 8: +/- 10V */
        /* See Appendix C of PCL-818HD User's Manual: page 117 for details */

/* D/A param[] definitions */

dataDA = DA_data;   /* Get the address of the D/A data buffer */
param[20] = FP_OFF(dataDA);        /* Offset of D/A data output buffer A */
param[21] = FP_SEG(dataDA);        /* Segment of D/A output bata buffer A */
param[22] = 0;          /*    Offset of D/A data buffer B. If B not used, set to 0 */
param[23] = 0;          /*    Segment of D/A data buffer B. If B not used, set to 0 */
param[24] = 1;          /*    D/A conversion number */
param[25] = 0;          /*    D/A conversion start channel */
param[26] = 0;          /*    D/A conversion stop channel */

/* param[45] holds the return error code, 0 if no error */
/* Appendix A of PCL-818HD User's Manual has full list or error codes */

/* INITIALISATION OF THE AD/DA CARD*/

pcl818HD(3, param);     /* Initialise driver */
        if (param[45] != 0) {board_error();}

pcl818HD(12, param);    /* D/A initialization */
```

```
        if (param[45] != 0) {board_error();}

pcl818HD(100, param);     /* Initialise card A/D */
        if (param[45] != 0) {board_error();}  /* check for errors */

/* Return any param[45] error code */
/* A param[45] value of 2 means the driver has not been loaded */
/* The PCL-818HD.EXE program loads the driver as a TSR program (P.3 of manual) */

/*results = fopen("RESULTS.CSV", "w");*/

/*LOAD THE LVDTs TO UPVOLT VALUE */
for (;;) {
        sci+=1;
        dataDA[0] = sci;
        pcl818HD(13, param);
                if (sci>up12volt)       {
                sci=up12volt ;
                dataDA[0] = up12volt ;
                pcl818HD(13, param);
                break;
                                        }
        }

/* PROGRAM LOOP */

while (exitloop==0)
{
        pcl818HD(101, param);     /* A/D conversion with S/W data transfer */
        if (param[45] != 0) {board_error();}  /* check for errors */
        displaydata();
        if (bioskey(1)==0) continue;
```

```
        readkey=bioskey(0);

        switch(readkey){

case ESC:
        exitloop=1;
        break;

case F1:
        results = fopen("RESULTS.CSV", "w");

                pcl818HD(101, param); /* A/D conversion with S/W data transfer */
                if (param[45] != 0) {board_error();}  /* check for errors */
                displaydata();
                if (record_LVDTs==1)
                fprintf(results," %1.3f, %1.3f, %s", Follower, Driven, asctime(tblock));

case DNARR:

        for(;sci-a*k>0 && !kbhit();sci=sci-a*k)
                {
                pcl818HD(101, param);     /* A/D conversion with S/W data transfer */
                if (param[45] != 0) {board_error();}  /* check for errors */
                displaydata();
                if (record_LVDTs==1)
                fprintf(results," %1.3f, %1.3f, %s", Follower, Driven, asctime(tblock));
                dataDA[0] = sci;
                pcl818HD(13, param);
                }

                        }
}
```

```
fclose(results);
return 0;
}

/* DISPLAY ACQUIRED DATA FROM BUFFER */
                /**************************************************
                The top four bits of each A/D data element hold the channel no.
                We mask off the top four bits from the 16 bit data then convert it
                to a voltage according to the gain and inout range
                **************************************************/

void displaydata (void)
{
        Follower = AD_data[0] & 0xFFF;
        Follower = ( (10 - (-10)) * Follower / 4096) + (-10);

        Driven = AD_data[1] & 0xFFF;
        Driven = ( (10 - (-10)) * Driven / 4096) + (-10);

        Follower_Vout = AD_data[2] & 0xFFF;
        Follower_Vout = ( (10 - (-10)) * Follower_Vout / 4096) + (-10);

        Driven_Vout = AD_data[3] & 0xFFF;
        Driven_Vout = ( (10 - (-10)) * Driven_Vout / 4096) + (-10);

        RO_Mon1 = AD_data[4] & 0xFFF;
        RO_Mon1 = ( (10 - (-10)) * RO_Mon1 / 4096) + (-10);

        RO_Mon2 = AD_data[5] & 0xFFF;
        RO_Mon2 = ( (10 - (-10)) * RO_Mon2 / 4096) + (-10);

        /****************************************
```

```
            (10 – (–10)     A/D input range (-10V to 10V)
            4096            Full scale for 12-bit A/D data
            Follower & Driven  : A/D input data
            (–10)           A/D input range (-10V)
        ********************************************/

/* Time code */

timer = time(NULL);         /* Gets the time of day */
tblock = localtime(&timer);  /* Converts date/time to a structure */

gotoxy(17,11);
if (record_LVDTs==0)
printf("LVDTs DATA ARE NOT RECORDED");
else
printf("LVDTs DATA WILL BE RECORDED DURING SEPARATION ");

gotoxy(24,13);
printf("%s", asctime(tblock));

gotoxy(17,15);
printf("Channel 0: Follower LVDT     = %1.3f Volts   ", Follower);
gotoxy(17,16);
printf("Channel 1: Driven LVDT       = %1.3f Volts   ", Driven);

/*if (record_LVDTs==1)
fprintf(results," %1.3f, %1.3f, %s", Follower, Driven, asctime(tblock));*/

gotoxy(17,18);
printf("Channel 2: Follower Vout/100 = %1.3f Volts   ", Follower_Vout);
gotoxy(17,19);
printf("Channel 3: Driven Vout/100   = %1.3f Volts   ", Driven_Vout);
```

```
gotoxy(17,20);
printf("Channel 4: RO Amplifier Mon1 = %1.3f Volts   ", RO_Mon1);
gotoxy(17,21);
printf("Channel 5: RO Amplifier Mon2 = %1.3f Volts   ", RO_Mon2);

gotoxy(22,23);
printf("Output voltage = %1.3f Volts      ", sci/409.6);
gotoxy(22,24);
printf("Output number = %4d     ", sci);
gotoxy(22,25);
printf("Speed of separation = %3.1f microns/sec  ", k);
}

/* BOARD ERROR FUNCTION */

void board_error(void)
{
        printf("\nDriver initialisation failed!");
        if (param[45] == 2) {
                printf("\nDriver not installed\nRun the PCL818HD.EXE program.");
                }
        printf("\nParam[45]=%d See Appendix A  page 98\n", param[45]);

        while(!kbhit()) {delay(10);}  /* waits until a key is pressed */

        exit(1);
}
```

C.3 Processing computer data

The computer program used (see section C.1.5) acquires LVDT voltage information from the A/D board at a rate of 8 readings per second. This information is stored along with time information in a CSV (comma separated variable) file. The software package Microsoft Excel can then be used to open and process the data. Initially the comma separated variable file contains information as shown in Table 23.

Follower LVDT [V]	Driven LVDT [V]	Time
A	B	C
5.36	5.16	Sun Feb 04 19:15:19 2001
5.31	5.13	Sun Feb 04 19:15:19 2001
5.28	5.04	Sun Feb 04 19:15:19 2001
5.28	5.05	Sun Feb 04 19:15:19 2001
5.14	5.01	Sun Feb 04 19:15:19 2001
5.15	4.92	Sun Feb 04 19:15:19 2001
5.16	4.93	Sun Feb 04 19:15:19 2001
5.01	4.88	Sun Feb 04 19:15:20 2001

Table 23 Sample of raw computer acquired data for calibration.

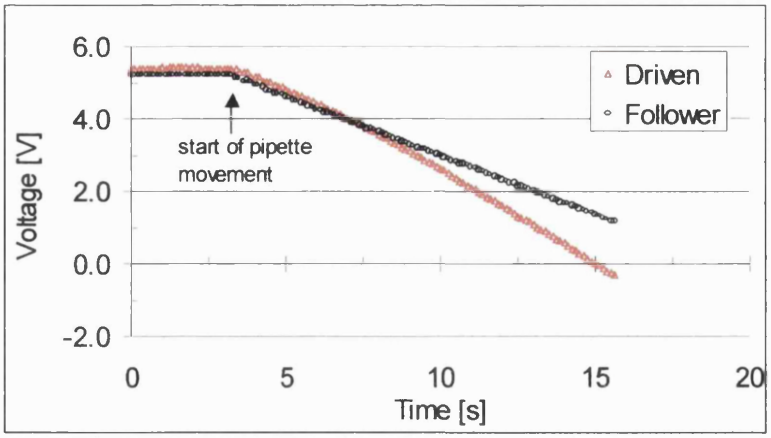

Figure C–6 Plot of driven and follower data aquired during calibration.

The initial work is done to calibrate the voltage reading in order to obtain the correspondent movement of the pipette. In this phase, the flexible pipette moves freely in water at desired speed (usually 1 μm/s). The plot in Figure C–6 shows the voltage acquired by both the follower and the driven during this movement. Initially it is necessary to calculate the change in voltage output of the LVDTs (columns 1 and 2). This is done by taking a value for the outputs of the LVDTs at zero movement (in this case 5.36 volts for the follower and 5.16 volts for the driven) and subtracting these values from the readings acquired any 0.125 s (frequency of acquisition decided in the software). If the set velocity is 1 μm/s, at the N^{th} reading both the driven and the follower have moved on 0.125 x N x 1 μm. From the variation of signal of the LVDT's during the same span of time (usually 6–7 seconds) the conversion factor movement/voltage were obtained. For the follower it resulted in the value of –1.81 μm/V, whilst for the driven the value –3.00 μm/V was obtained. These were typical values and have been used to calculate the force separation plot for liquid bridges

Different raw plot data are obtained during an experiment of liquid bridge separation.

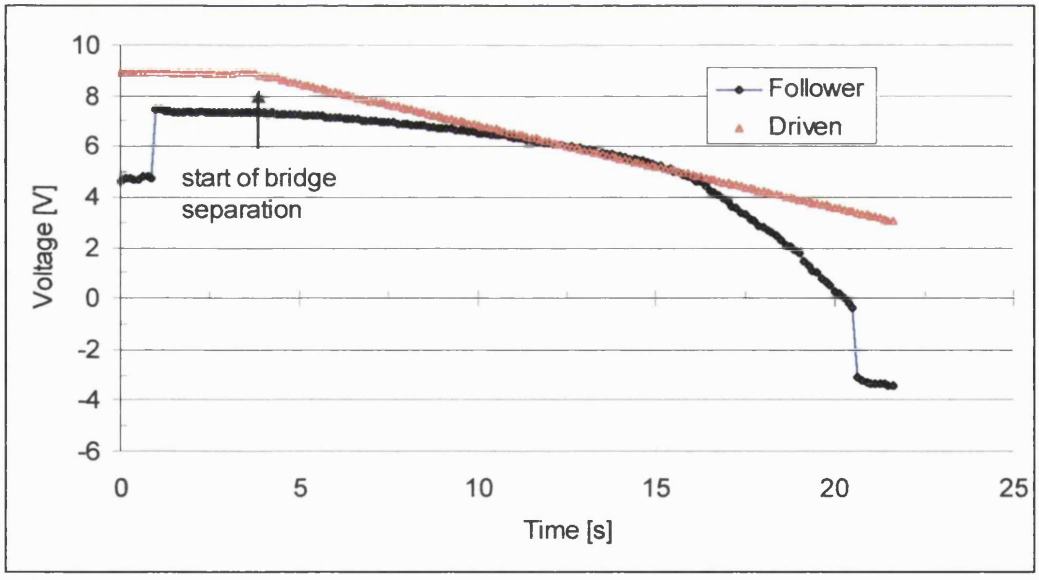

Figure C–7 Typical plot data for liquid bridge separation.

In Figure C–7 the typical plot of a liquid bridge separation is shown. The data are recorded before the liquid bridge is formed between the two particles. The static pipette

is approached, manually, to the flexible pipette and at some close proximity the bridge is formed, which is showed by the discontinuity recorded after ~1 s. The initial deflection of the pipette gives the initial value of the liquid bridge adhesion, F_{in}. After the separation is started, the driven expands linearly, whilst the movement of the follower is "retarded" by the resistance exerted by the liquid bridge. This behaviour explains the rounded shape of the follower LVDT as seen in Figure C–7. The second discontinuity shown on the follower curve indicates the rupture of the bridge (after ~20 s). At that point the recording is stopped.

To convert the voltage data into particle separation and force exerted on the flexible pipette requires a few simple calculations provided the spring constant of the pipette. and the initial separation between the particles are known (see Table 24). Initially it is necessary to calculate the change in voltage output of the LVDTs (columns 3 and 4). This is done by taking a reference value for the outputs of the LVDTs (in this case 7.319 V for the follower and 8.745 V for the driven) at the initial conditions of separation (6.467 μm) and force (0.465 μN) and subtracting these LVDTs values from new acquired readings.

The calibration of change of voltage with distance moved for the LVDTs (set by the electronics) is then used to calculate the movement of the LVDTs in microns. In this case the value in column 3 is multiplied by –1.80 to give column 5 and the value in column 4 by –3.02 to give column 6.

The distance moved by the follower plus the initial reference distance (6.467 μm) the separation distance between the particles (column 7)

The distance moved by the driven (column 6) subtracted from the distance moved by the follower LVDT (column 5) gives the amount of bend in the pipette in microns (column 8). This value can then be multiplied by the pipette force constant (in this case 0.06 μN/μm) to give the force exerted on the flexible pipette (column 9).

The last part of the Table 24 shows the discontinuity exhibited by the follower at the moment of rupture. Table 24 refers to the experiment indicated as B17 in section 6.2. The experimental rupture distance measured by image analysis was 19.4 μm, which is closer to the value obtained on the penultimate row (20.33 μm), when the liquid bridge is not yet broken. This situation was also confirmed in all the other experiments carried out using the electronic control capability of the MFB.

Follower (Volts) 1	Driven (Volts) 2	Δ Follower (Volts) 3	Δ Driven (Volts) 4	Follower move (μm) 5	Driven move (μm) 6	Separation (μm) 7	Pipette bend (μm) 8	Force (μN) 9
7.319	8.745	0	0	0		6.467	0	0.465
7.295	8.706	-0.024	-0.039	0.043	0.118	6.511	0.075	0.470
7.29	8.633	-0.029	-0.112	0.052	0.338	6.520	0.286	0.482
7.285	8.594	-0.034	-0.151	0.061	0.456	6.529	0.395	0.489
7.275	8.55	-0.044	-0.195	0.079	0.589	6.547	0.510	0.496
7.275	8.516	-0.044	-0.229	0.079	0.692	6.547	0.612	0.502
7.271	8.472	-0.048	-0.273	0.086	0.824	6.554	0.738	0.509
7.236	8.428	-0.083	-0.317	0.149	0.957	6.617	0.808	0.514
7.231	8.389	-0.088	-0.356	0.158	1.075	6.626	0.917	0.520
7.227	8.354	-0.092	-0.391	0.166	1.181	6.633	1.015	0.526
7.217	8.306	-0.102	-0.439	0.184	1.326	6.651	1.142	0.534
7.188	8.267	-0.131	-0.478	0.236	1.444	6.703	1.208	0.538
Readings before liquid bridge rupture								
-0.161	3.442	-7.48	-5.303	13.464	16.05	19.931	2.551	0.618
-0.386	3.403	-7.705	-5.342	13.869	16.13	20.336	2.264	0.601
-3.101	3.364	-10.42	-5.381	18.756	16.21	25.223		

Table 24 Sample of processed raw data for force versus separation curves for MFB experiments.

Appendix D: Additional data for the AFM experiments

This Appendix refers to the measurements of the DLVO interaction between glass ballotini and oil droplet submerged in water. This section describes the software used to control the AFM, the calibration of the voltage readings obtained from the PSD (position sensitive device) in order to convert them into the cantilever movement and the spreadsheet used to convert the PSD readings into the DLVO force.

D.1 Software used with the AFM

The software used to carry out an experiment with the AFM includes the programs used to control the vertical movement of the Burleigh motor, to log data from the PSD, and to acquire the movement of the glass cell using the Zygo interferometer. The programs used to control the Burleigh motor and the PSD were created using graphical programming environments under VisSim (Visual Solution Inc.) and softWIRE (softWIRE®), respectively, whilst the movement of the cell was monitored using the software ZMI 1000 provided by Zygo Corporation. VisSim and softWIRE provides a graphical environments in which it is possible to add blocks to log data from the acquisition electronic boards which receive signals from the Burleigh motor (CIO-DA08) and from the PSD (CIO-DA801)

i) Control of the Burleigh motor

The file *motor.vsm* drives the Burleigh controller (see section 5.2.1) that ultimately moves the piezo Zstage (InchWorm 701-00 motor; 25mm range no encoder) in vertical direction. A buzz or a ticking coming from the Zstage indicate proper functionality. The buzz is for high speed of movement (1mm/s). The controller is driven by frequency, which is transformed into velocity according to (5.2), which is repeated here for convenience and was given in the Burleigh instruction manual,

$$v_{motor}\,(mm/s) = \frac{2 * 0.0039}{\frac{1000}{frequency(Hz)} + 0.0002} \qquad (5.2)$$

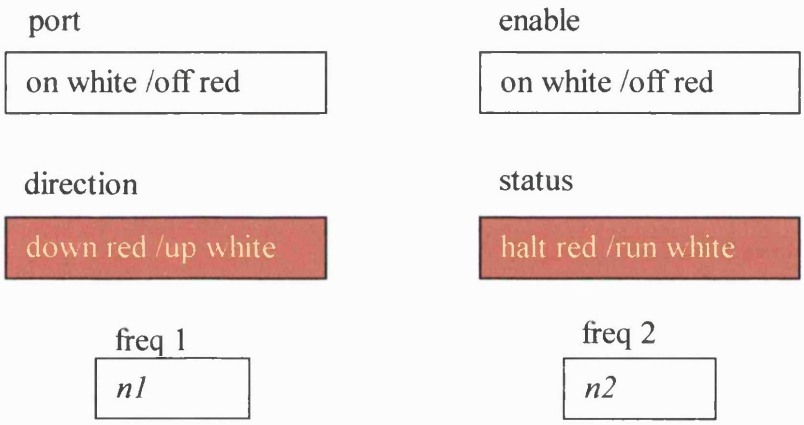

Figure D–1 Graphical layout of the program *motor.vsm* used under VisSim to control the Burleigh motor.

The software works by simply hitting the buttons with the pointer of the mouse which turns the background of the button white to red and vice versa accordingly whilst in the frequency fields (freq 1, freq 2) numbers are inputted. The port and enable buttons establish the communication with the CIO-DA08, whilst direction and status are used to drive the motor. working frequency of the motor and therefore velocity, can be modified changing the value of *n2* and *n1* that act directly on the output counter channels (OCCs) of the acquisition board.

The clocking frequency of the PCLK bus (pace clock) in the computer is 11.1 MHz and is divided by two at the entrance of the CIO-DAS08 board (5.55MHz) to be triggered by two OCCs in the board in order to obtain the required frequency for the Burleigh controller. Both OCCs can be varied in the range 0-65355 as integers.

OCC2 (*n2*) triggers the signal from the PCLK bus as it enters in the board (5.55MHz), whilst OCC1 (*n1*) operates on the frequency output from OCC2. Determination of

frequency of the PCLK bus was obtained using an oscilloscope-and measuring the frequency of OCC2 with *n2* =2 (reading = 2.777 MHz)

The frequency to be used in (5.2) to have the expected velocity can be obtained in different ways by playing either with *n1* or *n2* integer numbers. A table of *n1, n2* values is reported in Table 25.

v [μm/s]	*n1*	*n2*	Frequency sent to Burleigh motor [Hz]
0.01	8664	500	1.28
0.1	4813	90	12.8
1	481	90	128
10	48	90	1282
100	215	2	12886
1000	20	2	135135

Table 25 Value for *n1* and *n2* used to vary the vertical speed of the Burleigh motor in the range 10 nm - 1 mm.

ii) Acquisition from PSD

The data acquisition and control board CIO-DA801 acquires the amplified signal from the position sensitive device LSC 30-D (see section 5.2.1) used to tranform the laser beam reflected from the cantilever into a voltage output. Due to the high frequency of acquisition required during experiments of DLVO interaction (500 or 1000 Hz), VisSim was not able to comply with acquisition and, therefore, a different graphical programming software (softWIRE), available at University of Maine, was used instead. The layout of the program used (*PSDacq*) is shown in Figure D–2. The user can input the frequency and output data file. The program is first started to verify that the laser beam reflected from the back of the cantilever was correctly focused in the LSC 30-D and after the particle was approached in close proximity with the oil droplet using the Burleigh motor, the acquisition was finally started. An Excel file can store 32000 data per column and to avoid the inconvenience of recording only 32 s (at 1000 Hz) the *PSDacq* was programmed to rewrite on the same column. The engulfment of the

particle in the oil was signalled by an abrupt variation of the voltage and at that point the software was immediately stopped to avoid that rebuffering of data could overwrite valuable information. A typical output of the raw data file obtained using *PSDacq* has been shown in Figure 6-45.

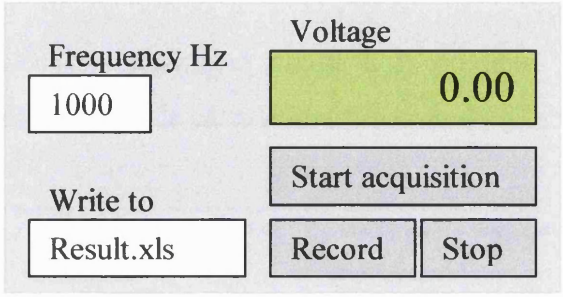

Figure D–2 Graphical layout of the program *PSDacq* used under softWIRE to acquire data from the LSC 30-D position sensitive device.

iii) Acquisition of cell movement

The acquisition of the glass cell movement, which has been used to transform the cantilever voltage into a displacement, has been done with the program ZMI 1000 provided from Zygo corporation. The software output is in the form of an array of data containing displacement and time of the acquisition. Data are copied into an Excel spreadsheet to carry out further analysis. The ZMI 1000 software allowed also to verify the nominal velocity of the glass cell inputted according to (5.2) with the measured value obtained from the Zygo interferometer. Variation between 5% and 10% were observed.

D.2 Cantilever voltage calibration and force spreadsheet

The conversion of the cantilever voltage signal into displacement is done forcing the cantilever to deform against the bottom of the glass cell (filled with water) which is driven at a known velocity. The voltage signal is recorded from *PSDacq* at a known frequency and therefore the $\frac{V}{s}$ constant is determined. Meanwhile the ZMI 1000

software records the effective speed of the cell ($\frac{\mu m}{s}$) and dividing the latter constant by the former the $\frac{\mu m}{V}$ calibration factor was obtained which resulted in the value of 1.35 for all the experiments.

Using the calibration factor determined above it is possible to determine the force separation curve by means of simple calculations illustrated in Table 26.

Time	PSD	Cantilever deflection	Force F	Droplet movement	Separation	F/R
(s)	(Volts)	(μm)	(N)	(nm)	(nm)	(N/m)
1	2	3	4	5	6	7
0	-0.0977	0.00E+00	0.00E+00	48.23	49.23	0.00E+00
0.002	-0.0977	0.00E+00	0.00E+00	48.13	49.13	0.00E+00
0.004	-0.0977	0.00E+00	0.00E+00	48.04	49.04	0.00E+00
0.006	-0.0928	6.59E-03	7.91E-10	47.94	48.94	9.62E-05
0.008	-0.0928	6.59E-03	7.91E-10	47.85	48.85	9.62E-05
Particle droplet interaction						
0.78	-0.0879	1.32E-02	1.58E-09	11.49	12.49	1.92E-04
0.782	-0.0830	1.98E-02	2.37E-09	11.40	12.40	2.89E-04
0.784	-0.0732	3.30E-02	3.96E-09	11.30	12.30	4.81E-04
0.786	-0.1270	-3.96E-02	-4.75E-09	11.21	12.21	-5.77E-04
0.788	-0.1221	-3.30E-02	-3.96E-09	11.11	12.11	-4.81E-04
Particle droplet engulfment						
1.022	-0.0977	-2.64E-02	-3.16E-09	0.38	1.38	-3.85E-04
1.022	-0.0977	-1.98E-02	-2.37E-09	0.19	1.19	-2.89E-04
1.024	-0.1025	-6.59E-03	-7.91E-10	0	1	-9.62E-05
1.026	-0.2539					

Table 26 Sample of processed raw data for force versus separation curves for AFM experiments.

The reference voltage (column 2) at time 0 (column 1)is used as te reference value to evaluate the cantilever deflection (column 3) at time t. This is obtained (column 3) by difference with the value at time 0 and multiplying the voltage variation by the calibration factor 1.35 $\frac{\mu m}{V}$. The cantilever deflection (column 3) is multiplied by the maniufacturer's cantilever spring constant (0.12 N/m for this experiment) and the experimental force is calculated (column 3). The particle droplet separation could not be measured experimentally since the interferometer failed to sense the oil-water interface (see section 5.2.3). In the calculations reported in this thesis, the separation just before particle-droplet engulfment it is assumed to be 1 nm (see section 5.2.3).. The engulfment of the particle is observed when the voltage reading shows an abrupt variation. From the data reported in Table 26 this happened between the time 1.024 s and 1.026 s where the voltage "jumps" from –0.102 V to –0.205 V. The particle droplet separation is considered 1 nm at t = 1.024 s, as shown in column 6. Separations at which particle and droplet are further apart is determined by summing the pre engulfment separation distance (1 nm) to the movement of the droplet. This latter movement is assumed to be equal to the movement of the cell, therefore, neglecting the deformation of the oil water interface. In this calculation the cantilever deflection was not taken into account because of the extreme oscillations of these value (Figure 6-45). The movement of the oil droplet (column 5) is obtained multiplying the time variation by the motor (glass cell) speed which resulted 47 nm/s as measured from the Zygo interferometer instead of the nominal value of 50 nm/s inputted by means of (5.2). Column 7 is obtained by dividing column 4 by the radius of the particle (8.2 μm). The frequency of acquisition of the cantilever signal for the data presented in Table 26 was 500 Hz. The data refers to the plot presented in Figure 6-46.

Appendix E: Publication, Conferences, Seminars and Company reports

E.1 Publications referred in this thesis

Rossetti, D., Pepin, X. and Simons, S. J. R., Rupture energy and wetting behaviour of pendular liquid bridges in relation to the spherical agglomeration process. *J. Colloid Interface Sci.*, Accepted for publication.

Rossetti, D. and Simons, S. J. R., A micro-scale investigation of liquid bridges in the spherical agglomeration process. *Powder Technol.*, **130** (1-3), 49–55 (2003).

Pepin, X., Rossetti, D. and Simons, S. J. R., Modelling pendular liquid bridges with a reducing solid-liquid interface. *J. Colloid Interface Sci.* **232**, 298-302 (2000).

Pepin, X., Rossetti, D., Iveson, S. M. and Simons, S. J. R., Modelling the evolution of pendular liquid bridges in the presence of large wetting hysteresis. *J. Colloid Interface Sci.* **232**, 289-297 (2000).

E.2 Other publications related to the work presented in this thesis

Simons, S.J.R. and Rossetti, D., Interparticle forces in spherical agglomeration. *Physicochemical Problems of Mineral Processing*, **36**, 159-172 (2002).

Simons, S. J. R., Pepin, X. and Rossetti, D., Predicting granular behaviour through micro-mechanistic investigations. *Int. J. Miner. Process.*, Accepted for publication.

Pepin, X., Simons, S. J. R., Blanchon, S., Rossetti, D. and Couarraze, G., Hardness of moist agglomerates in relation to interparticle friction, granule liquid content and nature. *Powder Technol.* **117**(1-2), 123-138 (2001).

E.3 Conference proceedings

Simons, S.J.R. and Rossetti, D. Interparticle forces in spherical agglomeration. *Physicochemical Problems of Mineral Processing Symposium XXXIX*, Wroclaw, Poland, 16th-18th September 2002.

Rossetti, D. and Simons, S.J.R. Investigation of liquid bridges and particle surface properties in spherical agglomeration processes. *Proc. 6th World Congress Chem. Eng.*, Melbourne, Australia, 23rd-27th September 2001.

Rossetti, D. and Simons, S.J.R. A micro-scale investigation of liquid bridges in the spherical agglomeration process. *Proc. 7th Int. Symp. Agglom.*, **1**, 137-146, Albi, France, 29th-31st May 2001.

Rossetti, D., Pepin, X. and Simons, S.J.R. Dewetting phenomena during liquid bridge separation. *Proc. AIChE Annual Meeting*, Los Angeles, USA, 12th-17th November 2000.

Rossetti, D. and Simons, S.J.R. A micro-scale investigation of liquid bridges in the spherical agglomeration process. *Proc. AIChE Annual Meeting*, Los Angeles, USA, 12th-17th November 2000.

Rossetti, D. and Simons, S.J.R. Towards sustainable mineral extraction: A micro-scale investigation of liquid bridges in the spherical agglomeration process. Symposium on Powder Technology – Future Trends, *Proc. 14th Int. Congr. Chem. Eng.*, CHISA, Prague, Czech Republic, 27th-31st August 2000.

Rossetti, D. and Simons, S.J.R. A micro-scale investigation of liquid bridges in the spherical agglomeration Process. *Particle Technology Forum 2*, Guildford, Surrey, 29th-30th June 2000.

Rossetti, D., Pepin, X. and Simons, S.J.R. Dewetting phenomena during liquid bridge separation. *Particle Technology Forum 1*, Birmingham, 1st-2nd September 1999.

Simons, S.J.R. and Rossetti, D. A micro-scale investigation of liquid bridge and surface properties in the spherical agglomeration process. Submitted to Int. Mineral Processing Conference XXII, Cape Town, South Africa, 2003.

E.4 Seminars and Company reports

Rossetti, D., Pepin, X., and Simons, S. J. R., A micro-mechanistic approach to the modelling of binder induced agglomeration. Presented at UMIST, Mineral Processing Research Day. Manchester (UK) 9th July 1999.

Simons, S.J.R., Rossetti, D. and Pagliai, P. (2001). Assessing the Performance of Different Binders in Relation to the Agglomeration of Paracetamol: A Feasibility Study Using A Novel Micro-Force Balance. Report presented to Merck, Sharp and Dohme.